

UC Berkeley

UC Berkeley Electronic Theses and Dissertations

Title

Engineering Principles for Quantitative Measurement Tools for Single-cell Biology and Pandemic Response

Permalink

<https://escholarship.org/uc/item/35s282qn>

Author

Gopal, Anjali

Publication Date

2021

Peer reviewed|Thesis/dissertation

Engineering Principles for Quantitative Measurement Tools for Single-cell Biology and
Pandemic Response

by

Anjali Gopal

A dissertation submitted in partial satisfaction of the

requirements for the degree of

Doctor of Philosophy

in

Bioengineering

in the

Graduate Division

of the

University of California, Berkeley

Committee in charge:

Professor Amy E. Herr, Chair

Professor Hana El-Samad

Professor Nir Yosef

Summer 2021

Engineering Principles for Quantitative Measurement Tools for Single-cell Biology and
Pandemic Response

Copyright 2021
by
Anjali Gopal

Abstract

Engineering Principles for Quantitative Measurement Tools for Single-cell Biology and
Pandemic Response

by

Anjali Gopal

Doctor of Philosophy in Bioengineering

University of California, Berkeley

Professor Amy E. Herr, Chair

From single cells to whole organisms, the development of quantitative tools underpin key advances in biology and medicine. In the past decade, novel microfluidic measurement tools have enabled the study of single-cell, and subcellular, systems providing insight into biological heterogeneity often masked by bulk biological measurements. In parallel, many emergency situations, including the decontamination of limited supplies of personal protective equipment (PPE) during the coronavirus 2019 (COVID-19) pandemic, requires the development of robust, quantitative workflows to ensure effective pathogen inactivation and minimize risk to the end user. In this work, we look at the fundamental principles behind quantitative tool development for two broad classes of problems: (1) single-cell immunoblotting, and (2) ultraviolet C (UV-C) decontamination of N95 filtering facepiece respirators (FFRs) during crisis capacity conditions.

First, we consider single-cell immunoblotting (scI), which enables detection of protein isoforms (proteoforms) from single cells via single-cell polyacrylamide gel electrophoresis (PAGE) and immunoblotting in a hydrogel. Several proteoforms, including the truncated HER2 isoform found in breast cancer tissue, often play key roles in disease progression and resistance. In order to detect and understand the mechanism of how these proteoforms occur, we investigate three key principles of scI: first, we assess factors that impact detection of multiple protein targets from the same cell. Specifically, we investigate the fundamental physicochemical principles that govern multiplex target detection in scI, and develop a quantitative system to assess protein target retention in hydrogels upon multiple immunoprobings rounds. Next, we investigate quantification principles for scI and assess ways in which detection of low abundance protein targets is impacted by different quantification methods. Specifically, by investigating segmentation-based quantification of scI, we find that we are able to detect more low-abundance protein targets than state-of-the-art methods. Third, we discuss preliminary investigations for measurements of multiple types of biomolecules from the same

cell, including proteoform and RNA detection. In particular, we investigate outstanding challenges in the simultaneous extraction and detection of RNA and protein during scI, and assess avenues for synchronizing the long binding timescales needed for RNA extraction with the short PAGE timescales necessary for single-cell proteoform detection.

Finally, we investigate quantitative principles for UV-C decontamination of N95 FFRs. We begin by surveying the literature for the current understanding of best practices for UV-C decontamination of N95s. We then explore the use of photochromic indicators (PCIs) to validate UV-C dose, and discuss how PCIs may allow end-users to take into account aspects such as respirator geometry and placement in a decontamination system when measuring applied dose. We conclude by discussing best practices for UV-C dose reporting, and highlight which types of common errors can confound dose measurements.

Taken together, we anticipate that the results of this work will advance the fields of both single-cell measurements and pandemic response. In the field of single-cell measurements, we anticipate that the conclusions of this study will provide strategies to aid in the understanding of proteoform dynamics and regulation within heterogeneous cell populations. In the field of pandemic response, we anticipate that the results of our UV-C decontamination work will not only aid in the re-use of N95 respirators during crisis capacity conditions, but will also aid in the development of quantitative workflows to decontaminate other types of PPE.

To Amma and Achan

Acknowledgments

“If I have seen further, it is by standing upon the shoulders of giants.”

—Sir Isaac Newton

This thesis is not only a culmination of years of hard work, but also of a reflection of the generosity of the vast numbers of people who helped my research get to where it is today.

First, I would like to acknowledge the various funding sources that helped support my graduate work: the Natural Sciences and Engineering Research Council of Canada’s Post-graduate Fellowship (NSERC PGS-D, 487496), UC Berkeley’s John and Elizabeth Lewis Scholarship, and the Siebel Foundation. My advisor, Prof. Amy E. Herr’s, additional funding from the National Institutes of Health and the Chan Zuckerberg Biohub Investigator Program were also critical in supporting this work.

I would like to thank many of the collaborators who worked with us on our various projects: first, I am grateful to Dr. Emery Goossens, Dr. Patrick Medina, and Prof. Rebecca Doerge, who defined some of the initial questions relating to segmentation and deep learning of single-cell immunoblots. Additionally, I am also grateful to the N95DECON consortium, who were instrumental in paving the way to have a group, and a forum, to collaborate with on our UV-C decontamination work. While the members of N95DECON are too numerous individually name in this section, I would like to give special thanks to Tyler Chen, Dr. Sylvia Smullin, Prof. Manu Prakash, and Prof. David Rempel for their leadership and guidance. I am also grateful to Joshua Cantlon and the rest of the Scienion Cellenone team for the countless hours they spent troubleshooting the Cellenone droplet printer with me. Finally, I am deeply grateful to Prof. Aaron Streets, and many members of the Streets lab, including Dr. Nick Altemose, Dr. Zoë Steier, Anushka Gupta, Annie Maslan, and Rodrigo Cotrim Chaves. To the Streets lab: your generosity in sharing your equipment and expertise was instrumental to the progress of one of my key research directions, and greatly enriched my understanding of the challenges of single-cell sequencing.

The Stanley Hall/QB3 community is a powerhouse that offers key resources and expertise to junior and senior researchers alike. I would like to express significant gratitude to Paul Lum of the BNC, Mary West of the CTAF, and Justin Choi of the FGL for many hours of consulting and conversation on experimental setup and workflows. QB3’s large administrative team supporting research staff and graduate students also deserve gratitude: thank you to Kristin Olson, Rocio Sanchez, Sarah Jane Taylor, Victoria Ross, Kathleen Sutton, April Alexander, and Jeannie Powers. I like to extend special thanks to Catherine Dea, who responded to every email and purchase order at the speed of light. Our lab would not be as functional without you. Additionally, the staff at shipping and receiving helped us manage many, many orders: thank you to Mike Bentley, Chris Hardin, Martin Moreno, and Kevin. Finally, I would be remiss if I did not take the time to thank the building staff and QB3 directors for ensuring that we were able to manage personal safety with lab access during

a global pandemic: thank you to Thom Opal, Harry Stark, Cherry Chung, Donna Hendrix, Susan Marqusee, Kris Thompson, Dave Rogers, and Geoff Bingaman.

The UC Berkeley/UCSF Graduate Program in Bioengineering gives us a special opportunity to work with faculty across two campuses, and I am deeply appreciative of all the time I had to connect with many of these faculty members. To my qualifying exam committee, Prof. Lydia Sohn, Prof. Aaron Streets, Prof. Bo Huang, and Prof. Clay Radke – thank you for pushing me on my fundamental knowledge and understanding of my research. To my dissertation committee members, Prof. Hana El-Samad and Prof. Nir Yosef, thank you for encouraging me to think about the “bigger picture” of my work, and to carefully plan out my next steps. In addition, I am grateful to the Bioengineering Association of Students (BEAST), which provided a home and a key support system in my first few years of graduate school. BEAST was one of the key reasons why I chose to do my graduate research at UC Berkeley, and I am still very appreciative for the engagement of our lively student body.

At this point, I would like to take the time to extend my deepest gratitude to the single most important person who defined and shaped my PhD: my graduate advisor, Prof. Amy E. Herr. There are many wonderful reasons why people may choose to pursue a scientific career (passion, intellectual freedom, pushing the boundary of knowledge) but Amy is singularly unique because she, above all else, cares about the *impact* she has on her students and the world. She is a scientist who is committed to the service of others, which is thoroughly demonstrated by her mentorship style. Every task she asks a student to do is geared toward their growth as a researcher. She has been endlessly supportive of all of my non-academic aspirations, from taking supplementary courses in statistics and machine learning, to doing an internship at a non-profit, to supporting my applications for fellowships in biosecurity and pandemic preparedness. Her energy is boundless, and she has 99th percentile grit. Amy: I have learned so much from you. I cannot thank you enough for giving me the opportunity to work in your lab.

Working with a team of researchers as talented as the Herr lab has been one of the greatest privileges of my PhD. I remember being starstruck by this group of ambitious, young scientists when I first arrived at UC Berkeley, and the profound respect I have had for my colleagues has not wavered during my full six years in the program. To Sam, Julea, and Kevin: thank you for being role models in my first couple of years in the lab; I really looked up to your example as I progressed through my many years of graduate school, and your mentorship shaped me into the scientist I am today. To Hector, Eli, John, Elaine, and Shaheen: thank you for being mentors and friends. I appreciated every tough question you threw at me during group meetings and qualifying exam practice talks. To Hector, especially: thank you for providing virtual advice even long after you had graduated (#belikehector). To Alisha, Ali, Andoni, and Kristine: I could not have asked for a better peer group to work with during graduate school. I have learned so much from each of you, and I am grateful that you “adopted” me into the 2016 cohort. To Kristine, especially: thank you for being one of the best friends I could have asked for; there were some days when our WhatsApp chat was the only thing that got me through the final stretch of a late-night experiment. Finally, to Alden, Louise, Ana, Gabi, Yaw, Preethi and Kunal: I am grateful for the ability to have

worked with each of you, and am continually blown away by your intellect, determination, and kindness. I truly consider myself extremely fortunate to have had such a phenomenal group of mentors, peers, and colleagues to work alongside while completing a PhD.

I would also like to thank the many people outside of school who supported me during these past six years. First, to the “Nanos”, aka Julia, Dushanth, Krishna, Kevin, Ammar, and Michael: thank you for every phone call, virtual movie night, and Christmas party. Our decade of friendship has been invaluable to me, and I cannot wait to see where this next decade takes us. To Lindsey, thank you for being the UCSF to my Berkeley; I appreciated walking every painful mile with you (including crying while the rest of our cohort graduated without us). To Ruby and Andrew: thank you for the many years of encouragement and support, and for continually pushing me to prioritize my mental health and well-being. To Elizabeth and Amber, thank you for giving me the tools for greater personal insight and reflection. To the Effective Altruism and rationality communities in the Bay Area and beyond: I am so grateful to have spent the last six years within a network of people who are committed to making the world a better place. Thank you for teaching me that there is no shame in caring deeply, thinking carefully, and trying hard. To Tara Aunty, Sreedharan Uncle, Tanu, and Srikanth: thank you for welcoming me so warmly into your home when I moved to California. I appreciated every Thanksgiving dinner I was able to attend over the last several years, and am hoping we can celebrate together again this November.

And finally, to my family: Amma, Achan, Chechi, Vineet Chettan, Ammuma, Mutachan, Latha Chechi, Sanjana, and Rohan. I would not be where I am without you. To Amma and Achan especially, thank you for investing in me, in education, and in supporting Chechi and me through every stage of our life. I realize that moving to a completely new country and raising two young girls could not have been easy. Your generosity, steadfastness, and love are what give me courage to take every step into the unknown. Thank you for every sacrifice you have made for us. I love you.

Contents

Contents	v
List of Figures	viii
List of Tables	x
1 Introduction	1
1.1 Background and Thesis Overview	2
1.2 The Importance of Single Cell Protein Measurements	3
1.3 Fundamentals of Single-cell Immunoblotting	4
1.4 Quantification Strategies for Single-cell Immunoblotting	6
1.5 Strategies for Multimodal Single-Cell Immunoblotting	7
1.6 Strategies for Quantitative UV-C Dose Measurements	9
Bibliography	10
2 Multiplexed in-gel microfluidic immunoassays: characterizing protein target loss during reprobing of benzophenone-modified hydrogels	15
2.1 Introduction	15
2.2 Methods	17
2.3 Results and Discussion	20
2.4 Conclusion	35
Bibliography	38
3 Segmentation-Based Analysis of Single-cell Immunoblots	43
3.1 Introduction	43
3.2 Theory and Data Analysis	46
3.3 Materials and Methods	52
3.4 Results	52
3.5 Discussion	60
Bibliography	63

4	Multimodal detection of protein isoforms and nucleic acids from low starting cell numbers	67
4.1	Introduction	67
4.2	Materials and Methods	68
4.3	Results and discussion	72
4.4	Conclusions	80
	Bibliography	82
5	Towards dual RNA sequencing and proteoform measurements from single cells	86
5.1	Introduction	86
5.2	Materials and Methods	88
5.3	Results and Discussion	91
5.4	Conclusion and Next Steps	100
	Bibliography	102
6	Current Understanding of UV-C Decontamination of N95 Filtering Face-piece Respirators	105
6.1	Background	105
6.2	Summary of literature review	108
6.3	Summary and outstanding questions	119
6.4	Conclusions	120
	Bibliography	122
7	Quantitative UV-C dose validation with photochromic indicators for informed N95 emergency decontamination	129
7.1	Introduction	129
7.2	Materials and Methods	132
7.3	Results and Discussion	140
7.4	Conclusions	153
	Bibliography	155
8	Best Practices for Germicidal Ultraviolet-C Dose Measurement for N95 Respirator Decontamination	159
8.1	Introduction	159
8.2	UV-C for N95 Respirator Decontamination	160
8.3	Key Germicidal UV-C Specifications: Wavelength and Dose	162
8.4	Critical UV-C Source and Detector Metrics	163
8.5	Common Measurement Pitfalls	165

8.6	Best Practices for UV-C Measurements and Methods	166
8.7	Reporting Summary Examples	170
	Bibliography	172
9	Conclusions and Future Directions	177

List of Figures

1.1	Overview of single-cell immunoblotting	5
1.2	Quantification of single-cell immunoblots	6
2.1	Hypothesized mechanism of immunoassay signal loss in BMPA hydrogels and device fabrication to test hypothesis.	21
2.2	Thermocycling experiments demonstrate stability of protein/fluorophore conjugates upon denaturation.	22
2.3	Monitoring loss of immobilized protein target from BMPA hydrogels during chemical stripping.	24
2.4	Data analysis workflow for stripping experiments using BMPA hydrogels with immobilized proteins.	25
2.5	Signal loss of immobilized protein target from BMPA hydrogels from rounds 11 – 29.	26
2.6	Monitoring SNR of immobilized protein targets from BMPA hydrogels during chemical stripping.	28
2.7	SDS and heat are primary contributors to protein loss during the stripping process.	29
2.8	Protein size is not a substantial contributor to protein loss.	31
2.9	Comparison of Fluorescence Loss Between Protein-Conjugate and Immunoreagents during Serial Stripping and Reprobing Cycles.	33
2.10	False-color micrographs of BMPA hydrogels immobilized with RNase-488 and immunoprobed with antibody.	34
2.11	Normalized intensity of residual immunoprobng fluorescence after stripping rounds.	35
3.1	Single-cell immunoblotting and downstream quantification interrogates isoform expression levels in single cells.	45
3.2	Protein band quantification methods between segmentation and Gaussian fitting are not equivalent.	47
3.3	Manual quality control measures enable users to filter out badly segmented separation lanes from downstream analysis.	49
3.4	Segmentation correlates well with Gaussian fitting for spot volume and SNR. . .	54
3.5	No significant difference in distributions of spot volume and SNRs for inferred positive separation lanes identified with Gaussian fitting pipeline versus both pipelines.	55

3.6	Decreasing protein band width leads to greater SNR truncation with Gaussian fitting.	57
3.7	Segmentation-based detection of ER α isoforms shows good agreement when $R_S > 0.6$	58
3.8	Deep learning accurately classifies and segments scI protein bands.	62
4.1	Multimodal measurements by fractionation PAGE coupled with laser excision of microwells into gel pallets for off-chip analysis of nucleic acids.	74
4.2	PCR amplification of TurboGFP DNA from a gel pallet containing a single TurboGFP-expressing U251 cell nucleus.	76
4.3	Photo-blotted and immunoprobed protein quantitation correlates with protein expression measured prior to lysis.	77
4.4	RT-qPCR amplification of mRNA from gel pallet containing single TurboGFP-expressing U251 cell nucleus.	79
4.5	Semi-RT-qPCR amplification of TurboGFP mRNA from gel pallets correlates with same-cell protein expression measurement.	80
5.1	Proposed Design for Dual Single-cell RNA Sequencing and Proteform Detection from Single Cells	87
5.2	Varying Lysis and Binding Conditions Increases mRNA Capture Rates to Beads	92
5.3	Varying PCTE Membrane Pore Sizes Changes Lysis Timescales.	95
5.4	Lysis Buffer Exchange Between DLB and 2X RIPA + 8M Urea Facilitates Protein Solubilization.	96
5.5	WTA Size Distributions Demonstrate Successful In Situ RT and PCR.	98
7.1	Mechanism and challenges of UV-C for N95 decontamination.	131
7.2	Robust color measurement facilitates UV-C dose quantification from two models of PCIs.	143
7.3	Comparison of calibration fit functions for PCI2.	144
7.4	Relative uncertainty on measurements using alternate color difference metrics.	146
7.5	Angular response affects quantification of spatial nonuniformity.	147
7.6	Quantifying PCIs elucidates UV-C treatment questions not measurable with radiometers.	149
7.7	The potential applications for UV-C quantification from PCIs could be broadened using widely available color measurement tools.	151
7.8	Quantitative in-process UV-C dose validation of N95 decontamination cycles using PCIs could be feasible using optical attenuation to extend the dynamic range beyond 1.0 J/cm^2	152
8.1	Factors affecting UV-C dose distribution and measurement for N95 respirator decontamination.	162

List of Tables

1.1	Benchmarking Table of Dual Single-cell Protein and RNA Measurement Techniques	8
2.1	P-Values for Mann-Whitney U-Tests Between Photobleaching Control and Treatment Group for Rounds 11 - 29	27
2.2	Physicochemical Properties of Proteins Immobilized in BMPA Hydrogels and their Respective Signal Losses upon 7 Rounds of Stripping	32
3.1	Change in Inferred Positive Separation with Gel Density	56
3.2	Properties of “False Positive” Micrographs Identified with the Deep learning Pipeline	61
5.1	Lysis Buffer Compositions	94
6.1	Efficacy of UV-C for inactivation of microorganisms	111
6.2	Impact of UV-C on N95 FFR integrity	115
6.3	Published implementation strategies for UV-C N95 treatment	118
7.1	Fit functions, inverse fit functions, and partial derivatives used in uncertainty calculations for calibrated measurements.	136
7.2	RM200QC measurement uncertainties $s_{\Delta E}$ for various metrics of color quantification and two models of PCI. Each uncertainty reports the standard deviation of N=15 measurements of replicate unexposed PCIs. We observe higher measurement uncertainty for PCI1, which we attribute to heterogeneity (dots and striations) in the colored PCI coating.	136
7.3	Specifications for robust UV-C measurements	141
8.1	Common pitfalls in UV-C dose measurement for N95 decontamination.	167
8.2	Importance of Considering Over- and Under-reporting of UV-C Dose	168

Chapter 1

Introduction

Materials reproduced, with permission, from:

A. Gopal and A.E. Herr, “Multiplexed in-gel microfluidic immunoassays: characterizing protein target loss during reprobing of benzophenone-modified hydrogels”, *Scientific Reports*, 2019.

A. Su*, S. M. Grist*, A. Geldert, A. Gopal, and A. E. Herr, “Quantitative UV-C dose validation with photochromic indicators for informed N95 emergency decontamination”, *PLOS ONE*, 2020.

E. Rosàs-Canyelles, A. J. Modzelewski, A. E. Gomez Martinez, A. Geldert, A. Gopal, L. He, and A. E. Herr, “Multimodal detection of protein isoforms and nucleic acids from low starting cell numbers”, *Lab on a Chip*, 2021.

S. M. Grist, A. Geldert, A. Gopal, A. Su, H. B. Balch, A. E. Herr, and the N95DECON Consortium, “Current Understanding of Ultraviolet-C Decontamination of N95 Filtering Facepiece Respirators”, *Applied Biosafety*, 2021.

A. Geldert*, H. B. Balch*, A. Gopal, A. Su, S. M. Grist, and A. E. Herr, “Best Practices for Germicidal Ultraviolet-C Dose Measurement for N95 Respirator Decontamination”, *J. Res. Natl. Inst. Stand. Technol.*, 2021.

A. Gopal and A. E. Herr, “Segmentation-Based Analysis of Single-cell Immunoblots”, *Electrophoresis*, 2021.

* Equal contributors

1.1 Background and Thesis Overview

From microscopic particles, including single cells and viruses, to whole organisms, the development of quantitative tools are critical for driving understanding and innovation in biology and medicine [1–4]. In the past decade, advances in quantitative measurements have stimulated fields of new inquiry in areas such as precision medicine, in which patient-centric measurements ranging from individual genetics to environmental factors to disease subtype are used to determine treatment options [5, 6]. A key example of the power of quantitative measurement tools occurred during the coronavirus 2019 (COVID-19) pandemic, wherein millions of individual patients were tested for COVID-19 through the use of reverse transcription, polymerase chain reaction (RT-PCR) tests [7, 8]. Without the development of PCR in 1983, rapid discovery and isolation of COVID-19 patients may have been infeasible during the pandemic.

The development of quantitative tools for single-cell biology has seen significant advancement over the past decade. However, outstanding challenges remain in several aspects of single-cell measurements, especially in the detection of single-cell proteoforms, which are protein isoforms arising from a range of processes including alternative splicing, alternative initiation to transcription, post-translational modifications, and others [9, 10]. Many of these proteoforms have been implicated in a range of disease states, including HER2+ breast cancer [11].

The development of quantitative workflows for crisis conditions has also seen significant advancement over the past year. During the COVID-19 pandemic, the development of decontamination workflows for personal protective equipment (PPE) required quantitative methodologies to ensure adequate viral inactivation and reusability of PPE [12–14].

In this dissertation, we shall broadly consider the advancement of quantitative tools for two key applications: single-cell proteoform measurements, and ultraviolet C (UV-C) decontamination of N95 filtering facepiece respirators. In the upcoming chapter, we will first review the importance of single-cell protein measurements, fundamentals of single-cell immunoblotting (scI), analysis principles for quantifying the results of single-cell immunoblotting, exploration of “multimodal” measurements, and finally, an overview of the importance of UV-C measurements for the COVID-19 response.

In chapter 2, we investigate the multiplexing capabilities of scI, specifically by evaluating the impact of stripping and reprobing chemistries on in-gel immunoassays. By utilizing fluorescently labeled target proteins, we quantify the loss in fluorescence signal as a proxy for protein loss during serial rounds of stripping, and assess the extent to which stripping buffer composition and physicochemical properties of proteins affect protein loss during the stripping and reprobing process.

In chapter 3, we evaluate quantification methodologies for scI, and compare the efficacy of segmentation algorithms to improve upon state-of-the-art Gaussian fitting approaches for scI. We investigate how separation resolution is a key factor that differentiates whether segmentation or Gaussian fitting approaches are more suitable for scI quantification, and investigate the use of deep learning models to further improve upon segmentation accuracy.

In chapters 4 and 5, we begin exploration of multimodal scI measurements, wherein RNA, DNA, and protein are detected from the same cell. Additionally, we lay the groundwork for dual single-cell RNA sequencing and immunoblotting measurements from the same cell, and investigate assay trade-offs during cell lysis and on-chip nucleic acid amplification.

In chapters 7 to 9, we investigate engineering principles of UV-C decontamination of N95 FFRs. We begin with a literature review on the current understanding of best practices for UV-C decontamination of N95 respirators. We then expand upon the current literature by outlining a workflow to assess photochromic indicators (PCI) for UV-C dose quantification and validation. Finally, we outline best practices for reporting of UV-C dose measurements on N95 respirators, and highlight how common errors in reporting can confound measurements.

1.2 The Importance of Single Cell Protein Measurements

The field of single-cell biology has seen rapid growth in the last decade, with the rise of new tools for single-cell sequencing, sorting, and imaging capabilities [15–17]. Single-cell measurement tools are critical for uncovering cellular heterogeneity that is masked in bulk measurements, where protein or nucleic acid measurements represent the “average” state from thousands to millions of cells [18]. Bulk measurements are especially susceptible to masking signal from rare cell subpopulations, such as circulating tumor cells [19]. Similarly, biospecimens with a small starting cell population (e.g., tumor biopsies or embryos) are also a poor fit for bulk assays, as these assays may not have the necessary sensitivity to detect low amounts of signal from few numbers of cells [20, 21].

The last decade has seen significant advancements in the field of single-cell nucleic acid measurements, including single cell DNA and RNA sequencing [15, 22, 23]. Single-cell RNA sequencing, in particular, offers an unbiased approach to measure hundreds to thousands of transcripts in single cells, allowing for the identification of critical biological phenomena such as cell subtypes and subpopulations, differentiation trajectories, and regulatory networks [15, 22]. However, single-cell RNA sequencing also has many disadvantages: first, due to factors such as transcriptional bursting and short lifetimes of mRNA molecules, transcriptome measurements are not always correlated with protein measurements, making them a poor proxy for determining the actual behaviour of the cell [24–26]. Second, RNA sequencing workflows are purported to have high RNA “dropout” rates; some estimates suggest that only 10% of the total transcriptome is captured in scRNA-seq workflows, leading to high technical variability [27, 28]. Finally, while RNA measurements can detect some isoforms, such as those formed by alternative splicing events, these techniques cannot detect isoforms that may have formed from post-translational modifications such as cleavage or phosphorylation events [21, 29, 30].

Conventional single-cell protein measurements, such as flow cytometry, or immunohisto-

chemistry or immunocytochemistry (ICC/IHC), can address several of the pitfalls of single-cell RNA measurements [31, 32]. Flow cytometry and ICC/IHC can directly measure protein through the use of targeted immunoreagents, reducing the technical variability present from transcript measurements [31, 32]. However, conventional single-cell protein measurements also suffer from non-specific binding of antibodies to off-target protein, confounding protein quantification. Furthermore, although the presence of isoform-specific antibodies, including antibodies that bind to certain epitopes or bind to phosphorylated proteins, can confer isoform specificity to ICC/IHC measurements, these antibodies are not always available, which limits protein target specificity [29, 33]. Tools such as single-cell mass cytometry also suffer from many of these same pitfalls, due to the fact that even mass cytometry-based approaches ultimately rely on immunoassay for readout and quantification [34].

A novel approach to single-cell protein measurements involves size- or charge-based separation of protein targets via a porous hydrogel matrix prior to protein target detection [21, 29, 33]. In the past decade, several assays have been developed that utilize these separation-based techniques, including single-cell western blotting, single-cell isoelectric focusing, single-cell differential detergent fractionation, single-cell identification and quantification separation (DUET), and others [21, 29, 30, 33, 35, 36]. We collectively refer to the techniques developed by Herr and co-authors as “single-cell immunoblotting” (scI), since the endpoint readout is an immunoassay of a single-cell protein blot. Although scI has the ability to confer isoform specificity to target protein, outstanding challenges remain in its sensitivity, ability to detect multiple proteins, and detection of multiple biochemical molecules [29, 37, 38]. We explore some of these challenges in the sections below.

1.3 Fundamentals of Single-cell Immunoblotting

Single-cell immunoblotting leverages microscale phenomena to miniaturize bulk electrophoretic separation methods, including western blotting and isoelectric focusing, in order to detect protein targets from picoliter volumes of cell lysate [21, 29, 33]. Cells are captured in 30 - 100 μm diameter microwells that are patterned onto 40 - 100 μm thick polyacrylamide (PA) hydrogels fabricated on glass slides (Figure 1.1A-B). Unlike with conventional western blotting, steps such as cell lysis, polyacrylamide gel electrophoresis (PAGE), and immunoblotting all happen in the same substrate [21, 29, 33]. Proteins are immobilized in the PA gel matrix via the use of benzophenone moieties, which perform hydrogen abstraction on proximal amino acid residues upon UV irradiation. Protein targets are then detected via labeling with primary, followed by secondary, antibodies. By utilizing small separation length scales (hundreds to thousands of microns) and rapid cell lysis and separation timescales (tens to hundreds of seconds), the final concentrations of proteins detected from scI still reside in the nanomolar range, allowing for immunoassay readout via laser microarray scanners (see Figure 1.1C) [21, 29, 33].

A critical factor in scI is the use of buffers to lyse cells *in situ* and inject proteins into the hydrogel during PAGE [21, 29, 33]. These dual functional lysis and electrophoresis

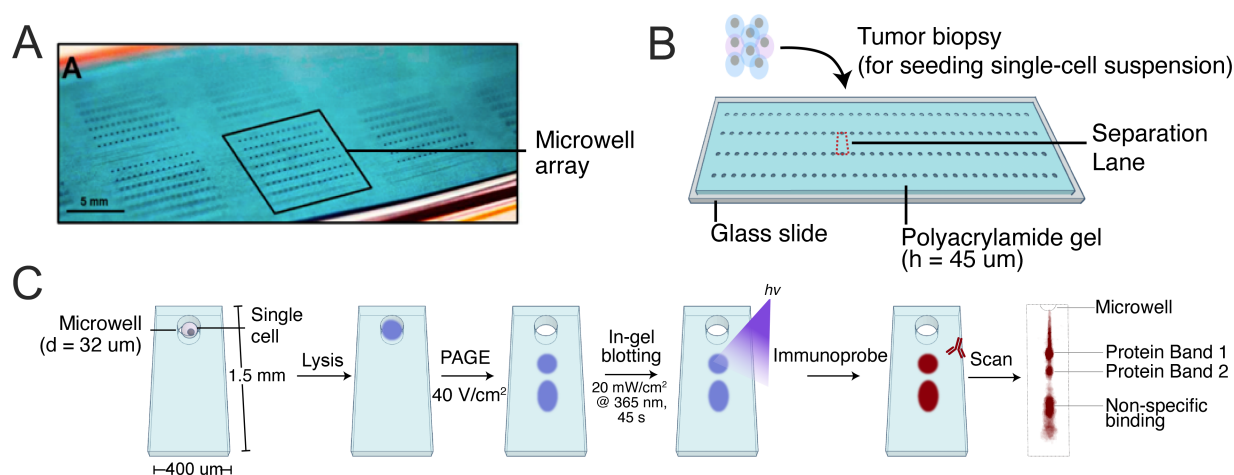


Figure 1.1: Overview of single-cell immunoblotting. (A) To fabricate scI chips, 40 - 100 μm thick PA gels are fabricated onto a 3" x 1" microscope slide. Image adapted from *Kang et al.*, 2016 [39]. In this image, blue dye has been added to the gel for ease of visualization. 30 - 100 μm diameter microwell arrays are patterned onto the PA gel. (B) Single-cell suspensions, such as that from a tumor biopsy, are seeded onto an scI chip. (C) Single cells are settled in 30 - 100 μm diameter microwells. By using a dual lysis and electrophoresis buffer, cells are lysed *in situ*, and proteins are injected into the gel during PAGE. UV irradiation activates benzophenone moieties to covalently link amino acid residues to the PA gel. Protein bands can be detected upon incubation with fluorescent antibodies. An example output from a single-cell immunoblot is seen on the right. Size separation of protein species enables detection of both protein isoforms, and off-target binding events.

buffers can affect key aspects of protein detection, including protein solubilization, injection profile dispersion, band broadening from factors such as joule heating, and preservation and detection of protein complexes [40–42]. In denaturing scI, the use of sodium or lithium dodecyl sulfate (SDS or LDS) groups allows for lysis of cell membranes, and confers negative charge to proteins, allowing for migration of protein species through the porous hydrogel towards the positive electrode upon application of an electric field. Additional reagents, such as sodium deoxycholate, Triton X-100, and urea also act to denature noncovalent protein interactions, improving protein solubilization and protein injection characteristics [40, 43].

Once cell lysate has been injected into, and photocaptured by, the benzophenone-functionalized PA gel, incubation with immunoreagents can be used to assess target protein [21, 29]. The majority of protein detection methods in scI follow conventional fluorescent immunoassay procedures: briefly, incubation with primary, followed by secondary labeled antibodies, can be used to detect specific protein targets. Furthermore, multiplex target detection can occur in one of two ways: first, utilizing antibodies with labels that span the 2 - 4 key wavelengths in microarray scanners can be used to detect multiple protein targets in one round

of immunoprobing. Second, stripping and reprobing approaches, in which an initial set of fluorescent antibodies are removed upon application of harsh denaturing agents such as SDS and β -mercaptoethanol, followed by reprobing with a new set of fluorescent antibodies, can be used to detect additional protein targets [37]. However, preliminary studies into stripping and reprobing chemistries have demonstrated a $\sim 50\%$ signal loss after 9 rounds of reprobing, which may limit multiplexing [29]. We discuss investigations to quantify the amount of protein loss during stripping and reprobing cycles in Chapter 2.

1.4 Quantification Strategies for Single-cell Immunoblotting

Protein targets in sCI take on Gaussian injection profiles, due to diffusional band broadening through the separation lane during PAGE [44]. By collapsing the two-dimensional (2D) separation profile into one-dimension (1D) by averaging the fluorescence intensity signal across the short axis of the separation lane, we can extract the corresponding electropherogram for the protein target of interest (see Figure 1.2) [44].

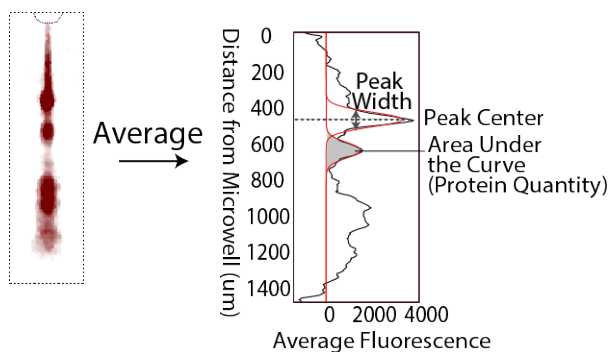


Figure 1.2: Quantification of single-cell immunoblots. Single-cell immunoblots are converted into a 1D electropherogram by averaging the fluorescence intensity signal across the short axis of the separation lane. By fitting the electropherogram to a Gaussian distribution, we can extract key parameters such as area-under-the-curve of the protein species, location of the peak center, and peak width.

The separation profile of a protein band can be approximated by a 1D Gaussian, as demonstrated in equation 1.1, where A represents the maximum amplitude of the Gaussian band, μ represents the peak center, and σ is proportional to the Gaussian peak width.

$$y = Ae^{\frac{-(x-\mu)^2}{2\sigma^2}} \quad (1.1)$$

In order to perform quantification of protein target, the area under the curve (AUC) of the 1D Gaussian profile can be calculated, by summing the averaged fluorescence intensity of the Gaussian $\pm 2\sigma$ from the peak center, μ . Signal from a Gaussian band is classified as a protein peak if the signal-to-noise ratio (SNR) of the band is ≥ 3 . In previously published quantification pipelines, the SNR is defined as the maximum amplitude of the Gaussian signal (A) divided by the background noise (standard deviation of background signal, $\sigma_{background}$) calculated from the edge of an individual separation lane [44] (see equation 1.2).

$$SNR = \frac{A}{\sigma_{background}} \quad (1.2)$$

In the evaluation of multiple proteoforms in the same separation lane, we additionally evaluate the separation resolution, R_S [45]. We define R_S in equation 1.3, where μ_1 and μ_2 correspond to the peak centers of the two protein targets of interest, and $4\sigma_1$ and $4\sigma_2$ correspond to each respective peak width [45]. When two protein targets are baseline resolved, ($R_S \geq 1.5$), there is a $< 1\%$ overlap in 1D Gaussian distributions [45].

$$R_S = \frac{|\mu_1 - \mu_2|}{\frac{1}{2}(4\sigma_1 + 4\sigma_2)} \quad (1.3)$$

Utilizing Gaussian fitting to quantify single-cell immunoblots has several advantages: the algorithms are computationally inexpensive, multiple protein targets can be quantified in a given separation lane (given $R_S > 0.5$), and it enables extraction of key electrophoresis parameters such as the peak center (μ) and peak width (4σ). However, Gaussian fitting approaches suffer when attempting to quantify protein bands with low SNR, significant noise near the protein band center, or when attempting to quantify protein bands with significant injection dispersion, leading to skew or kurtosis in the band profile. We assess alternative strategies for scI quantification in chapter 3.

1.5 Strategies for Multimodal Single-Cell Immunoblotting

An ongoing challenge in single-cell measurements is the detection of multiple biomolecules from the same cell. The detection of nucleic acids such as RNA, DNA, and protein can provide additional information about key biological questions such as elucidating regulatory networks, understanding transcriptional regulation, and cell subpopulation identification [15].

In the last decade, enormous progress has been made in tandem single-cell nucleic acid and protein measurements, especially tandem detection of RNA and protein. We describe a non-exhaustive list of several of these approaches in Table 1.1.

Approaches such as CITE-seq or REAP-seq, ECCITE-seq, and inCITE-seq have gained popularity in their ability to detect hundreds of protein targets, and thousands of transcripts, from single cells at high throughput [46–48, 52]. In these approaches, the detection of transcripts can occur through conventional bead- or barcode-based scRNA-seq, while proteins are

Table 1.1: Benchmarking Table of Dual Single-cell Protein and RNA Measurement Techniques

Assay Name	Type of Measurement	Measurement Technique	Drawbacks
CITE-Seq, REAP-Seq [46, 47]	100s of surface proteins + 100s of transcripts	Surface proteins: bar-coded antibodies with poly-A tails Transcripts: RNA sequencing	No intracellular proteins, no isoform detection without isoform-specific antibodies
inCITE-Seq [48]	<10 nuclear proteins + 100s of nuclear transcripts	Nuclear proteins: bar-coded antibodies with poly-A tails Transcripts: RNA sequencing	No cytosolic proteins, no isoform detection without isoform-specific antibodies
snapBlot [20]	Few cytoplasmic proteins + few transcripts	Cytoplasmic proteins: single-cell western blotting (including isoforms) Transcripts: qPCR	No detection of nuclear proteins, multiplexing of RNA is limited to few targets with qPCR, limited throughput (10s of cells)
INs-seq [49]	10s of intracellular proteins + 100s of transcripts	Intracellular proteins: fixation + FACS sorting Transcripts: bead or well-plate based RNA sequencing	No isoform detection without isoform-specific antibodies
PLA/PEA + qPCR [24]	Few proteins + few transcripts	Proteins: proximity ligation assay or proximity extension assay Transcripts: qPCR	No isoform detection without isoform-specific antibodies, lysate splitting reduces sensitivity
In-situ labeling approaches [50, 51]	Few proteins + few transcripts	Proteins: immunohistochemistry Transcripts: in-situ hybridization approaches	No isoform detection without isoform-specific antibodies, in-situ hybridization and immunohistochemistry sample prep approaches may be incompatible

detected through the use of antibodies barcoded with a poly-A tail. Due to the use of conventional immunoassay approaches for protein detection, techniques such as CITE-seq cannot detect proteoforms without isoform-specific antibodies which, as previously mentioned, are not always available for every unique protein isoform.

Dual measurement techniques that prepend electrophoretic separation of proteins prior to detection with an immunoassay, such as the snapBlot, have demonstrated the ability to detect proteoforms and RNA from low starting cell numbers without proteoform specific antibodies [20, 36]. However, the snapBlot can only detect cytoplasmic proteins, as it requires the use of mild lysis buffers to keep the nuclei intact for nuclear RNA detection via qPCR. As a result, these approaches limit the detection of membrane-bound proteoforms, or proteoforms that are found in the nucleus (e.g., transcription factors) [20, 36]. In chapters 4 and 5, we discuss additional strategies for performing RNA and proteoform measurements from the same cell.

1.6 Strategies for Quantitative UV-C Dose Measurements

Finally, we assess engineering principles for the development of quantitative methodologies for UV-C decontamination of N95 filtering facepiece respirators. Due to the shortage of N95 FFRs during the COVID-19 pandemic, the Centers for Disease Control and Prevention (CDC) had temporarily authorized the reuse of N95 FFRs for crisis capacity conditions [53]. UV-C radiation was identified as one of the most promising methods of decontamination of N95 FFRs. However, few standardized approaches exist for the development of UV-C decontamination workflows.

Quantitative measurements are essential for ensuring that UV-C decontamination of N95 FFRs achieves both pathogen inactivation (especially of SARS-CoV-2) and maintenance of respirator integrity (i.e., fit and filtration efficacy), while minimizing harm to the end-user. Critically, pathogen inactivation is dependent on both the wavelength and dose of UV-C applied to the respirator [54]. However, assessing the dose applied to UV-C respirators is dependent on several factors, including respirator geometry, UV-C system layout, placement of the respirator relative to the UV-C bulb, lamp instability, and more [55]. Furthermore, we find that choices in UV-C sensors can also have a large impact on the reported dose.

In chapters 6 - 7, we explore methods to validate and quantify the UV-C dose applied to N95 FFRs. We begin with a literature review on the current understanding of UV-C decontamination on N95 FFRs. We then explore approaches to develop a robust, quantitative workflow for assessing dose applied to N95 FFRs using photochromic indicators (PCI). Finally, we conclude with an overview of best practices for reporting UV-C dose measurements on N95 FFRs.

Bibliography

1. Coxon, C. H., Longstaff, C. & Burns, C. Applying the science of measurement to biology: Why bother? *PLoS Biology* **17**, e3000338. ISSN: 1545-7885. <https://journals.plos.org/plosbiology/article?id=10.1371/journal.pbio.3000338> (2019).
2. Sené, M., Gilmore, I. & Janssen, J. T. Metrology is key to reproducing results. *Nature* **547**, 397–399 (2017).
3. *Metrology in Biology — NIST* <https://www.nist.gov/bioscience/metrology-biology> (2021).
4. Squara, P., Imhoff, M. & Cecconi, M. Review Article: Metrology in Medicine: From Measurements to Decision, with Specific Reference to Anesthesia and Intensive Care. *Anesthesia and Analgesia* **120**, 66. [/pmc/articles/PMC4272233//pmc/articles/PMC4272233/?report=abstracthttps://www.ncbi.nlm.nih.gov/pmc/articles/PMC4272233/](https://pubmed.ncbi.nlm.nih.gov/3000338/) (2015).
5. Ashley, E. A. Towards precision medicine. *Nature Reviews Genetics* **2016 17:9** **17**, 507–522. ISSN: 1471-0064. <https://www.nature.com/articles/nrg.2016.86> (2016).
6. Dugger, S. A., Platt, A. & Goldstein, D. B. Drug development in the era of precision medicine. *Nature Reviews Drug Discovery* **2017 17:3** **17**, 183–196. ISSN: 1474-1784. <https://www.nature.com/articles/nrd.2017.226> (2017).
7. Vandenberg, O. *et al.* Considerations for diagnostic COVID-19 tests. *Nature Reviews Microbiology* **2020 19:3** **19**, 171–183. ISSN: 1740-1534. <https://www.nature.com/articles/s41579-020-00461-z> (2020).
8. *Total COVID-19 tests* <https://ourworldindata.org/grapher/full-list-total-tests-for-covid-19> (2021).
9. Arzalluz-Luque, Á. & Conesa, A. Single-cell RNAseq for the study of isoforms—how is that possible? *Genome Biology* **2018 19:1** **19**, 1–19. ISSN: 1474-760X. <https://genomebiology.biomedcentral.com/articles/10.1186/s13059-018-1496-z> (2018).
10. Ponomarenko, E. A. *et al.* The Size of the Human Proteome: The Width and Depth. *International Journal of Analytical Chemistry* **2016**. ISSN: 16878779 (2016).

11. Kang, C.-C. *et al.* Electrophoretic cytopathology resolves ERBB2 forms with single-cell resolution. *npj Precision Oncology* **2**, 10. ISSN: 2397-768X. <http://www.nature.com/articles/s41698-018-0052-3> (2018).
12. Rempel, D. *et al.* Hydrogen Peroxide Methods for Decontaminating N95 Filtering Facepiece Respirators. *Applied Biosafety*. <https://www.n95decon.org/team> (2021).
13. Grist, S. M. *et al.* Current Understanding of Ultraviolet-C Decontamination of N95 Filtering Facepiece Respirators. *Applied Biosafety*. www.liebertpub.com (2021).
14. Doyle, J. *et al.* Heat and Humidity for Bioburden Reduction of N95 Filtering Facepiece Respirators. *Applied Biosafety*. www.liebertpub.com (2021).
15. Stuart, T. & Satija, R. Integrative single-cell analysis. *Nature Reviews Genetics* **20**, 257–272 (2019).
16. Specht, E. A., Braselmann, E. & Palmer, A. E. A Critical and Comparative Review of Fluorescent Tools for Live-Cell Imaging. <http://dx.doi.org/10.1146/annurev-physiol-022516-034055> **79**, 93–117. <https://www.annualreviews.org/doi/abs/10.1146/annurev-physiol-022516-034055> (2017).
17. Hu, P. *et al.* Single Cell Isolation and Analysis. *Frontiers in Cell and Developmental Biology* **0**, 116. ISSN: 2296-634X (2016).
18. Altschuler, S. J. & Wu, L. F. Cellular Heterogeneity: Do Differences Make a Difference? *Cell* **141**, 559–563. ISSN: 00928674 (2010).
19. Millner, L. M. *et al.* Circulating Tumor Cells: A Review of Present Methods and the Need to Identify Heterogeneous Phenotypes. *Annals of clinical and laboratory science* **43**, 295. [/pmc/articles/PMC5060940//pmc/articles/PMC5060940/?report=abstract](https://pubmed.ncbi.nlm.nih.gov/24111247/)<https://www.ncbi.nlm.nih.gov/pmc/articles/PMC5060940/> (2013).
20. Rosàs-Canyelles, E. *et al.* Assessing heterogeneity among single embryos and single blastomeres using open microfluidic design. *Science Advances* **6**. ISSN: 23752548 (2020).
21. Kang, C.-c. *et al.* Single cell resolution western blotting. *Nature Protocols* **11**, 1508–1530. ISSN: 1754-2189. <http://dx.doi.org/10.1038/nprot.2016.089> (2016).
22. Hwang, B., Lee, J. H. & Bang, D. Single-cell RNA sequencing technologies and bioinformatics pipelines. *Experimental and Molecular Medicine* **50**. ISSN: 20926413. <http://dx.doi.org/10.1038/s12276-018-0071-8> (2018).
23. Gawad, C., Koh, W. & Quake, S. R. Single-cell genome sequencing: Current state of the science. *Nature Reviews Genetics* **17**, 175–188. ISSN: 14710064 (2016).
24. Darmanis, S. *et al.* Simultaneous Multiplexed Measurement of RNA and Proteins in Single Cells. *Cell Reports* **14**, 380–389. ISSN: 22111247. <http://dx.doi.org/10.1016/j.celrep.2015.12.021> (2016).
25. Larsson, A. J. M. *et al.* Genomic encoding of transcriptional burst kinetics. *Nature* **2019 565:7738** **565**, 251–254. ISSN: 1476-4687. <https://www.nature.com/articles/s41586-018-0836-1> (2019).

26. Schwanhäusser, B. *et al.* Global quantification of mammalian gene expression control. *Nature* **473**, 337–342. ISSN: 0028-0836. <http://www.nature.com/doi/10.1038/nature10098> (2011).
27. Westoby, J. *et al.* Obstacles to detecting isoforms using full-length scRNA-seq data. *Genome Biology* *2020 21:1* **21**, 1–19. ISSN: 1474-760X. <https://genomebiology.biomedcentral.com/articles/10.1186/s13059-020-01981-w> (2020).
28. Ziegenhain, C. *et al.* Comparative Analysis of Single-Cell RNA Sequencing Methods. *Molecular Cell* **65**, 631–643.e4. ISSN: 1097-2765. <http://www.cell.com/article/S1097276517300497/fulltext><http://www.cell.com/article/S1097276517300497/abstract>[https://www.cell.com/molecular-cell/abstract/S1097-2765\(17\)30049-7](https://www.cell.com/molecular-cell/abstract/S1097-2765(17)30049-7) (2017).
29. Hughes, A. J. *et al.* Single-cell western blotting. *Nature methods* **11**, 749–55. ISSN: 1548-7105. arXiv: NIHMS150003. <http://www.ncbi.nlm.nih.gov/pubmed/24880876> (2014).
30. Zhang, Y. *et al.* Detecting protein and post-translational modifications in single cells with iDentification and qUantification sEParation (DUET). *Communications Biology* **3**. <https://doi.org/10.1038/s42003-020-01132-8> (Aug. 2020).
31. Perfetto, S. P., Chattopadhyay, P. K. & Roederer, M. Seventeen-colour flow cytometry : unravelling the immune system. *Nature Reviews Immunology* **4**, 1160–1163 (2004).
32. Stack, E. C. *et al.* Multiplexed immunohistochemistry, imaging, and quantitation: A review, with an assessment of Tyramide signal amplification, multispectral imaging and multiplex analysis. *Methods* **70**, 46–58. <https://doi.org/10.1016/j.ymeth.2014.08.016> (Nov. 2014).
33. Tentori, A. M., Yamauchi, K. A. & Herr, A. E. Detection of Isoforms Differing by a Single Charge Unit in Individual Cells. *Angewandte Chemie*, 12431–12435 (2016).
34. Bandura, D. R. *et al.* Mass Cytometry : Technique for Real Time Single Cell Multitarget Immunoassay Based on Inductively Coupled Plasma Time-of-Flight Mass Spectrometry. *Analytical Chemistry* **81**, 6813–6822 (2016).
35. Yamauchi, K. A. & Herr, A. E. Subcellular western blotting of single cells. *Microsystems & Nanoengineering* **3**, 16079. ISSN: 2055-7434. <http://www.nature.com/articles/micronano201679> (2017).
36. Rosàs-Canyelles, E *et al.* Multimodal detection of protein isoforms and nucleic acids from mouse pre-implantation embryos. *Nature Protocols*, NP-PI200463 (2020).
37. Gopal, A. & Herr, A. E. Multiplexed in-gel microfluidic immunoassays: characterizing protein target loss during reprobing of benzophenone-modified hydrogels. *Scientific Reports* **9**, 1–12. ISSN: 20452322 (2019).

38. Vlassakis, J. & Herr, A. E. Effect of Polymer Hydration State on In-Gel Immunoassays. *Analytical Chemistry* **87**, 151022142613006. ISSN: 0003-2700. <http://pubs.acs.org/doi/10.1021/acs.analchem.5b03032> (2015).
39. Kang, C.-c. *et al.* Single-Cell Western Blotting after Whole-Cell Imaging to Assess Cancer Chemotherapeutic Response. *Analytical Chemistry*, 1042910436 (2014).
40. Tan, K. Y. & Herr, A. E. Ferguson analysis of protein electromigration during single-cell electrophoresis in an open microfluidic device. *The Analyst* **145**, 3732–3741. <https://doi.org/10.1039/c9an02553g> (2020).
41. Vlassakis, J. & Herr, A. E. Joule Heating-Induced Dispersion in Open Microfluidic Electrophoretic Cytometry. *Analytical Chemistry* **89**, 12787–12796. ISSN: 15206882 (2017).
42. Vlassakis, J. *et al.* Measuring expression heterogeneity of single-cell cytoskeletal protein complexes. <https://doi.org/10.1101/2020.09.12.294801> (Sept. 2020).
43. Rabilloud, T. Solubilization of proteins for electrophoretic analyses. *Electrophoresis* **17**, 813–829. ISSN: 1522-2683. <https://analyticalsciencejournals.onlinelibrary.wiley.com/doi/full/10.1002/elps.1150170503> (1996).
44. Vlassakis, J., Yamauchi, K. A. & Herr, A. E. Summit: automated gel electrophoresis analysis. *SLAS Technology* (2021).
45. Giddings, J. C. *Unified separation science* ISBN: 978-0-471-52089-4 (Wiley, New York, 1991).
46. Stoeckius, M. *et al.* Simultaneous epitope and transcriptome measurement in single cells. *Nature Methods* **14**, 865–868 (2017).
47. Peterson, V. M. *et al.* Multiplexed quantification of proteins and transcripts in single cells. *Nature Biotechnology* **35**, 936–939 (2017).
48. Chung, H. *et al.* Simultaneous single cell measurements of intranuclear proteins and gene expression. <https://doi.org/10.1101/2021.01.18.427139> (Jan. 2021).
49. Y, K. *et al.* Coupled scRNA-Seq and Intracellular Protein Activity Reveal an Immunosuppressive Role of TREM2 in Cancer. *Cell* **182**, 872–885.e19. ISSN: 1097-4172. <https://pubmed.ncbi.nlm.nih.gov/32783915/> (2020).
50. Schulz, D. *et al.* Simultaneous multiplexed imaging of mRNA and proteins with sub-cellular resolution in breast cancer tissue samples by mass cytometry. *Cell Systems* **6**, 25–36.e5. ISSN: 24054720. <https://doi.org/10.1016/j.cels.2017.12.001> (2018).
51. Arrigucci, R. *et al.* FISH-Flow, a protocol for the concurrent detection of mRNA and protein in single cells using fluorescence in situ hybridization and flow cytometry. *Nature Protocols* **12**, 1245–1260. <https://doi.org/10.1038/nprot.2017.039> (May 2017).
52. Mimitou, E. P. *et al.* Multiplexed detection of proteins, transcriptomes, clonotypes and CRISPR perturbations in single cells. *Nature Methods* 2019 16:5 **16**, 409–412. ISSN: 1548-7105. <https://www.nature.com/articles/s41592-019-0392-0> (2019).

53. CDC. *Decontamination and Reuse of Filtering Facepiece Respirators* <https://www.cdc.gov/coronavirus/2019-ncov/hcp/ppe-strategy/decontamination-reuse-respirators.html>. Apr. 2020.
54. Institute of Medicine, Board on Health Sciences Policy & Committee on the Development of Reusable Facemasks for Use During an Influenza Pandemic. *Reusability of Facemasks During an Influenza Pandemic: Facing the Flu* en. ISBN: 978-0-309-10182-0 (National Academies Press, Aug. 2006).
55. Su, A., Smith, B. E. & Herr, A. E. In Situ Measurement of Thermodynamic Partitioning in Open Hydrogels. *Analytical Chemistry* **92**, 875–883 (2020).

Chapter 2

Multiplexed in-gel microfluidic immunoassays: characterizing protein target loss during reprobing of benzophenone-modified hydrogels

Materials reproduced, with permission, from:

A. Gopal & A.E. Herr, “Multiplexed in-gel microfluidic immunoassays: characterizing protein target loss during reprobing of benzophenone-modified hydrogels, *Scientific Reports*, 2019.

2.1 Introduction

Assessing protein-mediated cell-signalling for a wide range of biological and clinical questions (e.g., proliferation [1], senescence [2], tumour progression [3]) benefits from bioanalytical techniques developed to interrogate complex cell systems (i.e., cell lysates [4–6], cell cultures [7–11], and tissue samples [12, 13]). Hydrogels are increasingly used as an immobilization substrate for immunoassays. Hydrogels are biologically inert [14], offer useful mass transport properties [14], are readily functionalized with biological and non-biological materials (e.g., extracellular matrix proteins or photoactivatable crosslinkers) [9, 10, 15] and are capable of forming either 2D or 3D structures [9, 15]. Furthermore, hydrogel-based assays have dramatically improved biological measurement capabilities. For instance, optical-clearing methods (e.g., CLARITY and expansion microscopy) utilize the mass transport and swelling properties of hydrogels to visualize intact brain tissue architecture [12, 13, 16]. Moreover, covalent chemistries are routinely used to bind cellular material to the hydrogel matrix, especially when rapid diffusion-driven dilution of solubilized biospecimens will degrade limits-of-detection [12, 13, 17, 18].

Recently, benzophenone has been utilized as the chemistry of choice to facilitate covalent attachment of biospecimen targets to otherwise inert materials, such as hydrogels.

Often, benzophenone is grafted onto a surface or incorporated into a hydrogel matrix such as polyacrylamide (“PA”) [4, 19, 20]; subsequent UV irradiation facilitates the formation of benzophenone free radicals that abstract hydrogen atoms from proximal peptide residues, resulting in covalent bond formation between the benzophenone group and nearby protein targets [21]. In some microfluidic devices, this entire process occurs in as little as 45 s [4]. Benzophenone photochemistry is used in a range of bioanalytical research, including the analysis of stem cell differentiation in spatially varying patterns of biomolecules [22], the development of microfluidic tools to understand enzyme and antibody kinetics [23, 24], and the development of separations to probe isoforms from few numbers of cells [4, 5, 20].

In hydrogels functionalized with benzophenone methacrylamide, detection of protein targets adopts standard immunocytochemistry (“ICC”) or immunohistochemistry (“IHC”) procedures [4, 22]. Specifically, a protein-decorated hydrogel is incubated with primary and secondary antibody probes, and subsequent wash steps remove non-specifically-bound immunoreagents. The secondary antibody probes are most commonly labeled with fluorophores. To read out signal, the hydrogel is imaged with a fluorescence microscope (including confocal and two-photon microscopes) or a laser scanner [4, 12, 18]. However, detecting multiple protein targets in one specimen (“multiplexing”) is subject to limitations of fluorescence imaging: in particular, multiplexing is restricted by the standard 4-6 colour channels available in conventional epifluorescence microscopes [25]. Combinatorial post-processing techniques (e.g., spectral unmixing [26]) and fluorophore bleaching or quenching chemistries [27] have been explored for single-cell ICC and IHC; however, both techniques rely on fluorescently-labeled primary antibodies, which may reduce anti-body-antigen binding affinity [28] and prohibit signal amplification made available by the use of secondary antibody probes for target detection [29].

An alternate method of multiplex target detection, which has been utilized in some ICC/IHC procedures [30–32], slab-gel western blots [33], and in optical clearing assays [12, 34] involves chemical “stripping and reprobing” or “de-staining and reprobing”. “Stripping and reprobing” chemistries utilize harsh denaturing agents, such as sodium-dodecyl-sulfate (“SDS”), urea, and/or β -mercaptoethanol, as well as the addition of heat, to remove immunoreagents from a sample, followed by reprobing of the sample with a new round of immunoreagents [33]. In slab-gel western blotting, proteins adhere onto the PVDF or nitrocellulose membrane via non-covalent interactions; as a result, protein species are denatured and unbound from the membrane upon each stripping cycle. Consequently, standard immunoblotting protocols recommend limiting the number of ‘stripping and reprobing’ cycles to 3-4 rounds [35]. Slab-gel western blotting with nitrocellulose and nylon membranes supports up to 6 rounds of chemical stripping [33]. Alternative stripping buffer cocktails, such as those containing glycine-HCl instead of SDS, have been shown to extend reprobing capabilities to detect up to 21 protein targets on PVDF membranes [35].

Our group has introduced photoactive hydrogels consisting of benzophenone methacrylamide co-polymerized with polyacrylamide (“BMPA hydrogels”) as the basis for a suite of electrophoretic protein cytometry (“EPC”) assays, including size-based electrophoresis, native electrophoresis, and isoelectric focusing, in order to detect proteoforms in single-cell

lysate [4–6]. Detection of protein targets occurs by heterogeneous immunoassays [4–6]. At present, we have reported detection of up to twelve sets of individual protein targets from each cell lysate using stripping and reprobing procedures [36] (see Figure 2.1). Furthermore, in a photoactive BMPA hydrogel, we expect minimal loss of immobilized protein targets during multiple stripping and reprobing cycles, as the targets are covalently immobilized to the hydrogel, and the stripping buffer (i.e., SDS, β -mercaptoethanol, and 50–60°C temperatures) is not expected to denature C-C covalent bonds (see Figure 1) [37–39]. However, our observations during stripping and reprobing suggest up to a 50% loss in immunoassay signal upon 12 rounds of reprobing [4]. Whether this immunoassay signal loss is due to immobilized protein loss from the hydrogel or due to other inefficiencies is not yet understood.

Consequently, in this study, we scrutinize the impact of stripping chemistries on protein targets covalently immobilized to BMPA hydrogels via benzophenone. We first develop BMPA hydrogels immobilized with fluorescently labeled proteins. With these hydrogels, we quantify the effect of harsh detergents on protein species upon multiple rounds of stripping. By utilizing fluorescently labeled proteins, we are able to quantify protein retention independent from immunoassay signal. With this system, we: (i) determine the behavior of protein signal upon 29 rounds of stripping, (ii) determine the mechanism of protein loss, and (iii) utilize the acquired knowledge to formulate design guidance for multiplexed, serial in-gel immunoassays.

2.2 Methods

Reagents

30% Acrylamide/bis-acrylamide (29:1) (A3574), N,N,N',N'-Tetramethylethylenediamine (T9281), ammonium persulfate (A3678), bovine serum albumin (A9418), sodium dodecyl sulfate (L4509), 2-mercaptoethanol (M3148), hydroxylamine hydrochloride (379921), trypsin inhibitor from soybean (65035), ribonuclease A from bovine pancreas (R5500), and albumin from chicken egg white (A5503) were purchased from Millipore Sigma. Tris-HCl, pH 6.8 (T1568) and Tris-HCl pH 8.8 (T1588) was purchased from Teknova Inc. Phosphate buffered saline (10X PBS Corning, 45001) was purchased from VWR. N-[3-[(3-Benzophenyl)-formamido] propyl] methacrylamide was synthesized by PharmAgra laboratories. Gibco™ Phosphate-buffered saline (1X PBS, 10010023), Alexa Fluor 488 Microscale Protein Labeling Kit (A30006), Alexa Fluor 488 TFP ester (A37570), and Alexa Fluor 633 goat anti-rabbit secondary antibody (A21071) were purchased from ThermoFisher Scientific. Bio-Gel P-6 Fine Resin (1504134) was purchased from Bio-Rad Laboratories. Nanosep MF Centrifugal Devices (0.2 μ m, ODM02C34) was purchased from Pall Laboratories. Tris Buffered Saline with Tween-20 (TBST-10X, 9997S) was purchased from Cell Signaling Technology. Ribonuclease A primary antibody (100 μ L, NBP1-69256) was purchased from Novus Biologicals. Deionized water (18.2 M Ω) was obtained from an Ultrapure Millipore filtration system. ArrayIt Microarray Gaskets (AHC1X16) were purchased from ArrayIt Corporation.

Borosilicate glass plates were purchased from McMaster-Carr (8476K17). Diamond-tipped scribes were purchased from Amazon (SCB-431.00).

Protein Labeling

Trypsin inhibitor from soybean (“TI”), ribonuclease A from bovine pancreas (“RNase”), and albumin from chicken egg white (“OVA”) were labeled in-house using the described protocol in the Alexa Fluor 488 Microscale Protein Labeling Kit. With the exception of reprobing experiments, molar ratios of dye:protein of 60, 19, and 0.67 were used for OVA, TI, and RNase, respectively, at the recommended protein concentration of 1 mg/mL, resulting in degrees-of-labeling of 3.1, 1.76, and 0.10 fluorophores per molecule of protein, respectively. For experiments that involved reprobing of RNase, a dye:protein molar ratio of 5 was used, resulting in a degree of labeling of 1.23. Finally, for batch OVA and TI labeling reactions, 1/10th volume of 1.5M hydroxylamine-hydrochloride was used to stop the labeling reaction after 15 min of incubation.

Fabrication of BMPA Hydrogels with Immobilized Protein

600 μL microcentrifuge tubes were blocked overnight with 10% BSA in 1x TBST. 7%T BMPA hydrogels were fabricated as previously described on silanized glass slides [4]. Prior to fabrication, glass slides were vertically scored with a diamond scribe 1.5” down the middle. After fabrication, BMPA gels were briefly incubated in 1X TBST and loaded into the ArrayIt Microarray gasket system (gel-side up). 80 μL of 1x TBST was loaded into each well. To load one-half of the BMPA gel with purified protein solution, 270 μL of 2.1 μM protein solution was created in a BSA-blocked microcentrifuge tube. TBST was aspirated out of 3 microwells of the ArrayIt Gasket, and each empty well was loaded with 80 μL of purified protein solution. The same procedure was repeated for the other half of the BMPA gel. BMPA gels were incubated with protein solution for 30 min, and then exposed to collimated UV light under a mercury arc lamp ($\sim 20 \text{ mW}/\text{cm}^2$ at 365 nm, Optical Associates, Inc.) for 300s. The gasket fixture was then disassembled, and BMPA gels were rinsed in 1x TBST overnight. After an overnight wash, BMPA gels were dried under an N_2 air stream, and broken in half, producing two half-gels. Half-gels were analyzed with a laser microarray scanner (Genepix 4300A, Molecular Devices) to measure the resulting fluorescence profiles.

Stripping Experiments

Harsh stripping buffer was made with 62.5 mM Tris-HCl (pH 6.8), 2% SDS, and 0.8% μ -mercaptoethanol. Wash buffer consisted of 1x TBST. For initial stripping experiments, BMPA gels with immobilized RNase-Alexa Fluor 488 (RNase-488) conjugates were created in triplicates for 3 experimental conditions: the photobleaching control, the buffer control, and the treatment group (see Figure 2a). Photobleaching control gels were kept dry during the duration of the experiment, but scanned with the remaining gels at the end of each

stripping cycle. Buffer control gels were incubated in 1x TBST at room temperature (25⁰C) for 1 hr. Treatment group gels were incubated in stripping buffer at 55-57⁰C for 1 hr. Both buffer control and treatment group gels were subsequently washed in 1x TBST for 1 hr, rinsed with DI water, and dried under a *N*₂ stream. All gels were scanned with a laser microarray scanner to track changes in fluorescence profiles.

Stripping Mechanism Experiments

To isolate components of stripping buffer that may be contributing to signal loss, buffers consisting solely of 62.5 mM Tris-HCl (pH 6.8), and solely of 62.5 mM Tris-HCl and 2% SDS were also created. Gels were created in triplicates for 4 sets of experimental conditions: the photobleaching control, which was kept protected from light; the detergent-only sample, where gels were incubated in Tris-HCl and 2% SDS at RT; the heat-only sample, where gels were incubated in Tris-HCl at 55-57⁰C; and the heat and SDS sample, where gels were incubated in Tris-HCl and 2% SDS at 55-57⁰C. Gels were incubated in their respective conditions for 1 hr. After incubation, all gels (except the photobleaching controls) were washed in 1x TBST for 1 hr, rinsed with DI water, dried under a nitrogen stream, and scanned with a laser microarray scanner.

Protein Molecular Mass Experiments

To determine the impact of molecular mass on protein signal loss, BMPA hydrogels immobilized with either 2.1 μ M OVA labeled with Alexa Fluor 488 (“OVA488”), or 2.1 μ M TI labeled with Alexa Fluor 488 (“TI488”), were created. Each protein species tested had two sets of gels created in triplicates: a photobleaching control, and the treatment group. Gels were fabricated, and measured, as described in the sections above. After fabrication, gels belonging to the treatment group were incubated in stripping buffer at 55-57⁰C for 1 hr. Gels were then washed in 1x TBST for 1 hr, rinsed with DI water, dried under a nitrogen stream, and scanned with a laser microarray scanner.

Reprobing Experiments

To determine the corresponding immunoassay signal loss with reprobing rounds, BMPA gels consisting of immobilized RNase-488 with DOL = 1.23 were fabricated as described above, at an initial in-solution concentration of 125 nM. Six gels were fabricated to create two sets of triplicates: the photobleaching controls and the treatment group. Initially, all gels were immunoprobed, which consisted of a 2 hr incubation with a 1:10 dilution of 1 mg/mL primary anti-RNase antibody in 2% BSA/TBST solution, followed by a 1 hr wash in TBST, another 1 hr incubation with a 1:20 dilution of 2 mg/mL of secondary antibody labeled with Alexa Fluor 633 in 2% BSA/TBST solution, and a final 1 hr wash in TBST. Since immunoreagent dilutions were fairly high, we used small volumes of immunoreagent solutions (40 μ L per gel) to conserve antibody, and performed immunoprobing by sandwiching

antibody solution between the gel and a glass plate. Gels were then rinsed with DI water, dried under a N_2 stream and imaged with a laser microarray scanner. Following the initial round of immunoprobng, photo-bleaching control gels were kept dry for the duration of the experiment, but scanned with the remaining gels at the end of each stripping and reprobing cycle. Gels from the treatment group were subjected to 1 hr of stripping with harsh stripping buffer at 55-57^o C, washed with TBST, and had any residual fluorescence scanned with the Genepix microarray scanner. Following this, the treatment group gels were reprobbed with an additional set of antibodies, as previously described. The treatment group was stripped and reprobbed in this manner for a total of 6 times.

Data Analysis and Quantitation.

Fluorescence micrographs of BMPA gels were analyzed using custom analysis scripts written in MATLAB R2018a. To align micrographs from sequential stripping experiments, we utilized the Speeded up Robust Features (SURF) algorithm from MATLAB’s Image Processing Toolbox. Statistical analysis of summed fluorescence intensity, and signal-to-noise ratios, were performed using R.

2.3 Results and Discussion

Several studies have demonstrated the use of stripping and reprobing chemistries for multiplexing, including reports of 7-10 additional rounds of reprobing in optical clearing assays [34], up to 10 rounds of additional reprobing in ICC/IHC using specialized immunoreagents linked to quantum dots [33], and for detection of up to 12 protein targets in EPC [36]. In EPC, the stripping procedure consists of incubating immunoprobbed BMPA gels in a cocktail of harsh detergents containing 2% SDS and 0.8% β -mercaptoethanol at 55-57^o C for > 1 hr [4]. BMPA gels are subsequently washed in 1x Tris-Buffered Saline with Tween-20 (“TBST”) for 1 hr to remove residual SDS and β -mercaptoethanol from the hydrogel. Once stripping of the detection antibody is complete, gels can be reprobbed to detect additional protein targets (see Figure 2.1).

In theory, the stripping procedure in EPC should not disrupt the covalent binding of the protein species to the BMPA matrix, due to the fact that SDS disrupts hydrophobic interactions in proteins [38] and β -mercaptoethanol disrupts disulfide bridges [39]. Furthermore, exposure to temperatures between 50-60^oC is anticipated to only disrupt additional non-covalent interactions (e.g., hydrogen bonds) [40]. Nevertheless, our observations of the stripping and reprobing phenomena have reported up to a 50% reduction in immunoassay signal while reprobing the same protein target [4]. Thus, as a first step, we sought to investigate whether the observed immunoassay signal loss could be attributable to loss of protein target from the BMPA hydrogel, due to denaturation of non-covalent protein-hydrogel interactions (e.g., hydrogen bonding [40, 41], hydrophobic interactions [42], or van der Waals forces⁴²) by application of detergents such as SDS and heat (see Figure 2.1).

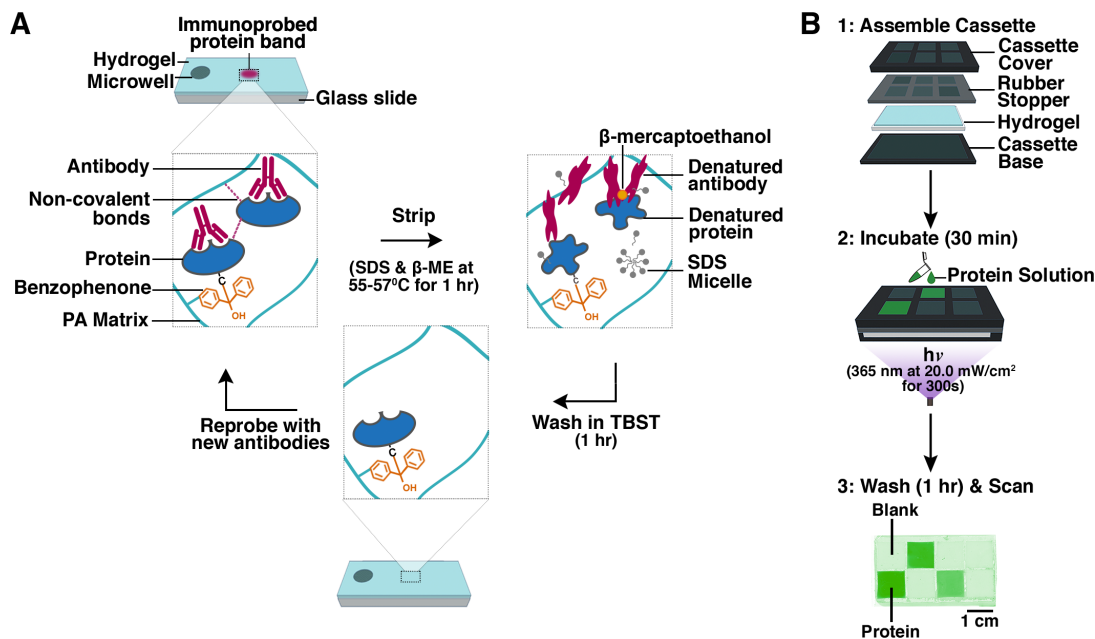


Figure 2.1: Hypothesized mechanism of immunoassay signal loss in BMPA hydrogels and device fabrication to test hypothesis. In BMPA hydrogels, protein targets of interest are covalently bonded to the hydrogel matrix by a benzophenone moiety. However, we hypothesize that some protein targets are immobilized in the gel matrix via non-covalent interactions (e.g., hydrogen bonding, hydrophobic bonding, or van der Waals forces). We hypothesize that the chemical stripping procedure used in multiplexing for hydrogel-based heterogeneous immunoassays denatures these non-covalent interactions, resulting in protein loss from the hydrogel. (b) To monitor and quantify protein loss from BMPA hydrogels during chemical stripping & reprobation, we used an ArrayIt Microarray Gasket to create physically isolated 1 cm² arrays in the hydrogel. We loaded purified protein conjugated with fluorescent dye into pre-selected arrays, and filled remaining arrays with buffer. After a 30 min incubation step, gels are exposed to UV irradiation (365 nm, at 20.0 mW/cm²) for 300s, and are subsequently washed and dried. Gels are scanned with a laser microarray scanner to measure fluorescence. We can now test our hypothesis by subjecting these hydrogels to multiple rounds of stripping and reprobation, wherein protein-conjugate fluorescence is used as a proxy for protein concentration, which allows us to monitor protein loss from the hydrogel across serial stripping rounds.

Development of BMPA Hydrogels with Immobilized Protein

To understand the mechanism of protein loss during stripping of BMPA hydrogels, we first sought to quantify protein signal in these hydrogels after several rounds of incubation in stripping buffer, in a manner that was independent of immunoassay signal. In order to create a model system, we incubated fluorescently labeled purified proteins with the BMPA

hydrogels. We did not use naturally fluorescent proteins (e.g., GFP), which have fluorescence that is often dependent on the secondary structure of chromophore-stabilizing polypeptide chains. For instance, GFP is highly susceptible to fluorescence loss by exposure to denaturants (SDS) at low pH (< 6.5) [43]. Instead, in our system, we labeled the target proteins with an Alexa Fluor dye, purported to be among the brightest and most photostable commercially available protein dyes [44]. Furthermore, previous studies of immobilized proteins in BMPA hydrogels have reported that micro-to-nanomolar quantities of protein conjugates labeled with Alexa Fluor dyes have fluorescence that linearly increases with protein molarity [24]. As a result, we measure protein-conjugate fluorescence intensity as a proxy for protein concentration in the hydrogel. Our protein target is Bovine Pancreatic Ribonuclease A (“RNase”), labeled in-house with Alexa Fluor 488 (“RNase-488”). Thermo-cycling experiments confirmed that the protein/dye conjugate does not lose fluorescence upon temperature cycling, as long as the temperature during the endpoint measurement is held constant (see Figure 2.2).

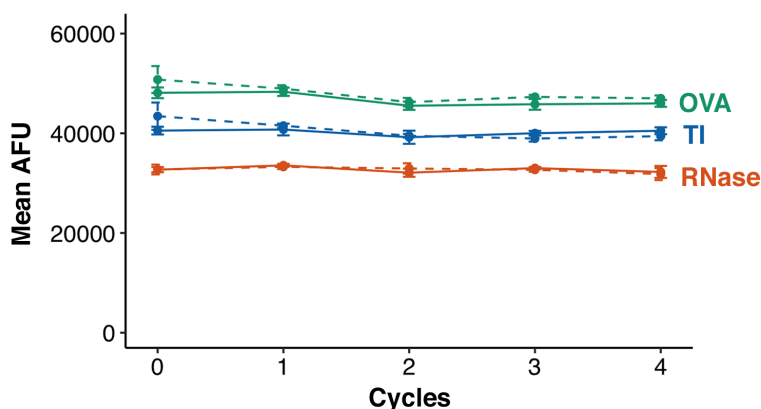


Figure 2.2: Thermocycling experiments demonstrate stability of protein/fluorophore conjugates upon denaturation. 1.05 mM concentrations of OVA, TI, and RNase protein-fluorophore conjugates in TBST were thermocycled for 4 rounds. After each round, fluorescence readings were taken from 100 μ L aliquots ($n = 5$) of each protein-fluorophore conjugate using a plate reader. Dotted lines represent photobleaching controls; solid lines represent samples that were subject to thermocycling. Differences in starting AFU can be attributed to differences in the degree-of-labeling of each protein conjugate.

To create hydrogels decorated with immobilized purified protein, we fabricated BMPA gels as previously described⁴, and used a gasket system (ArrayIt Microarray Gasket, ArrayIt Corporation, Sunnyvale, CA) to physically isolate regions of the BMPA gel and selectively dose these regions with protein (see Figure 2.1b). Furthermore, in each row of wells, we ensured that one of the two wells was filled with buffer to create “blank” regions for subsequent determination of gel background fluorescence. The purified protein solution was incubated

for 30 min, which corresponds to the 4τ diffusion time for large (i.e., 150 kDa) proteins into 30-40 μm thick BMPA gels [17, 45]. After incubation in protein solution, gels were irradiated with UV light for 300s to enable covalent bond formation between the benzophenone moieties and the purified protein species. The final gel consisted of three immobilized protein regions, which contained protein signal, surrounded by regions of background signal. With the development of BMPA hydrogels with immobilized protein, we then proceeded to subject these hydrogels to serial incubation cycles in stripping buffer in order to quantify protein loss after multiple stripping rounds.

Quantifying Protein-Conjugate Fluorescence after Multiple Stripping Cycles

In order to quantify protein loss after serial stripping cycles, (see Figure 2.3a), we developed a quantitative method to compare “before-and-after” fluorescence intensities of hydrogel micrographs after each round of incubation in stripping buffer. For each experiment, hydrogels were incubated in stripping buffer, or in one of two control conditions, for 1 hr. With the exception of photobleaching controls, all gels were also washed in 1X TBST for 1 hr. Gels were subsequently rinsed with DI water, dried under an N_2 stream, and scanned with a laser microarray scanner.

Once incubation experiments were complete, we defined the areas in each immobilized protein region from which protein signal would be collected for downstream analysis (see Figure 2.4). First, all fluorescence micrographs for a single gel were feature-matched and compiled into a TIFF stack using MATLAB’s implementation of the Speeded up Robust Features (‘SURF’) algorithm. Specifically, SURF extracts and utilizes local features of each micrograph [46] to align micrographs obtained after every stripping cycle to the initial micrograph. As a result, we are able to perform pixel-by-pixel fluorescence intensity comparisons between micrographs obtained in sequential stripping rounds. Once all micrographs were stacked and aligned, we identified a 5.49 mm x 5.04 mm region-of-interest (“ROI”) in each immobilized protein region.

We next sought to quantify the protein fluorescence from these ROIs across multiple stripping cycles. In order to quantify the fluorescence, we fit the distribution of pixel intensities in each ROI to a Gaussian distribution. To exclude effects from outlier pixels in each ROI (i.e., “hot” pixels with high intensity, or dark pixels with an intensity close to 0), we calculated the median intensity value of all pixels and re-scaled any pixel values that were greater than 4 standard deviations from the mean (corresponding to $< 1\%$ of the total distribution of pixels) to the median pixel value. We then summed all pixel values from the resulting distribution to calculate the total fluorescence intensity of each ROI. Furthermore, we performed background subtraction by identifying an identically sized ROI in a background region adjacent to each immobilized protein region, and subsequently quantified the fluorescence intensities from these background ROIs in the same manner described for protein ROIs. Finally, in order to have a direct comparison of protein fluorescence before

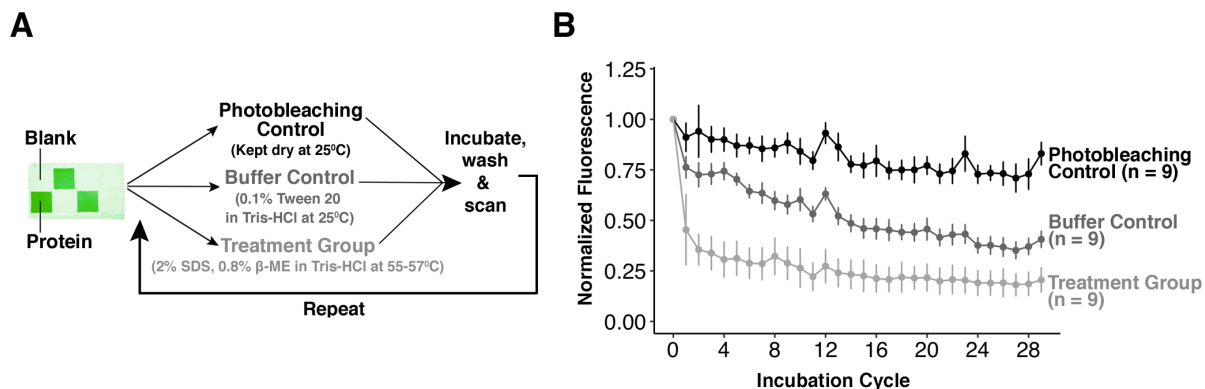


Figure 2.3: Monitoring loss of immobilized protein target from BMPA hydrogels during chemical stripping. (a) 9 sets of BMPA hydrogels with immobilized protein were fabricated. These hydrogels were split into 3 triplicate groups consisting of the photobleaching control, the buffer control, and the treatment group. Each group contains $n = 9$ immobilized protein regions. (b) After each round of incubation, the mean integrated density of each immobilized protein region was analyzed. 5.49 mm x 5.04 mm ROIs were defined in each immobilized protein region, from which fluorescence intensity values were summed and normalized to the starting fluorescence intensity. It is evident that the treatment group, which is incubated in stripping buffer, demonstrates substantial ($> 50\%$) loss in protein signal in the first 4 rounds of stripping. By contrast, the buffer control experiments demonstrate a steady decrease in fluorescence ($\sim 5\%$ per round) until round 16, at which point the rate of signal loss decreases.

and after stripping, we normalized the summed intensity value of each ROI from subsequent stripping cycles to the summed intensity value of the ROI obtained from the starting micrograph.

We posit that the formulation of a protein-conjugate fluorescence monitoring system across multiple stripping rounds provides a robust and quantifiable method of tracking the response of multiple types of proteins across multiple hydrogel systems (i.e., with different immobilization chemistries), in addition to BMPA hydrogels.

Investigating Protein-Conjugate Fluorescence after Sequential Stripping Rounds

We next scrutinized the hypothesis that the observed 50% decrease in immunoassay signal intensity after 12 rounds of immunoprobng [4] arises from loss of non-covalently-bound proteins from the BMPA gel. Although we anticipate that most immobilized protein species are covalently bound to the benzophenone moiety in the gel, a subset of protein molecules may be bound via non-covalent interactions (e.g., hydrogen bonding [40, 41], hydrophobic interactions [42], van der Waals forces [42]), either to the hydrogel matrix or to other covalently-bound proteins.

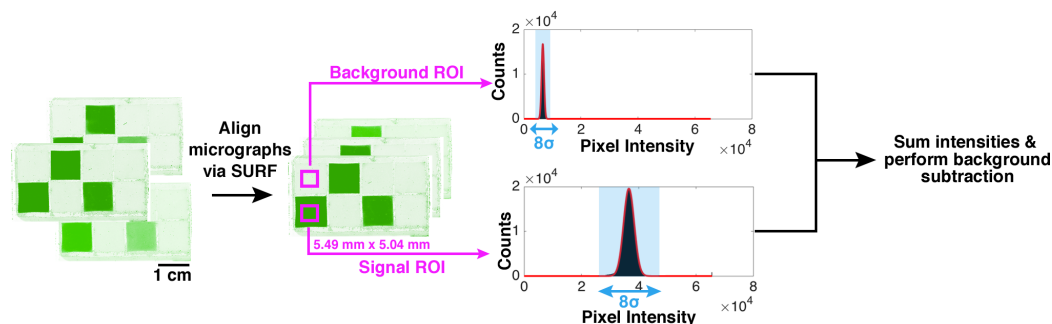


Figure 2.4: Data analysis workflow for stripping experiments using BMPA hydrogels with immobilized proteins. Micrographs from sequential stripping rounds are aligned and compiled into an image stack using the Speeded Up Robust Features function in MATLAB’s image processing toolbox. Once stacked, a 5.49 mm x 5.04 mm region-of-interest is identified for every immobilized protein region. The pixel intensities from each ROI are fit to a Gaussian distribution, and any outlier pixels ($> 4\sigma$ away from the mean) are re-scaled to the median pixel intensity value. These pixel intensities are then summed. A similar procedure is performed for adjacent background ROIs, which is subsequently used for background subtraction.

lently bound proteins in the gel. We hypothesized that non-covalent interactions of proteins not immobilized to benzophenone would be disrupted by harsh, ionic detergents (SDS) and incubation in elevated temperatures ($55\text{-}57^\circ\text{C}$ incubation for 1 hr). As a corollary, we further hypothesized that the majority of the protein loss would occur in the first 2-3 rounds of stripping, after which any remaining protein species would be covalently bound to the hydrogel matrix. Since we utilize protein fluorescence as a proxy for protein concentration, we anticipated a decrease in fluorescence intensity during the first 2-3 rounds of stripping, followed by a plateau in fluorescence.

Our results indicate that the first 5 stripping cycles see the majority of protein signal loss ($>50\%$ signal loss) from the treatment group (see Figure 2.3b). We observe gradual signal loss from the treatment group after round 5, which we attribute to repeated photobleaching of target by the laser microarray scanner. Similar levels of normalized signal are lost during rounds 11-29 for both the treatment group and the photobleaching controls, after normalization to round 11 (see Figure 2.5). To assess the similarity between the photobleaching controls and the stripping samples in rounds 11-22, we performed Mann-Whitney U-tests on the residual signal intensity in each round (see Table 2.1). The Mann-Whitney U-tests demonstrate that either (1) the p-value is greater than 0.05, indicating no significant differences between the two groups, or that (2) for groups where the p-value is < 0.05 , the treatment group has greater mean normalized fluorescence intensity (i.e., lower signal loss) than the photobleaching control group (see Table 2.1). Thus, between rounds 11-22, the signal lost from the treatment group during these cycles is indistinguishable from

photobleaching effects. As an important aside, we note that the spike in protein-conjugate signal intensity observed during cycle 12 is attributable to scanner variation, owing to a concomitant increase in signal intensity across all control conditions.

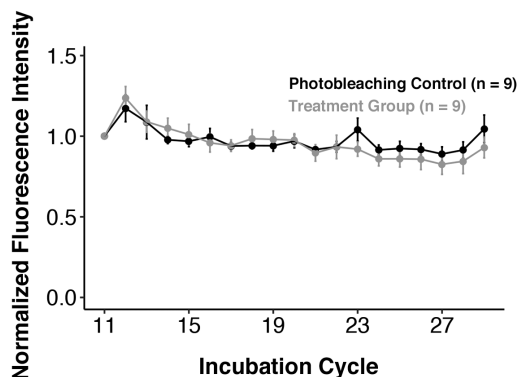


Figure 2.5: Signal loss of immobilized protein target from BMPA hydrogels from rounds 11 – 29. Signal from each ROI was normalized to the ROI signal from round 11. The overlapping traces between the photobleaching control and the treatment group suggests that the majority of signal loss observed in the treatment group after round 11 cannot be isolated from the effects of photobleaching and/or instrument variation. The slight decrease in the treatment group’s intensity during round 23 may be due to a 2 month gap between scanning round 22 and round 23; the time delay between the majority of other successive incubation cycles was < 1 week.

Furthermore, minor protein loss observed across all conditions at round 24 is attributed to a two-month delay between scanning round 23 and round 24 for all groups. Nevertheless, when we normalize the fluorescence signal intensity to round 23, we once again observe indistinguishable sample loss between the photobleaching control group and the treatment group during rounds 24 – 29.

Moreover, the majority of the signal loss from the buffer controls occurs during the first 16 cycles. We hypothesize that the difference in final protein-conjugate signal intensities between the treatment group and the buffer control arises from differences in buffer composition: although both conditions lead to protein denaturation and disruption of protein-protein or protein-hydrogel interactions, the stripping buffer contains SDS and is heated to 55-57 $^{\circ}$ C. By contrast, the detergent used in the buffer controls is Tween-20, which is a milder, non-ionic detergent that does not disrupt protein-protein or protein-hydrogel interactions as strongly; and moreover, the buffer control is incubated at room temperature (25 $^{\circ}$ C), which also results in less protein denaturation. By extension, we would hypothesize that harsher stripping conditions, such as those used in the CLARITY assay (consisting of stripping with 4% SDS at 60 $^{\circ}$ C for approximately 12 hr) [12] would likely result in greater protein losses

Table 2.1: P-Values for Mann-Whitney U-Tests Between Photobleaching Control and Treatment Group for Rounds 11 - 29

Round	P-Value	Group with Higher Mean Signal
11	N/A	N/A
12	0.190	Treatment
13	0.931	Treatment
14	0.008	Treatment
15	0.019	Treatment
16	0.258	Control
17	1.000	Treatment
18	0.094	Treatment
19	0.113	Treatment
20	0.931	Treatment
21	0.340	Control
22	1.000	Control
23	0.002	Control
24	0.011	Control
25	0.011	Control
26	0.011	Control
27	0.019	Control
28	0.136	Control
29	0.003	Control

during the first few rounds of stripping, and as a result, a corresponding plateau in signal loss during earlier stripping rounds.

We further hypothesize that the difference in plateau between the treatment group and the buffer control arises from differences in buffer composition: although both conditions lead to protein denaturation and disruption of protein-protein or protein-hydrogel interactions, the stripping buffer contains SDS and is heated to 55-57⁰C. By contrast, the detergent used in TBST, Tween-20, is a milder, non-ionic detergent that does not disrupt protein-protein or protein-hydrogel interactions as strongly; and moreover, the buffer control is incubated at room temperature (25⁰C), which also results in less protein denaturation. By extension, we would hypothesize that harsher stripping conditions, such as those used in the CLARITY assay (consisting of stripping with 4% SDS at 60⁰C for approximately 12 hr) [12] would likely result in greater protein losses during the first few rounds of stripping, and as a result, a corresponding plateau during earlier stripping rounds.

Additionally, we sought to understand the impact of the stripping buffer on the signal-to-noise ratios (“SNR”) of the BMPA hydrogels with immobilized protein (see Figure 2.6,

where each trace represents a single ROI). The SNR is characterized as the ratio between the mean signal intensity and the background noise. An $\text{SNR} \geq 3$ is a threshold for exceeding the limit-of-detection (“LOD”) of an assay. Since there is some variation in the starting intensity for every immobilized protein ROI, due to variation in protein entry into local regions of the BMPA hydrogel, we tracked the SNR of each ROI individually over multiple stripping cycles.

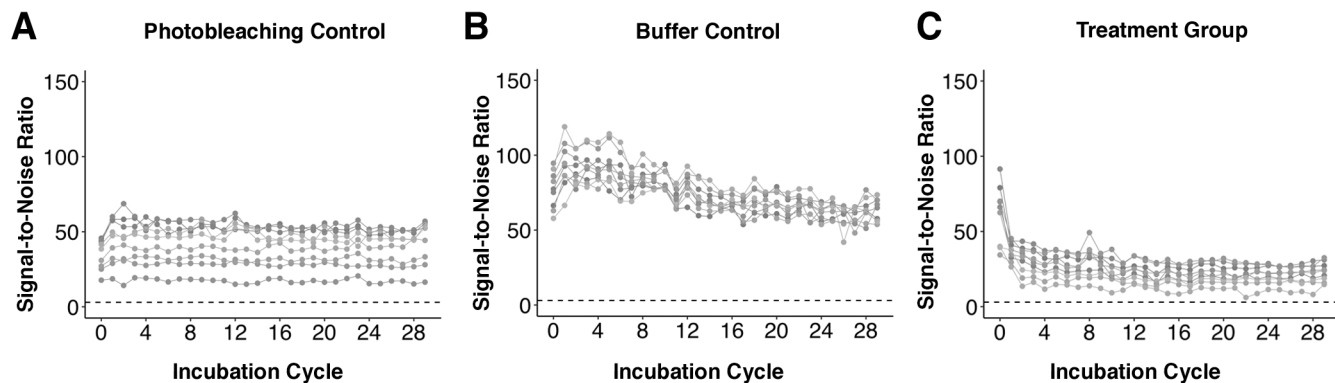


Figure 2.6: Monitoring SNR of immobilized protein targets from BMPA hydrogels during chemical stripping. (a)-(c) SNRs of the photobleaching controls, the buffer controls, and the treatment group, respectively. The SNRs of the photobleaching control gels demonstrate minimal fluctuation over 29 incubation cycles, whereas the SNRs of the buffer control gels demonstrate a steady decrease for the first 14-16 cycles, followed by a plateau. The SNRs of the treatment group demonstrate a dramatic decrease during the first 3-5 rounds of stripping, followed by a plateau for the remaining rounds. For all plots, each trace represents the SNR from one ROI in a BMPA hydrogel.

Our results demonstrate that the trends in SNR are similar to the trends in normalized fluorescence intensity values for each sample condition: the photobleaching control has minimal fluctuation in the SNR values, corresponding to photobleaching or measurement variation; the buffer control samples have a steady decrease in SNR until rounds 14-16, after which the values have minimal variation; and the treatment group has a sharp decrease in SNR, followed by a plateau. Moreover, for the treatment group, the greatest change in SNR occurs in the first 3-5 rounds, which is once again in agreement with the trend observed for normalized fluorescence intensity values.

Finally, by observing the ROI of the immobilized protein region with the lowest SNR value in the treatment group (an SNR of 6.35 at round 22), and by comparing this to the SNR value of the same ROI at round 4 (SNR = 12 for the same ROI at round 4), we can draw additional conclusions about the LOD our system: specifically, our results suggest that if the SNR of an observed ROI is above 12 by round 4, then the SNR of the same ROI will continue to remain above 3 (i.e., the LOD) for the remainder of the 29 stripping cycles.

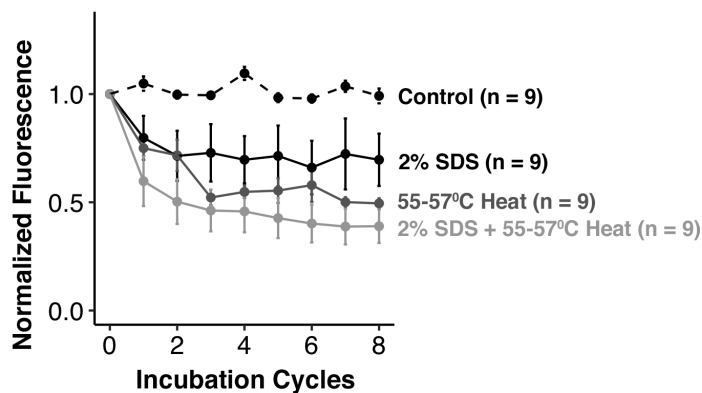


Figure 2.7: SDS and heat are primary contributors to protein loss during the stripping process. Four sets of triplicate BMPA hydrogels with immobilized RNase-488 were exposed to (i) photobleaching only (control), (ii) just detergent (2% SDS), (iii) just heat (55-57°C temperatures), or (iv) detergent and heat (2% SDS + 55-57°C heat). At round 8, the combination of the detergent and heat condition had the greatest fluorescence intensity loss ($61.1\% \pm 7.7\%$).

In accordance with western blotting, our observations suggests that low-abundance proteins should be immunoprobed first despite utilization of covalent chemistries for protein immobilization [33, 47], as our analysis indicates that any proteins that remain in the gel after the fourth stripping cycle will continue to remain in the gel for a minimum of 25 additional stripping cycles.

Investigating the Mechanism of Protein Loss from Stripping Rounds

We next sought to investigate the primary mechanism of protein loss from BMPA hydrogels after sequential stripping rounds. Recall, we hypothesized that the main mechanism of protein loss was disruption of non-covalent interactions between the protein and the hydrogel matrix, or from protein-protein species [40–42]. Moreover, we hypothesized that the primary contributors to protein loss are SDS and heat, as both SDS and heat disrupt hydrophobic bonds and van der Waals interactions, and heat also disrupts hydrogen bonding [37, 39]. By contrast, β -mercaptoethanol (the other main component of stripping buffer) primarily denatures disulfide bridges [38]. Although disulfide bridges are a critical component of immunoreagents, we do not anticipate that BMPA hydrogels with immobilized RNase-488 contain significant intermolecular disulfide bridges. Therefore, we hypothesized that the contribution of protein loss from β -mercaptoethanol would be minimal.

We created four sets of triplicates of BMPA hydrogels immobilized with RNase-488 (12 gels total), to examine the loss of protein signal upon exposure to only 2% SDS, only heat, and a combination of 2% SDS and heat. Our results indicate that, after 8 incubation cycles, the SDS-only treatment led to a $30.4\% \pm 12.1\%$ average decrease in fluorescence intensity, the heat-only treatment led to a $50.5\% \pm 5.7\%$ average decrease in fluorescence intensity, and the combination of the two conditions led to an average $61.1\% \pm 7.7\%$ average decrease in fluorescence intensity (see Figure 2.7). By contrast, the initial RNase-488 stripping experiments described in Figure 2, which used all stripping buffer components (SDS, β -mercaptoethanol, and heat), had an average $67.9\% \pm 9.0\%$ decrease in fluorescence intensity at round 8. A Mann-Whitney U-test indicated that the difference in fluorescence decrease between the SDS/heat-only experimental condition and the “full stripping buffer” experimental condition is not statistically significant (p-value = 0.07701); as a result, our hypothesis that the majority of protein signal loss occurs due to SDS and heat is not falsified. Furthermore, a Mann-Whitney U-test also reveals that the difference between the 2% SDS control (average signal loss of $30.4\% \pm 12.1\%$ at round 8) and the TBST buffer control performed in our initial experiment (average signal loss of $40.2\% \pm 4.5\%$ at round 8) are also not statistically significant (p-value = 0.1359), which indicates that TBST and SDS do not induce significantly different protein losses upon similar incubation timescales.

Based on these results, we recommend stripping buffer formulations that provide stringent removal of immunoreagents but without SDS or elevated temperatures. We anticipate that alternative formulations can be sought that retain immobilized target on BMPA hydrogels for a greater number of immunoprobings rounds, thus facilitating detection of lower-abundance proteins.

Understanding the role of Molecular Mass in Protein Loss

As a next step, we sought to understand the behaviour of protein loss with protein species of different molecular weights. Previous studies have reported that the photocapture efficiency of benzophenone varies with the molecular mass of each immobilized target protein species. Photocapture efficiencies of 75.2%, 93.1% and 97.5% were reported for trypsin inhibitor (“TI”, 20.1 kDa), ovalbumin (“OVA”, 42.7 kDa), and beta-galactosidase (116 kDa) respectively [17]. As a result, we hypothesized that the final protein fluorescence signal plateau would also vary in a size-dependent manner, with the smallest proteins experiencing the largest loss (corresponding to the lowest photocapture efficiency), and the largest proteins experiencing the smallest loss (corresponding to the largest photocapture efficiency).

We fabricated BMPA hydrogels with immobilized protein, consisting of either fluorescently labeled OVA or TI, and performed stripping experiments identical to those performed with RNase. Once again, each protein species had triplicate gels that functioned as either the photobleaching control or as the treatment group. Our results indicate that protein molecular mass is not a significant factor in protein loss (Figure 5). Although RNase, the smallest protein (13.7 kDa), had the greatest amount of protein loss ($71.4\% \pm 7.9\%$ at round 7), OVA

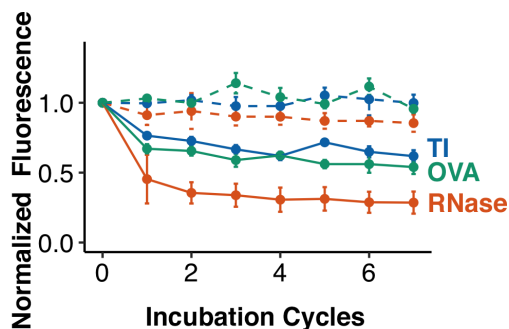


Figure 2.8: Protein size is not a substantial contributor to protein loss. Triplicate BMPA hydrogels with immobilized protein were created for each of OVA (42.7 kDa), TI (20.1 kDa), and RNase (13.7 kDa). Dotted lines represent photobleaching controls, whereas solid lines represent treatment groups. At round 7, the protein losses were $46.0\% \pm 5.0\%$, $38.2\% \pm 4.2\%$, and $71.4\% \pm 7.9\%$ for OVA, TI, and RNase, respectively, indicating minimal size-based correlation.

(42.7 kDa) and TI (20.1 kDa) had losses of $46.0\% \pm 5.0\%$ and $38.2\% \pm 4.2\%$ respectively, which contradicted our expectations.

Our results suggest that protein molecular mass is not a significant factor in protein loss (Figure 2.8). Although RNase, the smallest protein, has the greatest amount of protein loss, the trends in protein loss do not correlate with the molecular masses of the other two proteins, OVA and TI (see Table 2.2).

To reconcile this discrepancy, we first note that proteins immobilized in the BMPA hydrogels were incubated in a solution of 2% BSA/TBST prior to UV photocapture via benzophenone. However, previous studies of benzophenone photocapture efficiency utilized SDS to denature proteins prior to UV irradiation [17]. We expect that when proteins are denatured, benzophenone moieties have access to most amino acid residues in the peptide chain, from which hydrogen atoms can be abstracted for photocapture [21]. Although benzophenone does demonstrate residue-specific preferences during photocapture [21], we can nevertheless assume that, to a first approximation, photocapture efficiency scales with the amount of abstractable hydrogen atoms that are accessible to the benzophenone moiety. We further know that all amino acid residues in a peptide chain possess at least one abstractable hydrogen group (i.e., at minimum, the alpha carbon) [21]. Thus, under denaturing conditions, we expect that photocapture efficiencies scale with the size of the protein.

However, in non-denaturing conditions, we expect that not all amino acid residues would be accessible by the benzophenone (e.g., residues that are buried inside hydrophobic pockets of an amino acid chain). We investigated the hydrodynamic radius of the protein to be a proxy for the number of amino acids accessible to benzophenone, since globular proteins with larger radii would also have larger surface areas, and thus, more surface accessible amino acids. Previous studies estimate that the hydrodynamic radius of RNase, TI, and OVA, are

Table 2.2: Physicochemical Properties of Proteins Immobilized in BMPA Hydrogels and their Respective Signal Losses upon 7 Rounds of Stripping

Protein	Molecular Weight	Hydrodynamic Radius	Signal Loss
RNase	13.7 kDa ⁷	1.73 nm [48]	71.4% \pm 7.9%
OVA	42.7 kDa ⁷	2.65 nm [48]	46.0% \pm 5.0%
TI	20.1 kDa ⁷	3.4 nm [49]	38.2% \pm 4.2%

approximately 1.73 nm [49], 3.4 nm [48], and 2.65 nm [48] respectively; the rank ordering of these radii matches the rank ordering of signal loss observed for these protein targets (see Table 1). Thus, in non-denaturing conditions, we anticipate that protein retention is more correlated with hydrodynamic radius than protein molecular weight.

Based on these results, we recommend both (i) careful choice of immobilization buffer during photocapture with benzophenone and (ii) anticipation of either size-based, or hydrodynamic radius-based, signal loss for protein target, depending on the use of denaturing or non-denaturing buffer conditions.

Comparing Protein-Conjugate Fluorescence Loss to Immunoprobed Fluorescence Loss

Finally, in order to evaluate the contribution of protein loss to immunoassay signal loss, we next created two sets of triplicates (photobleaching control and treatment group) of BMPA hydrogels immobilized with RNase-488 and subjected these groups to serial rounds of stripping, followed by immunoprobing. We immobilized a smaller concentration of RNase-488 (125 nM in-solution concentration of RNase-488) with a higher degree of labeling of Alexa Fluor 488 (DOL = 1.23) in order to ensure that the concentrations of immunoprobing reagents, which were utilized at 0.1 mg/mL, would be in excess of the in-gel RNase-488 concentration, while also ensuring that we would be able to sufficiently visualize our RNase-488 conjugates during multiple stripping cycles. We stripped, and reprobated, our RNase-488 gels for a total of 6 times.

We quantified the fluorescence from our immunoprobed hydrogels in a manner identical to the quantification performed with our protein-conjugate hydrogels. Furthermore, we performed background subtraction from regions absent protein-conjugate (but incubated in immunoreagents) to account for any confounding signal from blank hydrogel regions. Our results demonstrate that the protein-conjugate fluorescence (see 2.9 6a) follows the same trend observed in our initial experiments of RNase-488 fluorescence loss after multiple stripping rounds as depicted in 2.3. In our stripping and reprobating experiments, the treatment group demonstrated a loss of 65.5% \pm 3.2% after 6 rounds ($n = 9$), with the majority of the protein loss occurring in the first 1-3 rounds. A Mann-Whitney U-test indicated no sig-

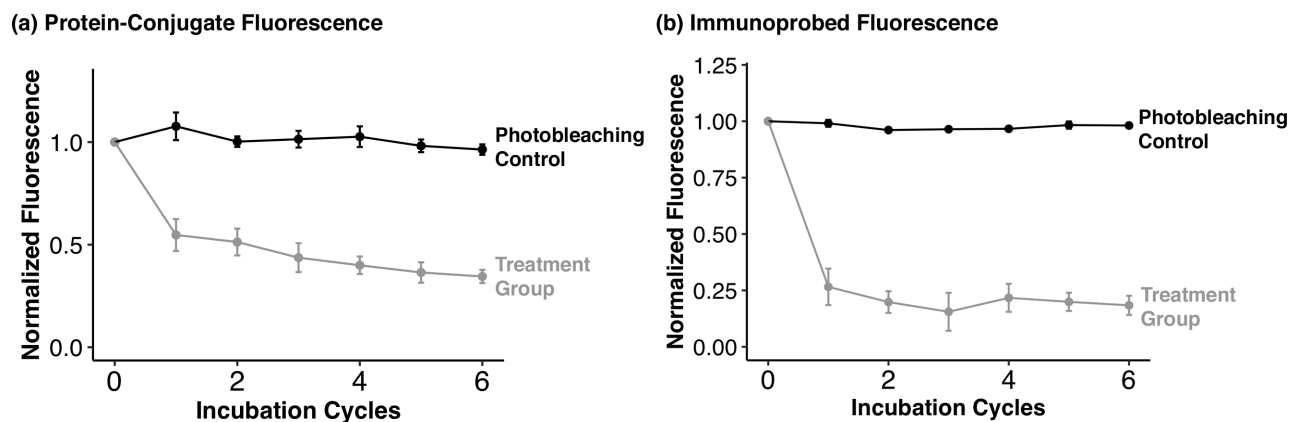


Figure 2.9: Comparison of Fluorescence Loss Between Protein-Conjugate and Immunoreagents during Serial Stripping and Reprobing Cycles. (a) Fluorescence loss of protein-conjugates in three BMPA hydrogels immobilized with RNase-488 (DOL = 1.3). Round 0 corresponds to the RNase-488 fluorescence after the initial immunoprobng round. (b) Fluorescence loss of immunoreagents in BMPA hydrogels immobilized with RNase-488 and immunoprobed with primary (Rb anti-RNase) and fluorescent secondary (Gt anti-Rb conjugated to Alexa Fluor 633) antibodies. Each incubation cycle following round 0 corresponds to one round of stripping, followed by immediate reprobing with new immunoreagents.

nificant difference (p -value = 0.077) between the observed fluorescence loss of the treatment group in the current experiment, and the observed fluorescence loss of the treatment group in the initial stripping experiment after 6 rounds of stripping ($71.2\% \pm 7.5\%$, $n = 9$).

Finally, we investigated loss of immunoassay signal after multiple reprobing rounds of our RNase-488 protein conjugate. We observed the majority of immunoassay signal loss in the first round; by round 6, the treatment group demonstrated $81.6 \pm 4.25\%$ signal loss ($n = 6$), which is substantially higher than the protein-conjugate fluorescence loss (see 2.9b). This result suggests that protein conjugate loss may be responsible for the majority, but not all, of immunoassay signal loss.

As an important aside, we observed spatially non-uniform probing results in one of the three gels in our treatment group, which we attribute to our reagent-sparing probing process (antibody concentration at 0.1 mg/mL; application of $40 \mu\text{L}$ solution using a glass plate [50]). We did not include results from the questionable gel in the preceding analysis (see Figure 2.10).

We hypothesize that any remaining immunoassay signal loss that is not attributable to protein loss may be caused either by (1) epitope masking due to the exposure of protein target to denaturing detergents, such as SDS, during the stripping procedure, or (2) hindered immunoreagent entry into the BMPA gel during successive immunoassay probing rounds. We put substantial weight on the second hypothesis because we have observed residual immunoreagent fluorescence after each stripping round, which increases after every reprobing

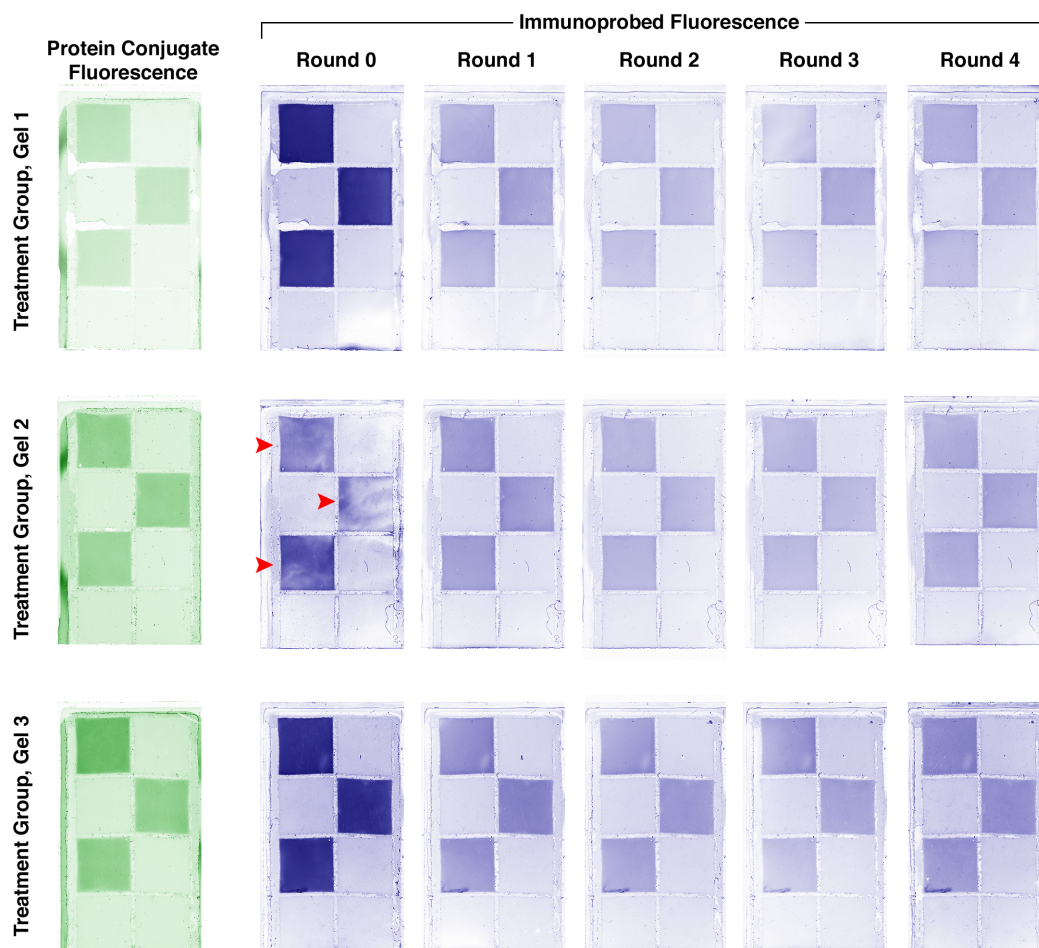


Figure 2.10: False-color micrographs of BMPA hydrogels immobilized with RNase-488 and immunoprobed with antibody. The green micrographs depict protein-conjugate fluorescence (RNase-488), whereas the blue micrographs represent immunoprobed signal after every round of stripping and reprobing. The initial immunoprobing round (Round 0) for gel 2 had large non-uniformities, which have been represented by the red arrows. All other micrographs, including micrographs obtained from further reprobing of gel 2, are uniform.

round (see 2.11). We suspect that this increase is due to entropic trapping of immunoreagents among the pores of the PA gel; although estimates of the antibody hydrodynamic radius (~ 5 nm) [51] are much smaller than estimates of the PA pore size for 7-8 %T gels ($\sim 50-90$ nm whilst utilizing a 3-4 % bis-acrylamide crosslinker concentration [52]), previous studies have demonstrated that a 1:10 difference in particle-to-pore size is sufficient for entropic trapping of solutes in a hydrogel matrix [53]. We can expect that entrapment of antibodies in the PA gel would hinder further immunoreagent entry, owing to inaccessible pores through which new immunoreagents can no longer migrate, which would ultimately reduce antibody-to-

analyte complex formation, and thus, result in additional signal loss.

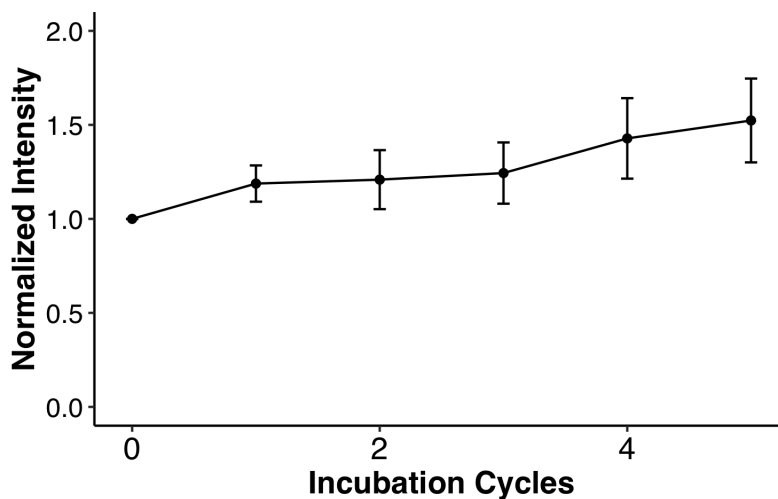


Figure 2.11: Normalized intensity of residual immunoprobng fluorescence after stripping rounds. Immunoprobnged gels that were stripped were scanned immediately after stripping but before reprobing ($n = 6$). Residual signal is attributable to immunoreagents that were not fully removed from the gel.

2.4 Conclusion

As a basis for design of multiplexed in-gel immunoassays, we scrutinized the effects of harsh denaturing detergents on protein targets covalently immobilized to a BMPA hydrogel. The majority of immunoassay signal loss is attributed to loss of non-covalently-bound proteins from the gel matrix, and occurs during the first 5 rounds of stripping. By tracking fluorescence signal from protein-fluorophore conjugates, we determine that protein loss plateaus starting from the 11th stripping round (if not earlier) and is maintained through the 29th stripping round. Our results suggest that, despite utilizing covalent chemistries to immobilize proteins to BMPA hydrogels, low-abundance protein targets should be immunoprobnged first, as in accordance with slab-gel western blotting best practices.

Moreover, we surmise that the main contributors to protein loss are (i) the SDS component of the stripping buffer and (ii) the elevated temperature used during the stripping procedure. The working conclusions suggest that the majority of protein loss is from proteins that are non-covalently bound to the hydrogel. We posit that the investigation of stripping buffers that do not use SDS or heat, but nonetheless remove the majority of immunoprobnges, may facilitate lower protein loss during successive immunoprobnging cycles.

We further conclude that the molecular mass of protein targets is not a significant contributor to protein loss during non-denaturing photocapture conditions, as differently sized proteins (i.e., RNase at 13.7 kDa, TI at 20.1 kDa, and OVA at 42.7 kDa) demonstrated little size-based correlation in their respective protein losses ($71.4\% \pm 7.9\%$, $38.2\% \pm 4.2\%$, and $46.0\% \pm 5.0\%$, respectively). In non-denaturing photocapture conditions, we hypothesize that hydrodynamic radius may be a better correlate for protein loss. Based on these results, we recommend choosing the order of protein target detection in successive immunoprobings not only based on protein abundance, but also based on the key physicochemical properties (e.g., molecular weight or hydrodynamic radius) that may modulate protein retention in different immobilization buffers (denaturing vs non-denaturing).

Our results are consistent with one of the key reported mechanisms for interaction between proteins and hydrogels: hydrogels routinely interact with proteins through non-covalent interactions, including hydrogen bonding [40, 41], electrostatic interactions [42], and van der Waals forces [42]. Furthermore, protein adsorption through non-covalent interactions facilitate incorporation of biomolecules onto hydrogel scaffolds for tissue engineering. These studies, coupled with our results, suggest that non-covalent interactions can modulate protein retention across a wide range of hydrogels [54]. Furthermore, the “gradual release” of proteins from the BMPA hydrogel system is similar to the controlled release of drugs or small molecules from modified PA hydrogels, some of which demonstrate release of $\sim 56\%$ and $\sim 77\%$ of their payload over the course of 24 and 75 hours respectively [55].

In benchmarking this system against other multiplexed immunoassays, we note that most studies assess antigenic recovery (i.e., presence or absence of protein target signal) [34]. Fewer studies quantify the amount of signal present between successive immunoprobings, when serial multiplexing strategies are used. Nevertheless, previous studies relating antigen losses from surfaces or membranes (e.g., nitrocellulose, nylon, or PVDF) report appreciable antigen signal retention for 3-6 rounds of immunoprobings with similar stripping buffers (i.e., SDS, β -mercaptoethanol, and heat) [33]. Alternative stripping buffer formulations, including those involving Glycine HCl, have reported antigenic detection for up to 21 rounds of protein targets on PVDF membranes [47]. The fact that BMPA hydrogels can extend stripping and reprobing cycles to 29 rounds without alternative stripping buffer formulations suggests that (1) BMPA hydrogels retain more antigen than membranes during successive stripping rounds, and that (2) alternate stripping buffer formulations may support even more antigen retention per round when used in conjunction with BMPA hydrogels.

Looking forward, we envision that optimizing assay chemistries may decrease protein losses during the first few rounds of stripping, enabling detection of low abundance proteins for more reprobing cycles. For instance, we are interested in exploring the potential of quenching and reprobing chemistries with heterogeneous immunoassays in hydrogels to reduce protein loss during the first few reprobing cycles [27]. We additionally surmise that further understanding of entropic trapping of antibodies in hydrogels during immunoprobings may provide additional clues as to the mechanism of immunoassay signal loss during stripping and reprobing rounds.

We anticipate that the results of this study will be broadly applicable to protein-hydrogel

bioanalytical tools, and may lead to greater adoption of the ‘stripping and reprobing’ method for increased multiplexing.

Bibliography

1. Yu, C., Woods, A. & Levison, D. The assessment of cellular proliferation by immunohistochemistry: a review of currently available methods and their applications. *Histochemistry* **24**, 121–31 (1992).
2. Campisi, J. & d’Adda di Fagagna, F. Cellular senescence: when bad things happen to good cells. *Nature Reviews Immunology* **8**, 729–740 (2007).
3. Christianson, T. A. *et al.* NH2-terminally truncated HER-2/neu protein: relationship with shedding of the extracellular domain and with prognostic factors in breast cancer. *Cancer Res* **58**, 5123–9. ISSN: 00085472 (1998).
4. Hughes, A. J. *et al.* Single-cell western blotting. *Nature methods* **11**, 749–55. ISSN: 1548-7105. arXiv: NIHMS150003. <http://www.ncbi.nlm.nih.gov/pubmed/24880876> (2014).
5. Tentori, A. M., Yamauchi, K. A. & Herr, A. E. Detection of Isoforms Differing by a Single Charge Unit in Individual Cells. *Angewandte Chemie*, 12431–12435 (2016).
6. Yamauchi, K. A. & Herr, A. E. Subcellular western blotting of single cells. *Microsystems & Nanoengineering* **3**, 16079. ISSN: 2055-7434. <http://www.nature.com/articles/micronano201679> (2017).
7. Xu, W. *et al.* Contact printing of arrayed microstructures. *Analytical and Bioanalytical Chemistry* **397**, 3377–3385. ISSN: 16182642 (2010).
8. Ornoff, D. M. *et al.* Co-fabrication of chitosan and epoxy photoresist to form microwell arrays with permeable hydrogel bottoms. *Biomaterials* **74**, 77–88. ISSN: 18785905. <http://dx.doi.org/10.1016/j.biomaterials.2015.09.032> (2016).
9. Tanase, C. P., Albulescu, R. & Neagu, M. Application of 3D hydrogel microarrays in molecular diagnostics: Advantages and limitations. *Expert Review of Molecular Diagnostics* **11**, 461–462. ISSN: 14737159 (2011).
10. Spencer, A. R. *et al.* Electroconductive Gelatin Methacryloyl-PEDOT:PSS Composite Hydrogels: Design, Synthesis, and Properties. *ACS Biomaterials Science & Engineering*, acsbiomaterials.8b00135. ISSN: 2373-9878. <http://pubs.acs.org/doi/10.1021/acsbiomaterials.8b00135> (2018).

11. Bettadapur, A. *et al.* Prolonged Culture of Aligned Skeletal Myotubes on Micromolded Gelatin Hydrogels. *Scientific Reports* **6**, 28855. ISSN: 2045-2322. <http://www.nature.com/articles/srep28855> (2016).
12. Chung, K. *et al.* Structural and molecular interrogation of intact biological systems. *Nature* **497**, 332–337. ISSN: 00280836. arXiv: NIHMS150003. <http://dx.doi.org/10.1038/nature12107> (2013).
13. Chen, F., Tillberg, P. W. & Boyden, E. Expansion Microscopy. *Science* **347** (2015).
14. Zhang, X., Li, L. & Luo, C. Gel integration for microfluidic applications. *Lab on a Chip* **16**, 1757–1776. ISSN: 14730189 (2016).
15. Kim, D. & Herr, A. E. Protein immobilization techniques for microfluidic assays. *Biomicrofluidics* **7**, 041501. ISSN: 1473-0197 (2013).
16. Chozinski, T. J. *et al.* Expansion microscopy with conventional antibodies and fluorescent proteins. *Nature Methods* **13**, 485–488. ISSN: 1548-7091. <http://www.nature.com/articles/nmeth.3833> (2016).
17. Hughes, A. J. & Herr, A. E. Microfluidic Western blotting. *Proceedings of the National Academy of Sciences of the United States of America* **109**, 21450–5. ISSN: 1091-6490. <http://www.pubmedcentral.nih.gov/articlerender.fcgi?artid=3535594&tool=pmcentrez&rendertype=abstract> (2012).
18. Appleyard, D. C., Chapin, S. C. & Doyle, P. S. Multiplexed Protein Quantification with Barcoded Hydrogel Microparticles. *Analytical Chemistry* **83**, 193–199 (2011).
19. Schneider, M. H., Tran, Y. & Tabeling, P. Benzophenone absorption and diffusion in poly(dimethylsiloxane) and its role in graft photo-polymerization for surface modification. *Langmuir : the ACS journal of surfaces and colloids* **27**, 1232–40. ISSN: 1520-5827. <http://www.ncbi.nlm.nih.gov/pubmed/21207954> (2011).
20. O’Neill, R. A. *et al.* Isoelectric focusing technology quantifies protein signaling in 25 cells. *Proceedings of the National Academy of Sciences* **103**, 16153–16158. ISSN: 0027-8424. <http://www.pnas.org/cgi/doi/10.1073/pnas.0607973103> (2006).
21. Dormán, G & Prestwich, G. D. Benzophenone photophores in biochemistry. *Biochemistry* **33**, 5661–5673. ISSN: 0006-2960 (1994).
22. Banks, J. M., Harley, B. A. & Bailey, R. C. Tunable, Photoreactive Hydrogel System to Probe Synergies between Mechanical and Biomolecular Cues on Adipose-Derived Mesenchymal Stem Cell Differentiation. *ACS Biomaterials Science and Engineering* **1**, 718–725. ISSN: 23739878 (2015).
23. Kapil, M. A. *et al.* Binding Kinetic Rates Measured via Electrophoretic Band Crossing in a Pseudohomogeneous Format. *Analytical Chemistry* **88** (2014).
24. Neira, H. D. & Herr, A. E. Kinetic Analysis of Enzymes Immobilized in Porous Film Arrays. *Analytical Chemistry* **89**, 10311–10320. ISSN: 15206882 (2017).

25. Dixon, A. R. *et al.* Recent developments in multiplexing techniques for immunohistochemistry. *Expert Rev. Mol. Diagn.* **15**, 1171–1186 (2015).
26. Tsurui, H. *et al.* Seven-color Fluorescence Imaging of Tissue Samples Based on Fourier Spectroscopy and Singular Value Decomposition. *Journal of Histochemistry & Cytochemistry* **48**, 653–662. ISSN: 0022-1554. <http://journals.sagepub.com/doi/10.1177/002215540004800509> (2000).
27. Gerdes, M. J. *et al.* Highly multiplexed single-cell analysis of formalin-fixed, paraffin-embedded cancer tissue. *Proceedings of the National Academy of Sciences of the United States of America* **110**, 11982–7. ISSN: 1091-6490. <http://www.ncbi.nlm.nih.gov/pubmed/23818604><http://www.pubmedcentral.nih.gov/articlerender.fcgi?artid=PMC3718135> (2013).
28. Vira, S. *et al.* Fluorescent labeled antibodies - balancing functionality and degree of labeling. *Analytical biochemistry* **402**, 146–150 (2011).
29. Dhawan, S. Signal amplification systems in immunoassays: Implications for clinical diagnostics. *Expert Review of Molecular Diagnostics* **6**, 749–760. ISSN: 14737159 (2006).
30. Wählby, C. *et al.* Sequential immunofluorescence staining and image analysis for detection of large numbers of antigens in individual cell nuclei. *Cytometry* **47**, 32–41. ISSN: 01964763 (2002).
31. Glass, G., Papin, J. A. & Mandell, J. W. SIMPLE: A sequential immunoperoxidase labeling and erasing method. *Journal of Histochemistry and Cytochemistry* **57**, 899–905. ISSN: 00221554 (2009).
32. Zrazhevskiy, P., True, L. D. & Gao, X. Multicolor multicycle molecular profiling with quantum dots for single-cell analysis. *Nature Protocols* **8**, 1852–1869. ISSN: 1754-2189. <http://www.nature.com/doi/10.1038/nprot.2013.112> (2013).
33. Kaufmann, S. H., Ewing, C. M. & Shaper, J. H. The erasable Western blot. *Analytical Biochemistry* **161**, 89–95. ISSN: 10960309 (1987).
34. Ku, T. *et al.* Multiplexed and scalable super-resolution imaging of three-dimensional protein localization in size-adjustable tissues. *Nature Biotechnology* **34**, 973–981. ISSN: 1087-0156. <http://www.nature.com/articles/nbt.3641> (2016).
35. Gallagher, S. *et al.* Immunoblotting and Immunodetection. *Current Protocols in Cell Biology* **83**, 10.8.1–10.8.28. <http://doi.wiley.com/10.1002/0471143030.cb0602s52> (2008).
36. Sinkala, E. *et al.* Profiling protein expression in circulating tumour cells using microfluidic western blotting. *Nature Communications* (2017).
37. Reynolds, J. A. & Tanford, C. Binding of Dodecyl Sulfate to Proteins at High Binding Ratios. Possible Implications for the State of Proteins in Biological Membranes. *Proceedings of the National Academy of Sciences* **66**, 1002–1007. ISSN: 0027-8424. <http://www.pnas.org/cgi/doi/10.1073/pnas.66.3.1002> (1970).

38. Jocelyn, P. C. Chemical reduction of disulfides. *Methods in Enzymology* **143**, 246–256 (1987).
39. Cooper, A. Heat capacity of hydrogen-bonded networks: An alternative view of protein folding thermodynamics. *Biophysical Chemistry* **85**, 25–39. ISSN: 03014622 (2000).
40. Patyukova, E. *et al.* Hydrogen Bonding Aggregation in Acrylamide: Theory and Experiment. *Macromolecules* **51**, 7032–7043. ISSN: 0024-9297. <http://pubs.acs.org/doi/10.1021/acs.macromol.8b01118> (2018).
41. Lu, P. & Hsieh, Y.-L. Organic compatible polyacrylamide hydrogel fibers. *Polymer* **50**, 3670–3679. ISSN: 0032-3861 (2009).
42. Suzawa, T. & Shirahama, H. Adsorption of plasma proteins onto polymer latices. *Advances in Colloid and Interface Science* **35**, 139–172. ISSN: 0001-8686 (1991).
43. Saeed, I. A. & Ashraf, S. S. Denaturation studies reveal significant differences between GFP and blue fluorescent protein. *International Journal of Biological Macromolecules* **45**, 236–241. ISSN: 01418130 (2009).
44. Panchuk-Voloshina, N. *et al.* Alexa Dyes, a Series of New Fluorescent Dyes that Yield Exceptionally Bright, Photostable Conjugates. *Journal of Histochemistry & Cytochemistry* **47**, 1179–1188. ISSN: 0022-1554. <http://jhc.sagepub.com/content/47/9/1179.full> (1999).
45. Vlassakis, J. & Herr, A. E. Effect of Polymer Hydration State on In-Gel Immunoassays. *Analytical Chemistry* **87**, 151022142613006. ISSN: 0003-2700. <http://pubs.acs.org/doi/10.1021/acs.analchem.5b03032> (2015).
46. Bay, H., Tuytelaars, T. & Van Gool, L. *SURF: Speeded Up Robust Features in Computer Vision – ECCV 2006* (eds Leonardis, A., Bischof, H. & Pinz, A.) (Springer Berlin Heidelberg, Berlin, Heidelberg, 2006), 404–417. ISBN: 978-3-540-33833-8.
47. Albiach, M. R., Guerri, J. & Moreno, P. Albiach, Multiple Use of Blotted Polyvinylidene Difluoride Membranes Immunostained with Nitro Blue Tetrazolium. *Analytical biochemistry*, 25–28 (1994).
48. Takeuchi, K. *et al.* Accuracy of Protein Size Estimates Based on Light Scattering Measurements. *Open Journal of Biophysics* **04**, 83–91. ISSN: 2164-5388. <http://www.scirp.org/journal/doi.aspx?DOI=10.4236/ojbiphy.2014.42009> (2014).
49. Wolf, W. J. Physical and chemical properties of soybean proteins. *Journal of the American Oil Chemists' Society* **54**, A112. ISSN: 0003021X. <http://doi.wiley.com/10.1007/BF02912385> (1977).
50. Kang, C.-c. *et al.* Single cell resolution western blotting. *Nature Protocols* **11**, 1508–1530. ISSN: 1754-2189. <http://dx.doi.org/10.1038/nprot.2016.089> (2016).
51. Jøssang, T., Feder, J. & Rosenqvist, E. Photon correlation spectroscopy of human IgG. *Journal of Protein Chemistry* **7**, 165–171. <http://link.springer.com/10.1007/BF01025246> (1988).

52. Holmes, D. L. & Stellwagen, N. C. Estimation of polyacrylamide gel pore size from Ferguson plots of linear DNA fragments. *Electrophoresis* **12**, 612–619 (1991).
53. Liu, L., Li, P. & Asher, S. A. Entropic trapping of macromolecules by mesoscopic periodic voids in a polymer hydrogel. *Nature Letters* **397**, 141–144. ISSN: 00280836. <http://www.nature.com/doi/10.1038/16426> (1999).
54. Zustiak, S. P., Wei, Y. & Leach, J. B. Protein-hydrogel interactions in tissue engineering: mechanisms and applications. *Tissue engineering. Part B, Reviews* **19**, 160–71. ISSN: 1937-3376. <http://www.ncbi.nlm.nih.gov/pubmed/23150926><http://www.pubmedcentral.nih.gov/articlerender.fcgi?artid=PMC3592387> (2013).
55. Makarand V. Risbud, Ramesh R. Bhond, R. R. B. Polyacrylamide-Chitosan Hydrogels: In Vitro Biocompatibility and Sustained Antibiotic Release Studies. *Drug Delivery* **7**, 69–75. ISSN: 1071-7544. <http://www.tandfonline.com/doi/full/10.1080/107175400266623> (2000).

Chapter 3

Segmentation-Based Analysis of Single-cell Immunoblots

Materials reproduced, with permission, from:

A. Gopal and A. E. Herr, "Segmentation-Based Analysis of Single-cell Immunoblots", *Electrophoresis*, 2021.

3.1 Introduction

Single-cell protein analysis is critically important for understanding cellular heterogeneity in a range of processes including cell development, differentiation, and cancer progression [1–3]. More specifically, detecting and quantifying protein isoform expression at the single-cell level greatly increases our ability to interrogate the human proteome [4–6]. While estimates suggest that there upwards of 19,000 human coding genes, each gene is estimated to have up to 100 unique proteoforms that can be generated by processes such as alternative splicing, post-translational modifications, or single-nucleotide polymorphisms [7, 8]. As a result, single-cell proteoform measurements are key to unlocking critical unknowns in the human protein landscape.

Miniaturization of analytical tools has provided new avenues for interrogating a range of key biological questions. Separation-based microscale assays enable new insights into fundamental biological phenomena, including analysis of DNA damage [9, 10], enzyme upregulation [11], metabolites [12–14], and binding interactions [15, 16]. For proteoform analysis, microscale assays such as single-cell immunoblots (scI) analyze dozens of protein targets (including isoforms) in arrays of tens to hundreds of single-cell separations [5, 17, 18]. In scI, a single-cell suspension (e.g., from a dissociated tumor biopsy) is seeded onto a 40-50 μm thick polyacrylamide (PA) gel (Figure 3.1A). To isolate each single cell, the PA gel itself is stippled with 30-40 μm diameter microwells, into which single cells are settled via gravitational sedimentation. A dual lysis/electrophoresis buffer facilitates in-situ cell lysis, followed by ultra-rapid sodium dodecyl sulfate polyacrylamide gel electrophoresis (SDS-PAGE) within

each single-cell lysate. After separation, the resultant protein bands are immobilized within the hydrogel matrix via a UV-activatable chemical crosslinker (benzophenone), and subsequent protein detection occurs by application of primary, followed by fluorescently labeled secondary antibodies (immunoblotting). The entire scI gel array is imaged via a laser microarray scanner. By dividing the array into individual separation lanes, protein and isoform expression profiles are surveyed within each single cell [17].

Substantial innovation has been made in the types of single-cell proteoforms detected [5, 18]. However, in order to ensure robust interrogation of key biological characteristics, including the underlying isoform expression level distribution, careful quantification of scI is needed. Currently, one-dimensional (1D) Gaussian fitting via non-linear least squares regression is the standard approach for scI quantification (Figure 3.1B) [19, 20]. Within a given separation lane, scI confers a two-dimensional (2D) Gaussian distribution to protein bands, due to diffusion during PAGE [17]. Similar to capillary zone electrophoresis [21, 22], collapsing the immunoblot profile into a 1D electropherogram and fitting the resulting separation profiles to a Gaussian distribution extracts key analytical parameters, including location of the protein band center (mean of the Gaussian distribution), total protein quantity (area under the curve (AUC)), and separation resolution, or the degree of separation between two molecular isoforms [19, 20].

However, Gaussian fitting also suffers several disadvantages: specifically, due to the compression of a 2D separation lane into a 1D electropherogram, noise in the vicinity of the protein band can affect quantification accuracy when utilizing Gaussian fitting [20]. Furthermore, quantifying protein peaks that have non-standard Gaussian diffusion profiles, including peaks with significant skew or kurtosis, may also suffer with conventional Gaussian fitting pipelines without tuning several additional fit parameters.

By contrast, segmentation is the state-of-the art approach in identifying protein expression levels in single-cell immunofluorescence measurements [23–25], in bulk 2D electrophoresis [26–29], and in other single-cell separations, such as comet assays [30]. Segmentation-based approaches can increase the accuracy of protein band quantification by utilizing the spatial information present in 2D separation profiles, and such approaches have been utilized for other single-cell measurements. However, to our knowledge, segmentation-based methods have not yet been applied to scI.

In this study, we investigate the use of segmentation-based approaches to robustly quantify scI (Figure 3.1C). We first develop and benchmark the quantification accuracy of a segmentation pipeline against the Gaussian fitting pipeline for scI [20]. Next, we explore the ability of segmentation-based methods to identify multiple protein isoforms from the same cell. Finally, we investigate automation of the segmentation process via deep learning. We use these results to uncover the principles of segmentation that may make it a more, or less, suitable method than Gaussian fitting for analyzing scI.

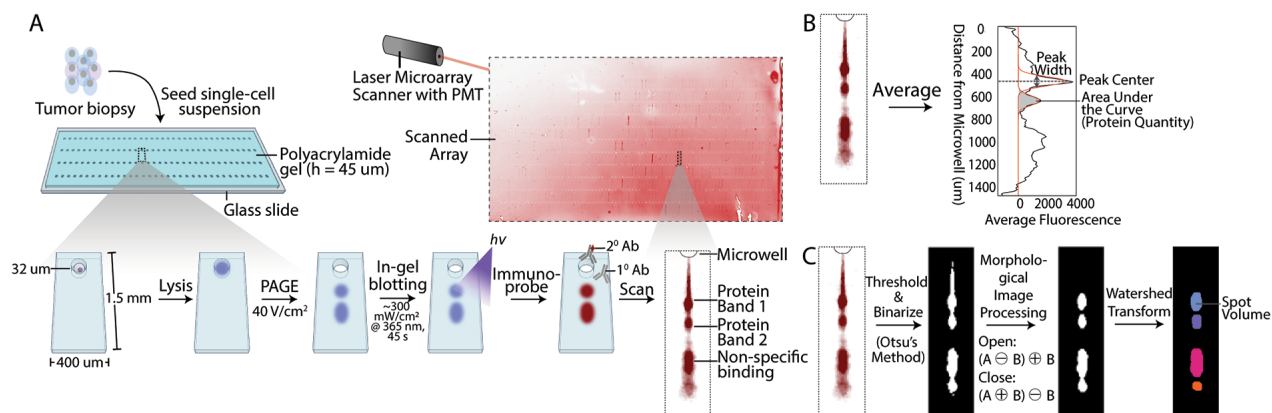


Figure 3.1: Single-cell immunoblotting and downstream quantification interrogates isoform expression levels in single cells. (A) Single-cell suspensions (e.g., consisting of dissociated cells from a tumor biopsy) are seeded onto a thin (45- μm height) PA gel fabricated on a microscope slide. The gel is stippled with microwells (between 30-40 μm in diameter), which are typically spaced 400 μm x 1000 μm apart. Single cells settle into microwells via gravitational sedimentation. The entire microfluidic chip is submerged in a bath of dual lysis/electrophoresis buffer, resulting in in-situ cell lysis, followed by SDS-PAGE. A UV-activated crosslinker chemistry (benzophenone) allows covalent immobilization of proteins to the hydrogel. To visualize protein bands, hydrogels are serially incubated with primary and fluorescently-labeled secondary antibodies, washed, dried under an N₂ stream, and scanned with a laser microarray scanner. The resulting array scan can be separated into individual separation lanes consisting of protein bands from single cells. (B) One-dimensional Gaussian fitting is performed by first averaging the fluorescence signal across the lateral axis of an individual separation lane. The resulting trace (black) can be fit to multiple Gaussian distributions (red), each corresponding to a protein band of interest. Gaussian fitting enables extraction of key characteristics of the electrophoretically-separated protein bands, including peak center (migration distance, which is correlated with protein molecular mass in denaturing PAGE), peak width, and protein quantity (area under the curve). (C) Segmentation involves thresholding and binarizing the separation lane pixels into background and foreground classes via Otsu's method. The resulting image is subject to morphological image processing (morphological open, close, and dilation steps with disk-shaped elements of user-specified sizes), followed by application of the Watershed transform to separate the foreground into distinct protein bands. Use of the Watershed transform also allows for identification of other segmented objects in the separation lane, which often occur due to non-specific binding of antibodies to other protein targets. With segmentation, the protein quantity (spot volume) is calculated by directly summing the intensities of the pixels corresponding to each individual protein band.

3.2 Theory and Data Analysis

In this section, we introduce the mathematical principles underpinning analysis of scI readouts for (1) protein target quantification, by comparing 1D Gaussian fitting and segmentation and (2) separation resolution of the protein targets of interest.

Gaussian Fitting Pipeline

To quantify protein bands identified by single-cell immunoblotting via Gaussian fitting, we used a previously published analysis pipeline [20]. Briefly, individual separation lanes from a scanned scI array undergo background subtraction by subtracting the average of 10 pixels from gutter regions (5 pixels from the leftmost and rightmost edge of the separation lane; Figure 3.2A). Separation lanes are then transformed into a 1D electropherogram by averaging across the lateral axis of the separation lane (Figure 3.2B). Gaussian fitting is performed on each individual trace via non-linear least squares regression.

Of separation lanes where a Gaussian fit is identified, additional quality control steps are used to ensure that identified bands are suitable for downstream analysis.

First, the coefficient of determination (R^2) of the Gaussian fit to the raw trace is assessed, and any peaks that cannot fit a Gaussian above a user-defined R^2 threshold (typically 0.7) is discarded from downstream analysis [20]. However, as R^2 values are primarily used to assess the goodness-of-fit of linear least squares models, we note that scrutinizing the R^2 value may not be the most appropriate metric to assess the goodness-of-fit of non-linear least squares regression to a Gaussian function [31].

Next, separation lanes are subject to a manual quality control step in which users discard separation lanes that have (i) Gaussian fits that were fitted to signal from an artefact (e.g., debris) in the separation lane, or (ii) punctate noise (peaks or troughs) in the region that is $\pm 2\sigma$ from the peak center. Finally, separation lanes with protein bands whose estimated SNR < 3 (as defined by the Gaussian fit) are discarded. Although utilizing a SNR < 3 quality control metric is essential for separating true signal from background noise, we discuss pitfalls of calculating the SNR of a 2D protein band from a 1D electropherogram in the section below.

Segmentation Pipeline

Identical to the Gaussian fitting pipeline, fluorescence micrographs of the individual separation lanes from a scanned scI array undergo background subtraction by averaging each of the 5-pixel gutter regions on either edge of the separation lane. All separation lanes are then overlaid into a single image, and the user is prompted to draw a rectangle encompassing the region containing the approximate centroids of the protein band(s) (see Figure 3.3A). Next, each individual separation lane undergoes thresholding and image binarization via Otsu's method. To reduce the presence of punctate noise, separation lanes are subject to a series of image erosion and dilation steps (morphological opening and closing). Finally, the resulting

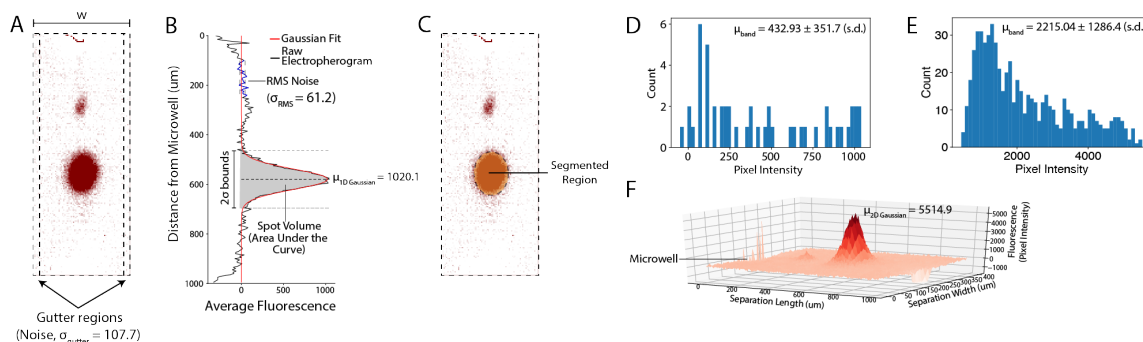


Figure 3.2: Protein band quantification methods between segmentation and Gaussian fitting are not equivalent. (A) Background subtraction of separation lanes, for both methods, involves identifying a 5-pixel gutter region on the edges of the separation lane where minimal protein signal is present. When quantifying the background noise from this gutter region, we assume that the distribution of pixels in this region is drawn iid from the global background distribution. (B) Averaging of the fluorescence intensity signal across the separation lane width produces a 1D electropherogram. The protein band in the electropherogram can be fit to a Gaussian function, in order to calculate metrics like SV (AUC) and SNR. The RMS noise can be calculated by evaluating $2\sigma_{\text{Trace}}$, where σ_{Trace} is the standard deviation of the electropherogram in a region away from the protein band center. (C) With segmentation, pixel intensities for the SV are summed only from the segmented region. Similarly, for SNR calculations, the signal term is calculated by averaging the pixel intensities from the segmented region. (D) The histogram of the pixels of the $\mu \pm 2\sigma$ region of the 1D electropherogram is distributed differently from the underlying 1D Gaussian distribution of the protein band. (E) A histogram of pixel intensities in the 2D segmented region of the micrograph. The average pixel value is $5 \times$ higher than the average value of the 1D electropherogram histogram. (F) The 2D protein band can be viewed as a 2D Gaussian distribution. The maximum amplitude of the 2D Gaussian is also approximately $5 \times$ higher than the maximum amplitude of the 1D Gaussian.

image undergoes a distance transform, which is then used as the seed for the Watershed transform (Figure 3.1C).

Otsu’s method suffers in cases where the amount of background pixels is substantially greater than the amount of foreground pixels, and when attempting to threshold noisy images [32]. Noise and uneven background in scI can result from various sources, including debris on the surface of the hydrogel, spatial variation from non-uniform immunoreagent distribution, non-specific interaction of immunoreagents with the hydrogel substrate, including benzopinacol groups [33, 34]. In the case of hard-to-segment separation lanes (i.e., separation lanes with significant noise), we allowed the user to specify threshold values that were fractionally smaller than the initial threshold found by Otsu’s method, in order to increase segmentation accuracy.

Once the segmentation map is produced via the Watershed transform, additional quality control steps filter out separation lanes with low-quality protein bands, or poorly segmented protein bands. First, all segmented regions outside of the user-defined rectangular boundaries are discarded. Next, separation lanes where the segmented regions-of-interest are larger than a user-specified maximum circularity (default = 1.5) or smaller than a user-specified minimum area (default = 125) are discarded. Of the resulting separation lanes, any lanes where the SNR of an identified protein band is < 3 are discarded. Finally, a manual quality control step is performed, where users are tasked with discarding separation lanes where (i) segmentation was performed on noisy artifacts, or (ii) where the presence of artifacts within the protein band would obscure downstream quantification (see Figure 3.3B).

Calculating Spot Volume

To assess how well either pipeline evaluates key protein band metrics, we first consider the total protein quantity that is present within a protein band. This parameter is termed the ‘spot volume’ (SV) in the separation science literature [26]. In immunoblotting, SV is a proxy for protein target expression, and therefore, has key implications for assessing biological variability across single cells [19].

With segmentation, SV is the sum of pixel intensities for the pixels identified as belonging to a protein band (Figure 3.2C). Thus, assuming that there are n pixels in a protein band, each having I_i fluorescence intensity after background subtraction, the $SV_{Segmentation}$ can be expressed as:

$$SV_{Segmentation} = \sum_{i=1}^n I_i \quad (3.1)$$

In contrast, the Gaussian fitting pipeline determines $SV_{Gaussian}$ by calculating the AUC of the protein band, within $\pm 2\sigma$ from the peak center, corresponding to $\sim 95\%$ of the Gaussian distribution (Figure 3.4b). Equation 3.2 describes this relationship, where μ corresponds to the peak center, σ corresponds to one standard deviation of the Gaussian distribution, and A corresponds to the maximum amplitude of the Gaussian distribution.

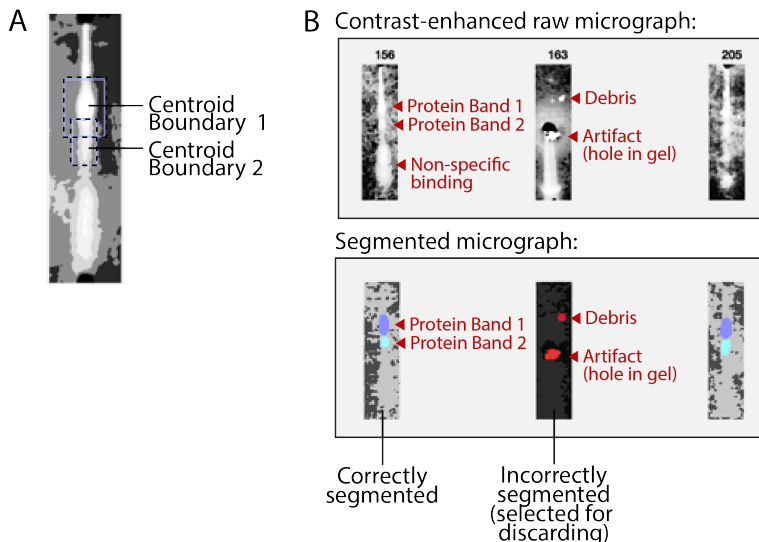


Figure 3.3: Manual quality control measures enable users to filter out badly segmented separation lanes from downstream analysis. A) Users are initially tasked with outlining the centroids of protein bands to narrow the search space of the segmentation algorithm. The displayed image is a superposition of all separation lanes within a given microarray. B) Manual quality control steps allow users to compare the contrast-enhanced micrographs (top) with the segmentation map (bottom) and select separation lanes that were poorly segmented for discarding. For instance, separation lane 156 has two correctly segmented bands (protein peak 1 and protein peak 2), whereas the segmentation map of separation lane 163 correspond to debris and other artifacts in the PA gel. Once a segmentation map has been marked for discarding, the map is colored red (foreground) and black (background).

$$SV_{Gaussian} = \sum_{x=\mu-2\sigma}^{x=\mu+2\sigma} A e^{\frac{-(x-\mu)^2}{2\sigma^2}} \quad (3.2)$$

The averaging operation that collapses each protein band into a 1D electropherogram will create an offset factor between $SV_{Segmentation}$ and $SV_{Gaussian}$. The offset factor is expected to be proportional to the width of the separation lane, w . However, since this averaging is primarily occurring across background-subtracted background pixels, the background pixel values are expected to sum to zero. As a result, we expect strong correlation between $SV_{Segmentation}$ and $SV_{Gaussian}$. Importantly, SV is considered a semi-quantitative metric, which is dependent on antibody probe affinity to the protein band, fluorescence characteristics of the antibody probe label, and the imaging modality [35, 36]. As such, the absolute SV values produced by each pipeline are less critical than maintaining the relative SV values between protein bands in a given dataset. Consequently, we posit that SV is a suitable benchmarking metric, allowing direct comparison of performance between the Gaussian fitting and

segmentation pipelines.

Calculating Signal-to-Noise Ratio

The SNR provides information about whether the measured protein quantity surpasses the lower limit of detection (LLOD) of an assay, and thus, whether the measured protein band is detectable. To calculate SNR according to the widely used definition in analytical chemistry (SNR_{AC}), we use equation 3.3, where μ_{signal} corresponds to the mean signal intensity of the protein band, $\mu_{background}$ corresponds to the mean signal intensity of the background region, and $\sigma_{background}$ corresponds to the background noise.

$$SNR_{AC} = \frac{\mu_{signal} - \mu_{background}}{\sigma_{background}} \quad (3.3)$$

Specifically, the LLOD for an assay is defined as the minimum analyte (protein) concentration that produces a readout signal with $SNR \geq 3$. For scI, if a protein band does not satisfy $SNR \geq 3$, the protein band is indistinguishable from noise, and is discarded from both pipelines prior to downstream analysis.

An alternate definition of SNR used in the separation science literature (e.g., capillary electrophoresis, chromatography) is defining SNR as the ratio between a Gaussian peak maximum (A_{signal} , where A refers to the maximum amplitude of a Gaussian band) and the root mean square noise (N_{RMS}) of a region of the chromatogram or electropherogram that does not contain protein signal ($2 \times \sigma_{trace}$) (Figure 3.2B) [21]. We refer to this formulation as SNR Electrophoresis/Chromatography ($SNR_{E/C}$) as given by equation 3.4:

$$SNR_{E/C} = \frac{A_{signal}}{N_{RMS}} = \frac{A_{signal}}{2 \sigma_{trace}} \quad (3.4)$$

SNR_{AC} and $SNR_{E/C}$ are not equivalent for a given protein band. Calculating the mean signal intensity of a protein band involves calculating the mean signal of the pixels in the protein band (Figure 3.2D; for a representative protein band, $\mu_{band} = 432.9$), which typically has a smaller mean value than the maximum amplitude of the protein band (Figure 3.2B; $\mu_{1DGaussian} = 1020.1$). In this manner, we can see that within either the 2D or the 1D case, $A_{signal} > \mu_{signal}$.

The noise term between Equation 3 and Equation 4 also differs. In SNR_{AC} , noise is the standard deviation in a region of the measurement that does not contain any signal. In previous discussions of scI, the noise term, $\sigma_{background}$, is calculated by evaluating the standard deviation of two thin (~ 5 pixel) gutter regions at the edge of the separation lane, where protein is not expected to be present (Figure 3.2A; $\sigma_{Gutter} = 107.7$). We assume that the pixels in the gutter region are drawn independent and identically distributed (*iid*) from the same distribution as the true background distribution, which we denote as σ_X . Thus, we approximate $\sigma_{gutter} \approx \sigma_x$.

However, when evaluating the RMS noise in $SNR_{E/C}$, we are not drawing from the same background distribution. Instead, we are calculating the standard deviation of a series of

averaged background pixels. Specifically, if X is an *iid* background pixel, we can expect a single averaged data point to be equivalent to $\frac{\sum X}{w}$, where w is the width of the lateral axis of the separation lane. From this, we can show that the RMS noise, $\sigma_{RMS} = 2\sqrt{\text{Var}(\frac{\sum X}{w})} = 2\frac{\sigma_X}{\sqrt{w}}$, which understates the true noise of the micrograph (σ_x) by a factor of $\frac{\sqrt{w}}{2}$. Finally, unlike chromatography and electrophoresis methods, it should also be noted that calculating σ_{trace} directly from the scI 1D electropherogram presents more challenges, due to the presence of other protein isoforms and non-specific bands along the length of the separation lane (see Figure 3.2B; $\sigma_{RMS} = 61.2$) [20]. Therefore, previous studies have typically used σ_{gutter} to evaluate noise [20].

Additionally, the SNR calculations also produce diverging results for 2D versus 1D calculations. Calculating the signal term in SNR_{AC} for the 2D case would involve calculating the average pixel intensity of the 2D protein band (see Figure 3.2E; $\mu_{band} = 2215.04$). In the 1D Gaussian case, this would involve calculating the average pixel intensity of an averaged 1D electropherogram (see Figure 3.2D; $\mu_{band} = 432.9$). As a result, the mean signal intensity value calculated in the 1D Gaussian case would be smaller than the average calculated in the 2D case.

A similar result occurs for $SNR_{E/C}$. In the 1D case, A_{signal} refers to the maximum amplitude of the 1D gaussian (Figure 3.2B; $\mu_{1DGaussian} = 1020.1$). In the 2D case, we can similarly calculate the maximum amplitude of the 2D multivariate Gaussian that defines a protein band injection profile (Figure 3.2F; $\mu_{2DGaussian} = 5514.9$). Similar to SNR_{AC} , the maximum amplitude of the 1D Gaussian would be smaller than the maximum amplitude of the 2D multivariate Gaussian, due to the averaging operation required to construct the 1D electropherogram.

In this manner, we can see that direct comparisons of SNR with the same method ($SNR_{E/C}$ or SNR_{AC}) across the 2D versus 1D case would produce a factor offset between the 1D case, as compared to the 2D case. However, when comparing between $SNR_{E/C}$ or SNR_{AC} across the two different dimensions, the relationship in SNR may not be as clear.

In accordance with standard practice in previous scI work, we adopt a definition of $SNR_{Gaussian} = \frac{A_{1D} \text{Signal}}{\sigma_{gutter}}$ when evaluating the SNR with the Gaussian fitting pipeline [20]. However, for the segmentation pipeline, we adopt a definition of $SNR_{Segmentation} = SNR_{AC}$, where $\sigma_{background} = \sigma_{gutter}$. Due to the differences in quantification methodology between $SNR_{Gaussian}$ and $SNR_{Segmentation}$, we expect the correlation between SNR values to be lower than SV correlation.

Calculating Separation Resolution

Separation resolution (R_S) defines how well-resolved neighboring protein bands are along a separation lane [37]. R_S is defined in equation 3.5, where μ_1 and μ_2 correspond to the Gaussian peak centers of the two protein bands under consideration, and $4\sigma_1$ and $4\sigma_2$ correspond to each respective peak width [37].

$$R_S = \frac{|\mu_1 - \mu_2|}{\frac{1}{2}(4\sigma_1 + 4\sigma_2)} \quad (3.5)$$

Importantly, R_S is typically calculated after neighboring protein bands are fit to a 1D Gaussian distribution. Baseline resolution ($R_S \geq 1.5$) separates two neighboring protein bands with $< 1\%$ overlap in 1D Gaussian distributions. However, achieving the more stringent baseline resolution can be infeasible (i.e., resolving multiple proteins targets in a fixed-length separation lane). At the other extreme, distinguishing neighboring protein bands can be infeasible when $R_S < 0.5$ [37].

3.3 Materials and Methods

scIs were run as previously described [17, 19]. Briefly, each microfluidic chip completes concurrent analysis of hundreds to thousands of individual cells, owing to an array of 1100 individual separation lanes each headed by a 30-32 μm diameter microwell for single-cell isolation and lysis [17, 19]. Electrophoresis SDS-PAGE separates protein targets based on differences in molecular mass. electrophoretic mobility, here a proxy for molecular mass. Much like a DNA or protein microarrays, the resulting scI readout is an array of fluorescence micrographs, with each micrograph reporting an immunoblot for one single cell (Figure 3.1A). By dividing the scanned array into individual separation lanes, we calculate protein expression profiles from each individual cell.

For benchmarking analysis, scIs were performed on a breast cancer cell line (MCF7 cells), where each cell has been transfected with GFP. We analyzed a total of five chips for this MCF7 dataset. An additional three chips were analyzed for the signal-to-noise ratio (SNR) fold change analysis with PA gels of varying pore sizes. For isoform separations, scIs were performed on an MCF7 cell line treated with tamoxifen. For SNR fold-change data using protein molecular mass, scI data was obtained from Kang et al., which assessed protein markers in a BT474 cell line [4].

3.4 Results

Benchmarking Results

To evaluate the robustness of segmentation-based methods versus conventional Gaussian fitting, we first benchmarked against *SV*. We analyzed protein bands from MCF7 scIs. From five chips, we analyzed the subset of separation lanes (117 lanes from a total of 6868 separation lanes) that were identified as containing a protein band (“inferred positive”) from both the segmentation and Gaussian fitting pipelines. Separation lanes that were inferred positive by only one of the two pipelines (104 lanes total, 17 from the Gaussian fitting pipeline, and 90 from the segmentation pipeline) were not included in this analysis, since the

pipeline that did not identify a protein band in the resulting separation lane would produce a SV value of zero, thus confounding benchmarking.

In testing the supposition of strong correlation between $SV_{Segmentation}$ and $SV_{Gaussian}$, we observe R^2 value > 0.99 (Figure 3.4A). Furthermore, in testing the supposition that an offset factor in SV would exist between the Gaussian fitting pipeline and the segmentation pipeline, we evaluate the slope of a linear regression model between the two datasets, and indeed observe an offset of 62.5. As a corollary supposition, we expected that the offset factor would approximate the width of the separation lane (80 pixels), which also appears to be supported here. Thus, we conclude that the segmentation pipeline is analyzing protein bands as accurately as the Gaussian fitting pipeline, for similar datasets.

We next assessed the correlation of estimated SNR values between the two pipelines. We expected the SNR correlation to be lower than the SV correlation, due to the differences in quantification methodology when evaluating SNR in each pipeline. Indeed, we observe a lower, but nevertheless strong, correlation ($R^2 = 0.941$) for SNR values between the segmentation and Gaussian fitting pipelines (Figure 3.4B).

Finally, we investigated whether one pipeline identified substantially more analyzable protein bands than another. Our results indicate that the segmentation pipeline identified $1.5 \times$ more separation lanes with protein bands as compared to the Gaussian fitting pipeline (Figure 3.4C; $p = 0.042$; segmentation identified a total of 207 separation lanes with protein bands, as compared to 131 identified by Gaussian fitting). We explore this increase in protein band identification in the next section.

Comparison of Inferred Positive Separation Lanes Across Methods

To understand why segmentation identified more separation lanes with protein bands than Gaussian fitting, we compared the distributions of SV and $SNRs$ of inferred positive separation lanes between both pipelines.

Given that we observed a factor offset between $SV_{Segmentation}$ and $SV_{Gaussian}$, we cannot directly compare distributions of SV values between the two pipelines. However, the majority of inferred positive separation lanes identified by Gaussian fitting ($n = 131$) was also inferred positive by segmentation ($n = 117$ inferred positive by both methods), compared to $n = 207$ inferred positive by segmentation alone (Figure 3.4D). Thus, we assumed that the 117 inferred positive separation lanes identified by both methods would sufficiently describe the full distribution of separation lanes inferred positive by Gaussian fitting.

We compared the overlapping subset of inferred positive separation lanes to those inferred positive by segmentation alone. Through this comparison, we observed that the distribution of separation lanes inferred positive with segmentation included significantly more low- SV and low- SNR protein bands (SV , $p = 0.0017$, Mann-Whitney U-Test; SNR , $p = 1.21 \times 10^{-5}$, Mann-Whitney U-Test) (Figure 3.4E, Figure 3.4F). In the converse comparison, wherein we compared the subset of separation lanes inferred positive by both methods against the full set of separation lanes identified by Gaussian fitting, we found no substantial differences between the two distributions (see Supplementary Figure 3.5; $p > 0.05$ for SV and SNR). Therefore, we

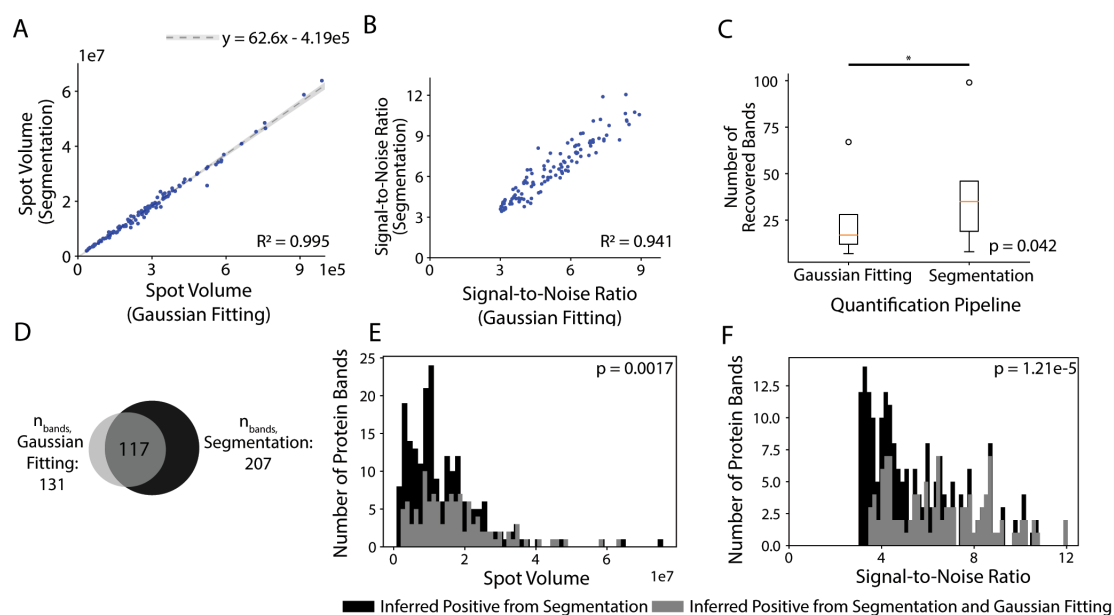


Figure 3.4: Segmentation correlates well with Gaussian fitting for spot volume and SNR. A) For the subset of separation lanes that were inferred positive by both Gaussian fitting and segmentation, the spot volume identified in each lane shows good agreement between the two pipelines ($R^2 = 0.995$). B) For the subset of separation lanes that were inferred positive by both Gaussian fitting and segmentation, the SNR of the separation lanes also shows good agreement ($R^2 = 0.941$), though smaller agreement than that of spot volume. C) When comparing the number of inferred positive separation lanes across $n = 5$ chips, segmentation identifies $1.5 \times$ more positive lanes than Gaussian fitting. The Wilcoxon signed-rank test was used to identify statistical significance ($p = 0.042$). D) Of the 207 separation lanes that were inferred positive by segmentation and 131 separation lanes that were inferred positive by Gaussian fitting, 117 were inferred positive by both. E) The separation lanes that were inferred positive by the segmentation pipeline had a greater number of low spot volume protein bands, compared to those that were inferred positive by both pipelines ($p = 0.0017$ for two-tailed Mann-Whitney U-test). F) The separation lanes inferred positive by the segmentation pipeline also had a greater proportion of low SNR protein bands, compared to the separation lanes inferred positive by both pipelines ($p = 1.21 \times 10^{-5}$ for two-tailed Mann-Whitney U-test). SV and SNR were evaluated using the segmentation pipeline.

conclude that the Gaussian pipeline is not identifying substantially different protein bands compared to the segmentation pipeline. We further conclude that the segmentation pipeline is, indeed, identifying more low abundance protein bands than the Gaussian fitting pipeline.

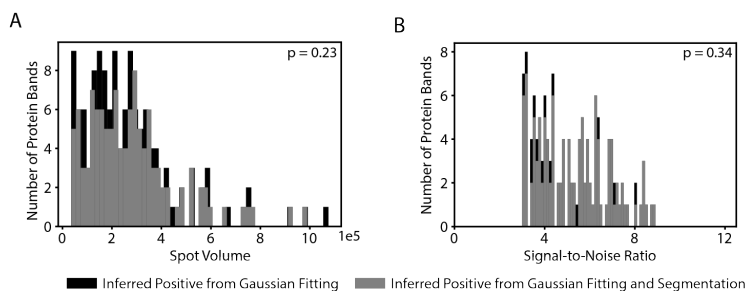


Figure 3.5: No significant difference in distributions of spot volume and SNRs for inferred positive separation lanes identified with Gaussian fitting pipeline versus both pipelines. A) The spot volume distributions for inferred positive separation lanes identified by Gaussian fitting (black) versus those inferred positive by both pipelines (grey), have substantial overlap ($p = 0.23$, from a two-tailed Mann Whitney U-test), even though Gaussian fitting identified strictly more protein bands (131 vs 117). B) Similarly, the SNRs of inferred positive separation lanes identified by Gaussian fitting (black) versus those inferred positive by both pipelines (grey) also have substantial overlap ($p = 0.34$, from a two-tailed Mann Whitney U-test). SV and SNR were evaluated via the Gaussian fitting pipeline.

Assessing SNR Fold Change with Varying Peak Width

We next wished to assess how SNR values for a single protein band would compare between the two pipelines. Although we determined that the segmentation pipeline identified more low-abundance protein bands, we hypothesized that due to the SNR attenuation in the Gaussian fitting pipeline (1) the SNR value for each protein band in the segmentation pipeline would be greater than the SNR value for each protein band in the Gaussian fitting pipeline; and (2) this “SNR fold change” value (the ratio of $SNR_{Segmentation}/SNR_{Gaussian}$) would increase as the lateral protein band width decreased. Specifically, we hypothesized that with decreasing protein band width, there would be increasing mean signal truncation with the Gaussian fitting pipeline (due to the lateral averaging, wherein narrow protein bands will have a greater number of abutting background pixels, summing to zero-pixel intensities). In tandem, we hypothesized there would be increasing mean signal intensity in the segmentation pipeline due to the smaller protein segments (a smaller number of low-intensity pixels, with high intensity pixels concentrated near the protein band center).

We sought to test our hypothesis by systematically modulating protein band widths in our separations. Protein band width is determined by several factors including electrophoresis

Table 3.1: Change in Inferred Positive Separation with Gel Density

Gel Density	Inferred Positive Separation Lanes by Gaussian Fitting	Inferred Positive Separation Lanes by Segmentation	$\frac{IP_{Segmentation}}{IP_{Gaussian}}$
6 %T	208	201	0.97
8 %T	242	255	1.05
10 %T	47	90	1.91

duration (diffusional band broadening), polyacrylamide gel pore size, protein molecular mass, and other factors [37–39].

We performed scI of MCF7-GFP cells on scI chips with varying gel densities (6%T, 8%T, and 10%T, where %T represents total acrylamide concentration). A greater gel density results in smaller pores in the polyacrylamide gel sieving matrix, thus inducing less band broadening during a given electrophoresis run time, and therefore, a smaller peak width (Figure 3.6A) [39]. Thus, we hypothesized that the SNR fold change would be greater for proteins electrophoresed in the denser gels.

Our results demonstrate that the SNR fold change does, indeed, increase as gel density increases (Figure 3.6B). In addition, we find that the ratio of inferred positive separation lanes ($IP_{Segmentation}/IP_{Gaussian}$) increases as %T increases (see Supplementary Table X). We attribute this finding to greater SNR truncation by the Gaussian fitting pipeline as %T increases, which may lead to a greater number of protein bands are going to have an estimated $SNR_{Gaussian} < 3$. Interestingly, for a 6%T gel, we notice that Gaussian fitting identifies more inferred positive separation lanes than segmentation, which indicates that in certain cases, Gaussian fitting may work as well as segmentation in identifying a maximal number of protein bands. However, as gel density increases to 10%T, segmentation identifies 90% more inferred positive separation lanes, compared to Gaussian fitting.

Finally, a similar test on proteins with varying molecular masses also demonstrated that as protein band width decreases, the SNR fold change increases (see Supplementary Note S4 and Supplementary Figure S4). While we expect the relationship between SNR fold change and protein molecular mass to be monotonically increasing, and not necessarily linear, we nevertheless observed that the R^2 value for a linear model between the two metrics to be 0.736. We hypothesize that some of the non-monotonicity observed in Supplementary Figure S3 stems from differences in antibody probe affinity and fluorescence signal from the immunoassay that contributes to variance in the results [6].

Assessing Isoform Quantification with Segmentation

We next turned to the question of whether segmentation can accurately quantify multiple isoforms in the same separation lane. As mentioned, Gaussian fitting has difficulty detecting isoforms with $R_S < 0.5$. Consequently, we sought to determine if segmentation requires a

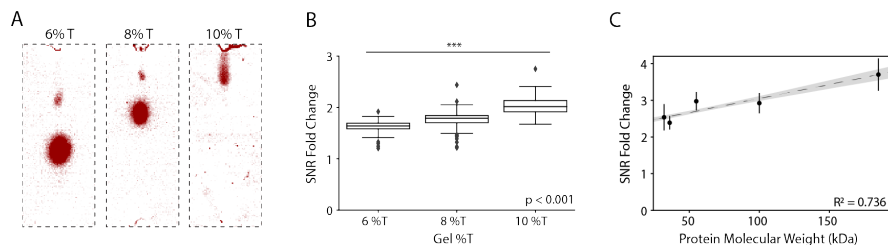


Figure 3.6: Decreasing protein band width leads to greater SNR truncation with Gaussian fitting. A) Greater gel densities (denoted by %T, total acrylamide concentration) lead to smaller pore sizes, which results in smaller band broadening (and a smaller migration distance) as proteins travel along the length of the separation lane. B) The ratio of SNR identified with the segmentation pipeline versus the Gaussian fitting pipeline (SNR fold change) increases as gel density increases, demonstrating that the Gaussian fitting pipeline truncates the SNR of smaller peaks to a greater extent with increasing gel density. C) The SNR fold change for peaks of varying molecular mass demonstrates an overall linear correlation ($R^2 = 0.736$), demonstrating that as protein molecular mass increases, the SNR fold change also increases

larger R_S for accurate quantification of isoforms, since the Gaussian fitting pipeline can account for partial fluorescence intensities from overlapping protein bands that are not baseline resolved, whereas the current instantiation of the segmentation pipeline cannot.

To assess the ability of the segmentation pipeline to distinguish between isoforms, we used a canonical scI dataset that aimed to resolve two estrogen receptor (ER) isoforms: ER- $\alpha 66$, a 66-kDa isoform, and ER- $\alpha 46$, a 46-kDa isoform in the breast cancer MCF7 cell line (Figure 3.7A). ER- $\alpha 46$ lacks a transactivation domain present in the larger isoform, and has been hypothesized to reduce proliferation of certain types of breast cancer [40]. Importantly, since both isoforms are detected with the same fluorescently labeled antibody probe, PAGE separation and accurate quantification is critical in assessing the stoichiometry of the isoform expression.

To assess agreement between the segmentation and Gaussian fitting pipelines, we once again compared SV values for separation lanes that were inferred positive by both pipelines. The SV values obtained by the two pipelines demonstrated good agreement for the first isoform (Figure 3.7B; $R^2 = 0.985$), whereas the SV values for the second isoform initially demonstrated poor agreement ($R^2 = 0.189$; Figure 3.7C).

We sought to further understand the source of discrepancy for the SV values of the second isoform. When evaluating the R_S of the inferred positive separation lanes, we observed an average of $R_S = 0.63 \pm 0.16$ (see Supplementary Figure S5A for an example of a separation lane with an above-average R_S). We hypothesized that when peaks had low separation resolution (Supplementary Figure S5B), the segmentation pipeline cannot account for areas of peak overlap, and therefore, would produce more quantification errors. Indeed, when

we restricted the subset of separation lanes analyzed to those that had an above-average separation resolution ($R_S \geq 0.63$), we achieved good agreement between SV values for the second isoform (Figure 3.7D; $R^2 = 0.826$). We, thus, conclude that the segmentation pipeline requires higher R_S between neighboring protein bands to appropriately distinguish multiple bands along a single separation lane. We further conclude that in cases where the separation resolution is insufficient ($R_S < 0.6$), Gaussian fitting may be a more appropriate approach for isoform quantification.

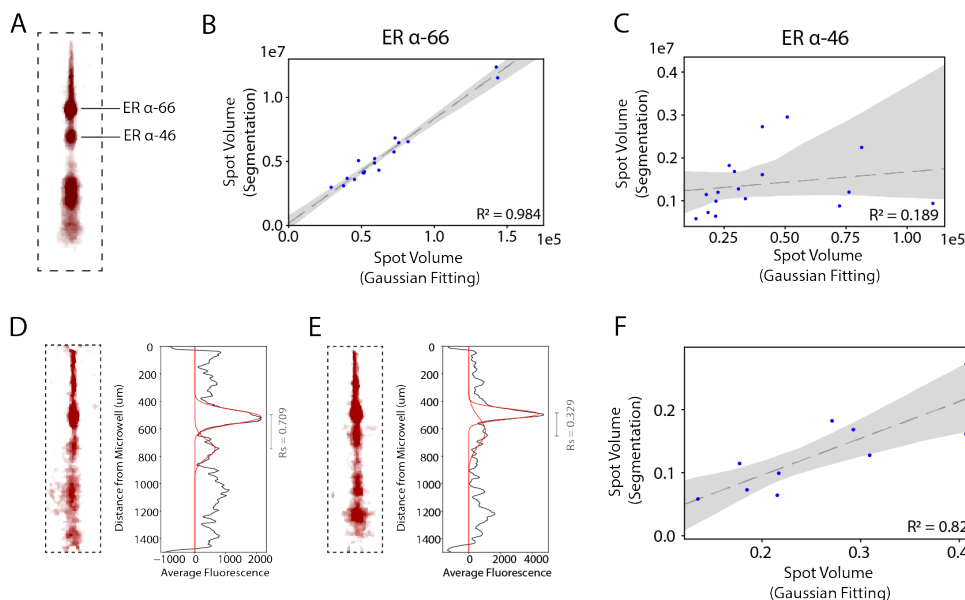


Figure 3.7: Segmentation-based detection of ER α isoforms shows good agreement when $R_S > 0.6$. a) ER- α 66 (66-kDa) and ER- α 46 (46-kDa) are separated on a PA gel by single-cell western blotting. B) Gaussian fitting and segmentation demonstrate good agreement of spot volumes of the more abundant isoform, ER- α 66 ($R^2 = 0.984$). C) Gaussian fitting and segmentation do not demonstrate good agreement of spot volumes of ER- α 46 ($R^2 = 0.189$). D) An example of a separation lane with ‘well-resolved’ protein bands (separation resolution, $R_S = 0.709$). E) An example of a separation lane with poorly resolved protein bands ($R_S = 0.329$). F) When assessing spot volumes of ER- α 46 from lanes that have $R_S > 0.6$, we find better agreement between the segmentation and Gaussian fitting pipelines ($R^2 = 0.826$).

Evaluating Automated Classification and Segmentation with Deep Learning

Finally, we explored the use of convolutional neural networks, which have had success in classifying and segmenting complex images, to automatically classify and segment protein bands [41–44]. Specifically, we hypothesized that neural networks could both (1) reduce

several of the manual parameter tuning and quality control processes required by the classical segmentation pipeline for every new chip and (2) classify and segment additional separation lanes that were missed by classical segmentation, due to the parameter complexity of the neural network offering increased sensitivity in detecting protein bands. In this manner, we anticipated that convolutional neural networks could further build upon the throughput and accuracy improvements offered by the classical segmentation pipeline. To assess the efficacy of convolutional neural networks in classifying and segmenting protein bands, we developed a deep learning pipeline that used a classification model in conjunction with a segmentation model to produce a final output consisting of a segmented protein band (Figure 3.8A).

Classification Model

For classification, we developed a model based on the AlexNet framework, and used separation lanes from our previous immunoblots of MCF7-GFP cells as inputs (Figure 3.8A) [41]. We performed an 80-10-10 split across the MCF7-GFP dataset for training, validation, and testing. However, to reduce bias in the model during training, we removed all separation lanes that contained protein bands, but were nevertheless discarded (inferred negative) in the segmentation pipeline due to quality control (e.g., poor segmentation, artifacts in the region of the protein band, estimated SNR < 3, etc.). However, for validation and testing, we did not remove such false negatives. Furthermore, due to the inherent class imbalance in scEPC datasets (only 10% of total separation lanes contained protein bands, whereas the remaining 90% of separation lanes did not), we oversampled separation lanes containing protein bands during training. In total, we used 5003 unique micrographs for training, and two separate sets of 686 unique micrographs for validation and testing. The model was trained using the cross-entropy loss function (see Equation 3.6). Our model was implemented with PyTorch, and trained on a GPU via Google Collaboratory.

For our test set for the AlexNet Model, we observed an area under the receiver operating characteristic (AUROC) value of 0.9913 (Figure 3.8B). From the softmax outputs of the AlexNet model, we identified our optimal threshold via maximizing the value of Youden’s J statistic on the validation set [45]. With this optimal threshold (0.043), we observed a classification accuracy on our test set of 98.1%. We scrutinized the precision and recall of our two classes (see Supplementary Table S2). Interestingly, we observed 100% recall for the positive class (all 14 separation lanes that contained protein bands were accurately identified), but only 52% precision (an additional 13 peaks were classified as false positives). However, we significantly increased the precision using the segmentation model (U-Net).

$$J = - \sum_{i=1} y_i \log \hat{y}_i + (1 - y_i) \log(1 - \hat{y}_i) \quad (3.6)$$

Segmentation Model

We used the inferred positive separation lanes classified by the AlexNet model as inputs into our second model to segment protein bands, using the U-Net framework, which has had wide

success in biomedical image segmentation [43]. U-Net utilizes a conventional encoder-decoder framework, with added skip connection between layers to improve segmentation accuracy. For our U-Net model, we utilized the 189 and 19 separation lanes that were inferred positive from our classical segmentation pipeline for training and validation, respectively. The model was trained using a pixel-wise cross-entropy loss function (see Equation S1). All models were implemented with PyTorch, and trained on a GPU via Google Collaboratory.

In our U-Net model, we observed a test set accuracy of 95.8%. However, we also evaluated the correlation of SV and SNR of separation lanes that were inferred positive with both the segmentation pipeline and the deep learning pipeline. After implementing a quality control metric to only select separation lanes with protein bands that had an $\text{SNR} \geq 3$, we observed R^2 values of 0.993 for SV (Figure 3.8C), and 0.966 for SNR (Figure 3.8D), indicating good agreement between the segmentation and deep learning pipelines for both metrics. Furthermore, after the $\text{SNR} \geq 3$ cut off, we once again observed 100% recall for the positive class, and precision of classification improved to 64%. However, upon more careful examination of the ‘false positive’ separation lanes identified by the deep learning pipeline, we noticed that 7 out of the 8 separation lanes did, in fact, contain protein bands that were missed by the classical segmentation pipeline (see Supplementary Note S6 and Supplementary Table S3), indicating that combining segmentation with deep learning allows for the identification of 50% more protein bands than classical segmentation approaches.










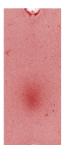


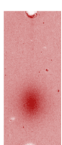


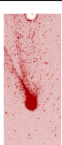





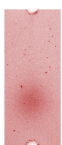


Our results suggest that the deep learning pipeline identifies additional protein bands that may be missed due to the stringent quality control steps needed in the segmentation pipeline. We further hypothesize that we can decrease the misclassification of the deep learning pipeline by improving the classification model, especially by increasing the number of training micrographs that contain artifacts similar to protein bands.

3.5 Discussion

In this work, we demonstrate that segmentation-based approaches can quantify scI as successfully as Gaussian fitting-based for singular protein bands. We additionally demonstrate that segmentation-based approaches can identify a greater number of low-abundance protein bands than Gaussian fitting approaches, due to the fact that Gaussian fitting-based approaches truncate a protein band’s estimated SNR. Furthermore, segmentation-based approaches become increasingly more useful as the peak widths of proteins bands decrease, as SNR truncation from Gaussian fitting increases as protein peak width decreases. From these results, we conclude that when analyzing protein bands with low peak widths, segmentation-based approaches may increase the total number of quantifiable protein bands for downstream analysis.

However, we find that segmentation-based approaches struggle with identifying single-cell isoform immunoblots when the separation resolution between isoforms is insufficient ($R_S < 0.6$). Thus, in such cases, we anticipate that Gaussian fitting may be more suitable in accurately quantifying isoform distributions.

Table 3.2: Properties of “False Positive” Micrographs Identified with the Deep learning Pipeline

Separation Lane	Raw Micrograph	Classical Segmentation Mask	U-Net Segmentation Mask	SNR from Classical Segmentation Mask	SNR from U-Net Segmentation Mask
Gel 1, #464				2.700	3.053
Gel 1, #963				0.0	4.229
Gel 1, #1060				0.0	5.451
Gel 2, #354				2.999	3.071
Gel 2, #683				3.656	4.169
Gel 2, #779				5.886	10.381
Gel 3, #910				2.747	3.984
Gel 3, #1436				2.776	3.063

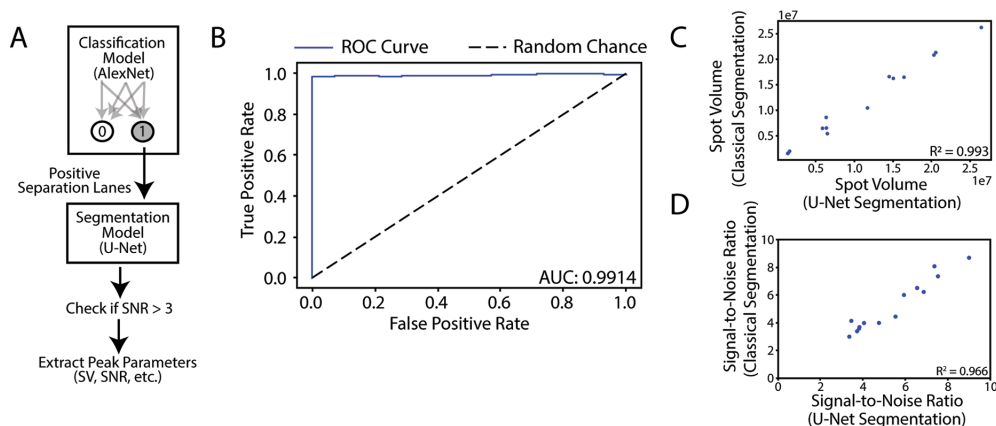


Figure 3.8: Deep learning accurately classifies and segments scI protein bands. (A) A classification model, based on the AlexNet architecture, initially classifies separation lanes into inferred positive or inferred negative separation lanes. The inferred positive separation lanes are then used as inputs into the U-Net model, which produces a segmentation mask for a given segmentation lane. The outputs of the U-Net model are then checked to ensure that the $\text{SNR} > 3$ in the segmented region. Key peak parameters can be extracted out of the subsequent separation lanes. (B) The area under the curve of the receiver operating characteristic (AUROC) of the classification model is > 0.99 , indicating high classification accuracy. (C) The spot volumes of the 14 separation lanes that were inferred positive by both classical segmentation and the deep learning pipeline demonstrate high correlation, indicating that the deep learning pipeline can accurately quantify and segment protein bands ($R^2 = 0.993$). (D) The SNRs of the 14 separation lanes that were inferred positive by classical segmentation and the deep learning pipelines also demonstrate high correlation ($R^2 = 0.966$).

Finally, we discover that deep learning can further increase the number of protein bands recovered by segmentation-based approaches, owing to the larger parameter complexity used in deep learning models to classify, and segment, protein bands in each individual separation lane.

We anticipate that the results of this study will aid in achieving greater accuracy for protein immunoblot quantification, including for quantification of other microfluidic (non-single-cell) immunoblots [34]. Looking forward, we envision that utilizing more sophisticated segmentation algorithms, such as 2D Gaussian fitting, may increase the accuracy of segmenting isoforms with $R_S < 0.6$, while also increasing the throughput of identifying low-abundance or low-peak width protein bands. Additionally, we surmise that segmentation-based approaches may open up inquiries into quantifying protein bands with significant injection dispersion, which may provide valuable insight into microfluidic assay design properties and technical variability [46].

Bibliography

1. Finotello, F. & Eduati, F. *Multi-omics profiling of the tumor microenvironment: Paving the way to precision immuno-oncology* 2018. www.frontiersin.org.
2. Labib, M. & Kelley, S. O. *Single-cell analysis targeting the proteome* 2020. www.nature.com/natrevchem.
3. Yu, C., Woods, A. & Levison, D. The assessment of cellular proliferation by immunohistochemistry: a review of currently available methods and their applications. *Histochemistry* **24**, 121–31 (1992).
4. Kang, C.-C. *et al.* Electrophoretic cytopathology resolves ERBB2 forms with single-cell resolution. *npj Precision Oncology* **2**, 10. ISSN: 2397-768X. <http://www.nature.com/articles/s41698-018-0052-3> (2018).
5. Tentori, A. M., Yamauchi, K. A. & Herr, A. E. Detection of Isoforms Differing by a Single Charge Unit in Individual Cells. *Angewandte Chemie*, 12431–12435 (2016).
6. Zhang, J. Q. *et al.* Linked optical and gene expression profiling of single cells at high-throughput. *Genome Biology* **21**. <https://doi.org/10.1186/s13059-020-01958-9> (Feb. 2020).
7. O’Leary, N. A. *et al.* Reference sequence (RefSeq) database at NCBI: Current status, taxonomic expansion, and functional annotation. *Nucleic Acids Research* **44**, D733–D745. ISSN: 13624962. <http://www.ncbi.nlm.nih.gov/books/> (2016).
8. Ponomarenko, E. A. *et al.* The Size of the Human Proteome: The Width and Depth. *International Journal of Analytical Chemistry* **2016**. ISSN: 16878779 (2016).
9. Li, R. & Shen, Y. An old method facing a new challenge: re-visiting housekeeping proteins as internal reference control for neuroscience research. *Life Sci* **92**, 747–751 (2013).
10. Shaposhnikov, S. A. *et al.* Single-cell gel electrophoresis (the comet assay): Loops of fragments? *Electrophoresis* **29**, 3005–3012. ISSN: 01730835 (2008).
11. Dickinson, A. J., Armistead, P. M. & Allbritton, N. L. Automated capillary electrophoresis system for fast single-cell analysis. *Analytical Chemistry* **85**, 4797–4804. ISSN: 00032700 (2013).

12. Chen, Y., Xiong, G. & Arriaga, E. A. CE analysis of the acidic organelles of a single cell. *Electrophoresis* **28**, 2406–2415. ISSN: 01730835. www.electrophoresis-journal.com (2007).
13. Liao, H. W. *et al.* Enhanced single-cell metabolomics by capillary electrophoresis electrospray ionization-mass spectrometry with field amplified sample injection. *Analytica Chimica Acta* **1118**, 36–43. ISSN: 18734324. <https://doi.org/10.1016/j.aca.2020.04.028> (2020).
14. Nemes, P. *et al.* Metabolic differentiation of neuronal phenotypes by single-cell capillary electrophoresis-electrospray ionization-mass spectrometry. *Analytical Chemistry* **83**, 6810–6817. ISSN: 00032700 (2011).
15. Tao, L. & Kennedy, R. T. Measurement of antibody-antigen dissociation constants using fast capillary electrophoresis with laser-induced fluorescence detection. *Electrophoresis* **18**, 112–117. ISSN: 01730835 (1997).
16. Yang, P. *et al.* Measurement of dissociation rate of biomolecular complexes using CE. *Electrophoresis* **30**, 457–464. ISSN: 01730835. www.electrophoresis-journal.com (2009).
17. Hughes, A. J. *et al.* Single-cell western blotting. *Nature methods* **11**, 749–55. ISSN: 1548-7105. arXiv: NIHMS150003. <http://www.ncbi.nlm.nih.gov/pubmed/24880876> (2014).
18. Yamauchi, K. A. & Herr, A. E. Subcellular western blotting of single cells. *Microsystems & Nanoengineering* **3**, 16079. ISSN: 2055-7434. <http://www.nature.com/articles/micronano201679> (2017).
19. Kang, C.-c. *et al.* Single cell resolution western blotting. *Nature Protocols* **11**, 1508–1530. ISSN: 1754-2189. <http://dx.doi.org/10.1038/nprot.2016.089> (2016).
20. Vlassakis, J., Yamauchi, K. A. & Herr, A. E. Summit: automated gel electrophoresis analysis. *SLAS Technology* (2021).
21. Bharadwaj, R., Santiago, J. G. & Mohammadi, B. Design and optimization of on-chip capillary electrophoresis. *Electrophoresis* **23**, 2729–2744. ISSN: 01730835 (2002).
22. Wehr, T. in *Encyclopedia of Physical Science and Technology* 355–368 (Elsevier, 2003).
23. Hamilton, N. Quantification and its applications in fluorescent microscopy imaging. *Traffic* **10**, 951–961. ISSN: 13989219 (2009).
24. McQuin, C. *et al.* CellProfiler 3.0: Next-generation image processing for biology. *PLOS Biology* **16** (ed Misteli, T.) e2005970. ISSN: 1545-7885. <https://dx.plos.org/10.1371/journal.pbio.2005970> (2018).
25. Wiesmann, V. *et al.* Review of free software tools for image analysis of fluorescence cell micrographs. *Journal of Microscopy* **257**, 39–53. ISSN: 00222720. <http://doi.wiley.com/10.1111/jmi.12184> (2015).

26. Dos Anjos, A. *et al.* New approach for segmentation and quantification of two-dimensional gel electrophoresis images. *Bioinformatics* **27**, 368–375. ISSN: 13674803 (2011).
27. Berth, M. *et al.* The state of the art in the analysis of two-dimensional gel electrophoresis images. *Applied Microbiology and Biotechnology* **76**, 1223–1243. ISSN: 01757598 (2007).
28. Kostopoulou, E., Zacharia, E. & Dimitris, M. *Accurate segmentation of 2D-PAGE images in Proceedings of the 20th European Signal Processing Conference* (2012).
29. Natale, M., Caiazzo, A. & Ficarra, E. in *2-D PAGE Map Analysis, Methods in Molecular Biology* (eds Marengo, E & Robotti, E) 203–211 (Humana Press Inc., New York, NY, 2016). https://link.springer.com/protocol/10.1007/978-1-4939-3255-9_12.
30. Hong, Y. *et al.* Deep learning method for comet segmentation and comet assay image analysis. *Scientific Reports* **10**, 18915. ISSN: 20452322. <https://doi.org/10.1038/s41598-020-75592-7> (2020).
31. Draper, N. R. & Smith, H. *Applied regression analysis* 3rd ed. ISBN: 978-0-471-17082-2 (Wiley, New York, 1998).
32. Liu Jianzhuang, Li Wenqing & Tian Yupeng. *Automatic thresholding of gray-level pictures using two-dimension Otsu method* in (Institute of Electrical and Electronics Engineers (IEEE), 2002), 325–327.
33. Geldert, A., Huang, H. & Herr, A. E. Probe-target hybridization depends on spatial uniformity of initial concentration condition across large-format chips. *Scientific Reports* **10**, 1–12. ISSN: 20452322. <http://dx.doi.org/10.1038/s41598-020-65563-3> (2020).
34. Hughes, A. J. & Herr, A. E. Microfluidic Western blotting. *Proceedings of the National Academy of Sciences of the United States of America* **109**, 21450–5. ISSN: 1091-6490. <http://www.pubmedcentral.nih.gov/articlerender.fcgi?artid=3535594&tool=pmcentrez&rendertype=abstract> (2012).
35. Pillai-Kastoori, L., Schutz-Geschwender, A. R. & Harford, J. A. A systematic approach to quantitative Western blot analysis. *Analytical Biochemistry* **593**, 113608. ISSN: 10960309 (2020).
36. Vlassakis, J. & Herr, A. E. Effect of Polymer Hydration State on In-Gel Immunoassays. *Analytical Chemistry* **87**, 151022142613006. ISSN: 0003-2700. <http://pubs.acs.org/doi/10.1021/acs.analchem.5b03032> (2015).
37. Giddings, J. C. *Unified separation science* ISBN: 978-0-471-52089-4 (Wiley, New York, 1991).
38. Ferguson, K. A. Starch-gel electrophoresis—Application to the classification of pituitary proteins and polypeptides. *Metabolism: Clinical and Experimental* **13**, 985–1002. ISSN: 00260495 (1964).

39. Tong, J & Anderson, J. L. Partitioning and diffusion of proteins and linear polymers in polyacrylamide gels. *Biophysical journal* **70**, 1505–13. ISSN: 0006-3495. <http://www.pubmedcentral.nih.gov/articlerender.fcgi?artid=1225077&tool=pmcentrez&rendertype=abstract> (1996).
40. Penot, G. *et al.* The human estrogen receptor- α isoform hER α 46 antagonizes the proliferative influence of hER α 66 in MCF7 breast cancer cells. *Endocrinology* **146**, 5474–5484. ISSN: 00137227 (2005).
41. Krizhevsky, A., Sutskever, I. & Hinton, G. E. ImageNet Classification with Deep Convolutional Neural Networks, 1097–1105. <https://papers.nips.cc/paper/4824-imagenet-classification-with-deep-convolutional-neural-networks> (2012).
42. Lecun, Y., Bengio, Y. & Hinton, G. *Deep learning* 2015. <http://colah.github.io/>.
43. Ronneberger, O., Fischer, P. & Brox, T. in *Lecture Notes in Computer Science* 234–241 (Springer International Publishing, 2015). https://doi.org/10.1007/978-3-319-24574-4_28.
44. Van Valen, D. A. *et al.* Deep Learning Automates the Quantitative Analysis of Individual Cells in Live-Cell Imaging Experiments. *PLOS Computational Biology* **12** (ed Meier-Schellersheim, M.) e1005177. ISSN: 1553-7358. <https://dx.plos.org/10.1371/journal.pcbi.1005177> (2016).
45. Youden, W. J. Index for rating diagnostic tests. *Cancer* **3**, 32–35. ISSN: 10970142 (1950).
46. Pan, Q., Yamauchi, K. A. & Herr, A. E. Controlling Dispersion during Single-Cell Polyacrylamide-Gel Electrophoresis in Open Microfluidic Devices. *Analytical Chemistry* **90**, 13419–13426. ISSN: 15206882. <https://pubs.acs.org/sharingguidelines> (2018).

Chapter 4

Multimodal detection of protein isoforms and nucleic acids from low starting cell numbers

Materials reproduced, with permission, from:

E. Rosàs-Canyelles, A. J. Modzelewski, A. E. Gomez Martinez, A. Geldert, A. Gopal, L. He, and A. E. Herr, “Multimodal detection of protein isoforms and nucleic acids from low starting cell numbers”, *Lab on a Chip*, 2021.

4.1 Introduction

The discovery of biomarkers for early detection, diagnosis, and therapy remains a persistent challenge across all fields of medicine [1–4]. Protein isoforms are prevalent disease-specific markers and can arise from a variety of events that involve DNA, mRNA and protein, including single nucleotide polymorphisms (SNPs), alternative splicing, or post-translational modifications (PTMs) [5–9]. Many studies have focused on identifying novel potential protein targets by inferring proteoforms from disease-specific modifications to DNA or mRNA [1, 6]. However, confirming if DNA or mRNA modifications encode protein isoforms that can become potential diagnostic or therapeutic targets requires multimodal assays that measure all molecules that are produced.

Because DNA, RNA, and protein molecules are the conduit for cellular-level information flow via the “central dogma”, simultaneous, same-sample detection of multiple molecular species can provide new insight [10, 11]. At the protein level, multimodal analysis is key to understanding gene regulatory networks and the source of variations in both the abundance and molecular forms of proteins expressed. For example, to understand mechanisms of over- or under-expression, multimodal measurements can ascertain the impact of DNA copy number variations on mRNA and protein expression levels [12–14]. In another example, combining proteoform measurements with upstream DNA and RNA measurements can indi-

cate whether proteoforms arise from DNA modifications, alternative RNA splicing, or PTMs. In addition to informing study of gene regulatory networks, multimodal measurements can facilitate more accurate cell subtype classification and lineage tracing [15–17].

Recently introduced technologies allow interrogation of the genome, epigenome, transcriptome, metabolome and proteome at single-cell resolution [18–27]. Multimodal tools that measure proteins and DNA and/or RNA from single cells allow us to link genome, transcriptome and proteome in challenging cell types with low availability, such as rare cell populations (e.g., circulating tumor cells, or CTCs) or stem cells [28], or other cells that cannot be expanded by culture (e.g., cells from biopsies) [22]. Measurements with single- or few-cell resolution are also essential to studying cell-to-cell heterogeneity and distinguishing different population distributions (e.g., bimodal vs. normally-distributed expression) which may have the same population mean expression level [29]. However, the specificity of the protein measurement in such assays typically relies on antibody probes alone, which are subject to nonspecific cross-reactivity and cannot detect isoforms without isoform-specific antibody probes. Thus, selective detection of specific protein isoforms is problematic when isoform-specific antibody probes are not available [30]. While Western blotting adds specificity by separating protein isoforms by mass prior to antibody-based detection, conventional Western blotting requires 10,000s of cells [28]. As a result, identifying different proteoforms arising from modifications to DNA or mRNA at the single- or few-cell scale remains extremely challenging. Recently introduced multimodal assays that perform multimodal protein isoform and nucleic acid detection were specifically designed for murine embryos, which are ~ 100 times larger in volume than somatic cells, and only demonstrated detection of mRNA and not DNA [31, 32].

Here, we perform same-cell DNA, mRNA and protein isoform immunoblotting measurements (triBlot) on low starting cell numbers (i.e. 1 to 100s of cells), which is a clinically relevant range that includes single CTCs and CTC clusters [33], as well as cells recovered from needle biopsies (100s) [34, 35]. Our technique first fractionates cells into nuclear and cytoplasmic compartments. The cytoplasmic fraction undergoes polyacrylamide gel electrophoresis (PAGE), while the nuclei are excised from the triBlot device and analysed for mRNA and/or DNA. We measure expression of protein isoforms from the cytoplasmic fraction of 1-100s cells, while achieving same-sample analysis of DNA and of mRNA retained in the nuclei where nuclear mRNA has been demonstrated to generally correlate well with whole-cell mRNA expression [36–38].

4.2 Materials and Methods

Chemical Reagents

Tetramethylethylenediamine (TEMED, T9281), ammonium persulfate (APS, A3678), β -mercaptoethanol (M3148), 30%T/2.7%C acrylamide/bis-acrylamide (37.5:1) (A3699), bovine serum albumin (BSA, A9418), Tyrode’s solution (T1788), trypsin 10X (59427C), digitonin

(D141), sucrose (S0389-500G), magnesium chloride (M8266) and HEPES (90909C) were purchased from Sigma-Aldrich. Triton X-100 (BP-151), phosphate-buffered saline (PBS, pH 7.4, 10010023), SYBR Gold (S11494), agarose (BP-1356-500) were purchased from Thermo Fisher Scientific. Premixed 10X tris-glycine electrophoresis buffer (25 mM Tris, pH 8.3; 192 mM glycine; 0.1% SDS) was purchased from Bio-Rad. Tris buffered saline with Tween-20 (TBST) was prepared from 20X TBST (sc-24953, Santa Cruz Biotechnology, Dallas, TX). Deionized water (18.2 M) was obtained using an Ultrapure water system from Millipore. N-[3-[(3-Benzoylphenyl)formamido]propyl] methacrylamide (BPMAC) was custom synthesized by Pharm-Agra Laboratories (Brevard, NC). GelSlickTM (50640) and LonzaTM GelBondTM PAG Film for Acrylamide Gels (BMA54746) was purchased from Lonza. Taq PCR kit (E5000S), proteinase K (P8107S) were purchased from New England Biosciences.

Buffer Compositions

Fractionation lysis buffer: 0.125 mg/mL digitonin, 1% v/v Triton X-100 and 0.5 X Tris-glycine. Nuclei wash buffer: 320 mM sucrose, 5 mM MgCl₂, 10 mM HEPES.

Cell Culture

U251 human glioblastoma cells were obtained from the UC Berkeley Tissue Culture Facility via the American Type Culture Collection and stably transduced with TurboGFP via lentiviral infection (multiplicity of infection 10). Cells were cultured in high-glucose Dulbecco's modified eagle medium (DMEM) (11965, Life Technologies) supplemented with 1 × MEM nonessential amino acids (11140050, Life Technologies), 100 U mL⁻¹ penicillin-streptomycin (15140-122, Life Technologies), 1 mM sodium pyruvate (11360-070), and 10% fetal bovine serum (JR Scientific, Woodland) in an incubator at 37°C with humidified 5% CO₂ air.

Device Fabrication

SU-8 wafers, fabricated by photolithography as previously reported [39], were used as molds to cast triBlot devices. SU-8 posts on wafers, which later translate into microwells in the PA gel, were 200 μm in diameter and 200 μm in height [31]. A modified wafer generating microwells 100 μm in diameter and 110 μm in height was used for triBlot assays of single cells. Briefly, PA precursor solution including acrylamide/bis-acrylamide (10%T) and 3 mM BPMAC was degassed with sonication for 9 min. 0.08% APS and 0.08% TEMED were added to precursor solution and solution was pipetted between the SU-8 wafer (rendered hydrophobic with Gel SlickTM solution) and a GelBondTM Film cut to the size of a standard glass microscope slide (25 mm × 75 mm). After chemical polymerization (20 min) the triBlot devices (thin PA gel layer covalently grafted onto the GelBondTM surface) were lifted from wafer, rinsed with deionized water and stored in hydrated (DI water) at 4°C until use.

Fractionation PAGE of 1-100s U251-TurboGFP cells.

TurboGFP-expressing U251 cells were harvested from tissue culture plates by incubation in trypsin/EDTA (15090046, Thermo) at 37°C for 5 min. Trypsin was inactivated by addition of FBS and cells were pelleted by centrifugation at 100 rcf. After removal of supernatant, cells were resuspended in PBS at 1×10^6 cells / mL. For triBlot assays of single cells, cells were settled using the CellenONE single-cell dispenser as described below. For all other experiments, cells were gravity settled as follows: 1 mL of this cell suspension was pipetted over the triBlot device and cells were allowed to settle into microwells for 10 min. Excess cells not settled into microwells were then washed off the PA gel surface with PBS and microwells were imaged by bright field and fluorescence microscopy (Olympus IX71 microscope, Lumen Dynamics X-cite fluorescence illumination source coupled to a liquid light guide (Lumatec, 805-00038), 10X (0.3 NA) objective (Olympus UPLANFL10X), DAPI (Omega XF02-2) and GFP (Chroma 49011 ET) filter cubes, and an Andor iXon+ EMCCD camera (DU-885K-C00-VP)) to collect data on number of cells per microwell and TurboGFP expression. The device was placed into an electrophoresis (EP) chamber, and fractionation lysis buffer (RT, 12 mL) poured over the gel and incubated for 1 min. fPAGE was performed at 40 V/cm for 2-3 min (depending on the assay). Immobilization of proteins by photocapture was carried out by illumination with UV light source (100% power, 45 s, Lightningcure LC5, Hamamatsu). Gels were quickly placed in ice-cold nuclei wash buffer, and buffer was exchanged three times before proceeding to laser excision. Nuclei remaining in wells can be laser-excised, while proteins immobilized on membrane can be probed with fluorescently-labeled antibody probes.

Laser excision of triBlot device into gel pallets

Gel pallets were excised from the device as previously described [31]. Briefly, the PA gel was kept hydrated at all times with nuclei wash buffer and kept over ice between excision events. A CO₂ laser cutter (HL40-5G-110, Full Spectrum Laser) was used to excise gel pallets from triBlot devices. The device was placed with the PA gel face down onto a clear acrylic sheet (McMaster-Carr) engraved with a 5 × 5 mm grid. Using a bright field microscope, microwells were aligned to be horizontally centered above a grid square and approximately 1 mm away from the top edge of each square. The laser was aligned over the left corner of a grid square and programmed to cut at 10% power, 20 speed and 1 pass.

Antibody Probes

Rabbit anti-TurboGFP (PA5-22688), AlexaFluor647-conjugated donkey anti-rabbit secondary (A31572) and AlexaFluor555-conjugated donkey anti-rabbit (A-31572) were purchased from Thermo Fisher Scientific.

Immunoprobng and Imaging

After laser excision, devices were washed in deionized water and a 25 mm \times 75 mm coverslip was placed over the hydrated PA gel. Devices were imaged in a microarray scanner (Genepix 4300A, Molecular Devices) for photo-blotted TurboGFP protein with the cover slip facing down. Devices were then washed in 1X TBST for at least 1 hr before probing with antibody probes. Primary antibody probes were incubated at 1:10 dilution (80 μ L/gel, in 2% BSA in 1 \times TBST), while fluorophore-conjugated secondary antibody probes were incubated at 1:20 dilution (80 μ L/gel, in 2% BSA in TBST). Devices were scanned again for fluorescence immunoblot signal.

Protein band image analysis

Protein expression was quantified by area-under-the-curve analysis (AUC) of immunoblots as previously described. Briefly, custom MATLAB scripts were used to fit Gaussian curves to protein band intensity profiles. Gaussian fit parameters of peak location and were used to calculate the AUC for a peak width of 4σ . Protein bands passed quality control metrics if signal-to-noise ratio (SNR) was higher than 3 and the Gaussian fit R^2 was equal to or greater than 0.6.

Single-gel pallet PCR

After laser excision, gel pallets were placed into a 0.5 mL PCR tube containing 2.5 μ L Molecular Grade water, 1 μ L SDS (17 μ M to final concentration of 3.4 μ M) and 1.5 μ L proteinase K. Tubes were incubated at 45 $^{\circ}$ C for 15 min followed by proteinase K inactivation by incubation at 95 $^{\circ}$ C for 20 min. Next, the following were added to each tube: 2.5 μ L TurboGFP primers (at 500 nM, purchased from Integrated DNA Technologies, sequences: (5'TGA TGG GCT ACG GCT TCT A, 5'GTG TTG CTG TGA TCC TCC TC), 1 μ L dNTPs (at 200 μ M, Taq PCR Kit), 0.25 μ L Taq polymerase (Taq PCR Kit), 5 μ L of Standard Taq Reaction Buffer 10 \times (Taq PCR Kit) and water up to 50 μ L. Template DNA (\sim 200 ng/ μ L) extracted TurboGFP-U251 lysate was added to positive control tubes. Negative controls did not contain DNA or gel pallets. For amplification of the TurboGFP gene, the following cycle steps were programmed using a thermal cycler (PTC-100TM, MJ Research Inc): the first stage at 95 $^{\circ}$ C for 10 min, the second stage (annealing at 51 $^{\circ}$ C for 30 s, extension at 72 $^{\circ}$ C for 30 s, denaturation at 95 $^{\circ}$ C for 30 s) for 45 amplification cycles, and a final stage at 72 $^{\circ}$ C for 10 min. PCR products were analyzed on a 1% agarose gel by EP. SYBR Gold was used at 1X to stain agarose gels and a ChemiDocTM XRS+Gel Imaging System (Bio-Rad) was used to image the DNA bands. Gels were analyzed by densitometry using ImageJ [40].

Single-cell deposition with cellenONE system

Single cells were deposited into 100 μm diameter and 110 μm deep microwells in the triBlot device with the cellenONE X1 Droplet Printer (Sciencion, Berlin, Germany) and a cellenONE PDC M Piezo Dispensing Capillary (PDC-20-CM). TurboGFP-U251 cells were diluted to a concentration of 300,000 cells/mL in PBS. The triBlot PA gel was briefly dried with a nitrogen stream before droplet deposition. Crosshair-shaped fiducial markers on the gel was used in conjunction with the “Find Target Reference Points” software function to align droplets to microwells. The target plate temperature was set to 4^oC to prevent the evaporation of deposited droplets. Single-cell occupancy in droplets was verified by imaging the interior of the PDC prior to droplet deposition. The PDC M deposits droplets of 350 – 400 pL in volume. After deposition, the single cells were immediately fractionally lysed.

Single-gel pallet quantitative reverse transcription Polymerase chain reaction (RT-qPCR)

Once excised, each gel pallet was transferred to one centrifuge tube, immediately followed by the addition of 20 μL of DNA/RNA ShieldTM (R1100, Zymo). Sample were stored in -80^oC until RNA preparation. RNA and DNA were isolated following the manufacturer’s protocol. Nucleic acids were eluted in 8 μL of water. Alternate mRNA and DNA isolation can be performed with Direct-zolTM RNA Miniprep Plus (Cat. R2070S, LOT: ZRC202000), RNA Clean & ConcentratorTM-5 Cat R1015S (10 preps), LOT: ZRC200969). All 8 μL of RNA sample was used for cDNA synthesis. Reverse transcription of mRNA to cDNA was accomplished with SuperScript IV First Strand Synthesis System (18091050, Thermo Fisher) as per manufacturer instructions. Pre-amplification was done on the resulting 20- μl cDNA sample using the Perfecta PreAmp SuperMix (95146 QuantaBio) as per the manufacturer’s instructions, and using the 14 cycle option and a subsequent 20x dilution into nuclease free water (am9937, Fisher). All RT-qPCR reactions were performed using SSO Universal SYBR Green SuperMix, as per manufacturer instructions (1725275, BioRad). Primer sequences used were TurboGFP (5’TGA TGG GCT ACG GCT TCT A, 5’GTG TTG CTG TGA TCC TCC TC). All RT-qPCR analyses were performed on the StepOnePlus Real Time PCR system (437660, Thermo).

4.3 Results and discussion

Design of same-cell protein and nucleic acid assay for low starting cell numbers

In order to perform multimodal measurements on the same mammalian cells, we developed an assay that integrates (i) electrophoretic separation of cytoplasmic proteins and (ii) extraction of nucleic acids from the nuclei. To do so, we designed the triBlot device, consisting of a

200 μm -thick polyacrylamide (PA) gel covalently bound to the treated surface of a flexible polyester film (GelbondTM PAG Film). The PA layer is in turn patterned with an array of microwells (200 μm in diameter) [32].

Our assay begins with settling cells into the microwells of the triBlot device (Figure 4.1a). Cells can be passively settled into microwells by gravity [41], or actively sampled either using a micromanipulator [42, 43] or a mouth-pipette assembly [31]. In terms of sample requirements, one microwell can hold from one single cell to ~ 200 cells. Given that the triBlot device has 45 microwells, 45 separate samples can be analyzed simultaneously, each sample ranging from a single cell to ~ 200 cells. Treatment of cells with fractionation lysis buffer [31, 44] for 1 minute achieves in situ lysis of the cytoplasmic fraction of cells (Figure 4.1a). An electric field is then applied for 2 to 3 minutes to (i) inject solubilized proteins through the microwell wall and into the PA gel layer and (ii) achieve fractionation PAGE (fPAGE), which separates cytoplasmic proteins by molecular mass along the separation lane, or region abutting the microwell. Proteins are then photo-blotted, or immobilized to the PA layer by 45-second long UV-light activation of benzophenone moieties incorporated in the PA gel matrix. After cytoplasmic fPAGE, the nuclei remain intact in the microwells. The polymer substrate of the triBlot device allows us to laser-excise areas of the gel, or gel pallets, containing the microwells with the fractionated nuclei. Nuclei-laden gel pallets are then placed into reaction vessels (Eppendorf tubes) in order to perform extraction and off-chip analysis of either DNA or mRNA. The remaining triBlot device is then immunoprobed for proteins with fluorescently-labelled antibody probes, yielding protein immunoblots from the original settled cells.

Questions surrounding rare-cell types, such as CTCs and CTC clusters, may require simultaneous analysis of a wide range of cell numbers. To determine the dynamic range of our assay, we utilized U251 human glioblastoma cells engineered to express the fluorescent protein TurboGFP in the cytoplasm, but not the nucleus [44]. Expression of fluorescent TurboGFP is a useful protein model for visualizing cell lysis, injection, fPAGE, and photo-blotting. We first settled TurboGFP-U251 cells stained with nuclear Hoechst dye into microwells (Figure 4.1b). After fractionation lysis, fPAGE and photocapture, we observed a TurboGFP band in the separation lane along with absence of TurboGFP fluorescence in the microwell, suggesting complete lysis and injection of the cytoplasmic proteins into the PA gel had been achieved (Figure 4.1b).

Next, to maintain the integrity of the nuclei we place the gel device in nuclei wash buffer. We then excised gel pallets containing the microwells (Figure 4.1c). Fluorescence imaging of the Hoechst-stained nuclei confirmed the presence of the nuclei in the microwells (Figure 4.1c). The remaining gel device was imaged for native TurboGFP signal and then incubated with primary antibody probes against TurboGFP followed by AlexaFluor555-conjugated secondary antibody probes and imaged for resulting TurboGFP immunoblots (Figure 4.1d). The detection of two bands in both the photo-blotted and the immunoprobed protein bands (Figure 4.1d) indicates the ability to discern protein isoforms using the same antibody probe. Isoforms of GFP, which are estimated to differ by less than 1 kDa in molecular mass, have been attributed to differential C-terminal cleavage by non-specific proteases during bacterial

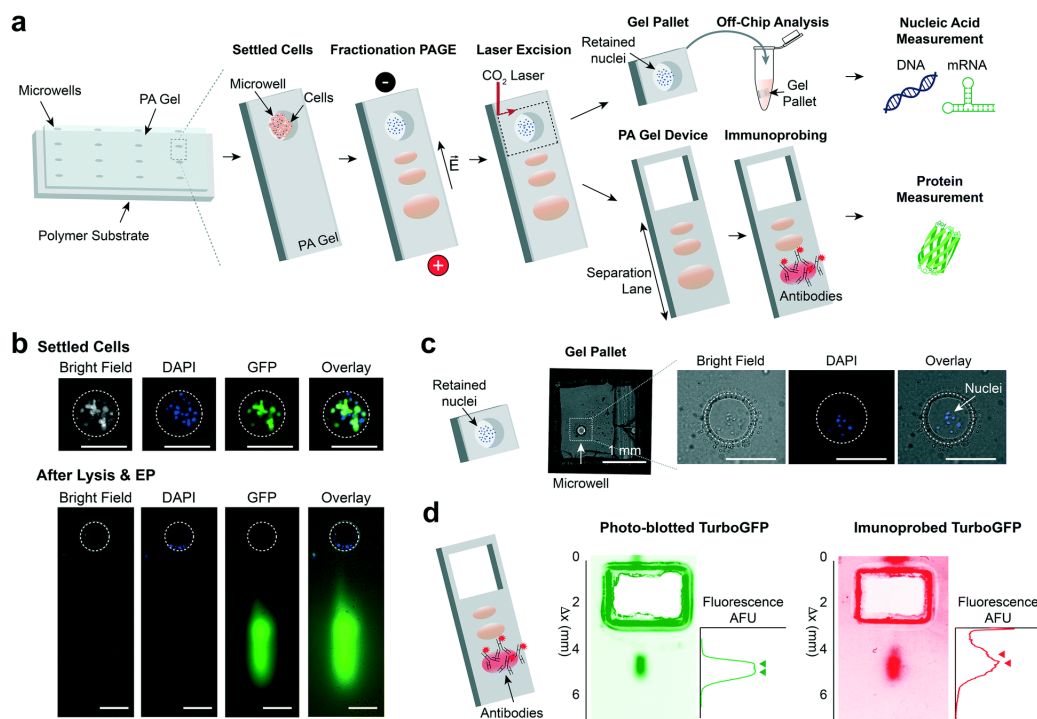


Figure 4.1: Multimodal measurements by fractionation PAGE coupled with laser excision of microwells into gel pallets for off-chip analysis of nucleic acids. (a) The same-cell nucleic acid and protein isoform immunoblotting device (triBlot) comprises a thin polyacrylamide (PA) gel covalently grafted to a polymer film and stippled with microwells. One to ~ 200 cells are settled into each microwell of the triBlot device and lysed with a fractionation lysis buffer. Application of an electric field injects the solubilized cytoplasmic proteins into the PA gel for separation by molecular mass. After protein sizing, the proteins are immobilized to the gel by UV-mediated activation of benzophenone that is polymerized into the PA gel matrix. A CO_2 laser excises $2 \text{ mm} \times 3 \text{ mm}$ gel sections circumscribing each nuclei-laden microwell, creating gel pallets that are suitable for off-chip DNA or mRNA analysis. Each protein sizing lane of the planar triBlot device is immunoprobed with fluorescently labeled antibody probes, yielding protein immunoblots indexed to each excised gel pallet. (b) Fractionation PAGE retains nuclei in microwells. Top row displays brightfield, DAPI and GFP micrographs of TurboGFP-U251 cells settled into a microwell, prior to the cell lysis step. On bottom, brightfield, DAPI and GFP fluorescence micrographs of microwell and abutting PA gel (separation lane) after fPAGE, when cytoplasmic proteins have been electrophoresed into the PA gel while nuclei remain in the microwell. (c) Gel pallets allow extraction of nuclei for off-chip analysis of nucleic acids. Brightfield micrograph shows one gel pallet. Retention of nuclei can be verified by the fluorescence imaging of the Hoechst-stained nuclei, as displayed in the merged micrographs of a gel pallet microwell. (d) Immunoblots of photo-blotted and immunoprobed TurboGFP. On the left, a false-color micrograph of photo-blotted TurboGFP protein after electrophoretic separation, with a corresponding intensity profile. On the right, a false-color micrograph of the TurboGFP immunoblot, with corresponding intensity profile. Arrowheads mark the position of each protein peak. Scale bars are $200 \mu\text{m}$, unless specified.

expression of recombinant proteins [45].

Extraction of gel pallets enables quantification of DNA from a single nucleus

We next sought to scrutinize the viability of nucleic acid analysis after gel pallet retrieval and determine detection limits. To do so, we performed amplification of the TurboGFP gene by polymerase chain reaction (PCR) from gel pallets containing a single nucleus (Figure 4.2a). We designed microwells to isolate single TurboGFP-expressing U251 cells (32 μm in diameter, 40 μm in height). After fPAGE of the cytoplasmic fraction, single nuclei retained in the microwells were excised into gel pallets. To verify retention of each nucleus, we used epifluorescence microscopy to inspect gel pallets for the Hoechst-stained nuclei. Gel pallets were then placed into separate reaction vessels (centrifuge tubes) for PCR amplification of the TurboGFP gene. PCR products were analysed on an agarose gel, revealing successful amplification of the TurboGFP from the gel pallet (Figure 4.2b, 4.2c). The presence of a PCR product of the same length as the positive control indicates amplification of the TurboGFP gene from the gel pallet sample, validating viability of DNA extraction from nuclei in gel pallets (Figure 4.2b, 4.2c). Densitometry analysis of the PCR product enables semi-quantitative analysis of the DNA present in the gel pallets (Figure 4.2d). Results indicate DNA can be retrieved from gel pallets from starting samples containing as few as a single nucleus per gel pallet.

Photo-blotting and immunoblotting protein fluorescence signal correlates with protein expression prior to lysis

We next evaluated the performance of our assay in measuring protein targets, namely, whether protein measured after lysis, fPAGE and immunoblotting accurately measures protein abundance prior to lysis. We used the TurboGFP protein in TurboGFP-expressing U251 cells as a measure of protein abundance. We first loaded an increasing number of cells into microwells of a triBlot device, from a single cell to ~ 200 cells (Figure 4.3a). We imaged the TurboGFP-U251 cells settled into microwells for TurboGFP fluorescence prior to lysis and computed whole-cell fluorescence intensity by area-under-the-curve analysis (AUC). We then ran fPAGE and scanned the triBlot device for photo-blotting native TurboGFP fluorescence. Finally, we immunoprobed the triBlot devices with primary antibody probes against TurboGFP (rabbit-anti-TurboGFP), followed by fluorophore-conjugated secondary antibody probes (AlexaFluor555 donkey-anti-rabbit), and imaged the devices for immunoprobed TurboGFP signal. To quantify the photo-blotting and immunoprobed protein peaks, we performed Gaussian curve fitting on the protein peak intensity profiles and used the Gaussian fit parameters (peak center and σ) to calculate the AUC for a peak width of 4σ . Quality control metrics were defined as signal-to-noise ratio (SNR) greater than 3 and a Gaussian fit $R^2 > 0.6$.

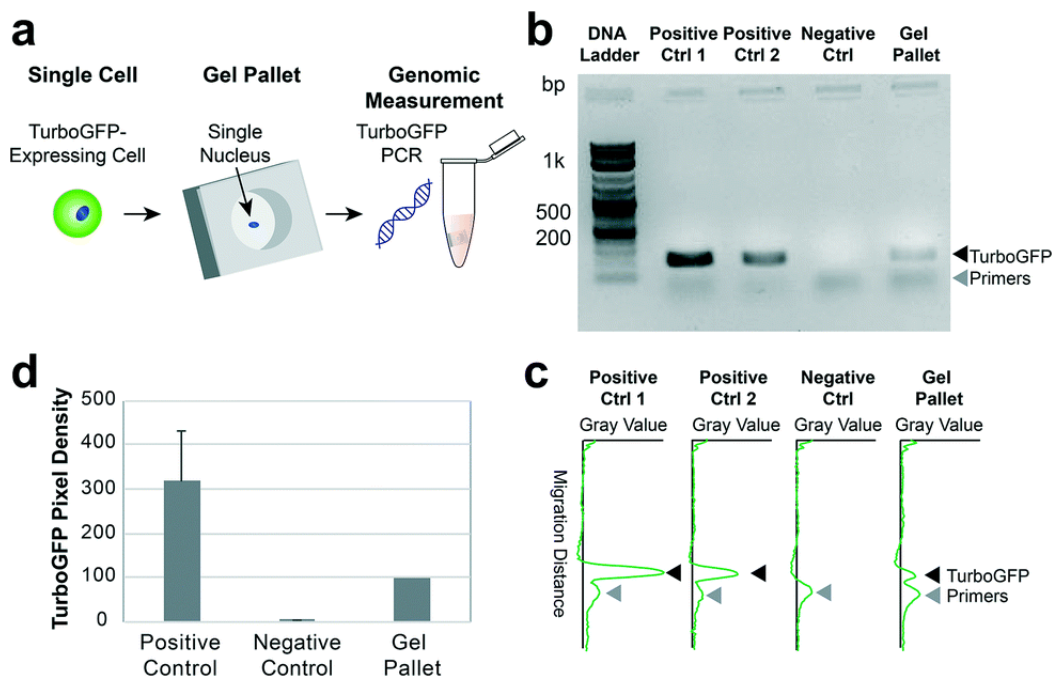


Figure 4.2: PCR amplification of TurboGFP DNA from a gel pallet containing a single TurboGFP-expressing U251 cell nucleus. (a) Schematic of gel pallets analyzed for TurboGFP DNA. (b) Agarose gel electrophoresis of DNA amplified for the TurboGFP gene by PCR from samples including: positive controls (10 ng DNA extracted from TurboGFP-U251 lysate), negative controls (no DNA) and gel pallet containing one TurboGFP-U251 nucleus. (c) Gray value intensity profiles for agarose gel lanes corresponding to positive controls, negative control and gel pallet containing a single TurboGFP-U251 nucleus. (d) Bar plots of densitometric quantitation of TurboGFP bands in agarose gel electrophoresis. Error bars indicate standard deviation for $n = 3$ replicates.

When comparing (i) whole-cell TurboGFP prior to lysis, (ii) native signal from the photo-blotted TurboGFP and (iii) immunoprobed signal from fluorophore-conjugated antibody probes against TurboGFP (Figure 4.3a), we found that whole-cell TurboGFP fluorescence demonstrated a positive linear association with signal quantified from both photo-blotted TurboGFP fluorescence and immunoblotted TurboGFP fluorescence (Pearson correlation, $\rho = 0.839$ and 0.902 , for $N = 9$ and 7 microwells, respectively). Photo-blotted and immunoprobed TurboGFP fluorescence also show a strong positive correlation (Pearson correlation, $\rho = 0.909$, $N = 7$ microwells, Figure 4.3b). These results suggest that endpoint immunoblots accurately estimate protein abundance in starting, intact cells. These results further suggest that endpoint immunoblotting can accurately quantify endogenous protein targets (not tagged with fluorescent labels) for which pre-lysis quantification is impossible. Finally, the limit of detection (LOD) for proteins has been experimentally determined to be 27,000 copies

[46], corresponding to single-cell levels of a median-expressed protein [47]. As with any immunoassay, the LOD is dependent on antibody probe affinity for protein target epitope.

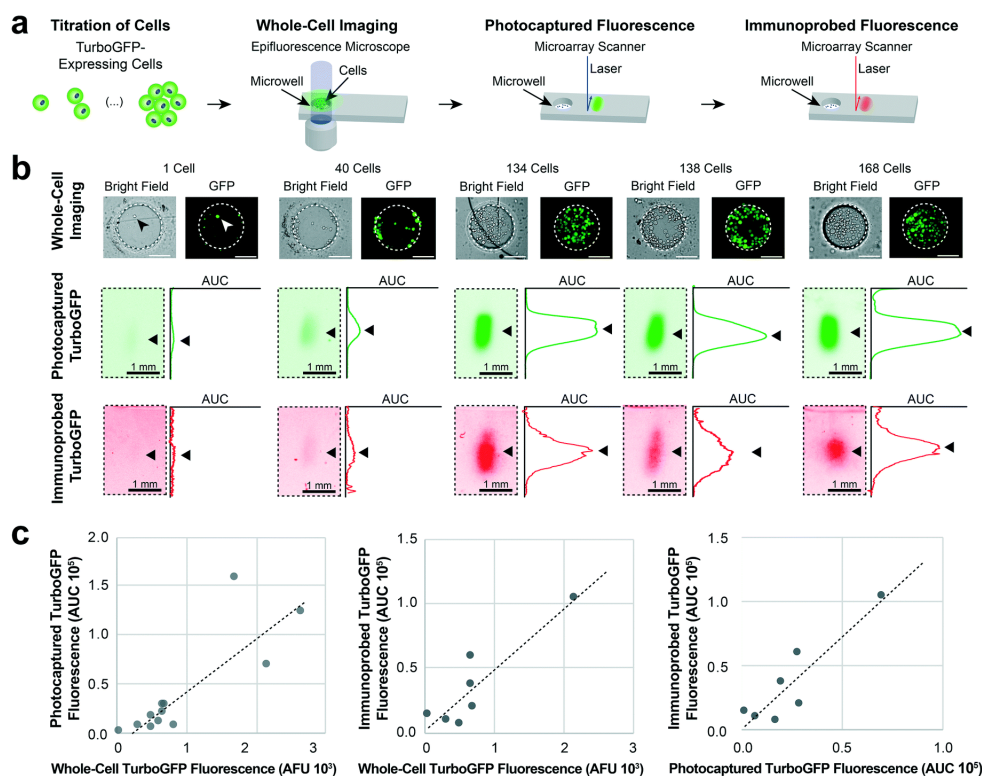


Figure 4.3: Photo-blotted and immunoprobed protein quantitation correlates with protein expression measured prior to lysis. (a) Schematic of experiment for quantifying TurboGFP protein at different stages of the same-cell nucleic acid and protein isoform measurement assay. (b) Brightfield and false color fluorescence micrographs of TurboGFP-expressing U251 cells settled into microwells. Cells were manually counted in ImageJ using overlay brightfield and GFP micrographs. Corresponding false color fluorescence micrographs of TurboGFP immunoblots imaged after photo-blotting and immunoprobing. Fluorescence intensity profiles are shown to the right of immunoblots. Black arrows mark the position of protein peaks. (c) Bivariate plots of whole-cell TurboGFP fluorescence prior to lysis, photo-blotted TurboGFP fluorescence (AUC) and immunoprobed TurboGFP fluorescence (AUC). Whole-cell TurboGFP fluorescence shows strong positive correlation with both photo-blotted and immunoprobed TurboGFP fluorescence (Pearson correlation, $\rho = 0.839$ and 0.902 , for $N = 9$ and 7 microwells, respectively). Likewise, photo-blotted and immunoprobed TurboGFP fluorescence show a strong positive correlation (Pearson correlation, $\rho = 0.909$, $N = 7$ microwells).

TurboGFP mRNA correlates with TurboGFP protein fluorescence measured prior to lysis, after fPAGE and after immunoprobing

We next examined whether mRNA collected from gel pallets correlates with protein expression. First, we examined if mRNA extracted from gel pallets containing single nuclei could be amplified. We used a single-cell droplet printer (cellenONE) to deposit single TurboGFP-expressing U251 cells into microwells of a triBlot device. After performing fPAGE with a 25 s lysis time, we excised gel pallets containing single nuclei and processed them for mRNA analysis (Figure 4.4a). We extracted and amplified mRNA from gel pallets and analysed amplified cDNA for TurboGFP by RT-qPCR (Figure 4.4b). To ensure the triBlot assay can support a single-cell LOD for mRNA, we used a kit that has been validated to detect transcripts from single cells by the manufacturer (Zymo). All samples prepared from gel pallets show higher expression (i.e. lower C_T values) than all negative controls (high or absent C_T values), including a sample containing TurboGFP-expressing U251 cDNA where the reverse transcriptase (RT) enzyme was left out (-RT), an RT mix only sample, a PreAmplification only sample and a sample containing primer but no cDNA sample to test for background primer dimer amplification (Figure 4.4b, 4.4c). Positive controls were cDNA from TurboGFP-U251 cell lysate (Pos Ctrl 1) and cDNA from a gel pallet containing multiple U251 nuclei (Pos Ctrl 2). Positive controls amplified either before or at similar C_T values as samples from gel pallets containing a single TurboGFP-expressing U251 cell (Figure 4.4b, 4c). Companion TurboGFP immunoblots showed protein peaks that passed the quality control metrics of SNR ≥ 3 and Gaussian fit $R^2 \geq 0.6$ (Figure 4.4d).

Finally, to examine correlations between mRNA and protein expression, we used passive gravity settling to load increasing numbers of cells into the microwells of a triBlot device. We loaded from 6 cells per microwell to 201 cells per microwell. After fPAGE and excision of the triBlot device into gel pallets, gel pallets were placed into separate reaction vessels containing DNA/RNA Shield solution (Zymo) to extract mRNA from retained nuclei (Figure 4.5a). While devices were immunoprobed with antibody probes against TurboGFP, isolated mRNA was first reverse transcribed and subsequent cDNA was analyzed for TurboGFP expression using semi-quantitative real-time PCR analysis (semi-RT-qPCR). Amplified cDNA was analyzed by agarose gel electrophoresis and bands were quantified by densitometry (Figure 4.5b). We observed an 85% yield for successful sample amplification, where 12 out of 15 samples had a detectable band at the correct TurboGFP amplicon length (Figure 4.5b, lanes 2–7, 9 and 11–15). To determine a failed amplification, we used the presence of a primer band and absence of a TurboGFP band (Figure 4.5b, lanes 8 and 10).

Results show that whole-cell fluorescence and photo-blotted protein signal are significantly correlated with mRNA levels (Pearson correlation, $\rho = 0.849$ and 0.843 , $N = 7$ microwells, for whole-cell TurboGFP fluorescence and photo-blotted TurboGFP, respectively, Figure 4.5c. Failed PCR amplification samples or samples with protein peaks that did not pass QC metrics of SNR ≥ 3 and $R^2 \geq 0.6$ were not considered). TurboGFP mRNA levels also show a strong positive association with immunoprobed TurboGFP signal (Pearson correlation, $N = 5$ microwells, $\rho = 0.907$, Figure 4.5c). These results validate the integrity of

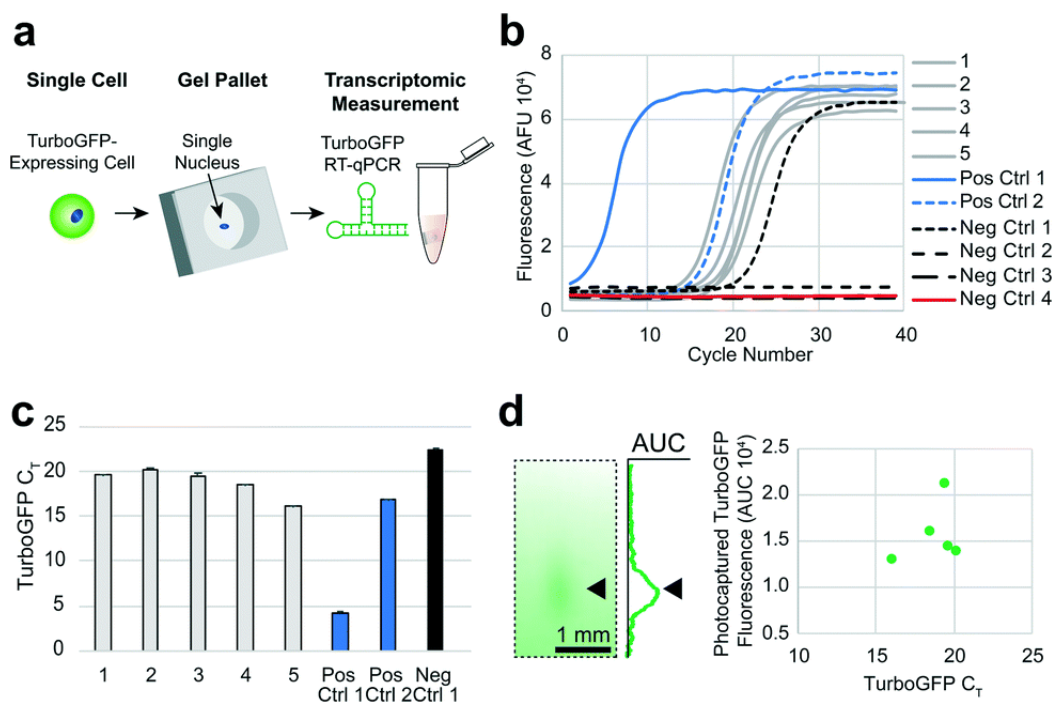


Figure 4.4: RT-qPCR amplification of mRNA from gel pallet containing single TurboGFP-expressing U251 cell nucleus. (a) Schematic of gel pallets analyzed for TurboGFP mRNA. (b) RT-qPCR amplification curves for TurboGFP from gel pallets containing a single nucleus (samples 1–5), positive controls (Pos Ctrl 1: cDNA amplified from TurboGFP-U251 lysate and Pos Ctrl2: gel pallet containing multiple TurboGFP-U251 nuclei) and negative controls (Neg Ctrl 1: cDNA from lysate without RT mix, Neg Ctrl 2: RT mix only, Neg Ctrl 3: PreAmplification mix only, Neg Ctrl 4: primers only with no cDNA to test for background from primer dimer amplification). (c) Bar graph of TurboGFP C_T values for all samples shown in panel (b) that amplified. Error bars indicate standard deviation for $n = 3$ replicates. (d) On left, false color fluorescence micrograph showing TurboGFP band from a single U251 cell with accompanying intensity profile to the right. Arrowheads mark the position of protein peak. On the right, bivariate plot of photocaptured TurboGFP fluorescence (AUC) and TurboGFP C_T values for samples containing a single U251 nucleus ($n = 5$ gel pallets containing a single U251 nucleus).

mRNA recovered from nuclei-laden gel pallets, and demonstrate that transcription levels can be quantified from same-cell mRNA and immunoblotting assay.

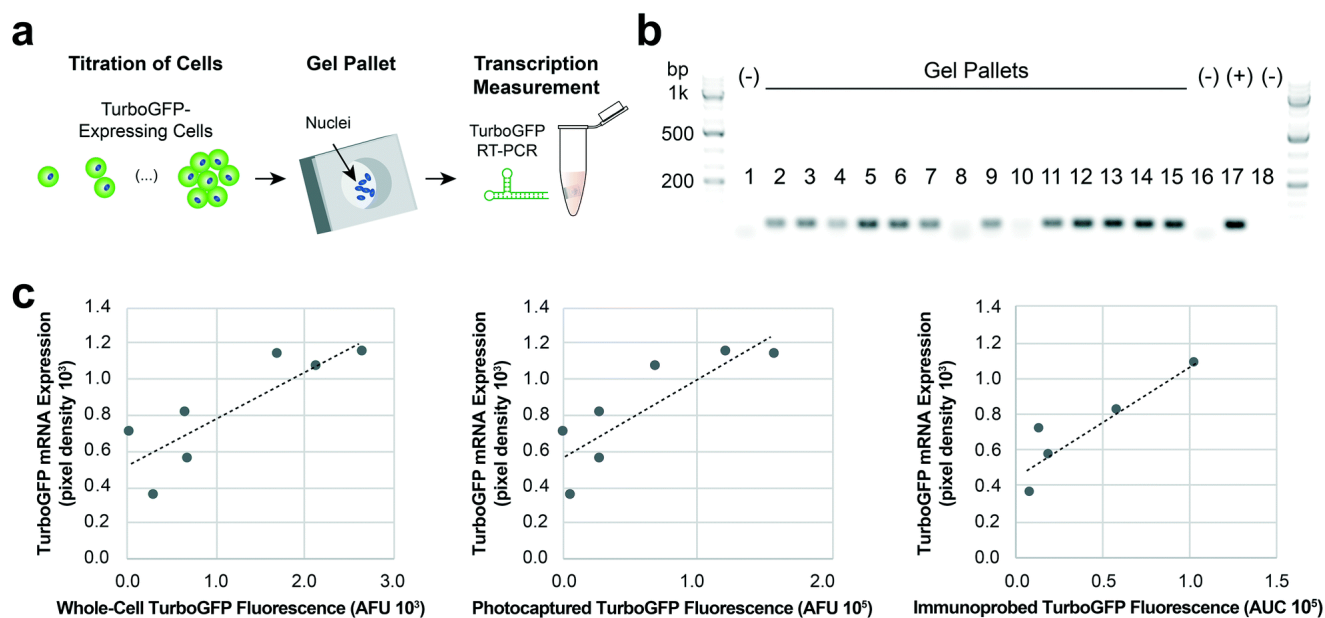


Figure 4.5: Semi-RT-qPCR amplification of TurboGFP mRNA from gel pallets correlates with same-cell protein expression measurement. (a) Schematic of analysis of gel pallets for TurboGFP mRNA. (b) Agarose gel electrophoresis of cDNA amplicons representing gel pallets with increasing number of cells (lanes 2–15). Negative controls include lanes 1 (no cells), lane 16 (–RT) and lane 18 (water). Positive control lane 17 containing TurboGFP plasmid (1 ng) was positive. DNA ladder used was Thermo 1 KB + DNA ladder. (c) Semi quantitative mRNA TurboGFP levels, measured from densitometry plots of cDNA agarose gel, demonstrate strong linear correlation with all protein measurements; whole-cell, photo-blotted and immunoprobed TurboGFP fluorescence (Pearson correlation, $\rho = 0.849$, 0.843 and 0.907 , for $N = 7$, 7 and 5 microwells, respectively).

4.4 Conclusions

Assessing whether specific modifications at the nucleic acid level drive important mechanisms in disease progression requires measuring all molecular types involved, including proteins, DNA and mRNA. Here we design an assay for simultaneous measurement of protein isoforms and nucleic acids from low starting numbers of mammalian cells. We demonstrate that signal from immunoprobed protein correlates strongly with protein expression prior to lysis in TurboGFP-expressing cells. We also measure both mRNA and DNA from retrieved nuclei, with positive amplification of TurboGFP gene and TurboGFP transcripts, demonstrating

our ability to recover, isolate and amplify nucleic acids from gel pallets. The cell number range over which we performed these measurements (from 1 to 100s of cells) includes the cell numbers relevant to tumor samples, including cells obtained from fine needle aspirates and CTC clusters.

Given the prevalence of protein isoforms across a wide range of diseases, tools that measure both nucleic acids and intracellular protein isoforms from the same cells are necessary to (i) reveal the mechanisms by which the events at the nucleic acid level (including SNPs, alternative splicing or PTMs) regulate the production of pathogenic proteoforms, and (ii) identify new disease-specific biomarkers for early detection, diagnosis, and therapy.

Moreover, as more efficient gene editing tools continue to emerge, strict evaluation of how both on-target and off-target edits affect the transcriptional and protein expression landscapes will become critical for safely translating these gene editing tools into clinical applications [48, 49]. Same-cell multimodal tools such as the one presented here will be instrumental in unequivocally linking modifications in protein expression profiles to on-target and off-target editing events.

Bibliography

1. Barrett, C. L. *et al.* Systematic transcriptome analysis reveals tumor-specific isoforms for ovarian cancer diagnosis and therapy. *Proceedings of the National Academy of Sciences of the United States of America* **112**, E3050–E3057. ISSN: 10916490 (2015).
2. Frankiw, L., Baltimore, D. & Li, G. Alternative mRNA splicing in cancer immunotherapy. *Nature Reviews Immunology* **19**, 675–687 (2019).
3. Martinez, B. I. & Stabenfeldt, S. E. Current trends in biomarker discovery and analysis tools for traumatic brain injury. *Journal of Biological Engineering* **13**, 1–12. ISSN: 17541611 (2019).
4. Ward, M. & Schofield, E. L. Biomarkers for brain disorders. *Therapy* **7**, 321–336. ISSN: 14750708 (2010).
5. Bruikman, C. S. *et al.* Netrin Family: Role for Protein Isoforms in Cancer. *Journal of Nucleic Acids* **2019**. ISSN: 2090021X (2019).
6. Climente-González, H. *et al.* The Functional Impact of Alternative Splicing in Cancer. *Cell Reports* **20**, 2215–2226. ISSN: 22111247 (2017).
7. Jovanov-Milošević, N. *et al.* Human fetal tau protein isoform: Possibilities for Alzheimer’s disease treatment. *International Journal of Biochemistry and Cell Biology* **44**, 1290–1294. ISSN: 18785875 (2012).
8. Lorentzian, A., Uzozie, A. & Lange, P. F. Origins and clinical relevance of proteoforms in pediatric malignancies. *Expert Review of Proteomics* **16**, 185–200. ISSN: 17448387. <https://doi.org/10.1080/14789450.2019.1575206> (2019).
9. Wei, J., Zaika, E. & Zaika, A. P53 family: Role of protein isoforms in human cancer. *Journal of Nucleic Acids* **2012**. ISSN: 20900201 (2012).
10. Ståhlberg, A. *et al.* Quantitative PCR analysis of DNA, RNAs, and proteins in the same single cell. *Clinical Chemistry* **58**, 1682–1691. ISSN: 00099147 (2012).
11. Stuart, T. & Satija, R. Integrative single-cell analysis. *Nature Reviews Genetics* **20**, 257–272 (2019).
12. Qui, S. *et al.* Analysis of plasma HER2 copy number in cell-free DNA of breast cancer patients: a comparison with HER2 extracellular domain protein level in serum. *Breast Cancer* (2021).

13. Ruggles, K. V. *et al.* Methods, tools and current perspectives in proteogenomics. *Molecular and Cellular Proteomics* **16**, 959–981. ISSN: 15359484 (2017).
14. Zhao, Y. *et al.* Nanoscale imaging of clinical specimens using pathology-optimized expansion microscopy. *Nature Biotechnology*, 757–764 (2017).
15. Louie, R. H. & Luciani, F. Recent advances in single-cell multimodal analysis to study immune cells. *Immunology and Cell Biology*, 157–167. ISSN: 14401711 (2021).
16. Nathan, A. *et al.* Multimodal single-cell approaches shed light on T cell heterogeneity. *Current Opinion in Immunology* **61**, 17–25 (2019).
17. Stoeckius, M. *et al.* Simultaneous epitope and transcriptome measurement in single cells. *Nature Methods* **14**, 865–868 (2017).
18. Albayrak, C. *et al.* Digital Quantification of Proteins and mRNA in Single Mammalian Cells. *Molecular Cell* **61**, 914–924. ISSN: 10974164 (2016).
19. Frei, A. P. *et al.* Highly multiplexed simultaneous detection of RNAs and proteins in single cells. *Nature Methods* **13**, 269–275 (2016).
20. Gawad, C., Koh, W. & Quake, S. R. Single-cell genome sequencing: Current state of the science. *Nature Reviews Genetics* **17**, 175–188. ISSN: 14710064 (2016).
21. Kawai, T. *et al.* Ultrasensitive Single Cell Metabolomics by Capillary Electrophoresis–Mass Spectrometry with a Thin-Walled Tapered Emitter and Large-Volume Dual Sample Preconcentration. *Analytical Chemistry* **91**, 10564–10572 (2019).
22. Macaulay, I. C., Ponting, C. P. & Voet, T. Single-cell multiomics: multiple measurements from single cells. *Trends in Genetics* **33**, 155–168. ISSN: 13624555 (2017).
23. Peterson, V. M. *et al.* Multiplexed quantification of proteins and transcripts in single cells. *Nature Biotechnology* **35**, 936–939 (2017).
24. Schwartzman, O. & Tanay, A. Single-cell epigenomics: Techniques and emerging applications. *Nature Reviews Genetics* **16**, 716–726. ISSN: 14710064 (2015).
25. Stegle, O., Teichmann, S. A. & Marioni, J. C. Computational and analytical challenges in single-cell transcriptomics. *Nature Reviews Genetics* **16**, 133–145. ISSN: 14710064 (2015).
26. Wu, M. & Singh, A. K. Single-Cell Protein Analysis. *Current Opinion in Biotechnology* **23**, 83–88 (2012).
27. Xue, M. *et al.* Chemical methods for the simultaneous quantitation of metabolites and proteins from single cells. *Journal of the American Chemical Society* **137**, 4066–4069. ISSN: 15205126 (2015).
28. Cai, X., Zheng, Y. & Speck, N. A. A western blotting protocol for small numbers of hematopoietic stem cells. *Journal of Visualized Experiments* **2018**, 6–9. ISSN: 1940087X (2018).

29. Altschuler, S. J. & Wu, L. F. Cellular Heterogeneity: Do Differences Make a Difference? *Cell* **141**, 559–563. ISSN: 00928674 (2010).
30. Trenchevska, O., Nelson, R. W. & Nedelkov, D. Mass spectrometric immunoassays for discovery, screening and quantification of clinically relevant proteoforms. *Bioanalysis* **8**, 1623–1633. ISSN: 17576199 (2016).
31. Rosàs-Canyelles, E. *et al.* Assessing heterogeneity among single embryos and single blastomeres using open microfluidic design. *Science Advances* **6**. ISSN: 23752548 (2020).
32. Rosàs-Canyelles, E. *et al.* Multimodal detection of protein isoforms and nucleic acids from mouse pre-implantation embryos. *Nature Protocols*, NP-PI200463 (2020).
33. Gkountela, S. *et al.* Circulating Tumor Cell Clustering Shapes DNA Methylation to Enable Metastasis Seeding. *Cell* **176**, 98–112.e14. ISSN: 10974172 (2019).
34. Lizotte, P. H. *et al.* Fine needle aspirate flow cytometric phenotyping characterizes immunosuppressive nature of the mesothelioma microenvironment. *Scientific Reports* **6**, 1–8. ISSN: 20452322 (2016).
35. Pritzker, K. P. & Nieminen, H. J. Needle biopsy adequacy in the era of precision medicine and value-based health care. *Archives of Pathology and Laboratory Medicine* **143**, 1399–1415. ISSN: 15432165 (2019).
36. Abdelmoez, M. N. *et al.* SINC-seq: Correlation of transient gene expressions between nucleus and cytoplasm reflects single-cell physiology. *Genome Biology* **19**, 1–11. ISSN: 1474760X (2018).
37. Grindberg, R. V. *et al.* RNA-sequencing from single nuclei. *Proceedings of the National Academy of Sciences* **110**, 19802–19807. ISSN: 0027-8424 (2013).
38. Tang, F. *et al.* RNA-Seq analysis to capture the transcriptome landscape of a single cell. *Nature Protocols* **5**, 516–535. ISSN: 17542189 (2010).
39. Kang, C. C. *et al.* Single cell-resolution western blotting. *Nature Protocols* **11**, 1508–1530. ISSN: 17502799 (2016).
40. Schneider, C. A., Rasband, W. S. & Eliceiri, K. W. NIH Image to ImageJ : 25 years of image analysis HISTORICAL commentary NIH Image to ImageJ : 25 years of image analysis. *Nature Methods* **9**, 671–675. ISSN: 1548-7091 (2012).
41. Kang, C.-c. *et al.* Single cell resolution western blotting. *Nature Protocols* **11**, 1508–1530. ISSN: 1754-2189. <http://dx.doi.org/10.1038/nprot.2016.089> (2016).
42. Rosàs-Canyelles, E. *et al.* Mouse-to-mouse variation in maturation heterogeneity of smooth muscle cells. *Lab on a Chip* **18**, 1875–1883. ISSN: 2050750X (2018).
43. Sinkala, E. *et al.* Profiling protein expression in circulating tumour cells using microfluidic western blotting. *Nature Communications* (2017).
44. Yamauchi, K. A. & Herr, A. E. Subcellular western blotting of single cells. *Microsystems & Nanoengineering* **3**, 16079. ISSN: 2055-7434. <http://www.nature.com/articles/micronano201679> (2017).

45. Hughes, A. J. & Herr, A. E. Microfluidic Western blotting. *Proceedings of the National Academy of Sciences of the United States of America* **109**, 21450–5. ISSN: 1091-6490. <http://www.pubmedcentral.nih.gov/articlerender.fcgi?artid=3535594{\&}tool=pmcentrez{\&}rendertype=abstract> (2012).
46. Hughes, A. J. *et al.* Single-cell western blotting. *Nature methods* **11**, 749–55. ISSN: 1548-7105. arXiv: NIHMS150003. <http://www.ncbi.nlm.nih.gov/pubmed/24880876> (2014).
47. Schwanhäusser, B. *et al.* Global quantification of mammalian gene expression control. *Nature* **473**, 337–342. ISSN: 0028-0836. <http://www.nature.com/doifinder/10.1038/nature10098> (2011).
48. Lee, H. & Jin-Soo Kim. Unexpected CRISPR on-target effects. *Nature Biotechnology* **36**, 703–704 (2018).
49. Zischewski, J., Fischer, R. & Bortesi, L. Detection of on-target and off-target mutations generated by CRISPR/Cas9 and other sequence-specific nucleases. *Biotechnology Advances* **35**, 95–104. ISSN: 07349750. <http://dx.doi.org/10.1016/j.biotechadv.2016.12.003> (2017).

Chapter 5

Towards dual RNA sequencing and proteoform measurements from single cells

5.1 Introduction

While single-cell immunoblotting (scI) excels at detecting a variety of proteoforms from single cells [1–3], outstanding questions remain about how proteoforms affect cellular subtypes, differentiation trajectories, and regulatory networks [4–6]. Addressing these questions requires the ability to combine proteoform detection with other measurement modalities, which is an outstanding challenge in measurement science. Specifically, the detection of other biological molecules, including DNA, RNA, metabolites, or lipids, can provide critical information about aspects such as cell state, cell subpopulations, and lineage mapping [7, 8].

Significant progress has occurred in the development of multimodal single-cell protein assays, including assays that combine detection of DNA and RNA with protein targets from single cells [7, 8]. Several of these assays use sequencing as the dominant method of RNA detection, which enables detection of hundreds of RNA targets, and may complement “targeted” approaches (protein immunoassays) by enabling discovery of newly enriched or underexpressed RNA targets in specific cell subpopulations [9–12]. However, the majority of these multimodal assays use immunoreagents as the primary detection mechanisms for protein, which typically (1) limits the detection of protein isoforms in cases where isoform-specific antibodies are not present (see Figure 5.1A) and (2) may suffer from non-specific binding to off-target proteins, confounding quantification [1, 3]. Some multimodal assays, such as the triBlot and snapBlot have successfully demonstrated detection of RNA, and electrophoretically separated protein targets, from few or single cells [13–15]. However, in these approaches, RNA is detected by quantitative reverse transcription PCR (RT-qPCR), which limits the amount of multiplexed RNA targets that can be detected, and further prevents the discovery of unknown RNA targets that may be enriched or underexpressed in

select subpopulations.

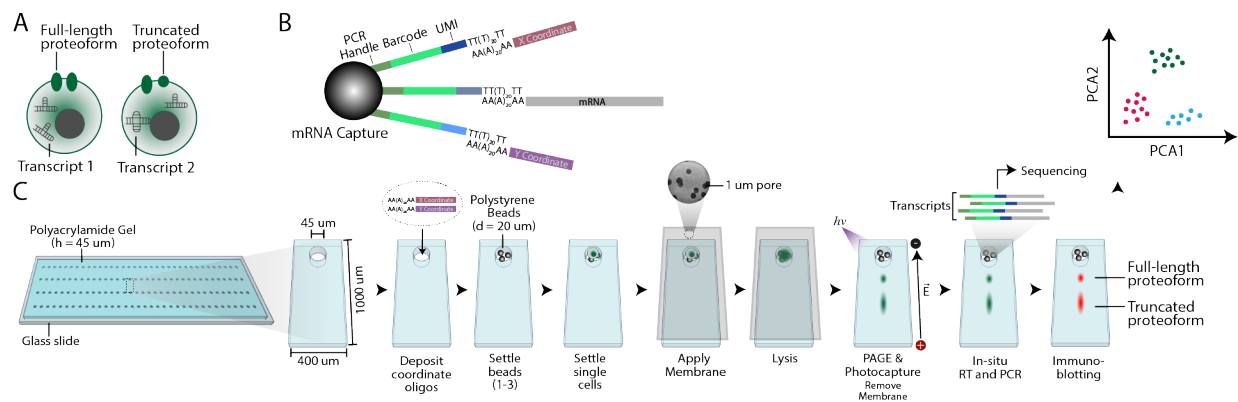


Figure 5.1: Proposed Design for Dual Single-cell RNA Sequencing and Proteoform Detection Platform. (A) In order to understand the relationship between proteoforms (e.g., alternatively-spliced full-length and truncated isoforms) and other molecules (mRNA), new measurement tools are required to simultaneously measure both sets of biomolecules in tandem. (B) Proposed bead-based transcript capture method. 20 μm -diameter polystyrene beads will be functionalized with barcodes consisting of a PCR handle, a bead-specific barcode, an oligo-specific UMI, and a poly-T tail. Both polyadenylated mRNA and coordinate oligos with poly-A tails are expected to hybridize onto functionalized beads. (C) To integrate single-cell immunoblotting with single-cell RNA sequencing, we propose the development of platform that uses a combination of uniquely barcoded beads and coordinate oligonucleotides to map transcripts back to their array location. Specifically, we aim to deposit X and Y coordinate oligonucleotides, followed by deposition of 2-3 barcoded polystyrene beads, into each microwell. After bead deposition, single cells will seeded onto chips, and settled via gravitational sedimentation. PCTE membranes with 1 μm pore sizes will be hybridized onto PA gels to prevent loss of transcripts from microwells. Cells will undergo *in situ* lysis, followed by PAGE and photocapture, in order to entrap electrophoretically-separated proteins into the hydrogel. During lysis, we also expect transcripts to hybridize onto the poly-T tails present in the barcoded beads. To amplify and extract captured transcripts, in situ reverse transcription and PCR will be performed on chips, after which amplified product will be extracted for downstream sequencing. To detect proteins, immunoprobings on chips will proceed as previously described [1, 3]. Protein and transcripts can then be quantified and used to assess characteristics such as cellular heterogeneity, and the presence of subpopulations.

In this study, we lay the groundwork towards the development of a dual single-cell RNA sequencing (scRNA-seq) and proteoform detection assay. Based on previously published single-cell RNA sequencing work, we aim to capture mRNA from single cells using a bead-based extraction method [16–18]. Oligonucleotides (oligos) consisting of a PCR handle, a unique bead barcode, unique molecular identifiers (UMIs), and a poly-T sequence are conju-

gated onto individual polystyrene beads using split-and-pool synthesis (see Figure 5.1B). 1-3 beads will be deposited to each microwell using a single-cell dispensing droplet printer [16] (see Figure 5.1C). Based on previously-published work that maps uniquely barcoded beads to spatial positions on an array, we aim to deposit X and Y coordinate oligos containing poly-A tails to each microwell [19]. Single cells will be settled via gravitational sedimentation, as previously described [1, 3]. Consistent with other single-cell RNA sequencing work, we expect to couple the open microarray system to a polycarbonate track etch (PCTE) membrane to increase hybridization of transcripts to beads. By optimizing lysis conditions, we expect to be able to both hybridize mRNA with poly-A tails to the poly-T region of conjugated polystyrene beads, while also ensuring efficient lysis and solubilization of protein targets. PAGE will allow separation of protein targets through the hydrogel matrix, while keeping the mRNA affixed to the polystyrene beads. By performing on-chip reverse transcription (RT) and PCR, we expect to be able to extract amplified cDNA from the beads for downstream library preparation and sequencing. Detection of electrophoretically separated proteins can then proceed via immunoassay. Once proteoforms and transcripts are detected from single cells, we can use dimensionality reduction and lineage tracing approaches to elucidate pathways responsible for proteoform formation [7, 20, 21]

To investigate the feasibility of a dual single-cell proteoform and RNA sequencing assay, we describe preliminary investigations undertaken to optimize mRNA lysis and binding timescales, assess lysis buffer compatibility for protein solubilization, and designs for on-chip RT and PCR. We anticipate that the results of this study will move us closer towards a proof-of-concept design for dual scI and RNA sequencing from the same cell.

5.2 Materials and Methods

Reagents

30% Acrylamide/bis-acrylamide (29:1) (A3574), N,N,N',N'-Tetramethylethylenediamine (T9281), ammonium persulfate (A3678), sodium dodecyl sulfate (L4509), bovine serum albumin (A9418), lithium chloride (SIAL-L9650-100G), lithium dodecyl sulfate (SIAL-L9781-25G), goat α -GAPDH (SAB2500450-100UG), and 30% PEG8000 (89510-1KG-F) were purchased from Millipore Sigma. Dynabeads M-280 Streptavidin (11205D), Dynabeads mRNA DIRECTTM Kit (61011), dithiothreitol (D1532), 0.5 M EDTA (AM9260G), Maxima H- reverse transcriptase (EPO0753), RNase Inhibitor (AM2696), UltraPure Distilled Water (10977023), donkey α -rabbit 647 (PIA32795), and donkey α -goat 555 (PIA32795) was purchased from Thermo Fisher Scientific. N-[3-[(3-Benzophenyl)-formamido] propyl] methacrylamide was synthesized by PharmAgra laboratories. ATCC-formulated Dulbecco's Modified Eagle's Medium (30-2002) was purchased from the American Type Culture Association (ATCC). HyClone Bovine Calf Serum (SH30073.02HI) was purchased from Cytiva Life Sciences. Rabbit α -vimentin (ab137321), goat α -GFP (ab6673), and rabbit α -beta tubulin (ab6046) were purchased from Abcam. Streptavidin-coated polystyrene beads (average diameter between 18.0

- 24.9 μm , part no. SVP-200-4) was purchased from Spherotech. Polycarbonate membrane filters of 10 nm pore size (PCT00125100), 1 μm pore size (PCT1029320), and 10 μm pore size (PCT10014220) were purchased from Sterlitech. 10 mM dNTPs (N0447L), Klenow Exonuclease (M0212S), and Exonuclease I (M0293S) was purchased from New England Biolabs. Agilent Hybridization Chamber (G2534A), High Sensitivity D5000 ScreenTape (5067-5592), and High Sensitivity D5000 Reagents containing Sample Buffer and Ladder (5067-5593) were purchased from Agilent Technologies. KAPA HiFi Hotstart Readymix PCR Kit (KK-2602) was purchased from Kapa Biosystems.

Template Switch Oligo (AAGCAGTGGTATCAACGCAGAGTGAATrGrGrG), dn-Smart Randomer (AAGCAGTGGTATCAACGCAGAGTGANNNGGNNNB), Smart PCR Primer (AAGCAGTGGTATCAACGCAGAGT), and biotinylated poly-T oligos (/5BiosG/ACACTCTTCCCTACACGACGCTCTTCCGATCTTTTTTTTTTTTTTTTTTTTTTTTTTTTTTTTTTTTTV N) was purchased from IDT. 20 μm polystyrene beads covalently modified with barcoded oligos (5'-beadlinker-TTTTTTTAAGCAGTGGTATCAACGCAGAGTACJJJJJJJJJJJJJ NNNNNNNNVTTTTTTTTTTTTTTTTTTTTTTTTTTTTTTTTTTTTTT-3') was custom ordered from Chemgenes.

Lysis Buffers

1X RIPA consists of 0.5% sodium dodecyl sulfate (SDS), 0.25 % sodium deoxycholate, 0.5 X Tris-Glycine, and 0.1% Triton X-100. Dynabeads Lysis and Binding (DLB) buffer consists of 100 mM Tris-HCl, pH 7.5, 500 mM LiCl, 1% lithium dodecyl sulfate (LiDS), 5 mM DTT, and 10 mM EDTA. 2X RIPA-like buffer consists of 1% SDS and 0.5% sodium deoxycholate, while all other components remain the same. For scI experiments, 0.1% Triton X-100 and 0.5 X Tris-Glycine was additionally added to DLB buffer.

Cell Culture

MCF7-GFP cells and NIH-3T3 cells were purchased from ATCC. U251 human glioblastoma cells were obtained from the UC Berkeley Tissue Culture Facility via the American Type Culture Collection, and stably transfected with TurboGFP via lentiviral infection (multiplicity of infection = 10). BT474 cells were obtained from Dr. Mark Pegram's laboratory in Stanford.

MCF7-GFP and BT474 cells were maintained in RPMI 1640 media supplemented with 1% penicillin/streptomycin and 10% fetal bovine serum (FBS), and maintained in a humidified 37°C incubator with 5% CO_2 . U251-tGFP cells were maintained in Dulbecco's modified eagle medium (DMEM), supplemented with 1% penicillin/streptomycin, 10% fetal bovine serum (FBS), and 1 \times nonessential amino acids. NIH-3T3 cells were maintained in ATCC-DMEM, supplemented with 1% penicillin/streptomycin and 10% bovine calf serum (BCS).

Bulk mRNA Extraction Experiments with Beads

For bulk mRNA extraction experiments, the extraction protocol in the Dynabeads mRNA DIRECTTM Kit was followed. Briefly, Dynabeads M-280 Streptavidin was conjugated to biotinylated oligos purchased from IDT (/5BiosG/ACACTCTTTCCCTACACGACGCTC TTCCGATCTTTTTTTTTTTTTTTTTTTTTTTTTTTTTTTTVN) using the protocol described in the Dynabeads kit. For extraction with Dynabeads, 200 μ L of Dynabeads bead suspension was added to cell lysate. Dynabeads were allowed to bind to mRNA for varying timescales (20s, 1 min, 5 min), and then were subject to several rounds of magnetic washing with wash buffers provided in the Dynabeads kit. mRNA was extracted by incubating the bead suspension at 72^oC, and quantified using the Qubit RNA High Sensitivity Assay.

For streptavidin-coated polystyrene beads, an identical protocol was followed for hybridization to the same biotinylated oligo. Beads were counted with a haemocytometer, and diluted to a concentration of 1 million beads per 200 uL, or 3 million beads per 200 uL. The mRNA extraction protocol was identical to the Dynabeads extraction protocol, but with spin down steps replacing magnetic washout steps. mRNA was once again extracted by incubating the bead suspension at 72^oC, and quantified using the Qubit RNA High Sensitivity Assay.

PCTE Membrane Lysis Imaging Experiments

To monitor lysis times of cells after application of PCTE membranes to hydrogels, we first fabricated 7 %T gels with 32 μ m microwells in arrays spaced 100 \times 100 apart. U251-tGFP cells were harvested and diluted in 1 \times PBS. Cells were settled on chips for 10 minutes. Prior to application, all membranes were etched under O₂ plasma for 30 s, under 45 mW RF power and 210 mTorr pressure. Membranes were then hydrated in 1 \times PBS. After cell settling, membranes were gently placed onto hydrogels with a glass slide, and then placed inside an Agilent Hybridization Chamber for 1-3 minutes. Chips were then removed from the Chamber, and placed onto a custom-built microscope Chamber.

15 %T, 500 m thick gel lids were made as previously described [22]. Gel lids soaked in lysis buffer were heated to 75^o C. Upon application of the gel lid to the chip in the microscope chamber, we recorded timelapse images of tGFP fluorescence every 0.5 s for 10 minutes per chip, using an Olympus IX-70 epifluorescence microscope. For analysis, we measured the fluorescence intensity of each cell within a given ROI and monitored the loss in fluorescence intensity after normalization to starting fluorescence.

Single-cell Immunoblotting

7%T, 30 or 32 μ m chips were fabricated as previously described [3]. For NIH-3T3 cells, we used chips with 30 μ m diameter microwells, whereas for MCF7-GFP cells, we used chips with 32 μ m diameter microwells. For initial experiments, we performed scI with gel lids incubated in 2 \times RIPA buffer + 8M Urea at 75C. For experiments with PCTE seals, we

utilized two sets of gel lids: one set soaked in Dynabeads Lysis and Binding Buffer (DLB), and another set incubated in $2\times$ RIPA buffer + 8M Urea, both heated to 75C.

After PAGE, NIH-3T3 gels were immunoprobed with 0.1 mg/mL dilutions of rabbit α -vimentin and goat α -gapdh for 2 hours, and MCF7-GFP gels were immunoprobed with 0.1 mg/mL dilutions of goat α -GFP and rabbit α -beta tubulin for 2 hours. Gels were then probed with 0.1 mg/mL donkey α -rabbit 647, and donkey α -goat 555 secondary antibodies for 1 hour. After each probing step, gels were washed for 30 minutes with TBST. After secondary probing washout, gels were dried under a N_2 stream and scanned with a Genepix Microarray Scanner (Molecular Devices, San Jose, CA).

RT and PCR Experiments

For all RT and PCR experiments, we utilized custom-synthesized 20 μm diameter polystyrene beads from Chemgenes, containing covalently bound oligos. mRNA was extracted from bulk cells as described in the “Bulk mRNA Extraction Experiments with Beads” section. RT and PCR was performed as described in Hughes *et al.* [18]. For all on-chip PCR experiments, BSA was added to a final concentration of 0.1 %. PCR product concentration was measured using the Qubit dsDNA High Sensitivity assay. Sizing experiments was performed on an Agilent TapeStation 4200 using the D5000 High Sensitivity ScreenTape assay.

5.3 Results and Discussion

Assessing Timescales for mRNA Binding and Extraction

To determine whether scRNA-seq could effectively be coupled with scI, we first assessed whether the rapid, in situ cell lysis and electrophoresis conditions required for immunoblotting could be made compatible with the long lysis and hybridization steps required for RNA capture and extraction [16–18]. In scI, rapid diffusion of protein from 40 - 100 μm thick hydrogels requires minimizing lysis and electrophoresis times. Typical lysis timescales range from 30 - 60 s and PAGE occurs in an additional 15 - 45 seconds [1, 3, 15, 23]. By contrast, for RNA sequencing workflows, hybridization times require tens of minutes [17, 18]. Thus, we wished to determine whether smaller lysis timescales could still effectively capture mRNA.

To assess whether scRNA-seq could be made compatible with shorter lysis and binding timescales, we first assessed estimates of transcript counts for previously-published bead-based scRNA-seq techniques. Techniques such as DropSeq and SeqWell have reported detection of 30 - 50,000 transcripts per single cell [16–18]. Assuming a median transcript length of 1000 - 2000 bp, and a combined cDNA and PCR reaction yield of 30% (a conservative estimate, given that some reverse transcriptases demonstrate reaction yields $> 100\%$ [24]), we expect to extract 0.083 - 0.276 pg of mRNA per single cell. However, other state-of-the-art dual measurement techniques such as INs-seq, which performs dual detection of protein

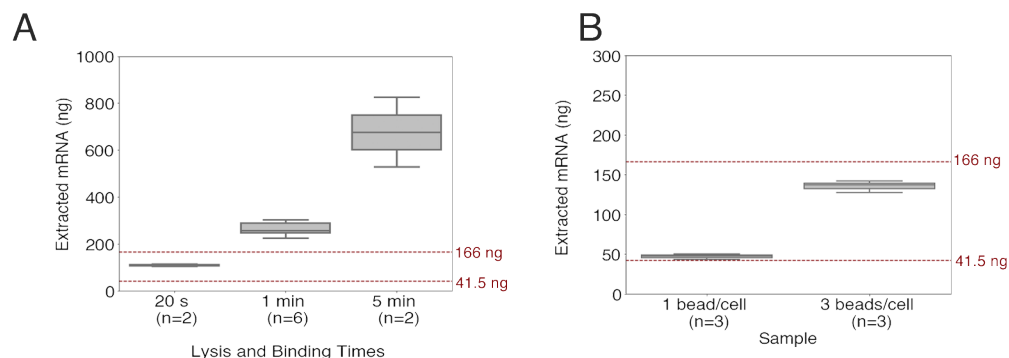


Figure 5.2: Varying lysis and binding conditions increases mRNA capture rates to beads. (A) 2- μm diameter streptavidin-coated magnetic beads (Dynabeads) shows an increase in the amount of mRNA extracted with increasing lysis and binding times. Even a 20 s lysis/binding step (on-par with scI lysis timescales) demonstrates an mRNA recovered that is above the estimated LLOD of 41.5 ng per 1 million cells. (B) With $\sim 20 \mu\text{m}$ streptavidin-coated polystyrene beads, increasing the bead count to 3 beads per cell can also increase mRNA capture rates. Dashed lines show the bounds for the estimated LLOD (between 41.5 ng to 166 ng of mRNA from 1 million cells.)

and mRNA from fixed cells, have demonstrated a 50-60% reduction in the number of unique transcripts detected per cell, when compared to fresh cells [12]. Therefore, an acceptable lower bound may be 0.0415 - 0.166 pg of mRNA per single cell, or a total of 41.5 to 166 ng of mRNA from 1 million cells.

To determine if the beads we wished to use meet the lower limit of detection, we assessed the RNA extraction efficiency from bulk cells with Dynabeads 2 μm -diameter streptavidin-coated magnetic beads, and $\sim 18 \mu\text{m}$ streptavidin-coated polystyrene beads. In each of these systems, we harvested 1 million cells from a breast cancer cell line (BT474) and captured mRNA using the protocol in the Dynabeads mRNA DIRECTTM Kit. For Dynabeads, we assessed mRNA extraction efficiency after 20 s, 1 min, and 5 min of combined lysis and binding times, where 5 min is the recommended lysis time specified in the kit. Our results demonstrate that even with a 20s extraction, magnetic beads can extract an average of 111 ng of mRNA from 1 million cells, which surpasses the estimated lower extraction limit of published dual measurement RNA sequencing assay (see Figure 5.2A). We next assessed the amount of mRNA extracted with polystyrene beads, using 1 minute lysis times. Our results demonstrate that with an extraction time of 1 minute, using 1 bead per cell leads to extraction of only 46.76 ng of mRNA from 1 million cells. However, by increasing the beads per cell to 3, we are able to further increase the amount of mRNA extracted to 135.2 ng from 1 million cells, a $3 \times$ increase from 1 bead per cell (see Figure 5.2B). In this manner, we show that we can increase the amount of mRNA extracted by increasing both the lysis time, and the number of beads utilized, to capture mRNA from cells.

Extending Lysis Times with PCTE Membranes

After determining lysis and binding time conditions to meet our LLOD for mRNA extraction, we wished to assess the compatibility of PCTE membranes with our standard scI assay. PCTE membranes, which have nominal pore sizes ranging from 10 nm - 20 μm , have been used in previous microwell-based single-cell RNA sequencing platforms in order to limit loss of transcripts from microwells, and in order to reduce cross-contamination of transcripts between adjacent microwells [17, 18]. However, while previous single-cell RNA sequencing platforms have used between 20 - 40 minute lysis and hybridization times for capturing transcripts, we wished to assess the feasibility of PCTE membranes to facilitate lysis times closer to 1 minute, in order to facilitate rapid *in situ* lysis, while still preventing excessive diffusion of proteins or transcripts outside of microwells.

Previous studies have assessed the permeability of PCTE membranes to proteins [25, 26]. The total open area of PCTE membranes is <1% for 10 nm pore-size membranes (with a pore density of 6×10^8 pores/cm²) and up to 16% for 1.0 μm pore-size membranes [27]. Since the thicknesses of these membranes range from 3 - 24 μm , the membrane can effectively be modeled as a rectangular sheet with cylindrical pores. Studies of diffusion of ~ 67 kDa proteins (e.g., bovine serum albumin) demonstrate that as pore sizes exceed 800 nm, the diffusion coefficients reach the free solution diffusion coefficients, whereas as membranes with pore sizes below 100 nm demonstrate an 80% decrease in diffusion coefficients [25]. However, these diffusion coefficients are also affected by aspects such as the pH of the solution, ionic strength, the protein's pI; thus, empirical observation of protein diffusion during lysis is still necessary [25].

To assess lysis timescales of cells while utilizing PCTE membranes, we seeded U251-tGFP cells into 7%T, 45 μm thick polyacrylamide hydrogel chips with 32 μm diameter microwells. Following a 10 minute settling and wash step, we hybridized PCTE membranes onto the polyacrylamide gels for 3 minutes with an Agilent Hybridization Chamber, as previously described [17, 18]. After hybridization, chips were placed onto a custom-built microscope chamber and imaged with an Olympus IX-70 microscope. For lysis, 15%T, 500 μm thick polyacrylamide gels soaked in lysis buffer and heated in a 75^oC water bath were coupled to the chip. We tested two different lysis buffers (DLB buffer and 1X RIPA buffer) and three different membranes (no seal, 10 nm pore-size membrane, and 1 μm pore-size membrane; although we aimed to test a 10 μm pore-size membrane, we found that the hybridization of these membranes to the chip was poor).

We hypothesized that the DLB buffer would have comparable, or faster, lysis timescales than 1X RIPA buffer, since the main reagents in 1X RIPA that lead to cell lysis are the SDS and sodium deoxycholate groups (see Table 5.1), and DLB buffer contains sodium lauryl sulfate, with higher molarity than the SDS found in 1X RIPA. By assessing timelapse images of tGFP fluorescence in microwells, we are able to determine the lysis timescales of cells under each of the different conditions (see Figure 5.3).

Our results demonstrate that without seals, both the DLB and 1X RIPA buffer have similar lysis timescales (see Figure 5.2A). By fitting the resulting lysis profiles the exponential

Table 5.1: Lysis Buffer Compositions

1X RIPA			Dynabeads Lysis/Binding Buffer		
Component	Percentage	Molarity (in 0.5 L)	Component	Percentage	Molarity (in 0.5 L)
SDS	0.5%	17.34 mM	Tris HCl	-	100 mM
Sodium Deoxycholate	0.25%	6.03 mM	LiCl	-	500 mM
Tris-Glycine	0.5X	-	LiDS	1%	36.72 mM
Triton-X 100	0.1%	-	DTT	-	5 mM
			EDTA	-	10 mM

distribution $y = A \exp(-\frac{t}{\tau})$, we are able to extract the rate parameter, τ of lysis. We find that a rate parameter, τ of 12.7 s and 17.6 s for the 1X RIPA, and DLB, distributions, respectively. Importantly, we notice that for 1X RIPA, 2τ (25.4s), which corresponds to the time required for decay of $> 85\%$ of fluorescence corresponds to the commonly-used lysis timescales (25 - 30s) for scI assays in previous studies with U251-tGFP cells [3, 23]. Furthermore, we find that with 10 nm pore-size membranes (Figure 5.2B), the lysis rate parameter is 45 s with DLB buffer. Interestingly, for 1X RIPA, we observe a poor fit with the exponential function ($\tau = 90.9$ s, with $R^2 = 0.84$ for the fit), and suspect that the seal is hindering cell lysis with 1X RIPA. By contrast, for 1 μm pore-size membranes (Figure 5.2C), the lysis rate parameter is $\tau = 19.6$ s with DLB buffer. We omitted the study of 1X RIPA with 1 μm pore sizes, as the lysis buffer we expect to use with the system would be DLB buffer, to ensure mRNA binding to beads prior to electrophoresis.

Since we wish to couple to 1 minute lysis times, we find that the 1 μm pore-size membrane with DLB have the closest matching characteristic timescale. From this study, we are able to demonstrate that by systematically modulating the PCTE membrane pore sizes, we are able to increase the characteristic lysis timescales of our system.

Assessing Lysis Compatibility with Single-cell Immunoblotting

After optimization of lysis times with the PCTE membrane, we wished to assess whether the combination of DLB and RIPA buffer would lead to adequate solubilization of key protein targets during scI. Importantly, protein solubilization is a function of several key factors, including reagent composition, temperature, lysis time, and others [3, 28, 29].

To assess compatibility of lysis buffers, we tested two different cell lines: a human breast cancer cell line (MCF7) transfected with GFP, and a mouse fibroblast cell line (NIH-3T3). Importantly, we anticipate that these two cell lines will be critical for species-mixing experiments that are used to demonstrate that new scRNA-seq techniques have low mRNA cross-contamination from adjacent cells. With species mixing experiments, we ideally aim to

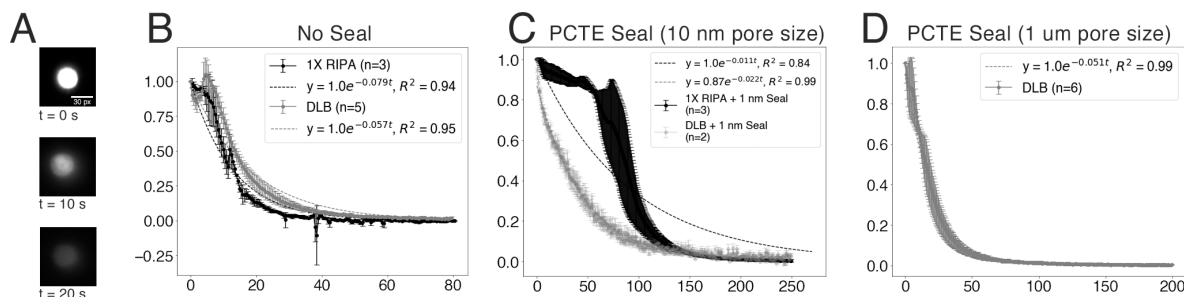


Figure 5.3: Varying PCTE Membrane Pore Sizes Changes Lysis Timescales. (A) Representative timelapse of U251-tGFP cell lysis with PCTE seal with $1 \mu\text{m}$ pore size. By tracking the tGFP fluorescence, we can determine the characteristic lysis timescale of the system. (B) With no PCTE seal, lysis with 1X RIPA and DLB buffer show similar lysis behaviours. By fitting to the exponential function $y = A \exp(-\frac{t}{\tau})$, we can extract rate parameters of $\tau = 12.7\text{s}$ for 1X RIPA and $\tau = 17.6\text{s}$ for DLB. With PCTE seals with 10 nm pore sizes, we observe characteristic timescales of $\tau = 45\text{s}$ for DLB and $\tau = 90.9\text{s}$ for 1X RIPA. However, given the poor fit of the exponential function to the 1X RIPA curve ($R^2 = 0.99$), we expect that the PCTE seal may be hindering lysis. (D) With a $1 \mu\text{m}$ pore size seal, we observe a rate parameter of $\tau = 19.6\text{s}$ with DLB.

detect either human or mouse transcripts (but not both) from each microwell. Concurrently, we aim to detect proteins specific to either the MCF7 or NIH-3T3 cell line, but not both, from each microwell. For MCF7-GFP cells, we can aim to use GFP as the unique protein that should not be found in NIH-3T3 cell lines. For NIH-3T3 cells, we can aim to detect the protein vimentin, which are highly expressed in epithelial cells, including fibroblasts, but are not found to be highly expressed in mesenchymal cells, including MCF7-GFP cells.

We first assessed the ability to detect GFP and vimentin in the two respective cell lines from regular scI conditions, and found that utilization of gel lids soaked in 2X RIPA-like buffer + 8M urea with 20 - 25 s lysis times, and 15 s electrophoresis conditions were sufficient to detect GFP in MCF7-GFP cell lines, and vimentin in NIH-3T3 cell lines (see Figure 5.4A). For MCF7-GFP cells, we detected 119 separation lanes with GFP protein bands that surpassed a signal-to-noise ratio (SNR) ≥ 3 . For NIH-3T3 cells, we detected 14 separation lanes with vimentin protein bands that surpassed an $\text{SNR} \geq 3$. While there were some separation lanes for MCF7-GFP cells that demonstrated vimentin expression, none of these lanes had protein bands with $\text{SNR} \geq 3$. From this experiment, we conclude that vimentin is an adequate marker for NIH-3T3, that is not highly expressed in MCF7-GFP cells. Distributions of expression levels for GFP and vimentin can be found in Figure 5.4B.

Next, we assessed whether lysis conditions that were compatible with mRNA extraction would also be compatible with scI. Specifically, we assessed whether a buffer exchange protocol, where cells would first be lysed with DLB buffer, and then electrophoresed with 2X RIPA-like buffer + 8M Urea would be sufficient to solubilize our proteins of interest. Buffer

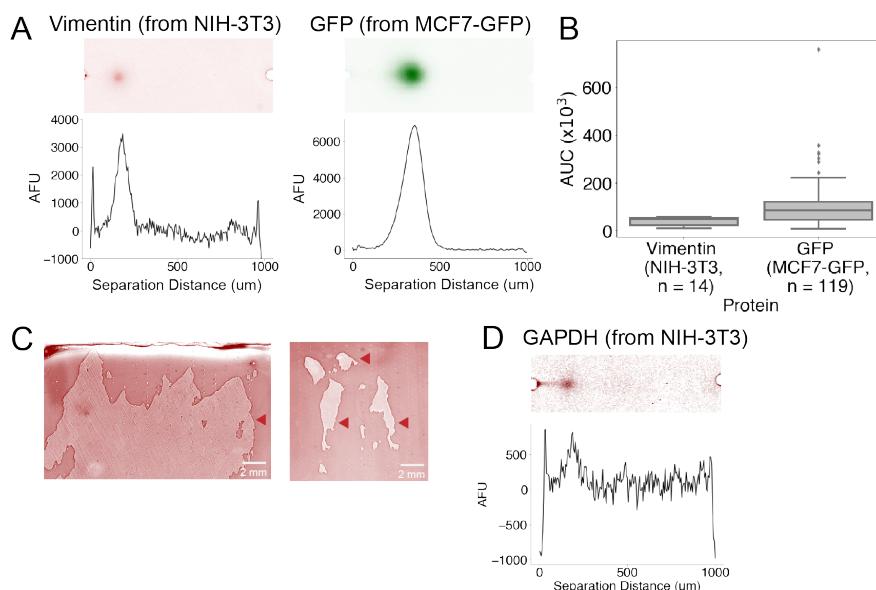


Figure 5.4: Lysis Buffer Exchange Between DLB and 2X RIPA + 8M Urea Facilitates Protein Solubilization. (A) By utilizing 2X RIPA + 8M Urea, we are able to detect vimentin from NIH-3T3 cell lines and GFP from MCF7-GFP cell lines. (B) Protein quantification of Vimentin ($n = 14$, from NIH-3T cells) and GFP ($n = 119$, from MCF7-GFP cells). (C) Use of PCTE seals during the full scI workflow leads to tearing of the hydrogel (red arrows), which suggests that for future work, the PCTE seal should be removed prior to the photocapture step. (D) 45 s lysis with DLB, followed by 20 s electrophoresis with 2X RIPA + 8M Urea demonstrates adequate injection and electrophoresis of vimentin. However, the presence of the PCTE seal confers additional background noise to the hydrogel.

exchange protocols have previously been used to tune electrophoresis run conditions, including reducing joule heating during electrophoresis run time [23]. To test the compatibility of lysis buffers, we performed scI of NIH-3T3 cells in 7%T, 32 μm diameter microwells. Given the optimal lysis time of 40 s using 10 μm PCTE membranes, we opted to use a 40 s lysis time, with 20 s electrophoresis conditions, with 10 μm PCTE seals. However, we note that due to the additional handling steps required in the buffer exchange, the gels are effectively still lysed for an additional 20 s (for a total of 1 minute) prior to PAGE separation.

Our results demonstrate that use of PCTE membranes with the full scI workflow, including UV-assisted photocapture, results in tearing of the hydrogel upon removal (see Figure 5.4C). We hypothesize that the benzophenone moieties in the PA gel are abstracting hydrogel atoms on the polycarbonate, leading to photocapture of the membrane to the hydrogel. However, we find that some gels have less tearing than others (see Figure 5.4C, right-hand side panel). Furthermore, in gels with minimal tearing, we nevertheless see solubilization of vimentin in many parts of the gel (see Figure 5.4D). Analysis through the Gaussian fitting

pipeline only identified 3 vimentin bands with an $\text{SNR} \geq 3.0$, which we attribute to the increased noise present in the gel due to the PCTE seal. We hypothesize that by reducing tearing of the gel (i.e., by removing PCTE membrane from the hydrogel prior to photocapture) and by utilizing additional segmentation efforts, we may be able to increase the amount of detectable vimentin bands.

From this experiment, we conclude that initial use of DLB buffer, followed by buffer exchange with 2X RIPA-like buffer + 8M urea, demonstrates promise in adequately solubilizing protein targets. For next steps, we aim to (1) remove the PCTE membrane from the hydrogel prior to photocapture, and (2) use segmentation to see if we can increase recovery of protein bands with $\text{SNR} \geq 3$.

Optimizing on-chip reverse transcription and PCR

We next assessed how effectively we could perform whole transcriptome amplification (WTA) from mRNA captured by our polystyrene beads. Specifically, optimizing the efficacy of RT and PCR is critical for ensuring that we have sufficient volumes of transcripts for downstream sequencing. We began by initially replicating the RT and PCR protocols described in the literature for other bead-based scRNA-seq assays [16–18]. In particular, techniques such as DropSeq and SeqWell are able to perform RT and PCR for up to 90,000 beads in one run. Thus, for our first experiment, we extracted 90,000/800,000 beads from a bulk RNA extraction experiment from 800,000 cells (approximating 1 cell per bead), and performed RT, ExoI digestion (to remove oligonucleotides on beads that were not hybridized to any mRNA [16, 17]), second-strand synthesis (which has been demonstrated to improve WTA [18]), and PCR on the subset of 90,000 beads.

From one replicate, we were able to collect 17.7 ng of mRNA from 800,000 cells. Despite starting with 90,000 beads at the beginning of RT, we noticed 50% bead loss at the end of second strand synthesis, and estimated that 39,000 beads remained. After performing PCR with these beads, we used 33% of the sample (a pool of 6 PCR tubes from a total of 18, as recommended by Hughes *et al* [18]) and performed ampure purification at a ratio of 0.6 \times . Across two replicates, we measured 228 ± 4.24 ng of DNA. Furthermore, analysis of the samples on an Agilent TapeStation demonstrated a smooth distribution from 400 - 2500 bp, in accordance with published RNA sequencing protocols (see Figure 5.5B) [16–18].

With tube RT and PCR providing a baseline comparison for successful WTA, we next assessed the feasibility of *in situ/on-chip* RT and PCR. A critical challenge with performing *on chip* WTA is that the PCR step requires high temperature cycling conditions (ranging from 95 - 98C) [17], which leads to rapid evaporation of fluid from open microarrays. Previous work with *in situ* PCR has utilized approaches such as sealing open microfluidic chips or glass slides with mineral oil, acrylic, coverslips, and other types of adhesives to prevent evaporation [6, 30, 31]. In particular, Frame-Seal Chambers have had particular success in creating seals over tissue slices affixed onto glass slides, preventing evaporation of PCR mix during cycling [30] (see Figure 5.5A).

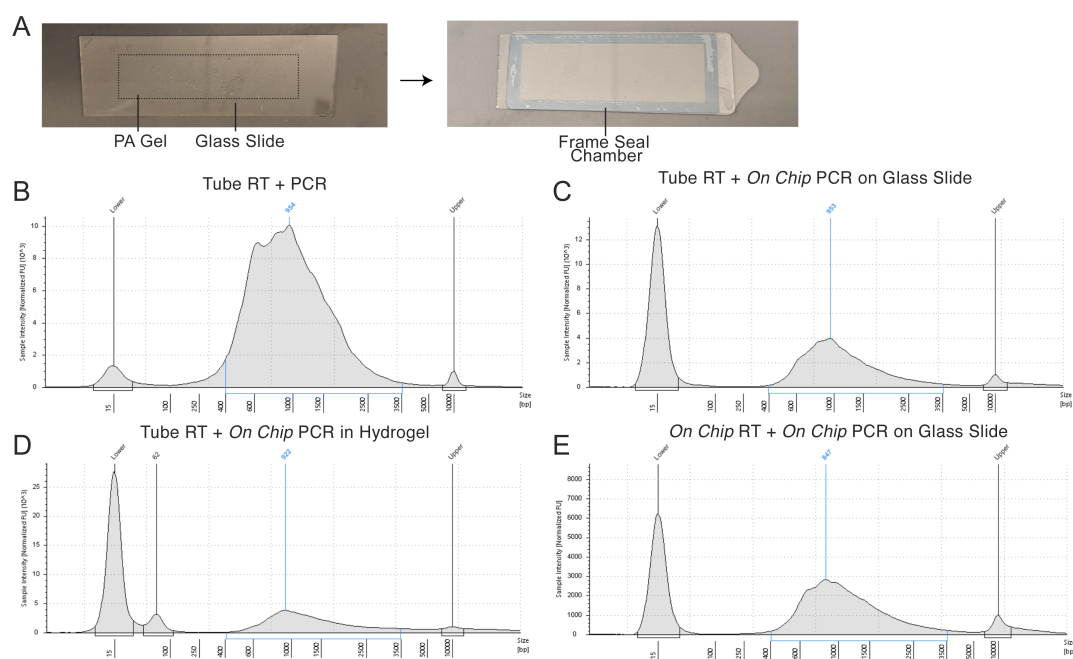


Figure 5.5: WTA Size Distributions Demonstrate Successful *In Situ* RT and PCR. (A) Example of a Frame-Seal Chamber affixed onto a scI chip. Hydrogels that are smaller than the dimension of the Frame-Seal Chamber (19 x 60 mm). The Frame-Seal Chamber consists of a rectangular adhesive, into which buffer can be loaded. A polyester cover is affixed on top to create the seal. (B) A representative electropherogram of PCR product from in-tube RT and PCR demonstrates a smooth size distribution of mRNA from 400 bp to 3500 bp. (C) *In Situ* PCR performed on a glass slide with 2000 beads once again shows a smooth distribution of mRNA from 400 bp to 3500 bp. (D) PCR performed on a scI chip shows a smooth distribution from 600 bp to 3500 bp. However, the long tail past 3500 bp and the presence of an attenuated upper marker (at 10,000 bp) may be indicative of incomplete cleanup of ampure beads. (E) PCR product recovered from a run where both RT, ExoI digestion, and PCR were performed “*in situ*”, on a glass slide. Once again, we see a smooth mRNA size distribution from 400 bp to 3500 bp.

We first assessed the suitability of Frame-Seal Chambers for PCR using beads that were (1) pipetted directly into a Frame-Seal Chamber affixed onto a glass slide, and (2) dispersed over a scI chip. Unlike regular PCR, where we can cycle approximately 2000 beads in 50 uL of PCR mix, Frame-Seal Chambers require at least 300 uL of volume. Thus, we performed PCR on 2000 beads in 300 uL of PCR mix in the Frame-Seal Chamber, using a custom-built thermocycler. With one replicate, we recovered 43.6 ng of PCR product. Compared to tube PCR, we attribute the 80% loss in product due to the fact that (1) we have an 83% decrease in total bead content for slide PCR compared to tube PCR, for which we assessed PCR product from a 12,000 bead reaction, and (2) with slide PCR, we are only able to recover ~200 of the 300 uL initially loaded into the Frame-Seal Chamber. In this manner, we can see that the product recovery from Frame-Seal PCR is slightly higher than what we would have expected, when accounting for the various losses in this process. Furthermore, sizing analysis once again demonstrates a smooth size distribution from 400 bp to 2500 bp, though with slightly lower concentrations, due to the fact that this product was at a concentration of 1.09 ng/uL (see Figure 5.5C).

For Frame-Seal PCR with a scI chip, we deposited 150 uL of bead suspension at a concentration of 200 beads/uL and allowed beads to settle into microwells via gravity sedimentation for 10 minutes. After settling, excess beads were washed away. Observation under brightfield suggested that 50% of the 1250, 45-um diameter microwells in the chip had 3 - 4 beads in each microwell, in addition to many beads adsorbing onto the surface of the PA gel. Overall, we estimate that the chip had between 2000 - 5000 beads containing cDNA. Following Frame-Seal PCR with 300 uL of PCR mix, we were able to recover a total of 21.2 ng of PCR product. Unfortunately, with hydrogel-based PCR, we were only able to recover 100 of the 300 uL of PCR mix loaded into the Frame-Seal Chamber, as we hypothesize that some amount of fluid is also responsible for hydrating the hydrogel. In future work, we aim to perform some rounds of washing of the hydrogel with mild surfactant solution (Tris-EDTA + 1% Tween 20 (TE-TW)) in order to recover more PCR product. Sizing analysis once again showed a smooth sizing distribution between 400 bp and 2500 bp, but with a longer right tail, demonstrating that we may not have completely removed Ampure beads following purification (see Figure 5.5D).

Finally, we assessed the efficacy of a full RT and PCR run *in situ*, wherein we began by extracting mRNA from cells in bulk (1 bead per cell), and performed RT and ExoI digestion on a glass slide for approximately 100,000 beads. For both the RT and ExoI steps, incubation was performed in an incubator, with the glass slide taped to a rotor, in order to evenly disperse the viscous RT and ExoI mix found in both reactions. We elected not to perform second strand synthesis for this first prototyping run, on account of the fact that second-strand synthesis steps involve a harsh base wash (a five minute rinse in 0.1M NaOH), which may negatively impact protein quantification in hydrogels. Instead, we performed PCR directly after ExoI digestion using 1000 beads. Importantly, during product recovery, we rinsed the gel with TE-TW and were able to recover an additional 100 uL of PCR product. Furthermore, in this step, we increased the amount of PCR cycles to a total of 18 cycles. From this process, we were able to recover a total of 81.2 ng of PCR product, which is a 2

× improvement of our previous PCR run. While the 2× improvement could be attributed to the additional PCR cycles, we estimate that we used half as many beads as the initial *in situ* PCR run (1000 in the full *in situ* run, compared to 2000 in the PCR-only *in situ* run). Once again, sizing analysis demonstrate a smooth distribution of amplified mRNA from 400 bp to 3000 bp (see Figure 5.5E).

Our results suggest that *in situ* RT and PCR holds promise as one way of amplifying cDNA from beads. Our next steps would include continuing this work in-gel and assessing whether a full single-cell RNA sequencing run can be performed in a hydrogel, before combining this with scI to produce a full dual-mode run.

5.4 Conclusion and Next Steps

In this study, we have laid the groundwork for a tandem scRNA-seq and proteoform measurement assay. We first demonstrated that by adjusting the lysis and binding timescales, and cell-to-bead ratios, we can tune the efficacy of mRNA capture to oligo-functionalized beads. We next demonstrated that by tuning the pore size of PCTE membranes, we can change the lysis timescales for cells in PAG microwells. Furthermore, we demonstrated that solubilization and electrophoresis of key proteins (vimentin) can occur during a buffer exchange step where cells are first lysed with DLB, and where subsequent electrophoresis occurs with 2X RIPA + Urea. Finally, we have demonstrated that by using Frame-Seal Chambers, we are able to perform *in situ* RT and PCR on glass slides with oligo-functionalized beads.

For next steps, we aim to test the efficacy of performing a full scRNA-seq run on a scI chip, and finally, evaluating the efficacy of a full dual-mode scRNA-seq and scI run. We anticipate that a dual-mode run will require additional optimization to effectively solubilize protein targets, while ensuring sufficient mRNA capture to beads; nevertheless, our initial experiments suggest that this optimization is possible. Further optimization may also be needed to ensure we can accurately trace transcript identities back to the microwell of origin, which we currently anticipate doing with the use of coordinate oligos [19]. Finally, integration of the data extracted from the two measurement modalities highlighted in this study (proteoform measurements and RNA sequencing) will require further investigation. While studies relating to integrated single-cell data analysis is becoming increasingly common [32], we anticipate that there will nevertheless be many open questions relating to the technical variance observed in both scRNA-seq and scI assays [7, 33, 34]

We believe our preliminary studies in this area has laid the groundwork for future dual single-cell immunoblotting and sequencing studies, and anticipate that results of several of the investigations in this chapter can also be applied to other potential dual-mode assays, including dual single-cell immunoblotting and DNA sequencing assays. Furthermore, we believe the optimization of *in situ* RT and PCR will be broadly applicable to the development of sequencing workflows in open microfluidic systems. Looking forward, we envision that single-cell multimodal assays for tandem measurements involving proteoforms and other biomolecules will provide greater insight into the relationship between proteoforms and cell

state and cell phenotype, which may further our understanding of key biological processes such as cell differentiation, development, and cancer progression.

Bibliography

1. Hughes, A. J. *et al.* Single-cell western blotting. *Nature methods* **11**, 749–55. ISSN: 1548-7105. arXiv: NIHMS150003. <http://www.ncbi.nlm.nih.gov/pubmed/24880876> (2014).
2. Tentori, A. M., Yamauchi, K. A. & Herr, A. E. Detection of Isoforms Differing by a Single Charge Unit in Individual Cells. *Angewandte Chemie*, 12431–12435 (2016).
3. Kang, C.-c. *et al.* Single cell resolution western blotting. *Nature Protocols* **11**, 1508–1530. ISSN: 1754-2189. <http://dx.doi.org/10.1038/nprot.2016.089> (2016).
4. Raj, B. & Blencowe, B. J. Alternative Splicing in the Mammalian Nervous System: Recent Insights into Mechanisms and Functional Roles. *Neuron* **87**, 14–27. ISSN: 0896-6273. <http://www.cell.com/article/S0896627315004110/fulltext><http://www.cell.com/article/S0896627315004110/abstract>[https://www.cell.com/neuron/abstract/S0896-6273\(15\)00411-0](https://www.cell.com/neuron/abstract/S0896-6273(15)00411-0) (2015).
5. Song, Y. *et al.* Single-Cell Alternative Splicing Analysis with Expedition Reveals Splicing Dynamics during Neuron Differentiation. *Molecular Cell* **67**, 148–161.e5. ISSN: 1097-2765 (2017).
6. Yap, K. & Makeyev, E. V. Functional impact of splice isoform diversity in individual cells. *Biochemical Society Transactions* **44**, 1079–1085. ISSN: 0300-5127 (2016).
7. Stuart, T. & Satija, R. Integrative single-cell analysis. *Nature Reviews Genetics* **20**, 257–272 (2019).
8. Ma, A. *et al.* Integrative Methods and Practical Challenges for Single-Cell Multi-omics. *Trends in Biotechnology* **38**, 1007–1022 (2020).
9. Stoeckius, M. *et al.* Simultaneous epitope and transcriptome measurement in single cells. *Nature Methods* **14**, 865–868 (2017).
10. Peterson, V. M. *et al.* Multiplexed quantification of proteins and transcripts in single cells. *Nature Biotechnology* **35**, 936–939 (2017).
11. Mimitou, E. P. *et al.* Multiplexed detection of proteins, transcriptomes, clonotypes and CRISPR perturbations in single cells. *Nature Methods* **16**, 409–412. ISSN: 1548-7105. <https://www.nature.com/articles/s41592-019-0392-0> (2019).

12. Y, K. *et al.* Coupled scRNA-Seq and Intracellular Protein Activity Reveal an Immunosuppressive Role of TREM2 in Cancer. *Cell* **182**, 872–885.e19. ISSN: 1097-4172. <https://pubmed.ncbi.nlm.nih.gov/32783915/> (2020).
13. Rosàs-Canyelles, E *et al.* Multimodal detection of protein isoforms and nucleic acids from mouse pre-implantation embryos. *Nature Protocols*, NP-PI200463 (2020).
14. Rosàs-Canyelles, E. *et al.* Assessing heterogeneity among single embryos and single blastomeres using open microfluidic design. *Science Advances* **6**. ISSN: 23752548 (2020).
15. Rosàs-Canyelles, E. *et al.* Multimodal detection of protein isoforms and nucleic acids from low starting cell numbers. *Lab on a Chip* **21**, 2427–2436. ISSN: 1473-0189. <https://pubs.rsc.org/en/content/articlehtml/2021/lc/d1lc00073j><https://pubs.rsc.org/en/content/articlelanding/2021/lc/d1lc00073j> (2021).
16. Macosko, E. Z. *et al.* Highly parallel genome-wide expression profiling of individual cells using nanoliter droplets. *Cell* **161**, 1202–1214. ISSN: 10974172. <http://dx.doi.org/10.1016/j.cell.2015.05.002> (2015).
17. Gierahn, T. M. *et al.* Seq-Well: portable, low-cost RNA sequencing of single cells at high throughput. *Nature Methods* 2017 14:4 **14**, 395–398. ISSN: 1548-7105. <https://www.nature.com/articles/nmeth.4179> (2017).
18. Hughes, T. K. *et al.* Second-Strand Synthesis-Based Massively Parallel scRNA-Seq Reveals Cellular States and Molecular Features of Human Inflammatory Skin Pathologies. *Immunity* **53**, 878–894.e7. ISSN: 1074-7613 (2020).
19. Zhang, J. Q. *et al.* Linked optical and gene expression profiling of single cells at high-throughput. *Genome Biology* **21**. <https://doi.org/10.1186/s13059-020-01958-9> (Feb. 2020).
20. Gayoso, A. *et al.* Joint probabilistic modeling of paired transcriptome and proteome measurements in single cells. ISSN: 26928205 (2020).
21. Lee, J., Hyeon, D. Y. & Hwang, D. Single-cell multiomics: technologies and data analysis methods. *Experimental & Molecular Medicine* **52**, 1428–1442. <https://doi.org/10.1038/s12276-020-0420-2> (Sept. 2020).
22. Yamauchi, K. A. & Herr, A. E. Subcellular western blotting of single cells. *Microsystems & Nanoengineering* **3**, 16079. ISSN: 2055-7434. <http://www.nature.com/articles/micronano201679> (2017).
23. Vlassakis, J. & Herr, A. E. Joule Heating-Induced Dispersion in Open Microfluidic Electrophoretic Cytometry. *Analytical Chemistry* **89**, 12787–12796. ISSN: 15206882 (2017).
24. Zucha, D. *et al.* Performance Comparison of Reverse Transcriptases for Single-Cell Studies. *Clinical Chemistry* **66**, 217–228. ISSN: 0009-9147. <https://academic.oup.com/clinchem/article/66/1/217/5688842> (2020).

25. Stroeve, P. *et al.* Protein diffusion through charged nanopores with different radii at low ionic strength. *Phys. Chem. Chem. Phys.* **16**, 21570–21576. <https://doi.org/10.1039/c4cp03198a> (2014).
26. Ileri, N. *et al.* Molecular transport of proteins through nanoporous membranes fabricated by interferometric lithography. *Phys. Chem. Chem. Phys.* **15**, 965–971. <https://doi.org/10.1039/c2cp43400h> (2013).
27. Sterlitech. *Polycarbonate Track Etch (PCTE) Membrane Filters* tech. rep. (). https://www.sterlitech.com/media/wysiwyg/pdfs/Sterlitech_Catalog2016_PCTE_.pdf.
28. Rabilloud, T. Solubilization of proteins for electrophoretic analyses. *Electrophoresis* **17**, 813–829. ISSN: 1522-2683. <https://analyticalsciencejournals.onlinelibrary.wiley.com/doi/full/10.1002/elps.1150170503> (1996).
29. D, L. Detergents: an overview. *Methods in enzymology* **463**, 603–617. ISSN: 1557-7988. <https://pubmed.ncbi.nlm.nih.gov/19892194/> (2009).
30. Bagasra, O. Protocols for the in situ PCR-amplification and detection of mRNA and DNA sequences. *Nature Protocols 2007 2:11* **2**, 2782–2795. ISSN: 1750-2799. <https://www.nature.com/articles/nprot.2007.395> (2007).
31. Wang, Y., Southard, K. M. & Zeng, Y. Digital PCR Using Micropatterned Superporous Absorbent Array Chips. *The Analyst* **141**, 3821 (2016).
32. Gayoso, A. *et al.* Joint probabilistic modeling of single-cell multi-omic data with totalVI. *Nature Methods* **18**, 272–282. <https://doi.org/10.1038/s41592-020-01050-x> (Feb. 2021).
33. Sinkala, E. *et al.* Profiling protein expression in circulating tumour cells using microfluidic western blotting. *Nature Communications* (2017).
34. Geldert, A., Huang, H. & Herr, A. E. Probe-target hybridization depends on spatial uniformity of initial concentration condition across large-format chips. *Scientific Reports* **10**, 1–12. ISSN: 20452322. <http://dx.doi.org/10.1038/s41598-020-65563-3> (2020).

Chapter 6

Current Understanding of UV-C Decontamination of N95 Filtering Facepiece Respirators

Materials reproduced, with permission, from:

S. M. Grist, A. Geldert, A. Gopal, A. Su, H. B. Balch, A. E. Herr, and the N95DECON Consortium, “Current Understanding of Ultraviolet-C Decontamination of N95 Filtering Facepiece Respirators”, *Applied Biosafety*, 2021.

6.1 Background

The COVID-19 pandemic has led to severe shortages of single-use N95 filtering facepiece respirators (FFRs) worn by healthcare workers and first responders, and ultraviolet-C (UV-C) irradiation has been identified by the Centers for Disease Control and Prevention (CDC) as one of the most promising methods for N95 FFR decontamination under crisis-capacity conditions [1]. UV-C is already implemented for airborne pathogen inactivation and other applications in hospitals [2]; however, UV-C decontamination of N95 FFRs involves additional considerations. Access to consolidated information on N95 FFR decontamination approaches is essential to maintaining a robust response to COVID-19. In this review, we examine the current understanding in the peer-reviewed literature regarding the use of UV-C irradiation for N95 FFR treatment.

In 2006, the US National Academies outlined that effective decontamination of personal protective equipment (PPE) like the N95 FFR requires (1) inactivation of pathogens (e.g., the SARS-CoV-2 virus), (2) maintenance of both the fit and filtration efficiency of the N95 FFR, and (3) harmlessness to the user (e.g., no toxic residues, minimal risk of cross-contamination) [3]. Here, we review and summarize the ability of UV-C decontamination to meet these critical criteria, in order to help inform risk management decisions under crisis-capacity conditions.

UV-C fundamentals and mode of action

UV-C inactivates pathogens primarily by introducing crosslinks between adjacent nucleic acid residues, thus damaging DNA and RNA and hindering reproduction [4–7]. Decontamination is critically dependent on two factors: the wavelength applied and the dose (fluence).

First, energy must be applied at the appropriate ultraviolet (UV) wavelength (i.e., the germicidal UV-C region of the electromagnetic spectrum, with high efficacy near 260 nm [8]). UV sources emitting at wavelengths much beyond 260 nm, such as sunlight at the earth's surface (after UV-C has been absorbed by the earth's ozone layer [9]), tanning bed lamps, or other consumer products, have minimal or no germicidal efficacy [7]. UV light at 254 nm has $> 10\times$ higher germicidal efficacy as compared to UV light at 300 nm or longer wavelengths [10].

Second, sufficient UV-C dose (fluence) must be delivered to the pathogens [7]. Fluence (J/cm^2) is defined as the integrated radiant (UV-C) power incident upon an infinitesimally small surface during the exposure period [11]. The term 'UV-C dose' (J/cm^2) is widely used in the decontamination literature to denote UV-C fluence [11]. 'Fluence' is the technically accurate term to describe the UV-C energy incident on the N95 surface, whereas 'dose' refers to the fraction of incident energy absorbed at that surface. Nevertheless, to remain consistent with the cited literature and field, we use the term 'dose' in this review when describing measured UV-C energy incident at the N95 surface. The minimum dose required for pathogen inactivation depends on both the irradiation wavelength and the specific pathogen, with some pathogens (e.g. certain bacterial spores) requiring much higher UV-C doses for inactivation than others (e.g. enveloped, single-stranded RNA viruses [12]). A pathogen's 'action spectrum' describes relative inactivation efficacy as a function of wavelength, and action spectra typically have a peak near 260 nm (the maximum absorption of nucleic acids [13]). The minimum dose required for inactivation also depends upon the material on or in which pathogens are present (e.g., air, surfaces, and aqueous media) [7].

Because biological validation of inactivation is often impractical or impossible to integrate into each and every treatment cycle, UV-C dose serves as the critical physical link between viral inactivation evidence and efficacy of each exposure. Dose (J/cm^2) is the product of irradiance (W/cm^2) and exposure time (s), assuming constant irradiance [11]. Because UV-C irradiance is dependent on the distance and angle from the UV-C source [14], UV-C irradiance or dose (integrated irradiance) needs to be empirically measured at the precise location of the objects to be decontaminated, in the specific configuration used for UV-C treatment. These measurements must be performed with UV-C sensors (e.g. radiometers, dosimeters, or sensor strips) with sensitivity to the germicidal wavelengths output by the UV-C source, specificity to the germicidal wavelength range, and appropriate dynamic range (range of measurable irradiances or doses).

Threshold for acceptable levels of SARS-CoV-2 inactivation

The efficacy of N95 decontamination methods is typically evaluated by assessing the \log_{10} reduction in active pathogens on N95 FFRs. For example, a 3- \log_{10} reduction (subsequently referred to as “3-log reduction”) corresponds to 99.9% inactivation of the pathogen being studied compared to a positive control. Per FDA guidelines for N95 FFR decontamination Emergency Use Authorizations (EUAs), ≥ 3 -log reduction in non-enveloped viral activity is required to achieve the minimally-acceptable “Tier 3” level of bioburden reduction [15]. Therefore, in this review, we emphasize ≥ 3 -log reduction of SARS-COV-2 or its analogues, based on the minimally-acceptable log-reduction listed in the FDA EUA guidance and in accordance with previous studies of UV-C N95 FFR decontamination [16, 17]. However, it is important to note that UV-C dose required to achieve ≥ 3 -log reduction is pathogen-dependent [7]. Thus, the UV-C dose required to achieve ≥ 3 -log reduction of SARS-CoV-2 (an enveloped virus) may not necessarily yield ≥ 3 -log reduction of non-enveloped virus, bacteria, or other pathogens required for various levels of FDA EUA approval.

Safety considerations

UV-C light is hazardous to human health, and as a result, sufficient skin and eye protection must be worn to protect processing personnel. According to the American Conference of Governmental Industrial Hygienists (ACGIH), the exposure dose limit per person per day is 0.003 J/cm² for UV radiation in the 200 nm - 315 nm region of the electromagnetic spectrum [18]; this same 0.003 J/cm² dose limit was identified by Directive 2006/25/EC of the European Parliament and of the Council for all ultraviolet radiation (180-400 nm [19]). Similarly, the National Institute for Occupational Safety and Health (NIOSH) recommends a total permissible 8-hour dose of approximately 0.0046 J/cm² for 260 nm irradiation, for unprotected eyes or skin [20]. Given the high UV-C irradiances emitted by sources typically used for UV-C decontamination, an unprotected user risks exposure to this dose in seconds under accidental illumination [21, 22]. Thus, proper engineering controls must be established prior to using UV-C systems to ensure that all users are adequately protected before the UV-C light source is turned on, and full PPE must be worn for eye and skin protection. Furthermore, in addition to UV-C concerns, processing personnel should treat all respirators (including ones that have undergone UV-C treatment) as contaminated, and wear appropriate PPE to reduce exposure risk to potential pathogens from respirator handling [23].

Literature review process

In writing this review, we aimed to summarize the current evidence regarding UV-C treatment of N95 FFRs with respect to the critical criteria outlined by the US National Academies: (1) inactivation of pathogens (e.g., the SARS-CoV-2 virus), (2) maintenance of both the fit and filtration efficiency of the N95 FFR, and (3) harmlessness to the user (e.g., no toxic residues) [3]. We searched Pubmed, Google Scholar, Google, and library databases for key-

words like “UV-C”, “N95”, “filtering facepiece respirator”, “decontamination”, “UVGI”, and “mask” to identify relevant primary research articles. Studies that are not yet peer reviewed should be interpreted with particular caution, so we elected not to include academic or commercial studies posted to preprint servers in this review. We do, however, cite relevant hospital implementations and other work (e.g. federal guidance and summaries from professional societies) that do not normally go through peer review prior to public availability.

6.2 Summary of literature review

Potential for SARS-CoV-2 inactivation

Several studies have demonstrated UV-C viral reduction of influenza and non-SARS-CoV-2 coronaviruses on N95 FFRs [16, 17, 24, 25]. These viruses are hypothesized to be suitable SARS-CoV-2 analogues because they are also enveloped, single-stranded RNA viruses. A non-peer-reviewed report to the US Food and Drug Administration (FDA) by the contracting research laboratory American Research Associates (ARA) [17] found that UV-C treatment of 1.0 J/cm² at the surface of N95 FFR coupons from one FFR model yielded no detectable virus (≥ 3.95 -log reduction) for six influenza and coronavirus strains considered, including MERS-CoV and SARS-CoV. Even when viral inoculations were covered with artificial soiling agents (skin oil or saliva), N95 coupons yielded no detectable virus after UV-C treatment. Similar UV-C doses were effective for H5N1 and H1N1 in separate, peer-reviewed studies (see Table 6.1) [24, 26]. At a UV-C dose of 0.5 J/cm², the viable virus remaining on N95 FFR coupons was 2–3 log lower than on positive control coupons, but detectable, indicating a UV-C dose of 0.5 J/cm² may be insufficient for viral inactivation [17].

In considering different models of N95 FFRs, Heimbuch & Harnish also studied the efficacy of UV-C viral inactivation across 15 different models (intact FFRs rather than coupons) [17]. In 11 out of the 15 models tested, a UV-C dose of 1.0 J/cm² at the N95 surface was effective in inactivating H1N1 influenza by ≥ 3 -log. The same study found that UV-C treatment was effective for the elastic straps of only 4 of 15 models; thus, straps may require a secondary decontamination method. N95 FFR models with a hydrophilic facepiece were less effectively decontaminated with UV-C than hydrophobic models [17]. Similarly, related studies measured ≥ 3 log reduction in H1N1 viability on the facepieces of 12 of 15 tested models and on the elastic straps of 7 of 15 tested models [16].

In addition to the N95 FFR model, other factors may influence UV-C inactivation efficacy. High humidity decreases UV-C efficacy on generic surfaces [27] and on the surfaces of N95 FFRs [28], suggesting that a drying step prior to N95 FFR treatment could be beneficial. Soiling agents (including from saliva and mucus) have been found to reduce UV-C inactivation efficacy of MS2 bacteriophage from N95 FFRs [28]. The effect of soiling agents on UV-C treatment efficacy likely depends on the exact concentration and composition of the soiling agent, and/or how the soiling agent is applied (e.g., mixed in with pathogens

or applied on top of pathogen inoculation). In addition to fluids such as saliva and mucus [28], sunscreen or other types of cosmetics may further attenuate UV-C irradiation during treatment [29]. Attenuation may be dependent on the thickness and absorption coefficients of the applied materials [30].

Pathogen inoculation mode may also impact UV-C treatment efficacy: N95 FFRs inoculated with larger MS2 droplets (9-10 μm) generally had lower UV-C bioburden reduction efficiencies in response to a 3.6 J/cm^2 dose as compared to FFRs inoculated with smaller MS2 aerosols (1-2 μm) [28]. Given that studies use a variety of methods to apply pathogens on an N95 FFR (aerosols, droplets, and/or pipetted solution), the question of whether pathogen application method impacts UV-C treatment efficacy merits further study. It is also important to note that the impact of soiling agents and pathogen application method may differ depending on pathogen type, just as the minimally-acceptable UV-C dose depends on pathogen type (as described in the next section). For example, MS2 is commonly used as a surrogate virus in inactivation studies due to its high culturability [31], but as a non-enveloped virus, MS2 generally requires higher UV-C doses for inactivation as compared to enveloped viruses similar to SARS-CoV-2 (Table 6.1).

Together, the studies reported in the ssRNA enveloped virus section of Table 6.1 suggest a minimally-acceptable UV-C dose of approximately 1.0 J/cm^2 for 3-log inactivation of viruses similar to SARS-CoV-2 on N95 material. Research on UV-C inactivation of SARS-CoV-2 is ongoing. Smith *et al.* observed that 0.63 J/cm^2 of 254 nm UV-C light led to a substantial reduction of SARS-CoV-2 RNA infectivity in cell culture for only one out of three N95 models tested [32]. It should be noted that this RNA-based assessment of viral infectivity differs from the plaque or fifty percent tissue culture infectious dose (TCID₅₀) assays more commonly employed for viral inactivity measurements. It remains unclear whether UV-C would more fully decontaminate SARS-CoV-2 from multiple N95 models if a dose above the minimally-acceptable 1 J/cm^2 were applied, or if respirators were inoculated with a lower SARS-CoV-2 titer that more closely represents a realistic exposure expected for a healthcare worker. Ozog *et al.* also characterized SARS-CoV-2 inactivation at multiple locations on intact N95 FFR facepieces and straps exposed to 254-nm UV-C. The authors report that $\sim 1.5 \text{ J}/\text{cm}^2$ of 254-nm UV-C applied to both sides of the N95 yielded ≥ 3 -log inactivation of SARS-CoV-2 in all studied locations on the facepieces of 1 out of 5 N95 models and on the straps of 2 out of 5 N95 models studied [33]. However, measurement of ≥ 3 -log inactivation was not possible on many models, because the difference between the limit of detection of the TCID₅₀ assay used to assess viral activity and the viral activity on the control N95 not treated with UV-C was often < 3 -log. Additionally, Kohli *et al.* demonstrate (with a similar UV-C system) that the UV-C dose varies across the surface of the N95 FFR34; thus, as with many studies on decontamination of intact N95 respirators, the actual dose at each location studied may differ substantially from the 1.5 J/cm^2 nominal dose.

Other recent studies have investigated the impact of LED and pulsed UV sources on SARS-CoV-2 inactivation on N95s. One recent manuscript reports SARS-CoV-2 inactivation in one N95 FFR model after UV-C treatment using an LED source [34]. However, caution should be exercised in interpretation or adoption of the reported approach, as the reported

UV-C dose was calculated based on a single manufacturer-specified irradiance value, when irradiance may actually change over source lifetime due to slight changes in configuration and decay in LED output. As a result, even though the results suggest that UV-C LED sources could be promising, the study is difficult — perhaps even impossible — to accurately reproduce. Similarly, another recent manuscript reporting SARS-CoV-2 inactivation after UV treatment with a pulsed xenon source also shows significant viral inactivation (>4.79 -log); however, the dose associated with this level of inactivation is not reported [35]. These data underscore the importance of accurate measurement and reporting of wavelength and UV-C dose for reproducible viral inactivation protocols. An American Society for Testing and Materials (ASTM) standard for evaluating UV-C efficacy for inactivating influenza virus on textile surfaces like N95 FFRs has been developed [36]. In addition to describing appropriate experimental steps, the standard stresses the importance of accurate, rigorous UV-C dose measurements.

Efficacy of UV-C on inactivation of other pathogens

UV-C susceptibility of different pathogens in air, water, and on surfaces

The UV-C dose required to inactivate pathogens in air, water, and on surfaces is organism-dependent, due to organism-to-organism differences in nucleic acid structure and nucleotide content, as well as varying amounts of UV-absorbing proteins and other photoprotective components [12]. Higher UV-C doses are generally required to inactivate bacterial and fungal spores, as compared to viruses and vegetative bacteria [7]. Among viruses, $\sim 3x$ higher UV-C doses are required to inactivate viruses with double-stranded RNA or DNA on surfaces, as compared to single-stranded viruses; higher dose requirements in double-stranded viruses are attributable to more robust repair mechanisms, as the second strand can serve as a template for repair [27]. While enveloped viruses are generally more susceptible to inactivation by mechanical and chemical agents [37], it is unclear whether the UV-C susceptibility of enveloped and non-enveloped viruses differ. Blazquez *et al.* found that in water, enveloped viruses were inactivated with lower UV-C doses than non-enveloped viruses [38]. However, the mechanism for the observed difference between enveloped and non-enveloped virus susceptibility in water is not understood, nor is it clear whether the same pattern holds for viruses in air or on substrates.

UV-C susceptibility of different pathogens on N95 FFRs and textiles

UV-C irradiation has been shown to yield ≥ 3 -log reduction of several pathogens from N95 FFRs at higher doses than required on nonporous surfaces, due in part to reduced UV-C transmittance through the layers of the FFR material [39]. The minimum UV-C dose required to inactivate both enveloped and nonenveloped viruses on N95 FFRs is several hundred-fold higher than doses typically used for decontamination of similar pathogens on nonporous surfaces [12], in air, and in solution (Table 6.1), because UV-C light is attenuated

upon passing through the N95 FFR layers. UV-C irradiances that reach the internal N95 filtering media are ~3-400x lower than the irradiance at the FFR surface, depending on FFR model [39]. Additionally, due to this limited and model-dependent UV-C transmission through N95 FFRs [40], both sides of the FFR should be illuminated with the minimally acceptable UV-C dose, and this dose may not effectively decontaminate all layers of varying FFR models.

Different pathogens are also expected to have different UV-C susceptibility on N95 FFRs, although the study of UV-C inactivation of different pathogens on N95 FFRs is limited. MS2, a nonenveloped virus, has generally been reported to require higher UV-C doses to achieve 3-log reduction from N95 FFRs [39, 41] as compared to enveloped influenza and coronaviruses [16, 17]; however, it is unclear whether other differences in study design (e.g., FFR model and method of virus application to the FFR) also contribute to the difference in required UV-C dose. While UV-C has been demonstrated to inactivate several species of vegetative bacteria and bacterial spores on N95 FFRs and other textiles [42–47], 3-log reduction was not always demonstrated and it is unclear how many bacterial pathogens would be inactivated by the 1.0 J/cm² UV-C dose required for coronavirus inactivation on N95 FFRs. For example, UV-C inactivation of *C. difficile* on N95 FFRs has not been studied. However, much higher UV-C doses are required to inactivate *C. difficile* spores on surfaces (~0.17-0.63 J/cm²) [48] as compared to MS2 on surfaces (~0.006-0.010 J/cm²) [27]. It is unclear whether the same trend (higher UV-C doses required to inactivate *C. difficile* spores as compared to MS2 on surfaces) would hold true in the case where these organisms are on N95 FFRs. Additionally, *E. faecium* in polycotton swatches was inactivated to a lower degree (<1.97-log reduction) by UV-C [46] as compared to laundering (3- to 4-log reduction) [49]. While UV-C treatment is expected to significantly reduce the risk of contamination, not every pathogen present on an FFR may be decontaminated by UV-C; thus, healthcare personnel should continue to handle the respirator as if contaminated and reuse only their own FFR. Any UV-C treatment approach should be accompanied by an industrial hygiene workflow involving user training and sterile processing to minimize risk of cross-contamination [23].

Table 6.1: Efficacy of UV-C for inactivation of microorganisms

Author	Organism, soiling agent, & method of application	Material	UV-C Dose	Efficacy	Light Source
Influenza & coronavirus strains: ssRNA enveloped virus					
Ozog et al., 2020 [33]	SARS-CoV-2; 10 μ L drop pipetted on strap and multiple locations on N95 facepiece	5 N95 FFR models (3M 1860, 8210, 8511, 9211; Moldex 1511)	1.5 J/cm ²	\geq 3-log reduction for 1/5 FFR model facepieces and 2/5 FFR model straps	254-nm UV-C (Custom-manufactured by Daavlin; Byron, OH)
Fischer et al., 2020 [34]	SARS-CoV-2; 50 μ L pipetted on	N95 FFR (AOSafety N9504C)	Approx. 1.98 J/cm ² (estimated from manufacturer-specified irradiance)	Approx. 3-log reduction	LED high power UV germicidal lamp (260-285 nm; LEDi2)

Smith et al., 2020 [32]	Pooled SARS-CoV-2 clinical samples; 100 μ L pipetted on	N95 FFR (medical grade: 3M 1860, 3M 1870+; industrial grade: 3M 8511)	0.63 J/cm ²	Substantial reduction in infectivity (via SARS-CoV-2 RNA measurement) for only the 3M 1870+ FFR model	254-nm UV-C (General Electric 30W Germicidal T8 bulb)
Lore et al., 2012 [24]	H5N1 droplets	N95 FFR (3M 1860, 3M 1870)	1.8 J/cm ²	>4-log reduction	254-nm UV-C (Ultraviolet Products, Upland CA, USA)
Mills et al., 2018 [16]	H1N1. 1 μ L drops of suspension pipetted on. Artificial saliva or artificial skin oil were placed on top of dried virus solution to study the effects of soiling.	N95 FFR (15 models)	1.0 J/cm ²	\geq 3-log reduction for 12/15 FFR model facepieces and 7/15 FFR model straps for all soiling conditions	254-nm UV-C (Fresh-Aire UV; Jupiter FL)
Heimbuch & Harnish, 2019 - Option Task B [17]	Influenza strains (H1N1, H5N1, H7N9), MERS-CoV, SARS-CoV, all pipetted as 1 μ L drops and dried. Artificial saliva or artificial skin oil were placed on top of dried virus solution to study the effects of soiling.	N95 FFR (3M 1870)	1.0 J/cm ²	No detectable virus (\geq 3.95-log reduction) for all organisms for all soiling conditions	254-nm UV-C (Mineralight® XX-20S 20-W UV bench lamp)
Heimbuch & Harnish, 2019 - Base Task 4 [17]	H1N1, pipetted as 1 μ L drops and dried. Artificial saliva or artificial skin oil were placed on top of dried virus solution to study the effects of soiling.	N95 FFR (15 models)	1.0 J/cm ²	\geq 3-log reduction for 11/15 FFR models and 4/15 FFR straps for all soiling conditions	254-nm UV-C (Fresh-Aire UV; Jupiter FL)
Walker & Ko, 2007 [25]	Murine hepatitis virus (coronavirus)	Air	1.83 $\times 10^{-3}$ J/cm ²	3-log reduction* *estimated based measured viral susceptibility to UV-C in air	254-nm UV-C (Lumalier, Memphis, TN)
MS2: ssRNA nonenveloped virus					
Vo et al., 2009 [41]	MS2 droplets	N95 FFR (Willson N1105)	4.32 J/cm ²	3-log reduction	254-nm low-pressure mercury arc lamp (5.5 mg Hg; lamp type TUV 36TS 4P SE; lamp voltage 94 V; lamp wattage, 40 W.)
Fisher & Shaffer, 2011 [39]	MS2 aerosol	N95 FFR (6 models)	0.32-40 J/cm ² (equates to 0.1 J/cm ² at the internal filtering medium)	\geq 2.9-log reduction	254-nm UV-C (TUV 36T5 40 W, Philips, Somerset NJ)
Woo et al., 2012 [28]	MS2 droplets (9-10 μ m) and aerosol (1-2 μ m), in water, beef extract (BE), or artificial saliva (AS)	N95 FFR (3M 1870)	3.6 J/cm ²	Droplets: 4.8-, 2.7-, 2.5-log reduction in water, BE, AS Aerosols: 5.2-, 3.0-, 2.7-log reduction in water, BE, AS	254-nm UV-C (UVG-11, UV Products, Cambridge, UK)

Tseng & Li, 2007 [27]	MS2	Surfaces	$\sim 0.006-0.010$ J/cm ²	>3-log reduction	254-nm UV-C (TUV 8W/G8 T5, Philips Electronic Instruments, Eindhoven, The Netherlands)
Vegetative Bacteria & Bacterial Spores					
Lin et al., 2018 [45]	Bacillus subtilis spores, aerosolized	N95 FFR (3M 8210)	2.27 J/cm ² , 5.7 J/cm ²	2.27 J/cm ² → ~ 2.7 -log reduction 5.7 J/cm ² → No detectable spores	254-nm UV-C (UVGL-58, VUP LLC, Upland, CA)
Bentley et al., 2016 [42]	E. coli, P. aeruginosa, S. aureus (drug-sensitive and drug-resistant), S. pseudointermedius (drug-sensitive and drug-resistant). 1-2 mL suspension pipetted on.	Microfiber, polyester, and cotton fabric swatches	0.27 J/cm ²	>2.5-log reduction for all bacteria on all fabrics. No detectable bacteria in 20/24 conditions.	254-nm UV-C (American Ultraviolet Inc., Lebanon, IN)
Wallace et al., 2019 [48]	<i>C. difficile</i> spores (with and without tri-part soiling agent) MRSA and MS2 (with and without 5% FBS)	Glass & plastic	0.17-0.63 J/cm ²	<i>C. diff.</i> : mean 2.1-log reduction with soiling agent across all UV-C doses; mean 3.2-log reduction without soiling agent across upper 3 doses. MRSA: mean 2.9-log reduction with FBS, mean 3.4-log reduction without FBS MS2: mean 3.7-log reduction with FBS, mean 2.9-log reduction without FBS	254-nm UV-C (Lightbest Co., Ltd, Changzhou, China)
Vegetative Fungi					
Fu et al., 2020 [43]	5 Candida strains	Bed Sheets	0.075 J/cm ²	>3-log reduction in all strains	254-nm UV-C (Thermo Fisher Scientific, Waltham, MA)

Sunlight is not likely to be an effective decontamination approach for N95 FFRs

The CDC does not list sunlight as an appropriate method of N95 FFR decontamination [50]. UV-C radiation from sunlight is absorbed by the top layer of the atmosphere and negligible UV-C radiation reaches the surface of the earth [51]. The ultraviolet component of sunlight at the earth's surface consists of UV-A (320-400 nm) and UV-B (280-320 nm) radiation. UV-A radiation is considered non-germicidal, while UV-B radiation has germicidal effects which are much weaker than that of UV-C [7]. Theoretical calculations for the necessary

sunlight exposure time needed to achieve UV-B germicidal effects in US cities (equivalent to a 1.0 J/cm² UV-C dose) suggest timescales of 57 - 5000 days, depending on season and geographic location [10]. Furthermore, studies with simulated sunlight showed minimal to no effect in inactivating MS2 and human adenovirus on the surface of fresh produce [52].

UV-B radiation has some germicidal effects; studies of UV-B irradiation on MS2 bacteriophage and murine noroviruses (MNV) in aqueous suspension demonstrated a 4-log reduction with UV-B doses of 0.909 J/cm² and 0.367 J/cm², respectively [53]. To reach these doses, 0.34-4.2 hours of sunlight exposure would be required, assuming UV-B irradiance from sunlight of ~60-300 μW/cm² (though UV irradiance from sunlight varies significantly depending on geographic location, season, and time of day) [54]. For comparison, 4-log reduction of MS2 in phosphate buffered saline solution [55] required ~0.07 J/cm² of UV-C – over an order of magnitude lower. UV-C dose required for viral inactivation in N95 FFRs is several hundred-fold higher than for viral inactivation in water, air, or on hard nonporous surfaces (Table 6.1) [7]. Sunlight reaching the earth’s surface does not contain UV-C, but we would expect a similar trend, with orders of magnitude higher UV-B doses being required for viral inactivation on N95s as compared to in water/air/nonporous surfaces. Thus, many days of sunlight exposure would be required to achieve a sufficient virucidal UV dose on N95 FFRs, in agreement with theoretical estimates [10, 56].

There is no evidence in the peer reviewed literature of viral inactivation of SARS-CoV-2 on N95 FFRs by sunlight. Thus, extensive experimental verification and biological validation must be performed before considering sunlight as a decontamination method for N95 FFRs.

Integrity of N95 filtering facepiece respirators after UV-C treatment

Controlled laboratory studies have subjected 15 N95 FFR models to 10–20 donning/doffing cycles and UV-C treatment (1.0–1.2 J/cm² per cycle), then assessed: strap elasticity (with Imada force tester), particle penetration and breathing resistance (TSI 8130 automated filter tester to evaluate respirator function according to the CDC58), and fit factor (Static Advanced Headform StAH connected to TSI Portacount 8038 automated breathing machine, subjected to a 240-s respiration test, testing for a fit factor ≥ 100) [17]. Although donning and doffing yielded a statistically significant difference in fit factor for some models, minimal detrimental effects due to UV-C exposure specifically were observed for respirator fit, air flow resistance, or particle penetration from this dose (10 cycles, 1.0–1.2 J/cm² per cycle) of UV-C [17]. Similarly, another study found that doses of 1-10 J/cm² of UV-C light (either at 254 or 265 nm) did not significantly affect filtration efficiency, material properties, pressure drop, or tensile strength of two N95 FFR models [57]. Other evaluations corroborated acceptable FFR performance after low dose ultraviolet germicidal irradiation (UVGI) treatment [58], although Ozog *et al.* did report (in a Letter to the Editor) that certain N95 FFR models failed qualitative fit testing either after 1-2 cycles (1.5 J/cm² per side, per cycle) or prior to any UV-C exposure at all, highlighting the importance of verifying N95 FFR fit regularly

[59]. To approximate multiple decontamination cycles, application of 18.4 J/cm² (to the exterior convex surface) and 4.6 J/cm² (to the interior concave surface) 254-nm UV-C to three N95 respirator models was performed, and was found to significantly decrease fit factor, but fit factors remained above the acceptable threshold of 100 [32]. At 10²–10³ higher UV-C doses (120–950 J/cm²), a substantial effect (>90% in some cases, but highly variable across N95 FFR models) on respirator material breaking strength was observed [60]. As variation in response to UV-C is to be expected from different N95 FFR models, the respirator must pass the ‘user seal check’ as recommended by the CDC after decontamination to ensure respirator fit integrity is maintained [61].

As summarized in Table 6.2, the minimum 1.0 J/cm² UV-C dose necessary for SARS-CoV-2 analogue inactivation on N95 FFRs has been found to minimally impact N95 fit and filtration performance over 10-20 treatment cycles. Aside from the effect of UV-C itself, it is possible that repeated donning and doffing may cause FFR fit to reach unacceptable levels within a shorter number of cycles. One study found N95 FFR fit to decline with each donning and doffing without additional decontamination processes; for some N95 models, fit was found to fall below OSHA standards after 5 don/doff cycles, while others maintained fit for >15 don/doff cycles[64].

Table 6.2: Impact of UV-C on N95 FFR integrity

Author	FFR Mode	UV-C dose (J/cm ²)	Particle Penetration	Breathing Resistance (mmH ₂ O) (max = 25)	Respirator Material Damage	Strap Damage	Source
Heimbuch & Harnish, 2019 [17]	N95 FFRs (15 models)	1.0-1.2	0.18-3.29 (10 cycles) 0.12- 2.74 (20 cycles)	4.53-14.93	No observable effect from UV-C. Some fit degradation from donning/doffing.	No significant difference from UV-C alone. Some fit degradation from donning and doffing.	254-nm UV-C (Fresh-Aire UV, Jupiter, FL)
Lindsley et al., 2015 [60]	3M 1860 3M 9210 GE 1730 KC 46727	120-950 120-950 120-950 120-950	1-2.5% 1-2.5% 3-5% 3-5%	10-13 10-13 10 15-20	General decrease of strength 120 J/cm ² dose = 2 layers significantly impacted 950 J/cm ² = 10 layers significantly impacted	Statistically significant decrease in breaking strength for dose ≥ 590 J/cm ² (≥ 10% decrease of mean strength)	254-nm UV-C

Zhao et al., 2020 [57]	3M 1860, Moldex 1500	1.0-10	< 3% (no effect of UV-C)	No significant change after irradiation	No change in contact angle, no new peaks or decrease in peak height in FTIR spectra, no apparent change in material structure by electron or optical microscopy	No significant change after irradiation	254-nm and 265 nm
Smith et al., 2020 [32]	3M 1860, 1870+, and 8511	18.4 at exterior surface, 4.6 at interior surface	Significantly reduced "FIT score", but average "FIT score" remains acceptable at ≥ 100 (2-log particle reduction threshold).	Not studied	Not studied	Not studied	254-nm UV-C (General Electric 30W Germicidal T8 bulb)
Ozog et al., 2020 [59]	3M 1860, 9210, 8210; Cardinal Health N95 R/S; Moldex 1512	1.5 to each side of FFR	Passed saccharin solution aerosol qualitative fit test [62] for 20/25 cycles (3M 1860), 2/2 cycles (3M 9210), 1/2 cycles (3M 8210 and Cardinal Health N95 R/S), 2/3 cycles (Moldex 1512)	Not studied	Not studied	Not studied	254-nm UV-C (Daavlin Desktop UVC Germicidal Lamp)

US federal guidelines: CDC, FDA, OSHA

Due to a limited supply of N95 FFRs in this unprecedented COVID-19 pandemic, the CDC has provided guidance that healthcare workers can practice extended use or limited reuse of N95 FFRs [63]. In addition, the CDC has provided guidance to hospitals on methods for decontaminating N95 FFRs during a crisis [1]. Consistent with all N95 FFR treatments for reuse, UV-C is viewed as risk mitigation for extraordinary circumstances rather than complete decontamination [63].

At present, the US Occupational Health and Safety Administration (OSHA) states that cosmetics or other barriers not be present during regular respirator use [29]. EUAs that the FDA has granted for other methods of N95 FFR decontamination during the COVID-19 pandemic also stipulate that cosmetics not be present on respirators sent for decontamination [64]. After decontamination, the CDC recommends that a 'user seal check' is performed when the respirator is donned to ensure adequate seal [50]. A user seal check after every decontamination cycle is especially important because there is evidence that the fit factor of N95 respirators decreases with numerous don/doff cycles [65].

Other applications of UV-C for pathogen reduction

UV-C decontamination is also in broader use: per the recommendations of the CDC and the Healthcare Infection Control Practices Advisory Committee (HICPAC), UV-C light (254 nm peak) is widely used in US healthcare facilities for pathogen reduction in air [2], and UV-C has found extensive use in water treatment [8]. In some settings, UV-C is also used for surface decontamination [66]. NIOSH offers guidelines for applying upper-room UVGI to kill or inactivate airborne tuberculosis bacteria in hospitals [67].

Any new methods for UV-C treatment should be verified through an institution's internal review processes prior to implementation, which may include applying for an FDA EUA15 and referencing frequently updated CDC guidelines.

Implementation strategies

The University of Nebraska Medical Center (UNMC) published one of the first protocols [21] demonstrating implementation of UV-C treatment of N95s (including N95 FFR handling logistics and treatment), which has been the basis of additional research and discussion for UV-C treatment of N95 FFRs during the 2020 SARS-CoV-2 pandemic [22, 23]. The UNMC protocol exposes each side of N95 FFRs to 0.9–1.2 J/cm², depending on FFR position within the treatment field²¹. This UNMC Process Flow is a 51-step process defined by role (healthcare worker, courier, UVGI associate) and covers the safe handling (intake, transport, processing, return), labeling (UV-C-decontaminated N95 FFRs should be returned to their specific original user as the process is not expected to be sterilizing) [23], and ancillary PPE and hygiene required for the protocol. As with any decontamination strategy, an appropriate industrial hygiene workflow involving user training [68], sterile processing, and other critical considerations must be implemented to avoid cross-contamination or damage to the N95. The Association for Professionals in Infection Control and Epidemiology (APIC) has recently disseminated guidance for infection prevention workflows for UV-C treatment of N95 FFRs during the COVID-19 crisis, in collaboration with N95DECON²³. Additional implementation strategies are summarized in Table 6.3.

All but one surveyed minimum-dose data demonstrating active viral reduction on N95 FFRs (Table 6.1) used low-pressure mercury UV-C sources with peak emission at 254 nm. Because both pathogen inactivation and light transmittance (through materials like N95 layers) are wavelength-dependent [7], sources with different emission spectra (e.g., LED sources, medium-pressure mercury sources, or pulsed xenon sources) could also be effective for viral inactivation but will have different minimum doses for bioburden reduction or enveloped viral inactivation. Implementation of these sources must specifically assess the minimum dose through viral inactivation studies with accurate dose measurements. Both research and validation dose measurements for any sources must use appropriate, wavelength-matched detectors.

Validation of (1) UV-C viral inactivation and (2) subsequent N95 FFR reuse suitability (e.g., filtration efficiency, fit factor) is widely considered in the peer-reviewed literature and

Table 6.3: Published implementation strategies for UV-C N95 treatment

Authoring group	Implementation type	UV-C source type
University of Nebraska Medical Center [21]	Hospital protocol for room-scale N95 UV-C treatment with full processing workflow (with personnel roles)	254 nm UV-C (ClorDiSys Torch)
University of Chicago Medical Center [22]	Hospital protocol for room-scale N95 UV-C treatment with full processing workflow	254 nm UV-C (Surfacide Helios)
APIC [23]	Implementation guidance for infection prevention workflows for N95 UV-C treatment	N/A
Ontiveros, <i>et al.</i> 2020 [69]	Peer-reviewed study on characterization of a room-scale hospital UV-C treatment system for N95 processing	254 nm UV-C (Diversey MoonBeam3)
Purschke, <i>et al.</i> 2020 [70]	Peer-reviewed study on design and characterization of cabinet-based N95 UV-C treatment system targeted at lower-resource settings	254 nm UV-C
Baer, <i>et al.</i> 2020 [71]	Peer-reviewed ray-trace modeling workflow for UV-C N95 treatment chamber design	254 nm UV-C
Bentancor and Vidal, 2018 [72]	Peer-reviewed design of a room-scale UV-C treatment system (not designed for N95 UV-C treatment specifically)	254 nm UV-C

should be considered for all new processes [16, 17, 24, 65]. Both of these critical features are dependent on UV-C dose, as summarized in Tables 1 and 2. UV-C treatment design must exceed a value of 1.0 J/cm^2 for all surfaces of each N95 FFR and the delivered dose should ideally be verified with every UV-C cycle, but periodically at a minimum (e.g., daily, after a set number of cycles). Dose measurements should be performed with an accurately calibrated (e.g. traceable to standards such as those from the National Institute of Standards and Technology) UV-C-specific sensor to measure the irradiance or dose at each FFR position. Variation in irradiance is anticipated across the exposure area; the total exposure time should be chosen such that all N95 FFR surfaces are exposed to at least the minimally acceptable dose of 1.0 J/cm^2 .

As is true with any form of light, shadowing reduces the dose of light that a target

receives. Thus, shadows on the target N95 FFR(s) should be avoided by: (1) providing UV-C illumination to both sides of the FFR, and/or flipping the N95 FFRs mid-treatment to ensure all surfaces are exposed to the minimally-acceptable UV-C dose, (2) lining walls, ceiling, and other surfaces with UV-C-reflective materials to increase delivered UV-C dose [73], and (3) ensuring there are no obstructions or materials between the N95 FFRs and the UV-C source that could block the line-of-sight or attenuate the UV-C before reaching the N95. It is important to note that standard soda-lime and borosilicate glass block almost all UV-C light [74]. In addition to shadowing, it is important to note that irradiance depends on the distance from the source as well as the incident angle of UV-C light on the N95 surface by Lambert's Cosine Law [14]; as such, the complex 3D morphology of the N95 surface can impact dose delivered to various regions of the respirator and needs to be considered when designing UV-C treatments.

It is imperative to use caution and validate each source, as not all UV sources provide the required UV-C wavelength range, irradiance, or irradiance uniformity. Even more worrisome, there have been reports of UV sources falsely claiming to be germicidal, with emitted wavelength ranges not consistent with germicidal efficacy. In addition, UV-C sources emitting wavelengths below 210 nm can produce ozone [7], which is hazardous to human health. As a result, it is critical to measure the wavelength and irradiance of UV-C sources with sensors specific to UV-C to ensure sources emit radiation within the UV-C germicidal range (200-280 nm with peak efficacy at ~ 260 nm). Viral inactivation efficacy has been reported to be $\sim 10X$ lower at 300 nm (beyond UV-C range) compared to 254 nm [8, 56], highlighting the importance of using appropriate sources emitting in the UV-C range. The measured UV-C-specific irradiance values should then be used to calculate the time required to reach a minimum UV-C dose in excess of 1.0 J/cm^2 across all N95 FFR surfaces.

6.3 Summary and outstanding questions

Important points and open questions regarding UV-C treatment of N95 FFRs are summarized here:

1. Direct exposure to UV-C light is harmful to humans. Proper engineering controls must be established prior to using UV-C systems to ensure that all users are protected from the UV-C light source before the light is turned on [18, 20].
2. UV wavelengths of 175–210 nm can generate ozone, which is hazardous to human health. Some low pressure UV lamps and most medium pressure UV lamps emit some 185 nm UV and thus will generate ozone [7]; if there is the possibility of ozone generation, adequate ventilation should be confirmed within the working area to minimize ozone risk to operators. If possible, select UV-C sources with minimal or no ozone generation.

3. UV-C only inactivates viruses subjected to at least the minimum UV-C dose. There remain open questions about UV-C penetration into the materials of the various N95 FFR models used in healthcare, as the amount of penetration likely varies widely across N95 FFR models [39, 70]. Although the ARA report [17] and related peer-reviewed literature¹⁶ demonstrate >3 -log viral reduction (measured from fluid extraction from the N95 FFR materials as described in the ASTM standard for viral inactivation testing [36]), live virus could persist inside the N95 FFR after UV-C treatment. As such, UV-C and other deactivation approaches should be viewed as risk mitigation for extraordinary circumstances rather than complete decontamination. Additionally, shadowed or highly angled regions of the N95 may be exposed to lower-than-expected UV-C doses and thus pathogens in these locations may be less-effectively inactivated.
4. The configuration or orientation of UV-C light sources may generate shadows (as is the case for any type of light, not just UV-C), and the configuration of N95 FFRs should be designed to avoid or mitigate shadow generation on the FFR surface. For instance, UV-reflective materials may be used and/or N95 FFRs may be rotated and/or flipped to ensure that the adequate dose is applied across the entire surface area of the FFR (and this dose should be validated with a UV-C-specific sensor).
5. Reports have demonstrated residual virus on N95 FFR straps after UV-C exposure (likely due to the ability of N95 FFR attachment straps to twist and be shadowed from the UV-C light), suggesting a need for supplementary decontamination of the elastic straps [16, 17]. Mills *et al.* suggest wiping N95 FFR straps with a compatible disinfectant [16]. If this additional step is employed, extra caution should be used to avoid touching the N95 FFR facepiece as common disinfectant chemicals can degrade N95 FFR function [75].
6. Although ≥ 1.0 J/cm² dose of UV-C resulted in ≥ 3 -log reduction in viral activity of SARS-CoV-2 analogues, such an observation does not imply full decontamination of the N95 FFR, as the N95 may still be contaminated with other pathogens that might not be similarly susceptible to UV-C irradiation (Table 6.1).

6.4 Conclusions

UV-C N95 treatment protocols should be implemented only if there is a dire shortage of N95 FFRs and appropriate federal and institutional approvals. While no peer-reviewed reports directly describe the minimum dose for SARS-CoV-2 inactivation on N95 materials at the time of this review, estimates can be drawn from the extensive body of literature evidence for similar viruses. Accurate measurements of dose and wavelength in forthcoming SARS-CoV-2 inactivation studies would outline effective and reproducible protocols for this virus. Currently, the existing research suggests that, if implemented properly with validation of the delivered UV-C dose to the FFR, it is likely that UV-C applied at a minimum dose of

≥ 1.0 J/cm² inactivates SARS-CoV-2 on the outer layers of non-shadowed regions of N95s based on results from similar viruses [16, 17, 24]. As all but one of the dose measurements for viral inactivation reported here used 254 nm sources, there is an opportunity for future research to rigorously assess minimum doses required for viral inactivation with the diverse landscape of UV-C sources and matched detectors. UV-C has shown promise as an effective method for inactivation of viruses and bacterial spores on N95 respirator material; however, UV-C cannot inactivate pathogens that are not irradiated with the minimum dose. For that reason, UV-C may not effectively decontaminate inner layers of the FFR and an auxiliary method of decontamination is suggested for elastic straps.

We note that as of September 26, 2020, no EUA has been granted for UV-C decontamination of N95 FFRs. Because UV-C processes to inactivate SARS-CoV-2 on N95 FFRs are not expected to result in sterilization (killing of all microorganisms), N95 FFRs treated with UV-C should be returned to the same user to avoid user-to-user cross contamination. N95 FFR model-dependent viral inactivation efficacy has been reported. We stress that (i) after each round of irradiation, a user seal check should be performed, (ii) extended cycles of doffing and re-donning may affect FFR fit, and (iii) that the FFR should not be considered fully decontaminated after UV-C treatment, as there may be other pathogens contaminating the FFR whose activity may not be fully reduced by UV-C. Thus, UV-C treatment should be viewed as risk management rather than complete decontamination or sterilization. Healthcare personnel should continue to handle the respirator as if the PPE is contaminated and reuse only their own N95 FFR.

Bibliography

1. CDC. *Decontamination and Reuse of Filtering Facepiece Respirators* <https://www.cdc.gov/coronavirus/2019-ncov/hcp/ppe-strategy/decontamination-reuse-respirators.html>. Apr. 2020.
2. Schulster, L. M. *et al. Guidelines for environmental infection control in health-care facilities. Recommendations from CDC and the Healthcare Infection Control Practices Advisory Committee (HICPAC)* (American Society for Healthcare Engineering/American Hospital Association, Chicago IL, 2004).
3. Institute of Medicine, Board on Health Sciences Policy & Committee on the Development of Reusable Facemasks for Use During an Influenza Pandemic. *Reusability of Facemasks During an Influenza Pandemic: Facing the Flu* en. ISBN: 978-0-309-10182-0 (National Academies Press, Aug. 2006).
4. Anderson, J. G. *et al.* Inactivation of food-borne enteropathogenic bacteria and spoilage fungi using pulsed-light. *IEEE Trans. Plasma Sci. IEEE Nucl. Plasma Sci. Soc.* **28**, 83–88 (Feb. 2000).
5. Ito, A. & Ito, T. Absorption spectra of deoxyribose, ribosephosphate, ATP and DNA by direct transmission measurements in the vacuum-UV (150-190 nm) and far-UV (190-260 nm) regions using synchrotron radiation as a light source. *Photochem. Photobiol.* **44**, 235–236 (Sept. 1986).
6. Jay, J. M. *Modern Food Microbiology* 5th (Springer, Boston, MA, 1995).
7. Kowalski, W. *Ultraviolet Germicidal Irradiation Handbook: UVGI for Air and Surface Disinfection* en. ISBN: 978-3-642-01998-2 978-3-642-01999-9. <http://link.springer.com/10.1007/978-3-642-01999-9> (2020) (Springer Berlin Heidelberg, Berlin, Heidelberg, 2009).
8. EPA. *Ultraviolet Disinfection Guidance Manual for the Final Long Term 2 Enhanced Surface Water Treatment Rule* <https://nepis.epa.gov/Exe/ZyPDF.cgi?Dockey=600006T3.txt> (Nov. 2006).
9. EPA. *UV Radiation* Accessed: 2020-08-05. <https://www.epa.gov/sunsafety/uv-radiation-1>.
10. Sagripanti, J.-L. & Lytle, C. D. Inactivation of influenza virus by solar radiation. en. *Photochem. Photobiol.* **83**, 1278–1282 (Sept. 2007).

11. Bolton, J. R. & Linden, K. G. Standardization of Methods for Fluence (UV Dose) Determination in Bench-Scale UV Experiments. EN. *Journal of Environmental Engineering* **129**. Publisher: American Society of Civil Engineers, 209–215. ISSN: 0733-9372. <https://ascelibrary.org/doi/abs/10.1061/%28ASCE%290733-9372%282003%29129%3A3%28209%29> (2021) (Mar. 2003).
12. Malayeri, A. *et al.* Fluence (UV Dose) Required to Achieve Incremental Log Inactivation of Bacteria, Protozoa, Viruses and Algae. *IUVA News* **18**, 4–6 (Sept. 2016).
13. Pirnie, M. *et al.* *Ultraviolet disinfection guidance manual for the final long term 2 enhanced surface water treatment rule: EPA 815-R-06-007* (EPA, 2006).
14. Reifsnnyder, W. E. Radiation geometry in the measurement and interpretation of radiation balance. en. *Agricultural Meteorology* **4**, 255–265. ISSN: 0002-1571. <http://www.sciencedirect.com/science/article/pii/000215716790026X> (2020) (July 1967).
15. Center for Devices & Radiological Health. *Decontamination Bioburden Reduction Systems for Face Masks Respirators* Publication Title: U.S. Food and Drug Administration. <https://www.fda.gov/regulatory-information/search-fda-guidance-documents/recommendations-sponsors-requesting-euas-decontamination-and-bioburden-reduction-systems-face-masks> (2020).
16. Mills, D. *et al.* Ultraviolet germicidal irradiation of influenza-contaminated N95 filtering facepiece respirators. *Am. J. Infect. Control* **46**, e49–e55 (July 2018).
17. Heimbuch, B. & Harnish, D. *Research to Mitigate a Shortage of Respiratory Protection Devices During Public Health Emergencies* tech. rep. (Applied Research Associates, Sept. 2019).
18. *Product: Ultraviolet Radiation: TLV(R) Physical Agents 8th Edition Documentation: ACGIH* <https://www.acgih.org/forms/store/ProductFormPublic/ultraviolet-radiation-tlv-r-physical-agents-8th-edition-documentation> ().
19. *Directive 2006/25/EC - artificial optical radiation* <https://osha.europa.eu/en/legislation/directives/directive-2006-25-ec-of-the-european-parliament-and-of-the-council-of-5-april-2006> ().
20. *Criteria for a recommended standard... occupational exposure to ultraviolet radiation* <https://www.cdc.gov/niosh/docs/73-11009/default.html> (Oct. 2018).
21. Lowe, J. J. *et al.* *N95 Filtering Facepiece Respirator Ultraviolet Germicidal Irradiation (UVGI) Process for Decontamination and Reuse* tech. rep. (Nebraska Medicine, Apr. 2020).
22. Brickman J, Scott C, Courtad C, et al. *Optimization, Validation, and Implementation of a UV Disinfection Method for N95 Face Masks* <https://static1.squarespace.com/static/5e8126f89327941b9453eeef/t/5eacab4783c6b418d137baf3/1588374356749/UCMC+Surfacide+Mask+UVGI+Process+Validation+and+Process+v6.pdf>. Accessed: 2020-4-27.

23. APIC. *APIC and N95DECEN suggested guidance for infection prevention and workflow for UV-C decontamination of N95 FFRs during COVID-19* <https://www.n95decon.org/files/apic-uvc>. June 2020.
24. Lore, M. B. *et al.* Effectiveness of Three Decontamination Treatments against Influenza Virus Applied to Filtering Facepiece Respirators. en. *Ann. Occup. Hyg.* **56**, 92–101 (Jan. 2012).
25. Walker, C. M. & Ko, G. Effect of ultraviolet germicidal irradiation on viral aerosols. en. *Environ. Sci. Technol.* **41**, 5460–5465 (Aug. 2007).
26. Heimbuch, B. K. *et al.* A pandemic influenza preparedness study: use of energetic methods to decontaminate filtering facepiece respirators contaminated with H1N1 aerosols and droplets. eng. *Am. J. Infect. Control* **39**, e1–9 (Feb. 2011).
27. Tseng, C.-C. & Li, C.-S. Inactivation of Viruses on Surfaces by Ultraviolet Germicidal Irradiation. en. *J. Occup. Environ. Hyg.* **4**, 400–405 (Apr. 2007).
28. Woo, M.-H. *et al.* Effects of relative humidity and spraying medium on UV decontamination of filters loaded with viral aerosols. en. *Appl. Environ. Microbiol.* **78**, 5781–5787 (Aug. 2012).
29. OSHA. *OSHA Technical Manual, Section VIII - Use of Respirators* https://www.osha.gov/dts/osta/otm/otm_viii/otm_viii_2.html#8 ().
30. Mayerhöfer, T. G. & Popp, J. Beer's law derived from electromagnetic theory. en. *Spectrochim. Acta A Mol. Biomol. Spectrosc.* **215**, 345–347 (May 2019).
31. Tseng, C.-C. & Li, C.-S. Inactivation of Virus-Containing Aerosols by Ultraviolet Germicidal Irradiation. en. *Aerosol Science and Technology* **39**, 1136–1142. ISSN: 0278-6826, 1521-7388. <http://www.tandfonline.com/doi/abs/10.1080/02786820500428575> (2020) (Dec. 2005).
32. Smith, J. S. *et al.* Effect of various decontamination procedures on disposable N95 mask integrity and SARS-CoV-2 infectivity. *Journal of Clinical and Translational Science*, 1–14.
33. Ozog, D. M. *et al.* The effect of ultraviolet C radiation against different N95 respirators inoculated with SARS-CoV-2. en. *International Journal of Infectious Diseases* **100**, 224–229. ISSN: 1201-9712. <http://www.sciencedirect.com/science/article/pii/S1201971220307098> (2020) (Nov. 2020).
34. Fischer, R. J. *et al.* Effectiveness of N95 Respirator Decontamination and Reuse against SARS-CoV-2 Virus. en. *Emerg. Infect. Dis.* **26** (June 2020).
35. Simmons, S. *et al.* Deactivation of SARS-CoV-2 with Pulsed Xenon Ultraviolet: implications for environmental COVID-19 control. en. *Infect. Control Hosp. Epidemiol.*, 1–19. ISSN: 0899-823X, 1559-6834 (Aug. 2020).

36. ASTM International. *Standard Test Method for Determining Antimicrobial Efficacy of Ultraviolet Germicidal Irradiation against Influenza Virus on Fabric Carriers with Simulated Soil* tech. rep. E3179-18 (Apr. 2019).
37. World Health Organization. *Guidelines on viral inactivation and removal procedures intended to assure the viral safety of human blood plasma products* (2004).
38. Blázquez, E. *et al.* Evaluation of the effectiveness of the SurePure Turbulator ultraviolet-C irradiation equipment on inactivation of different enveloped and non-enveloped viruses inoculated in commercially collected liquid animal plasma. *PLoS ONE* **14**. ISSN: 1932-6203. <https://www.ncbi.nlm.nih.gov/pmc/articles/PMC6383881/> (2020) (Feb. 2019).
39. Fisher, E. M. & Shaffer, R. E. A method to determine the available UV-C dose for the decontamination of filtering facepiece respirators. - PubMed - NCBI. *J. Appl. Microbiol.* **110**, 287–295 (2011).
40. Fisher, E. M., Williams, J. L. & Shaffer, R. E. Evaluation of microwave steam bags for the decontamination of filtering facepiece respirators. en. *PLoS One* **6**, e18585 (Apr. 2011).
41. Vo, E., Rengasamy, S. & Shaffer, R. Development of a Test System To Evaluate Procedures for Decontamination of Respirators Containing Viral Droplets. *Applied and Environmental Microbiology* **75**, 7303–7309. ISSN: 0099-2240. <https://www.ncbi.nlm.nih.gov/pmc/articles/PMC2786399/> (2020) (Dec. 2009).
42. Bentley, J. J. *et al.* Can ultraviolet light C decrease the environmental burden of antimicrobial-resistant and -sensitive bacteria on textiles? en. *Veterinary Dermatology* **27**. eprint: <https://onlinelibrary.wiley.com/doi/pdf/10.1111/vde.12377>, 457–e121. ISSN: 1365-3164. <https://onlinelibrary.wiley.com/doi/abs/10.1111/vde.12377> (2020) (2016).
43. Fu, L. *et al.* Different efficacies of common disinfection methods against candida auris and other candida species. en. *Journal of Infection and Public Health*. ISSN: 1876-0341. <http://www.sciencedirect.com/science/article/pii/S1876034120300095> (2020) (Jan. 2020).
44. Kenar, L. *et al.* Comparative Sporicidal Effects of Disinfectants after Release of a Biological Agent. en. *Military Medicine* **172**, 616–621. ISSN: 0026-4075, 1930-613X. <https://academic.oup.com/milmed/article/172/6/616-621/4578073> (2020) (June 2007).
45. Lin, T.-H. *et al.* Relative survival of Bacillus subtilis spores loaded on filtering facepiece respirators after five decontamination methods. *Indoor Air* **28**, 754–762. ISSN: 1600-0668. (2020) (2018).
46. Smolle, C. *et al.* Effectiveness of automated ultraviolet-C light for decontamination of textiles inoculated with Enterococcus faecium. en. *Journal of Hospital Infection* **98**, 102–104. ISSN: 0195-6701. <http://www.sciencedirect.com/science/article/pii/S0195670117304401> (2020) (Jan. 2018).

47. Tomas, M. E. *et al.* The Ebola Disinfection Booth: Evaluation of an Enclosed Ultraviolet Light Booth for Disinfection of Contaminated Personal Protective Equipment Prior to Removal. en. *Infection Control & Hospital Epidemiology* **36**. Publisher: Cambridge University Press, 1226–1228. ISSN: 0899-823X, 1559-6834. <https://www.cambridge.org/core/journals/infection-control-and-hospital-epidemiology/article/ebola-disinfection-booth-evaluation-of-an-enclosed-ultraviolet-light-booth-for-disinfection-of-contaminated-personal-protective-equipment-prior-to-removal/86B0D7B2C3861C8E116AFED9219E6D82> (2020) (Oct. 2015).
48. Wallace, R. L., Ouellette, M. & Jean, J. Effect of UV-C light or hydrogen peroxide wipes on the inactivation of methicillin-resistant *Staphylococcus aureus*, *Clostridium difficile* spores and norovirus surrogate. en. *Journal of Applied Microbiology* **127**, 586–597. ISSN: 1365-2672. (2020) (2019).
49. Tano, E. & Melhus, \. *Level of decontamination after washing textiles at 60°C or 70°C followed by tumble drying* **1**. Publication Title: Infection Ecology & Epidemiology (2014).
50. *Decontamination and Reuse of Filtering Facepiece Respirators using Contingency and Crisis Capacity Strategies*. Centers for Disease Control tech. rep. (Centers for Disease Control. National Center for Immunization and Respiratory Diseases (NCIRD), Division of Viral Diseases, Mar. 2020).
51. CDC. *Guidelines for Environmental Infection Control in Health-Care Facilities: Recommendations of CDC and the Healthcare Infection Control Practices Advisory Committee (HICPAC)* tech. rep. (U.S. Department of Health, Human Services, Centers for Disease Control, and Prevention (CDC)., July 2019).
52. Carratalà, A. *et al.* Effect of temperature and sunlight on the stability of human adenoviruses and MS2 as fecal contaminants on fresh produce surfaces. en. *Int. J. Food Microbiol.* **164**, 128–134. ISSN: 0168-1605, 1879-3460 (June 2013).
53. Lee, J. E. & Ko, G. Norovirus and MS2 inactivation kinetics of UV-A and UV-B with and without TiO₂. en. *Water Research* **47**, 5607–5613. ISSN: 0043-1354. <http://www.sciencedirect.com/science/article/pii/S0043135413005265> (2020) (Oct. 2013).
54. Heisler, G. M. *et al.* Solar Ultraviolet-B Radiation in Urban Environments: The Case of Baltimore, Maryland. en. *Photochemistry and Photobiology* **80**, 422–428. ISSN: 1751-1097. <https://onlinelibrary.wiley.com/doi/abs/10.1111/j.1751-1097.2004.tb00108.x> (2020) (2004).
55. Beck, S. E. *et al.* Comparison of UV-Induced Inactivation and RNA Damage in MS2 Phage across the Germicidal UV Spectrum. en. *Appl. Environ. Microbiol.* **82**. Publisher: American Society for Microbiology, 1468–1474. ISSN: 0099-2240, 1098-5336 (Mar. 2016).

56. Lytle, C. D. & Sagripanti, J.-L. Predicted Inactivation of Viruses of Relevance to Biodefense by Solar Radiation. en. *Journal of Virology* **79**. Publisher: American Society for Microbiology Journals Section: VACCINES AND ANTIVIRAL AGENTS, 14244–14252. ISSN: 0022-538X, 1098-5514. <https://jvi.asm.org/content/79/22/14244> (2020) (Nov. 2005).
57. Zhao, Z. *et al.* Germicidal Ultraviolet Light Does Not Damage or Impede Performance of N95 Masks Upon Multiple Uses. Publisher: American Chemical Society (June 2020).
58. Viscusi, D. J. *et al.* Evaluation of five decontamination methods for filtering facepiece respirators. en. *Ann. Occup. Hyg.* **53**, 815–827. ISSN: 0003-4878, 1475-3162 (Nov. 2009).
59. Ozog, D. *et al.* The importance of fit testing in decontamination of N95 respirators: A cautionary note. en. *Journal of the American Academy of Dermatology* **83**, 672–674. ISSN: 0190-9622. <https://www.sciencedirect.com/science/article/pii/S0190962220308355> (2021) (Aug. 2020).
60. Lindsley, W. G. *et al.* Effects of Ultraviolet Germicidal Irradiation (UVGI) on N95 Respirator Filtration Performance and Structural Integrity. *Journal of Occupational and Environmental Hygiene* **12**. Publisher: Taylor & Francis, 509–517. ISSN: 1545-9624. <https://doi.org/10.1080/15459624.2015.1018518> (2020) (Aug. 2015).
61. CDC. *Filtering out Confusion: Frequently Asked Questions about Respiratory Protection* <https://doi.org/10.26616/NIOSHPUB2018130> (Apr. 2018).
62. *Occupational Safety and Health Standards: Appendix A to §1910.134 - Fit Testing Procedures (Mandatory)* tech. rep. (OSHA, Aug. 2004). <https://www.osha.gov/laws-regs/regulations/standardnumber/1910/1910.134AppA> (2021).
63. CDC. *Recommended Guidance for Extended Use and Limited Reuse of N95 Filtering Facepiece Respirators in Healthcare Settings* <https://www.cdc.gov/niosh/topics/hcwcontrols/RecommendedGuidanceExtUse.html#ref16> (Mar. 2020).
64. Battelle. *Instructions for Healthcare Personnel: Preparation of Compatible N95 Respirators for Decontamination by the Battelle Memorial Institute Using the Battelle Decontamination System* <https://www.fda.gov/media/136532/download> (Mar. 2020).
65. Bergman, M. S. *et al.* Evaluation of Multiple (3-Cycle) Decontamination Processing for Filtering Facepiece Respirators. *Journal of Engineered Fibers and Fabrics* **5**. Publisher: SAGE Publications Ltd STM, 155892501000500405. ISSN: 1558-9250. <https://doi.org/10.1177/155892501000500405> (2020) (Dec. 2010).
66. Marra, A. R., Schweizer, M. L. & Edmond, M. B. No-Touch Disinfection Methods to Decrease Multidrug-Resistant Organism Infections: A Systematic Review and Meta-analysis. *Infect. Control Hosp. Epidemiol.* **39**, 20–31 (Jan. 2018).
67. *Environmental Control for Tuberculosis: Basic Upper-Room Ultraviolet Germicidal Irradiation Guidelines for Healthcare Settings* tech. rep. (U.S. Department of Health et al., Mar. 2009).

68. Beam BL, H. K. A. *N95 Respirator Limited Reuse - Healthcare Professionals Providing Clinical Care* <https://app1.unmc.edu/nursing/heroes/mpv.cfm?updateindex=132&src=yt..> Accessed: 2020-4-17. 2020.
69. Ontiveros, C. C. *et al. Characterization of a commercially-available, low-pressure UV lamp as a disinfection system for decontamination of common nosocomial pathogens on N95 filtering facepiece respirator (FFR) material* 2020.
70. Purschke, M. *et al. Construction and validation of UV-C decontamination cabinets for filtering facepiece respirators. Appl. Opt.*
71. Baer, T., Hesselink, L. & Wilde, J. *Modeling UV-C Irradiation Chambers for Mask Decontamination using Zemax OpticStudio* 2020.
72. Bentancor, M. & Vidal, S. Programmable and low-cost ultraviolet room disinfection device. *HardwareX* **4**, e00046 (Oct. 2018).
73. Rutala, W. A. *et al. Room decontamination using an ultraviolet-C device with short ultraviolet exposure time. en. Infect. Control Hosp. Epidemiol.* **35**, 1070–1072 (Aug. 2014).
74. International Ultraviolet Association. *UV FAQs* <http://www.iuva.org/UV-FAQs>. Accessed: 2020-4-18.
75. Viscusi, D. J., King, W. P. & Shaffer, R. E. Effect of Decontamination on the Filtration Efficiency of Two Filtering Facepiece Respirator Models. *en. J Int Soc Resp Prot* **24**, 15 (2007).

Chapter 7

Quantitative UV-C dose validation with photochromic indicators for informed N95 emergency decontamination

Materials reproduced, with permission, from:

A. Su*, S. M. Grist*, A. Geldert, A. Gopal, and A. E. Herr, “Quantitative UV-C dose validation with photochromic indicators for informed N95 emergency decontamination”, *PLOS ONE*, 2020.

* Equal contributors

7.1 Introduction

Ultraviolet (UV) light in the UV-C wavelength range is one of three promising methods identified by the United States Centers for Disease Control and Prevention (CDC) for N95 respirator decontamination as a shortage mitigation strategy during the COVID-19 pandemic [1]. Building upon years of literature evidence demonstrating that specific UV-C doses inactivate viruses while preserving respirator fit and filtration [2–5], UV-C decontamination of N95 respirators has become a rapidly expanding area of interest for both research and implementation [6]. However, effective UV-C bioburden reduction (while appearing straightforward) requires exquisite attention to detail in both treatment design and validation of treatment parameters. Challenges and intricacies of UV-C measurements can stymie study translation when UV-C dose measurements reporting viral inactivation are not robustly characterized. Innovation is urgently needed to introduce new measurement workflows that are both quantitatively robust and translatable across UV-C systems and facilities.

UV-C pathogen inactivation critically depends on two physical properties: wavelength and dose (or fluence), where dose is defined as integrated irradiance over the exposure time.

Longer UV C wavelengths (240-280 nm) inactivate pathogens like SARS-CoV-2 by damaging their genetic material (absorption peak near 260 nm) [7] (Figure 7.1(a)); far UV-C also damages proteins [8]. Because UV-C decontamination relies upon pathogen interaction with electromagnetic radiation, efficacy depends on direct line-of-sight between the UV-C source and surface. As is well established in the literature, UV-C irradiance, and therefore integrated dose, is attenuated throughout the thickness of an N95 respirator due to reflection, absorption, and scattering of UV-C photons as light passes through each porous N95 material layer (Figure 7.1(b)) [9]. Thus, in contrast to nonporous surfaces, effective decontamination of N95 respirators requires that the minimally acceptable UV-C dose is delivered not just to viral particles on the exterior surface, but also to those that may be embedded in interior N95 layers. Because integrating dosimeters into intact respirators is infeasible, decontamination efficacy throughout the N95 is typically measured in the peer-reviewed literature as a function of UV-C dose applied to the N95 surface. The established approach to quantify the minimum surface UV-C dose for N95 decontamination is to directly assess active virus recovered from throughout the N95 layers (e.g., using the $TCID_{50}$ assay) vs. surface dose [3, 10, 11]. On the majority of N95 models, studies (almost all of which used 254 nm low-pressure mercury light) support $\geq 1.0 J/cm^2$ UV-C dose across the entire N95 surface for ≥ 3 -log reduction of SARS-CoV-2 analogues on the majority of N95 models [2, 4, 12]: a 100-1000X higher dose than that required for non-porous surface decontamination [13].

An augmented approach has measured UV-C attenuation through the N95 layers, then used this attenuation to scale the surface dose and quantify the inner-layer UV-C dose delivered to embedded viral particles [9]. Critically, measured attenuation varied by a factor of ~ 100 between N95 models [9]; furthermore, the wide variation in N95 morphology enhances inter-model differences in applied UV-C dose because irradiance depends on the incident angle per Lambert's cosine law [14]. Likely because of the impact of both model-dependent attenuation and morphology on UV-C dose reaching the N95's inner layers, UV-C viral inactivation efficacy on N95s varies between models [3, 4, 9].

UV-C measurement challenges are further amplified by radiometer complexities [15]. The accuracy and relative uncertainty of digital UV-C radiometers are established through calibration to a known standard (e.g., from the National Institute of Standards and Technology) [16]; however, accuracy is dependent on sensor linearity, spectral sensitivity, and angular response [15, 17] (Figure 7.1(c)). Though some countries have adopted standards for inter-comparison of sensors [18], no universal standards exist. Consequently, there is large variability between sensors in environments differing from the calibration setup, causing reproducibility challenges without meticulous detail in reporting. Furthermore, these instruments are costly, limited, low-throughput, and bulky, precluding measurements on complex 3D surfaces (which require fine spatial resolution and ideal angular response). As a result, UV-C dose is often not robustly characterized, and relative doses over the 3D N95 surface have not yet been empirically quantified.

Photochromic, color-changing UV-C indicators (PCIs) for surface decontamination are commercially available and address challenges presented by digital sensors. Due to their low

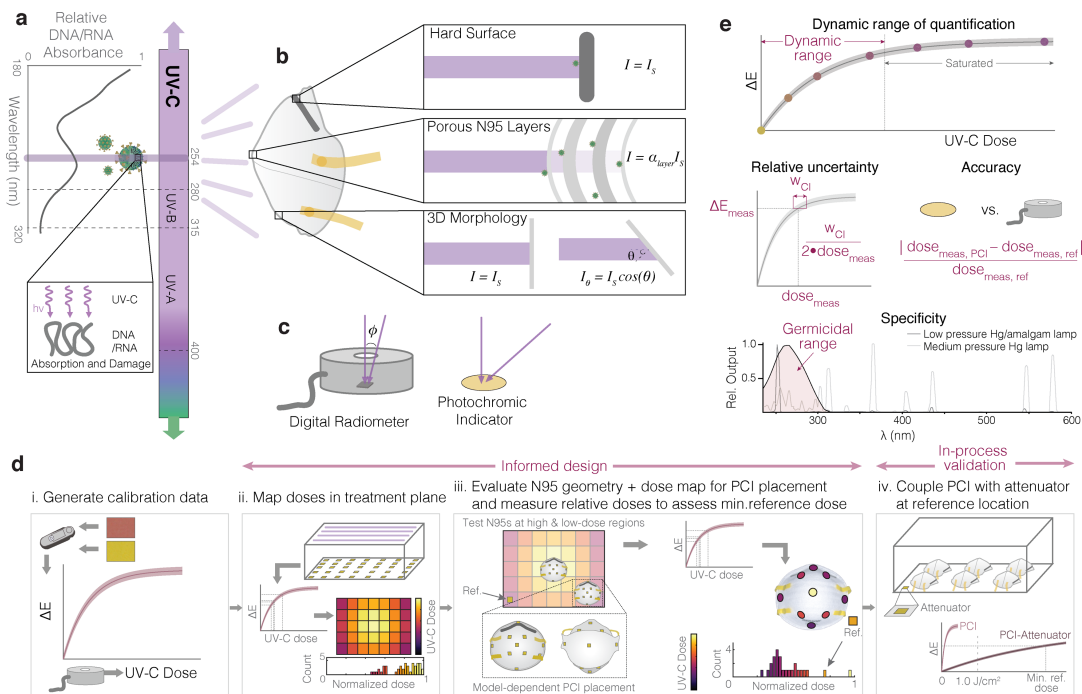


Figure 7.1: Mechanism and challenges of UV-C for N95 decontamination. (a) UV-C at 254 nm primarily inactivates pathogens by damaging genomic material (absorption peak near 260 nm). (b) The multilayer porous N95 materials and 3D morphology reduce the irradiance (and thus dose) available for pathogen inactivation compared to the irradiance that reaches nonporous surfaces (I_s), like the metal nosepiece (α layer represents the layer-dependent attenuation factor). (c) UV-C detectors often have angle-dependent responses that differ from the ideal cosine response expected from a surface such as flat photochromic indicators. (d) The introduced workflow allows end users to both design and validate their UV-C systems, reducing source- and sensor-specific inaccuracies. Critically, assessment of treatment area dose nonuniformity informs N95 placement during on-N95 measurements; on-N95 measurements in turn determine minimum reference PCI doses that yield ≥ 1.0 J/cm^2 to all N95 surfaces. On-N95 measurements are designed to specifically measure steep-angled or potentially shadowed N95 regions. (e) Robust UV-C measurements must meet key specifications, including dynamic range of quantification (before the indicator saturates), relative measurement uncertainty (determined from error propagation from the confidence intervals on the calibration curve fit), accuracy of the measurement compared to a calibrated standard sensor, and specificity of the PCI response to the germicidal wavelength range (in order to accurately report germicidal activity). Nucleic acid absorbance spectrum modified from Voet et al. [14]. SARS-CoV-2 diagrams adapted from an image by Maya Peters Kostman for the Innovative Genomics Institute.

cost and small, flexible form factor, PCIs are ideal for characterizing UV-C uniformity and have been applied for this characterization in hospital rooms [19]. PCIs are intended for qualitative validation; however, there has been effort to quantify color change (a topic of broader interest [20–25]) to characterize water sterilization reactors [26].

In this work, we introduce a novel PCI-based dose quantification workflow (Figure 7.1(d)) for informed design and validation of UV-C decontamination systems. We first demonstrate that PCI color quantification can yield UV-C-specific quantitative dose measurements with high accuracy (Figure 7.1(d, i)). We then use this relationship between color change and UV-C dose to show how PCIs can be implemented by end users: high throughput dose mapping within the treatment plane (Figure 7.1 (d, ii)), combined with assessment of dose distribution across the N95 surface (Figure 7.1(d, iii)) allow PCIs to highlight critical locations to monitor (both on-respirator and on the treatment plane) for informed design. Relative dose measurements using PCIs can then be made on N95s positioned in the identified treatment locations (Figure 7.1(d, iv)) in order to establish the minimum color change reference PCIs on the treatment plane must undergo for all N95 surfaces to receive $\geq 1.0J/cm^2$. Finally, we study how the addition of optical attenuator materials in front of the PCIs can extend the quantifiable UV-C dose range to $\geq 1.0J/cm^2$ (Figure 7.1(d, iv)), enabling the final critical step of the workflow: in-process dose validation during every decontamination cycle.

7.2 Materials and Methods

UV-C sensors

A Model 308 data-logging UV radiometer equipped with a 254 nm sensor (Optical Associates, Inc., OAI) was used for all irradiance measurements. An ILT1254/TD UV-C (International Light Technologies, ILT) radiometer with a near-ideal cosine angular response was used for secondary validation of irradiance measurements. Both radiometers are NIST-traceable and were calibrated within 2 months of data collection. Dose was calculated from irradiance data measured by the OAI meter and data logging software over the exposure time: $dose = \Sigma_{t_{exposure}}(Irradiance \cdot \Delta t)$.

UV-C sources

Two different Spectroline UV treatment systems (same dimensions) were used as the UV-C source for all experiments. The XL-1500 Spectrolinker (“System 2”) was equipped with six low-pressure mercury bulbs (BLE-1T155, uvebay.com). In order to record the dose delivered in this enclosure using the radiometer, the OAI meter was wrapped in UV-C blocking material (PVC) and placed along the back wall of the chamber. This meter was plugged into a Microsoft Surface Pro tablet wrapped in multiple layers of UV-C blocking materials positioned on the left-hand side of the chamber floor. The tablet was controlled remotely using TeamViewer to record irradiance values over time. All photochromic indicator

dose-response curves were measured near the center of the chamber, beside the Surface tablet. In addition, a Spectroline HCL-1500 (with the same chamber materials and dimensions as System 2, referred to as ‘System 1’) equipped with six low pressure amalgam bulbs (BLE-1T155, Spectroline) was generously donated by Spectroline with a small notch in the door to accommodate a sensor cable. With this modified instrument, data logging could be performed with the meter and tablet outside of the UV-C chamber.

UV-C dose-response of photochromic indicators

Commercial photochromic indicators (PCIs) marketed for UV-C detection from two different companies were assessed: UVC 100 Dosimeter Dots from Intellego (‘PCI1’) and Control-Cure[®] UV-C Intensity Labels (N010-004) from UV Process Supply (‘PCI2’). Dose measurements were quantified by integrating irradiance measurements logged by the OAI radiometer over time using a custom Python script. PCIs were placed on a plastic container of similar height to the sensor (16 mm). The irradiance at the PCI location was verified to be within 0.01 mW/cm² of the irradiance at the radiometer location prior to measurements. PCIs were cut into pieces and a single sample was placed on either the digital sensor or plastic container and exposed during bulb warm-up to serve as a saturated reference. D65 L*a*b* measurements of both saturated and unsaturated reference PCIs were recorded using an RM200QC spectrophotometer (X-Rite). After bulb warm-up, sample PCIs were irradiated for a set amount of time using the “time” operating mode of the UV-C treatment system. After UV-C exposure, the color of the exposed PCI was immediately (within 5 minutes) assessed using the RM200QC spectrophotometer (set to report the average of three measurements of each sample).

Quantifying dose-response curves of photochromic indicators

D65 L*a*b* measurements of PCI color assessed using the RM200QC spectrophotometer, along with UV-C doses (integrated from irradiance measurement logs of the radiometer readings: $dose = \sum_{t_{exposure}} (Irradiance \cdot \Delta t)$) were compiled into a spreadsheet format using custom Python scripts, and then analyzed in MATLAB using scripts custom-written for this application. In order to minimize the impact of imaging/measurement conditions on the PCI color measurement, color difference from an unexposed PCI was assessed in all cases, rather than absolute PCI color. There are a range of color difference metrics [20], and for this work we quantified and compared several.

CIELAB (1976) color difference was computed as the Euclidean distance between the L*a*b* values of the exposed (E) and reference (unexposed, R) PCIs:

$$CIELAB\Delta C = \sqrt{(\Delta L^*)^2 + (\Delta a^*)^2 + (\Delta b^*)^2}$$

ΔL^* , Δa^* , and Δb^* are the differences between the exposed and reference sensor L*a*b* coordinates. Similarly, the L*a*b* colors were converted to the RGB color space using built-in MATLAB functions and the Euclidean RGB color difference was computed as:

$$RGB\Delta C = \sqrt{(\Delta R)^2 + (\Delta G)^2 + (\Delta B)^2}$$

Similar as in the L*a*b* color space, ΔR , ΔG , and ΔB are the differences between the exposed and reference RGB coordinates. We also plotted, as a function of exposure dose, the differences in individual components ΔR , ΔG , and ΔB , as well as differences in lightness ($\Delta L^* = L^*_E - L^*_{R^*}$), chroma ($\Delta C^* = C^*_E - C^*_{R^*}$), and the CIE 1976 Metric Hue Difference ($\Delta H^* = s\sqrt{2 \cdot (C^*_E C^*_{R^*} - a^*_E a^*_{R^*} - b^*_E b^*_{R^*})}$), where $s=1$ if $a^*_{R^*} b^*_E > a^*_E b^*_{R^*}$ and -1 otherwise [20].

We compute red, green, and blue channel colorimetric absorbance as [23]:

$$\text{Abs}_{\text{RGB}} = -\gamma \log(I_{\text{RGB}}/I_{\text{RGB},0})$$

where γ is the device-dependent gamma correction factor, I_{RGB} is the red, green, or blue channel intensity of the exposed sensor and $I_{\text{RGB},0}$ is the respective intensity of the unexposed reference sensor. I_{RGB} was computed from the RM200QC-measured L*a*b* values using the ‘lab2rgb’ MATLAB function with γ assumed to be 1. Finally, we computed the sets of equations for the CIEDE2000 ΔE color difference, as defined by Luo, Cui, and Rigg [27]. Our MATLAB implementation of CIEDE2000 was tested using the example color pairs presented by Luo, Cui, and Rigg [27], and found to yield the reported ΔE values for the 10 sample-reference pairs.

Extending the dynamic range of photochromic indicators

In order to assess the amount by which the dynamic range of the PCIs could be extended, two different filter materials were studied: a mounted 1.3 OD neutral density filter (NDUV13A, Thorlabs) and 1.10 mm thick Borofloat glass specified with 80/50 scratch/dig (Precision Glass & Optics). PCIs were placed on the plastic container underneath the filter material while the radiometer recorded unfiltered irradiance over time. UV-C transmission was measured using the OAI digital radiometer and calculated as the peak irradiance through the filtering material divided by the peak irradiance in the absence of filtering material.

Characterizing variability across the treatment plane

An 279.4 mm \times 431.8 mm paper grid with 63.5 mm markings was centered on the floor of the treatment plane. After bulb warm-up, the digital UV-C radiometer was placed at specified grid locations and peak irradiance was recorded over 15-20 seconds. The irradiance at the center of the treatment plane was verified to remain constant every 3-6 measurements to minimize variability caused by bulb output changes. The irradiances at all designated spatial locations were measured in triplicate. For PCI measurements, indicators were secured to the spatial locations on a copy of the 63.5 mm grid using double-sided tape. The grid was then inserted into the treatment system atop the master grid. The digital radiometer was placed in its designated location for data logging. After exposure, PCIs were transferred to a consolidated layout for RM200QC analysis and measured within \sim 15 minutes.

Quantifying unknown doses using photochromic strips

In order to quantify unknown UV-C doses (e.g. across the treatment plane of the UV-C exposure system, or across the surface of an N95 respirator), color measurements from the RM200QC were read in from a spreadsheet into a custom MATLAB script. Previously-generated calibration datasets (CIEDE2000 measured with the same instrument vs. known UV-C dose, as described in “Quantifying dose-response curves of photochromic indicators” above) were read in and fitted with calibration functions. For each measurement, the L*a*b* color values for the exposed PCI and unexposed PCI reference (measured on the same day with the same instrument) were read in and the CIEDE2000 ΔE between this pair was computed as previously described. The UV-C exposure dose was predicted from the CIEDE2000 ΔE using the calibration curve. First, the inverse of the fit function was used to predict the dose from the color change. For the fit function corresponding to first-order reaction kinetics:

$$dose(\Delta E) = -b \cdot \ln(1 - \Delta E/a)$$

For the fit function corresponding to second-order reaction kinetics:

$$dose(\Delta E) = \frac{\Delta E}{1/2 \cdot a^2 \cdot b - a \cdot b \cdot \Delta E}$$

To estimate the uncertainty on the predicted dose measurement, methods for estimating uncertainties of calibrated values via propagation of error, along with uncertainties on the fitted parameters (standard deviations s_a and s_b) and ΔE measurement (standard deviation $s_{\Delta E}$), were used to estimate the variance of the measured value u_{dose}^2 [28]:

$$u_{dose}^2 = \left(\frac{\delta dose}{\delta a}\right)^2 s_a^2 + \left(\frac{\delta dose}{\delta b}\right)^2 s_b^2 + \left(\frac{\delta dose}{\delta \Delta E}\right)^2 s_{\Delta E}^2 + 2 \left(\frac{\delta dose}{\delta a}\right) \left(\frac{\delta dose}{\delta b}\right) s_{ab}$$

Where $s_{a,b}$ denotes the covariance between a and b . To complete this computation, s_a , s_b , and s_{ab} were computed from the curve fit covariance matrix, and the partial derivatives of the inverse fit functions used in the computation of are as described in Table 7.1.

The ΔE measurement uncertainty $s_{\Delta E}$ was measured from the standard deviation of 15 replicate measurements of unexposed PCI1 or PCI2 using the RM200QC, each compared to the same measurement of an exposed (saturated) PCI1 or PCI2, respectively. To understand the uncertainty on each type of color quantification, this standard deviation was calculated for color quantification via CIEDE2000 ΔE , CIELAB 1976 ΔC , RGB ΔC , ΔR , ΔG , ΔB , ΔL , ΔC , ΔH , and colorimetric absorbances Abs_R , Abs_G , and Abs_B . The resulting uncertainties are presented in Table 7.2.

Ninety-five percent confidence intervals for predicted doses from each curve fit ($\alpha = 0.05$) were predicted from the estimated variance (u_{dose}^2) as : [29]

$$CI = dose_{meas} \pm \sqrt{u_{dose}^2} \cdot t_{1-\alpha/2, v}$$

Table 7.1: Fit functions, inverse fit functions, and partial derivatives used in uncertainty calculations for calibrated measurements.

Fit Type	First-Order	Second-Order
Fit function	$\Delta E = a \left\{ 1 - e^{-\frac{dose}{b}} \right\}$	$\Delta E = \frac{1}{2}a^2 \cdot b \cdot dose + a \cdot b \cdot dose$
Inverse fit function	$dose(\Delta E) = -b \cdot \ln(1 - \Delta E/a)$	$dose(\Delta E) = \Delta E/2 \cdot a^2 \cdot b - a \cdot b \cdot \Delta E$
$\delta dose \delta a$	$-b \cdot \Delta E a^2 - a \cdot \Delta E$	$4\Delta E(\Delta E - a)b \cdot a^2(a - 2 \cdot \Delta E)^2$
$\delta dose \delta b$	$-\ln(1 - \Delta E/a)$	$-2 \cdot \Delta E a \cdot b^2 \cdot (a - 2 \cdot \Delta E)$
$\delta dose \delta \Delta E$	$ba - \Delta E$	$2b \cdot (a - 2 \cdot \Delta E)^2$

Table 7.2: RM200QC measurement uncertainties $s_{\Delta E}$ for various metrics of color quantification and two models of PCI. Each uncertainty reports the standard deviation of N=15 measurements of replicate unexposed PCIs. We observe higher measurement uncertainty for PCI1, which we attribute to heterogeneity (dots and striations) in the colored PCI coating.

Model	PCI1	PCI2
CIEDE2000	0.273	0.083
ΔC_{CIELAB}	1.215	0.397
ΔC_{RGB}	0.010	0.0020
ΔR	0.0063	0.0015
ΔG	0.0029	0.0015
ΔB	0.011	0.0071
ΔL	0.263	0.106
ΔC	1.443	0.450
ΔH	1.227	0.495
Abs_R	0.0029	6.66×10^{-4}
Abs_G	0.0015	7.13×10^{-4}
Abs_B	0.012	0.014

where $t_{1-\alpha/2,v}$ is the student's t-inverse cumulative distribution (tinv in MATLAB), and v is the degrees of freedom for the calibration curve fit.

In experiments where triplicate PCI measurements of unknown doses were acquired and quantified using the calibration curve process described above, the measured doses were first equalized by correcting with a factor related to the dose logged by the radiometer during each exposure to correct for differences in the exposure time/dose between replicate measurements. To perform this correction, the doses measured from the PCI color change (as well as the confidence intervals and standard deviation of the measured value $\sqrt{u_{dose}^2}$) were multiplied by a target dose (constant across the replicate datasets) and divided by the logged OAI radiometer dose. After this correction for slight differences in the dose to which the

PCIs were exposed, the uncertainty estimated from the standard deviation of the replicate measurements was combined with the uncertainty from the calibration fit measurements by root sum of squares:

$$u_{total} = \sqrt{u_{dose}^2 + u_{rep}^2}$$

Where u_{dose}^2 is as described above, and u_{rep}^2 is the squared standard deviation of replicate measurements. For several datasets, dose measurement data are presented as relative doses ($dose_{norm}$), normalized to measurements at a different location or in a different experimental setup:

$$dose_{norm} = dose_{meas} dose_{ref}$$

For these normalized measurements, the uncertainty is calculated from the uncertainties on both the measured and reference estimated doses via propagation of error as follows:

$$u_{norm} = |dose_{norm}| \sqrt{\left(\frac{u_{total,meas}}{dose_{meas}}\right)^2 + \left(\frac{u_{total,ref}}{dose_{ref}}\right)^2}$$

Measured doses were plotted as heatmaps and histograms using the ‘inferno’ perceptually uniform, colorblind-friendly colormap, which was created by Stéfan van der Walt and Nathaniel Smith and adapted from Python’s matplotlib for use in MATLAB[®] by Ander Biguri [30].

Photochromic indicator response to non-germicidal light

A 300 nm longpass filter (46-417, Edmund Optics) was used to assess the reactivity of the PCIs to wavelengths longer than the germicidal (200-280 nm) UV-C range. For each experiment, one PCI was placed beneath the longpass filter on top of the plastic container and one PCI was placed on the digital sensor as an unfiltered control. Post-exposure color was measured using the RM200QC. In order to assess the reactivity of the PCIs to sunlight, both models of commercial PCIs were taped to the same white background using double-sided tape and covered with black cardstock during transport outside. The exposure to sunlight began at 17:50 on May 30th, 2020 in Berkeley, CA, USA, when the UV index [31] was reported as 1 by Apple Weather. The color change was recorded over 5 minutes via iPhone 8 video. Both pre- and post-exposure PCIs were imaged using the Nikon D5500 and quantified using the RM200QC.

Measuring dose received by N95 respirator surface

PCIs were affixed to the appropriate location on the surface of a NIOSH-approved Gerson 1730 N95 respirator using double-sided tape. Due to the limited dose range of the PCIs,

preliminary experiments were conducted to determine an exposure time that caused all PCIs to change color within the dynamic range of the color calibration curves. For all but one condition, the exposure time was set for 8 seconds. For two exposures using PCI2 to quantify dose on a peripheral N95, the time was set for 19 seconds to take advantage of more of the PCI2 indicators' range. These differences in exposure were compensated for in the analysis workflow described above. The respirator was positioned in its marked location within the UV-C source (either center or periphery). The straps were spread away from the respirator to minimize shadowing. For measurements of the respirator on the periphery of the treatment plane, the straps were taped together and tucked under the respirator. The OAI radiometer, with a corresponding PCI on top, was placed in its designated location for irradiance logging. The color of all PCIs after exposure was recorded using the RM200QC.

Assessing alternative imaging systems (iPhone, flatbed scanner, and digital SLR)

After each PCI exposure, the exposed indicator was imaged between unexposed and saturated references with the iPhone and Nikon D5500 within a FotodioX LED Studio-in-a-Box (FOSIAB2424, B&H) with the grey background installed. A platform was frequently inserted underneath the grey background to raise the PCIs closer to the cameras. The included diffuser sheet was cut and installed to cover the LED lights but not the top hatch. Within the Studio-in-a-Box, raw images of the PCIs were acquired using a Nikon D5500 equipped with a 40 mm macro lens or using Halide on an iPhone X at 2X optical zoom. The settings for both cameras were set manually and kept consistent within each experiment. At the conclusion of each experiment, the PCIs were scanned using VueScan (set to acquire raw images) on a flatbed scanner (LiDE 400, Canon).

Color quantification from different imaging systems

In order to compare color quantification from the RM200QC spectrophotometer 'gold standard' tool with that from more widely available imaging devices, images of the PCIs acquired with multiple imaging devices were compared. These images were either (1) a set of images (one for each exposed PCI), each containing the exposed PCI between an unexposed and saturated PCI, with nearby white-balance region and Pantone[®] color match to the exposed PCI (iPhone and digital SLR images), or (2) a single image of all of the exposed PCIs from a dose-response experiment, along with a single unexposed and single saturated PCI, on a white background (flatbed scanner images). iPhone and DSLR images were acquired after each exposure; scanner images were acquired once all exposures in an experiment were complete. Raw images (.DNG for iPhone X, .NEF for DSLR, .TIF for flatbed scanner) were acquired and converted to .TIF format to be read into MATLAB[®] and analyzed using custom scripts.

In the image analysis script, each image was read in sequentially and the user prompted to draw rectangular areas over (a) the exposed PCI, (b) the Pantone[®] match to the PCI, (c)

the white region proximal to the PCI(s), (d) the unexposed PCI, and (e) the saturated PCI. In all cases, care was taken to draw a region encompassing only the region of interest (i.e., not edges, dust, or shadowed regions). For the first type of data (1: an image for each PCI), all 5 regions were denoted on each image (for each exposed PCI). For the second type of data (2: a single image for all PCIs), a single region was denoted for the white, unexposed, and saturated regions for all exposed PCIs, with only the PCI region denoted for each exposure dose (Pantone[®] matches were not imaged in the second type of imaging workflow). After all regions on each image were selected, the average RGB value for the white region was used to white-balance and exposure-correct the image before computing the average RGB values for the other region types. The RGB value for each region was then converted to the L*a*b* color space using MATLAB[®]'s built-in `rgb2lab` function. RGB and L*a*b* values from the processed images were then subjected to the same processing for color difference calculations as described above for the measured RM200QC L*a*b* values in “Quantifying dose-response curves of photochromic indicators”.

CIEDE2000 color differences from an unexposed PCI, computed from each image type as well as the RM200QC measurements of the same set of PCIs, were fitted to the appropriate calibration function and plotted (along with 95% prediction intervals) as a function of exposure dose, in order to compare the relative dose-responses and calibration uncertainties measured with each tool. The squared sum of the residuals from the curve fit (SSE) for each dataset was computed and compared as a metric of calibration robustness for each color readout method.

Visualizing reduced UV-C transmission through permanent marker ink

To demonstrate spatially-resolved measurement, we visualized the UV-C shadowing abilities of permanent marker ink. The “Cal” university logo was drawn with Sharpie[®] permanent marker on a UV-C-transmissive ($\sim 82\%$ transmittance) plastic plate sealer adhesive film. The plastic film with permanent marker logo was then placed atop a PCI1 indicator within the UV-C treatment plane and exposed to UV-C for ~ 10 s (applied UV-C not precisely controlled as this was a qualitative test). After exposure, the film and exposed PCI were imaged using the flatbed scanner.

Assessing temporal fluctuations in irradiance

Irradiances over time logged using the OAI radiometer either during system warm-up or during long-exposures after warm-up were parsed from the output .txt files using a custom Python script and read into MATLAB[®]. Warm-up datasets approximated the variance that would be present in applied conditions because the time since previous use was not controlled (the datasets began with the lamps in varying states of warm-cool). Each dataset was analyzed to automatically detect the iteration (i_{end}) at which lamp shutoff occurred (from the change from the previous measurement). The irradiance data were plotted until

2 measurements prior to that measurement iteration (i_{end-2}). For the system warm-up datasets, warm-up rise time was computed as the time for the irradiance to rise from 10% of the maximum recorded value to 90% of the maximum recorded value. For the long exposure datasets, the output degradation was assessed by extracting the irradiance degradation slope from linear least-squares curve fitting.

The estimated time to reach 1.0 J/cm^2 from each exposure was computed as the target dose (1.0 J/cm^2) divided by the mean irradiance. To assess the effects of temporal instability of the lamp output, this calculation was computed for both a mean irradiance at the beginning of each exposure (taking the mean irradiance over the 10th to 20th iterations of the data logger) and a mean irradiance at the end of each exposure (taking the mean irradiance over the last 11 iterations prior to the detected end point (i_{end} , automatically detected from lamp shutoff as described above)).

7.3 Results and Discussion

UV-C dose measurements are frequently the only link between viral inactivation studies and implementation of each decontamination cycle. Decontamination efficacy and safety consequently depend on robust UV-C measurements, defined by several critical metrics (Figure 7.1(e)) for which we have defined marginal and ideal values (Table 7.3). Here, we introduce a new technique using PCIs to address three critical challenges hindering UV-C decontamination processes: (1) accurate and high-throughput characterization of the UV-C treatment plane (Figure 7.1(d, ii)), (2) spatially-resolved dose quantification across complex 3D structures placed within the treatment plane (Figure 7.1(d, iii)), and (3) translatable and reproducible in-process measurements to validate the dose of $\geq 1.0 \text{ J/cm}^2$ delivered to all N95 surfaces during every UV-C treatment cycle (Figure 7.1(d, iv)).

Novel photochromic indicator quantification accurately assesses spatial nonuniformities in UV-C treatment systems

PCIs have the potential to fill three urgent gaps in UV-C dose validation; however, a quantitative rather than qualitative readout strategy is required. To assess the indicators' suitability for contributing to informed design of UV-C treatment processes, we introduce a novel quantification workflow and demonstrate the capability to capture spatial heterogeneity within a UV-C treatment system from a single exposure. We first assessed whether UV-C dose could be quantified from the color change of commercially-available PCIs; quantification relies upon distinct, reproducible color change that follows a known, predictable relationship. Measurement of color differences between the sample and a reference (rather than absolute colors) improves quantification robustness as the difference between two colors measured under the same conditions is less sensitive to many confounding effects [20, 21]. To test whether two models of commercial PCIs (Intellego UVC 100 Dosimeter Dots: 'PCI1', and UV Process Supply UV-C Intensity Labels: 'PCI2') could meet the specifications of Table

Table 7.3: Specifications for robust UV-C measurements

No.	Metric	Units	Marginal Value	Ideal Value
1	Dose measurement range (in-process validation)	J/cm ²	> 1.0	> 3.0
2	Dose measurement range (informed design)	J/cm ²	> 0.1	> 0.3
3	Relative uncertainty on dose measurement (CI)	%	< 20	< 10
4	Accuracy	%	> 80	> 90
5	Sensitivity to non-germicidal longer wavelengths	%	< 5	< 1

1. The marginal dose measurement dynamic range for in-process validation (≥ 1.0 J/cm²) is based upon the marginally-acceptable dose to be delivered to each and every N95 surface for 3-log inactivation of enveloped viruses (based on peer-reviewed evidence in the scientific literature [3, 4, 12]). The measurement method needs to be able to discern whether this dose has been exceeded. Ideally, the measurement range would be higher (> 3.0 J/cm²) as the location of the reference sensor during decontamination may receive a higher dose than the N95 surface receiving the lowest dose due to shadowing and the model-dependent angles of the N95 surfaces.

2. Because informed design of N95 decontamination systems and processes can use relative dose measurements, the necessary dose measurement dynamic range for informed design can be lower than that for in-process validation. > 0.1 J/cm² was chosen as the marginal value for this application to ensure that the UV-C exposure times for informed design were no less than 1/10th those for in-process validation. As informed design uses the same exact UV-C exposure system as that used for the actual decontamination process, low dynamic range PCIs would require very short exposure times because the systems are designed to deliver ≥ 1.0 J/cm² during a reasonable exposure time. These short exposure times during informed design may (1) not be feasible or (2) introduce unacceptable degrees of run-to-run variability.

3. The calibration uncertainty for very well characterized UV-C radiometers is 5% [32] (although many radiometers will not reach this level due to sources of error in UV-C measurements [33]). As measurement solutions like photochromic indicators (PCIs) have advantages over even the best calibrated radiometers (e.g. form factor), we identified a marginal target for PCIs of 4 times the value for radiometers, and an ideal target as twice the radiometer value. These values (20% and 10%, respectively) allow reasonable ‘safety factors’ of $< 50\%$ to be implemented to ensure minimally-acceptable doses are reached. Safety factors are multipliers on the target dose to take into account uncertainty on the measurements (e.g. for 20% total propagated uncertainty, one may want to use a safety factor of 1.5 and ensure at least ≥ 1.5 J/cm² was delivered to all N95 surfaces)

4. Accuracy values (how well measurements align with a calibrated, NIST-traceable reference measurement) were chosen to align with target relative uncertainty.

5. Ideally, UV-C measurements for decontamination characterization and validation should only report irradiance/dose within the germicidal range (UV-C extends to 280 nm; germicidal efficacy at 300 nm is $< 10\%$ of that at 254 nm). We selected marginal and ideal values such that the measurement response to > 300 nm was 1-2 orders of magnitude less than that to < 300 nm light from a commonly employed low-pressure mercury/amalgam source.

7.3, we exposed them to UV-C doses measured with a calibrated radiometer, quantified their color using an RM200QC spectrophotometer (outputting single-point $L^*a^*b^*$ values), and computed the CIEDE2000 [27] industry-standard color difference (ΔE) from an unexposed indicator as a function of UV-C dose (Figure 7.2(a)). Both PCI models showed visually-discernable color change up to $\sim 0.15 \text{ J/cm}^2$. PCI1 (Figure 7.2(a)) has a higher maximum ΔE of ~ 45 compared to ~ 25 for PCI2 (Figure 7.2(b)). Higher maximum ΔE will lead to lower relative uncertainty for a constant color difference measurement uncertainty.

We next scrutinized whether fitting the ΔE vs. dose data to a calibration function could predict UV-C dose from ΔE with relative dose measurement uncertainty below the 10-20% thresholds. We fit the data to calibration functions based upon first- and second-order reaction kinetics. For PCI1, we used a fit function corresponding to first-order reaction kinetics (a, b are fit parameters):

$$\Delta E = a \left\{ 1 - e^{-\frac{dose}{b}} \right\}$$

while for PCI2 we observed better goodness-of-fit with a fit function corresponding to second-order reaction kinetics (Figure 7.3):

$$\Delta E = \frac{\frac{1}{2}a^2 \cdot b \cdot dose}{1 + a \cdot b \cdot dose}$$

We note that although these fit functions serve as effective calibration functions with high goodness-of-fit, the current implementation does not facilitate extraction of reaction parameters (e.g., reaction order, reaction rate) from the curve fit because the relationship between CIEDE2000 and colored reaction product concentration is not known. Furthermore, the unknown chemical composition of the commercial PCIs confounds determination of reaction parameters. Colorimetric absorbance of dye on paper has been found to deviate from Beer's Law [23], so careful calibration of colorimetric absorbance over a range of known dye concentrations is required to quantify concentrations or reaction kinetics from colorimetric absorbance on paper [34]. Nevertheless, adoption of colorimetric absorbance approaches will be useful to inform design of new optimized chemistries for PCI materials.

We assessed the precision of the measurement by comparing the width of the dose measurement confidence intervals (CIs) to the respective dose values (Figure 7.2(b)). The relative 95% CIs on UV-C doses measured with the calibration function (from known CIEDE2000 color differences) were considerably larger for PCI2 than for PCI1 suggesting that PCI1 is better-suited to robust UV-C quantification. Dose quantification uncertainties are dependent on the ΔE uncertainty of the measurement tool. Using an experimentally determined ΔE uncertainty of 0.273 for PCI1 and 0.083 for PCI2 (see Methods), we find that the two PCI models yield disparate relative uncertainties on the dose measurements. At a dose of $\sim 0.1 \text{ J/cm}^2$, PCI1 relative CI width (width of the CI divided by the measured dose) is 12.1%, equivalent to 6.05% relative uncertainty and meeting the $< 10\%$ ideal relative uncertainty target. At the same dose, PCI2 relative CI width is 21.2%, equivalent to 10.6% relative uncertainty. PCI2 thus does not meet the ideal relative uncertainty target but does meet the

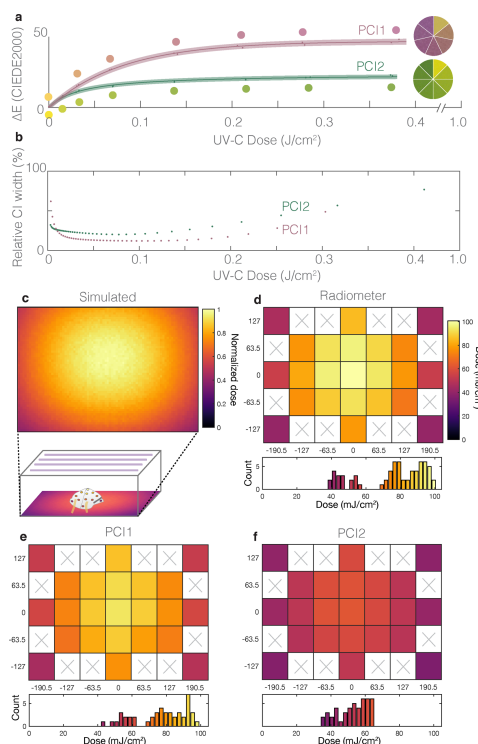


Figure 7.2: Robust color measurement facilitates UV-C dose quantification from two models of PCIs. (a) CIEDE2000 color difference between exposed and unexposed Intellego UVC Dosimeter Dot (PCI1, pink) and UV Process Supply UVC Intensity Label (PCI2, green) as a function of UV-C dose. Dose-responses for PCI1 were fit with a calibration function corresponding to first-order reaction kinetics (Eq 1: $R^2 = 0.998$; $a = 47.1$ (46.1, 48.1); $b = 80.4$ (74.6, 86.3); 95% confidence interval on fit parameters reported in parentheses). Dose responses for PCI2 were fit with a calibration curve corresponding to second-order reaction kinetics (Eq 2: $R^2 = 0.992$; $a = 47.7$ (45.9, 49.5); $b = 0.00060$ (0.00049, 0.00072)). PCI color is depicted by the RM200QC-measured color values (circles) and digital SLR camera (DSLR) image swatches in the comparison wheels. For each PCI type, the datapoints within the shaded region denote individual PCI measurements, line denotes best fit, and shaded region denotes 95% prediction interval on prediction of color change from observation of UV-C dose. (b) Relative quantification uncertainties using the PCI calibration workflow. Plots depict quantified 95% confidence intervals on measurements of UV-C dose from CIEDE2000 color difference between exposed and unexposed PCIs, normalized to and as a function of UV-C dose. (c-f) heatmaps and histograms of delivered UV-C dose to locations across the treatment plane, quantified with (c) Zemax OpticStudio simulations (plot depicts relative dose), (d) digital radiometer (with correction factor, mean of $N = 3$ measurements at each location), (e) PCI1 (mean of $N = 2$ measurements at each location), and (f) PCI2 (mean of $N = 2$ measurements at each location). The PCI2 model appears to underestimate both dose and nonuniformity. Heatmaps in (d-f) are plotted on the same color scale (up to the radiometer maximum measured dose), while heatmap in (c) depicts dose normalized to the highest value observed. White regions with ‘ \times ’s in (d-f) were not measured.

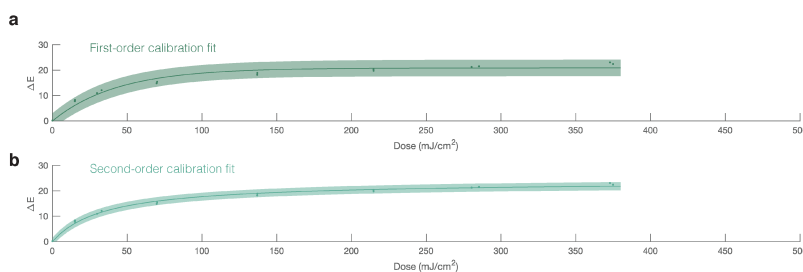


Figure 7.3: Comparison of calibration fit functions for PCI2 based on first-order reaction kinetics (a) and second-order reaction kinetics (b) for PCI2. Using the second-order reaction kinetics results in better fit and smaller confidence intervals. For the first-order fit (a), $R^2 = 0.967$, $a = 20.9$ (19.7, 22.0), $b = 43.0$ (33.5, 52.6). For the second-order fit (b), $R^2 = 0.992$, $a = 47.7$ (45.9, 49.5), $b = 0.00060$ (0.00049, 0.00072). In each plot, fitted data are represented as points, best fit lines are represented as solid lines, and 95% prediction intervals are plotted as shaded regions on each plot.

marginally-acceptable 20% relative uncertainty target. PCI1 relative uncertainty remains < 10% up to $\sim 0.20 \text{ J/cm}^2$. These results highlight the importance of quantifying the ΔE measurement uncertainty of the color measurement tool in order to accurately predict PCI dose quantification uncertainty. The PCI1 relative quantification uncertainty, while higher than that established for calibration of UV-C radiometers under ideal conditions [32], should still facilitate dose quantification as long as appropriate safety factors (i.e., a multiplier >1) are included in dose calculations to account for the propagated relative uncertainty and ensure minimum doses are met.

Robust color quantification metrics that are well-suited to calibration should vary with applied UV-C dose in a reproducible and quantifiable manner with low relative quantification uncertainty. To better understand the calibration capacity of other standard metrics of color quantification, we scrutinized the relative quantification uncertainty on alternate color difference/color distance formulae: CIELAB 1976 (Euclidean ΔC) and Euclidean RGB ΔC (Figure 7.4). To isolate specific color components well-suited to calibration, we also compared absolute differences in the red, green, and blue (ΔR , ΔG , ΔB) components and lightness, chroma, and hue (ΔL , ΔC , ΔH) components between exposed and unexposed PCIs. We fit each metric to the same calibration functions defined in the Methods. Relative CI widths for each of these 9 color metrics were computed by comparing the PCI dose measurement CI widths to the respective dose values. Not surprisingly, the most favorable color difference metrics were dependent on PCI type. Given the benefits of CIEDE2000 for robust color difference determination across the full color space of different PCI color changes [27], we chose to use CIEDE2000 for all subsequent quantification of both PCI models used in this study. We acknowledge, however, that different color metrics may be optimal for characterizing a single specific PCI model. For PCI1, the difference in hue angle (ΔH) yielded

low quantification uncertainty ($< 10\%$ beyond 250 mJ/cm^2) and may be an avenue for future research to improve quantification robustness compared to CIEDE2000 for certain PCI models. Additionally, measurements of the PCI material optical spectra as a function of exposure dose may help developers of new PCI chemistries identify the most promising color metrics for dose quantification. We note that these PCIs are governed by reaction kinetics; thus, environmental factors (e.g. temperature and humidity) are expected to affect the rate of color change with dose [35, 36]. Additionally, we have observed PCI color instability after exposure; thus, PCIs should be quantified immediately (within 10-20 minutes of exposure for these models). Although the PCI1 quantifiable dynamic range of $< 0.2 \text{ J/cm}^2$ is not sufficient for in-process validation ($\geq 1.0 \text{ J/cm}^2$ to all N95 surfaces [2-4]), it meets the $\geq 0.1 \text{ J/cm}^2$ marginal threshold to assess relative doses for informed design of UV-C treatment systems.

Having established a novel PCI quantification workflow, we next asked whether PCI measurements could scrutinize spatial dose uniformity within a UV-C treatment system as the first step towards informed design of N95 decontamination (Figure 7.1(d, ii)). Guiding principles of optics dictate that irradiance nonuniformities will be present in nearly any UV-C treatment system; however, the accuracy and reproducibility of UV-C measurements is hindered by a lack of standardization of critical sensor properties such as angular response, which can drastically impact readings [17, 33] (with system-dependent impact). In the absence of a calibration reference, the sensor angular response can be obtained (either through measurement [17] or through the manufacturer) and used with optical modeling to estimate spatially-dependent system- and sensor-specific correction factors. We first mapped UV-C dose within a Spectroline HCL-1500 UV-C source using simulation (Figure 7.2(c)) and 23 individual OAI 308 radiometer measurements (Figure 7.2(d)). We observed that the radiometer under-reports irradiance and dose due to its nonideal angular response (Figure 7.5); the reported readings (Figure 7.2(d)) are post-correction. After correction, the irradiance measured near the corners of the treatment plane is $\sim 40\%$ of that measured at the center.

We leveraged the nonuniform treatment plane irradiance to validate our quantification workflow by comparing PCI doses (quantified using the appropriate calibration curve depicted in Figure 7.2(a)) to corrected radiometer measurements (Figure 7.2(e-f)). The relative quantification error ($|dose_{PCI} - dose_{radiometer}|/dose_{radiometer}$) for PCI1 is $7\% \pm 7\%$ (mean \pm standard deviation of $N=23$ spatial measurements averaged across $N=2$ replicates), meeting the $> 90\%$ accuracy target. In contrast, the relative quantification error for PCI2 is $28\% \pm 10\%$, failing to meet the marginal $> 80\%$ accuracy target. While it is unclear why PCI2 performs so discordantly in this test, the good agreement between PCI1 and the radiometer suggests not only that our PCI quantification workflow can capture spatial nonuniformities in a single UV-C exposure (compared with 23 radiometer exposures), but also that color difference quantification should facilitate new classes of measurements not feasible with radiometers.

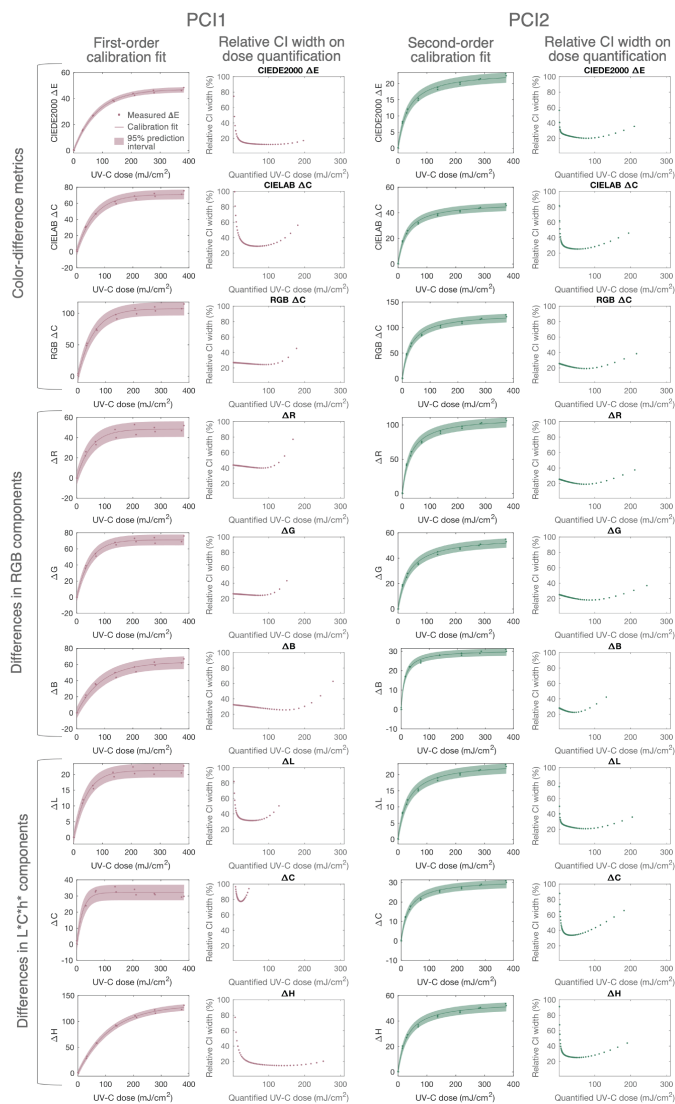


Figure 7.4: Relative uncertainty on measurements using alternate color difference metrics. Calibration curve fits and relative width of 95% confidence intervals on quantified PCI UV-C doses using alternate metrics of color change as a function of UV-C exposure dose. Color difference metrics reporting the lowest relative uncertainty vary by PCI type, as expected from the different color-changing behaviors of the two PCI models. For the two PCI models considered in this study, difference in hue angle (ΔH) and overall color difference (CIEDE2000 ΔE , Euclidean CIELAB 1976 color difference ΔC , and Euclidean RGB ΔC) appear to be suitable color difference metrics for dose quantification.

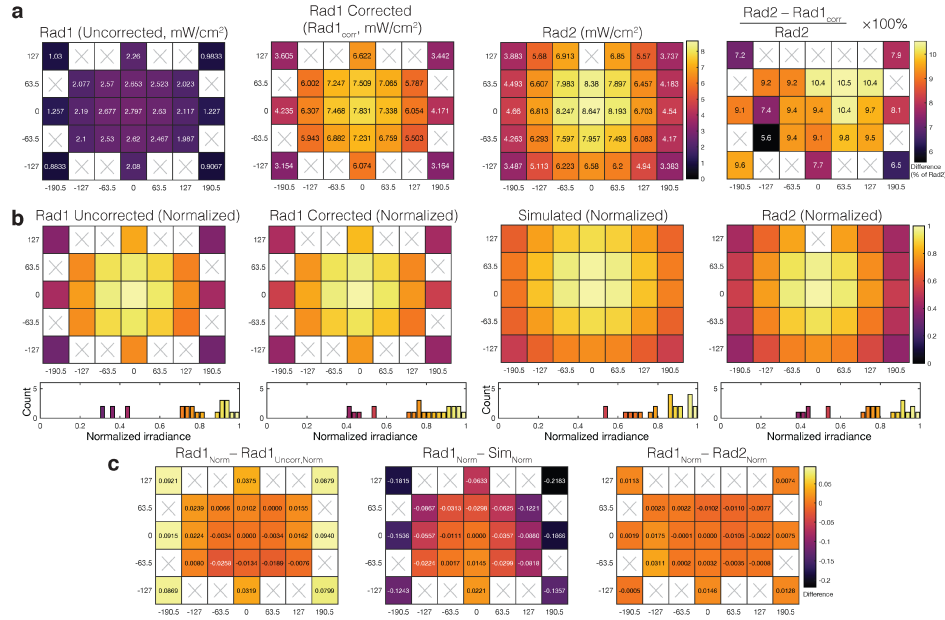


Figure 7.5: Angular response affects quantification of spatial nonuniformity. (a) Two UV-C sensors report $\sim 3X$ difference in irradiance within the exposure system due to discrepancies in their angular responses (Rad1 has nonideal angular response; Rad2 has near ideal cosine angular response as measured by the manufacturer). Correction of Rad1’s angular response with a virtual calibration factor yields irradiance profile in good agreement with Rad2 (within 11% across the treatment plane). (b) Normalized corrected Rad1 measurements agree well with normalized Rad2 measurements and Zemax simulations of the treatment system, although simulations underestimate nonuniformity in irradiance. Each plot shows a heatmap of irradiance values normalized to the center location above a histogram of measured normalized irradiances (showing the mean of $N=3$ measurements for the experimental (Rad1/Rad2) measurements). (c) Differences between the corrected and uncorrected normalized Rad1 measurements reveal that the uncorrected Rad1 overestimates nonuniformity in irradiance by nearly 10%. Differences between the normalized corrected Rad1 and simulations reveal that simulations underestimate nonuniformity in irradiance by over 20%. Differences between the normalized corrected Rad1 and Rad2 measurements reveals that the corrected Rad1 accurately captures irradiance nonuniformities within 3%. All three heatmaps in (c) plotted on the same scale. White regions with ‘x’ were not measured. Rad1 is an OAI 308 meter equipped with a 254 nm sensor. Rad2 is an ILT1254/TD radiometer. Each experimental (Rad1 or Rad2) plot depicts the mean of $N=3$ measurements.

Photochromic indicator quantification facilitates new types of measurements for informed design of UV-C treatment

PCI quantification facilitates measurements not possible with bulky radiometers, such as dose mapping across complex 3D morphologies. To highlight the impact of our workflow, we mapped relative UV C doses across the 3D morphology of a Gerson 1730 N95 respirator in three orientations (Figure 7.6(a)) informed by the treatment area dose mapping (Figure 7.2(c-e)). We exposed PCI1 indicators applied to the exterior and interior N95 surfaces to sub-saturating UV-C treatments (Figure 7.6(b-d)). Limited by PCI dynamic range, the exposure times were insufficient for decontamination, but measured relative dose delivered to different respirator regions (informed design, Fig 1(d,iii)). We observe that while system nonuniformities alone suggest $\sim 2.5X$ irradiance nonuniformity across the treatment plane (Figure 7.2(c-f)), on-N95 measurements show that nearly 20X disparity exists (Figure 7.6(b-d)).

The respirator morphology has a striking impact on delivered dose: even in the center of the treatment plane there are regions on the exterior (convex) N95 surface that receive only $\sim 25\%$ of the dose at the apex (Figure 7.6(c)). There is similar but less dramatic nonuniformity present on the respirator interior (exposed concave side-up) (Figure 7.6(d)). Perhaps most strikingly, there are regions of a respirator in the treatment plane periphery that receive only 6% of the dose at the apex of the central N95 (Figure 7.6(e)). Due to the angular dependence of irradiance [14] as well as respirator self-shadowing stemming from the 3D morphology with respect to the UV-C source, the entire N95 surface must be considered when estimating UV-C dose for decontamination; measuring the irradiance in an empty system does not sufficiently predict irradiance on the N95 surface. Scientific evidence suggests that all N95 surfaces must receive $\geq 1.0 \text{ J/cm}^2$ UV-C dose for 3-log bioburden reduction of enveloped viruses [2–4]; however, our results show that 1.0 J/cm^2 delivered to the apex of the central N95 in this system would result in only 0.06 J/cm^2 applied to the side of an N95 placed in the periphery of the treatment plane. While this dose heterogeneity is certainly system- and N95 model-specific, it underscores the challenges of N95 decontamination and the critical importance of considering complex 3D geometries when designing and validating decontamination workflows.

In contrast with single-point radiometers, each PCI also records spatially-resolved doses (Figure 7.6(e)). As many N95 decontamination implementations track N95s using permanent marker labelling, we assessed whether such labels might shadow underlying respirator layers by positioning a pattern (‘Cal’) drawn on UV-C-transmitting film, ovetop a PCI1 during exposure. We observe pattern transfer onto the indicator (Figure 7.6(e)), suggesting that material underneath marker labels is not as effectively decontaminated as unmarked regions. These examples of on-respirator dose quantification and spatially-resolved measurement illustrate the novel, robust measurements PCIs can provide when combined with suitable, spatially-resolved readout tools (vs. the single-measurement spectrophotometer), better informing UV-C treatment design.

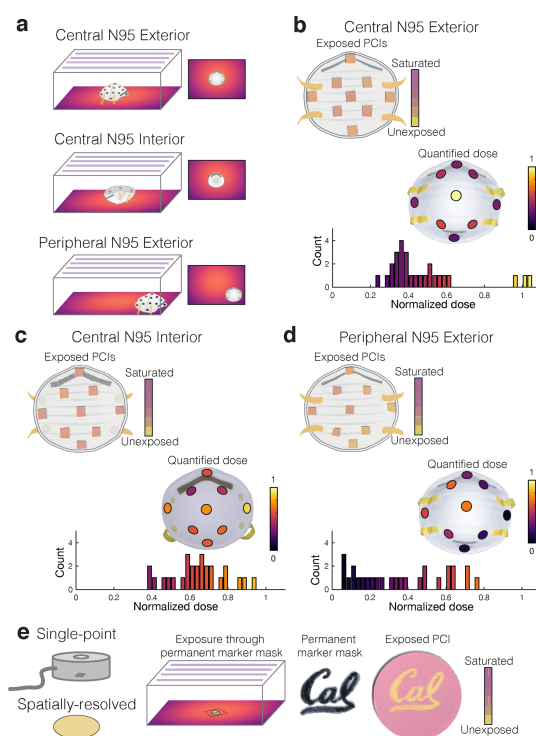


Figure 7.6: Quantifying PCIs elucidates UV-C treatment questions not measurable with radiometers. (a) Illustration of the three sets of on-N95 measurements, mapping dose across: (1) the exterior of an N95 placed in the treatment plane center (highest-dose region), (2) the interior of an N95 placed in the treatment plane center, (3) the exterior of an N95 placed in the treatment plane periphery (lowest-dose region). (b-d) Scanned PCI1 images and corresponding UV-C dose quantified from PCI1 at various respirator surface locations. Although PCI color differences can appear subtle, quantification reveals substantial dose variation. Each relative dose measurement is normalized to the measurement at the apex of the central ‘convex-up’-oriented (exterior) respirator. Scanned images show a representative replicate, on-N95 heatmaps plot the mean of $N = 3$ measurements, while the histograms below each measurement plot all individual measurements. (b) Exterior of central respirator; $\sim 3 - 4\times$ dose difference is measured across the respirator surface. (c) Interior of central respirator. (d) Exterior of peripheral respirator. The corner-facing side of the N95 at the peripheral location is only exposed to $6.3 \pm 1.1\%$ of the dose delivered to the apex of the central respirator. (e) PCIs are 2-dimensional surface-like sensors that facilitate spatially resolved measurements. We leveraged this characteristic to show that permanent marker (‘Cal’ pattern) on a UV-C-transparent film placed atop PCI1 can mask UV-C exposure, suggesting that markings on respirators should be minimized. PCI1 changes from yellow to pink as it is exposed to higher UV-C doses (see Figure 7.2A); yellow regions correspond to areas shadowed by the marker.

Device-specific calibration facilitates quantification using widely-available imaging tools

To overcome spectroradiometer limitations (e.g., cost, availability, and throughput) as well as capture spatial information already recorded in the PCIs, we generated and assessed device-specific calibration curves using widely-available imaging tools under controlled lighting conditions. The calibration curves were generated from raw images of PCIs acquired using a flatbed scanner (Canon LiDE-400), digital SLR camera (DSLR, Nikon D5500), and smartphone (iPhone X) (DSLR and iPhone images were acquired in a light box to provide isolation from ambient illumination). All tools captured the entire surface of both the exposed PCI as well as an unexposed reference. The resulting calibration curves were then compared to those generated with data from the RM200QC (Figure 7.7(a)). We observe the highest CIEDE2000 ΔE values from measurement with the cameras. Though the flatbed scanner measures the lowest ΔE values, its measurements correspond with those of the RM200QC and conveniently do not require a light box. We further assessed the squared sums of the residuals (SSE) for all fits as a measure of calibration accuracy (Figure 7.7(b)). We observe the lowest SSE for the RM200QC, but all imaging approaches yield PCI1 quantification meeting the 10% ideal target relative uncertainty for a $\sim 0.10 \text{ J/cm}^2$ dose. No PCI2 quantification met the ideal target, consistent with the model's higher relative uncertainty (Figure 7.2). The color measurement literature stresses that careful control of lighting conditions (e.g. using an enclosed light box or contact measurement) is critical in order to minimize variation induced by changes in ambient lighting [21, 37]. Even under identical lighting conditions with tight control of acquisition parameters, different imaging devices have different spectral sensitivities and color processing. For this reason, device-specific calibration (using a stringent color reference chart with a range of known colors) has been proposed as an essential step for image-based color quantification for several applications [22, 23, 37, 38]. A smartphone algorithm has been generated for this purpose [25], and flatbed scanners may be a promising, accessible approach provided raw images are acquired (e.g. with third-party software). Overall, these results suggest that with rigorous characterization and proper implementation, widely-available imaging tools are appealing for spatially-resolved PCI quantification.

Optical engineering extends the quantifiable dose range for in-process validation of UV-C dose during N95 decontamination

The commercial market for UV-C PCIs has focused on hard surface UV-C decontamination processes with orders-of-magnitude lower doses than required for N95 decontamination, and thus, at this time of this study, we determined that there were no PCIs for purchase that met the dose range requirements for in-process validation of N95 decontamination. Given the benefits of PCIs over radiometers, we next assessed whether a single 'snap-shot' dose/irradiance measurement could be extrapolated to accurately estimate the time required for the minimum dose specification (i.e., is irradiance temporally constant?) (Figure 7.8(a)).

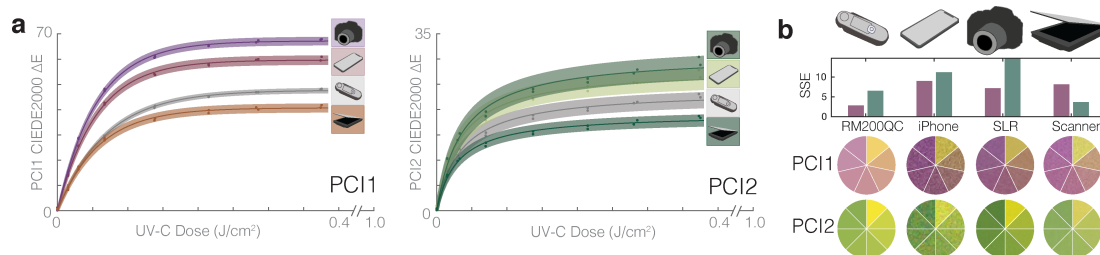


Figure 7.7: The potential applications for UV-C quantification from PCIs could be broadened using widely available color measurement tools. (a) Comparison of calibration curve fits of CIEDE2000 ΔE from an unexposed sensor vs. UV-C dose, for PCI1 and PCI2 colors quantified using the digital SLR and iPhone X in a light box, RM200QC spectrophotometer, and flatbed scanner. Datapoints within the shaded region denote individual PCI measurements, line denotes best fit, and shaded region denotes 95% prediction interval on prediction of color change from observation of UV-C dose. (b) Squared sum of the residuals (SSE) for each curve fit in (a), along with color comparison wheels showing indicator color at various doses as captured by the different imaging devices. Quantification of the dose-dependent relative uncertainty for each of the 8 curve fits is presented in S14 Fig.

Irradiance was found to substantially depend on UV-C system, warm-up status, and length of exposure, necessitating innovation to extend the quantifiable PCI dose range for in-process validation of UV-C N95 decontamination.

There are two potential solutions to extend the PCI dose range: (1) engineer the indicator (e.g. modified chemistry), or (2) engineer the system surrounding the indicator. Towards (2), we assessed the capacity of several materials to attenuate the UV-C reaching the indicator to a sufficient degree to facilitate dose quantification beyond 1.0 J/cm^2 (Figure 7.8(c-d)). We observe that commercial UV neutral density filters (1.3 OD) extend the quantifiable dose ($< 10\%$ relative measurement uncertainty on the PCI1 measurements) from 0.15 J/cm^2 up to 5.0 J/cm^2 to meet the in-process validation dose specification (Table 7.3). After validating that the quantifiable dose range could be extended beyond 1.0 J/cm^2 with attenuation, we investigated a less expensive, widely-available glass option. Although standard borosilicate or soda-lime glass slides and cover slips block UV-C and are thus not appropriate filter options, 1.1 mm Borofloat[®] glass offers much higher UV-C transmission [39] and is available in a range of sizes and shapes from multiple suppliers. The Borofloat[®] glass filters extended the quantifiable range of both PCIs beyond 1.0 J/cm^2 (Figure 7.8(c-d), with the PCI1 measurement uncertainty remaining below 10% up to 1.5 J/cm^2 (below 20% up to 2.0 J/cm^2).

The dose-response curves presented in Figure 7.8(c-d) illustrate how precise optical attenuators can be coupled with PCIs to extend quantifiable dose range; however, the implementation of this type of approach requires careful characterization. First, before implementing any filter material, both the filter-to-filter transmittance variability and the transmittance change with UV-C exposure (e.g. due to solarization [40]) need to be characterized. Trans-

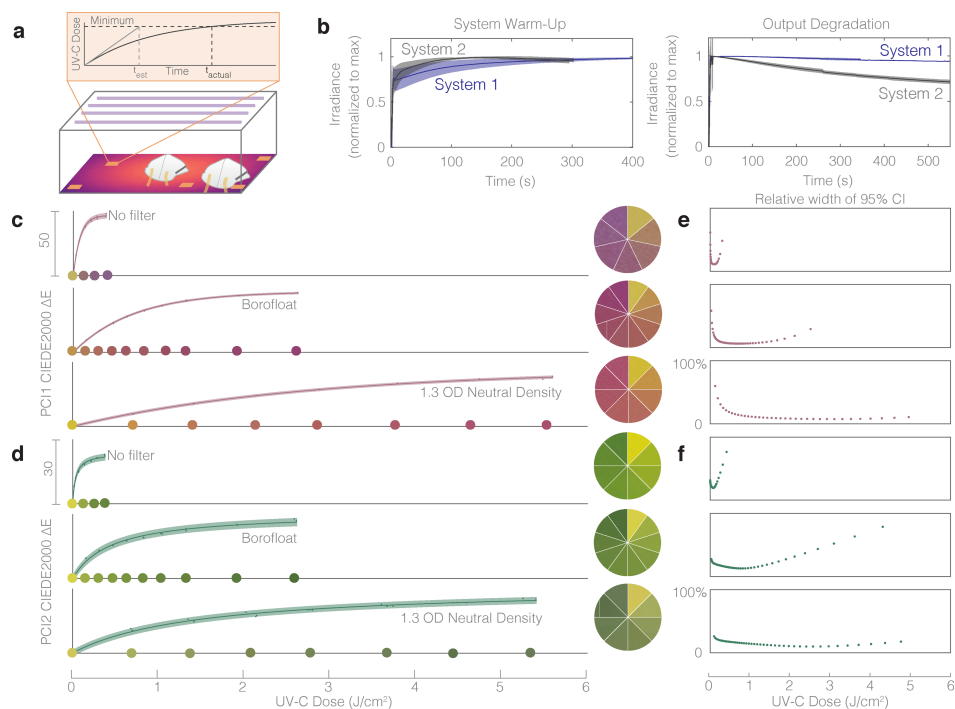


Figure 7.8: Quantitative in-process UV-C dose validation of N95 decontamination cycles using PCIs could be feasible using optical attenuation to extend the dynamic range beyond 1.0 J/cm^2 . (a) Treatment durations calculated from single ‘snap-shot’ dose measurements inaccurately assume constant irradiance by disregarding bulb warm-up and thermal output degradation during exposure. (b) Two near-identical UV-C exposure systems have significantly different output profiles over time, both during warm-up (left), and during long exposures (right). Plots depict mean (line) and standard deviation (shaded region) of the replicate measurements: $N = 16$ (System 1 warm-up); $N = 10$ (System 2 warm-up); $N = 19$ (System 1 long exposure); $N = 11$ (System 2 long exposure). (c-d) 1.1 mm thick Borofloat glass and 1.3 OD neutral density filters extend the dynamic range of (c) PCI1 and (d) PCI2 sensors. PCI1 no filter $R^2 = 0.998$, $a = 47.1$, $b = 80.4$. PCI1 with Borofloat filter $R^2 = 0.999$, $a = 47.3$, $b = 699$. PCI1 with 1.3 OD neutral density filter $R^2 = 0.998$, $a = 44.2$, $b = 2728$. PCI2 no filter $R^2 = 0.992$, $a = 47.7$, $b = 0.00060$. PCI2 with Borofloat filter $R^2 = 0.990$, $a = 61.8$, $b = 3.63 \times 10^{-5}$. PCI2 with 1.3 OD neutral density filter $R^2 = 0.992$, $a = 62.7$, $b = 1.10 \times 10^{-5}$. Color comparison wheels show PCI colors corresponding to doses marked along the x-axis, except in “No Filter” cases due to space constraints on the x-axis. Datapoints within the shaded region denote individual PCI measurements, line denotes best fit, and shaded region denotes 95% prediction interval on prediction of color change from observation of UV-C dose. (e-f) The relative width of quantified 95% confidence intervals on UV-C dose measurements from CIEDE2000 color difference between exposed and unexposed samples of (e) PCI1 and (f) PCI2, as a function of UV-C dose, plotted to the right of the corresponding dose-response curve.

mittance variability contributes to the uncertainty on any filtered dose measurement, while transmittance changes determine the usable lifetime of a filter (single-use vs. reuse). Second, the filter transmittance angular response needs to be assessed. Angular response can vary from the ideal cosine response based on a number of factors, including the angle-dependent optical path length through the attenuator or the angle-dependent reflectance. For a glass filter, these can be modelled using the Beer-Lambert law coupled with the Fresnel equations and Snell's law [41]. Third, filter materials should either be combined with a validated UV-C-specific photochromic indicator or have well-controlled transmission spectra to avoid a filter-indicator pair that primarily detects non-germicidal UV-A or UV-B wavelengths [7, 42]. Many common materials such as glass and plastics have lower UV-C transmission than that at longer wavelengths [7], and thus can filter out the critical wavelength range to be measured. The ideal filter would block all non-germicidal light and attenuate UV-C; however, as solarization rapidly changes transmittance and translatability requires inexpensive, widely-available materials, the ideal filter is not easily attainable. Neutral density or even higher UV-C (than longer wavelength) attenuation are acceptable when coupled with UV-C specific PCIs. Although important properties of the filter-indicator pair need to be characterized prior to implementation, the extension of quantifiable dose demonstrated in Figure 7.8(c-d) illustrates how Borofloat[®] glass or other attenuating materials can help to address the urgent need for in-process UV-C validation, complementing future innovation in photochromic chemistry.

7.4 Conclusions

Quantifying color from PCIs addresses urgent needs in UV-C dose measurement for (and beyond) N95 respirator decontamination. By tailoring established color measurement protocols to PCIs, we designed and validated a photochromic quantification workflow and then applied it to conduct measurements not robustly quantifiable with existing tools. Novel aspects of our workflow include quantifying CIEDE2000 for PCIs, implementing calibration informed by chemical kinetics, and quantifying PCI dose measurement uncertainty. Our workflow quantified performance specifications and revealed that while performance was highly PCI model-dependent, one indicator model met all specifications for informed design of UV-C N95 treatment systems: UV-C dose measurement range up to 0.15 J/cm^2 with relative measurement uncertainty of 8.3% at 0.1 J/cm^2 , $< 5\%$ response to UV-A/UV-B, and $> 90\%$ accuracy compared to a calibrated digital radiometer. Our workflow enabled on-respirator dose quantification, identifying nearly 20X dose nonuniformity across different N95 surface regions within a treatment system. As a result, the target dose delivered to the treatment plane within the UV-C system may need to be much higher than 1.0 J/cm^2 to ensure that all N95 surfaces are exposed to $> 1.0 \text{ J/cm}^2$. Because these dose nonuniformities across the N95 surface are model- and configuration-dependent, each treatment system should be characterized with the N95 models *in situ* for informed design of UV-C N95 treatment processes. PCI calibration curves for widely-available imaging tools like flatbed scanners,

iPhones, and DSLRs also meet minimum performance specifications and facilitate accessible, spatially-resolved dose measurements. In future work, intercalation of PCIs between each N95 material layer would quantify spatially resolved UV-C attenuation in the interstices of each porous layer, improving our understanding of complex multi-layer materials. Finally, PCI dynamic range can be extended by coupling with optical attenuators of known transmittance. Although important open questions remain for these attenuators (such as optical transmission stability and angular response), filter-coupled PCIs are promising for high-throughput in-process dose validation for UV-C N95 decontamination. We anticipate that the PCI quantification workflow will be widely applied to meet the current urgent validation need, facilitating (1) informed design of UV C treatment protocols to ensure that all N95 surfaces are exposed to the minimum dose, (2) in-process dose validation of each cycle, and (3) robustness characterization of new PCI materials.

Bibliography

1. CDC. *Decontamination and Reuse of Filtering Facepiece Respirators* en-us. source: [www.cdc.gov](https://www.cdc.gov/coronavirus/2019-ncov/hcp/ppe-strategy/decontamination-reuse-respirators.html). Feb. 11, 2020. <https://www.cdc.gov/coronavirus/2019-ncov/hcp/ppe-strategy/decontamination-reuse-respirators.html>.
2. Lore, M. B. *et al.* Effectiveness of Three Decontamination Treatments against Influenza Virus Applied to Filtering Facepiece Respirators. *The Annals of Occupational Hygiene* **56**, 92–101. ISSN: 0003-4878 (Aug. 22, 2011).
3. Mills, D. *et al.* Ultraviolet germicidal irradiation of influenza-contaminated N95 filtering facepiece respirators. en. *American Journal of Infection Control* **46**, e49–e55. ISSN: 01966553 (July 2018).
4. Brian Heimbuch, D. H. *Research to Mitigate a Shortage of Respiratory Protection Devices During Public Health Emergencies* tech. rep. [Online; accessed 2020-03-27] (2019).
5. Lindsley, W. G. *et al.* Effects of Ultraviolet Germicidal Irradiation (UVGI) on N95 Respirator Filtration Performance and Structural Integrity. *Journal of Occupational and Environmental Hygiene* **12**. publisher: Taylor Francis, 509–517. ISSN: 1545-9624 (Aug. 3, 2015).
6. Lowe, J. J. *et al.* *N95 Filtering Facemask Respirator Ultraviolet Germicidal Irradiation (UVGI) Process for Decontamination and Reuse* en. Tech. rep. (2020). <https://www.nebraskamed.com/sites/default/files/documents/covid-19/n-95-decon-process.pdf>.
7. Kowalski, W. *Ultraviolet Germicidal Irradiation Handbook: UVGI for Air and Surface Disinfection* en. DOI: 10.1007/978-3-642-01999-9. ISBN: 978-3-642-01998-2. <http://link.springer.com/10.1007/978-3-642-01999-9> (Springer Berlin Heidelberg, Berlin, Heidelberg, 2009).
8. Beck, S. E. *et al.* Wavelength-Dependent Damage to Adenoviral Proteins Across the Germicidal UV Spectrum. en. *Environmental Science Technology* **52**, 223–229. ISSN: 0013-936X, 1520-5851 (Jan. 2, 2018).
9. Fisher, E. & Shaffer, R. A method to determine the available UV-C dose for the decontamination of filtering facepiece respirators: UV-C decontamination of respirators. en. *Journal of Applied Microbiology* **110**, 287–295. ISSN: 13645072 (Jan. 2011).

10. Ozog, D. M. *et al.* The Effect of Ultraviolet C Radiation Against Different N95 Respirators Inoculated with SARS-CoV-2. en. *International Journal of Infectious Diseases*. ISSN: 12019712 (Sept. 2020).
11. Cadnum, J. L. *et al.* Effectiveness of Ultraviolet-C Light and a High-Level Disinfection Cabinet for Decontamination of N95 Respirators. en. *Pathogens and Immunity* **5**. number: 1, 52–67. ISSN: 2469-2964 (May 2, 2020).
12. Heimbuch, B. K. *et al.* A pandemic influenza preparedness study: Use of energetic methods to decontaminate filtering facepiece respirators contaminated with H1N1 aerosols and droplets. en. *American Journal of Infection Control* **39**, e1–e9. ISSN: 01966553 (Feb. 2011).
13. Tseng, C.-C. & Li, C.-S. Inactivation of Viruses on Surfaces by Ultraviolet Germicidal Irradiation. en. *Journal of Occupational and Environmental Hygiene* **4**, 400–405. ISSN: 1545-9624, 1545-9632 (Apr. 23, 2007).
14. Reifsnyder, W. E. Radiation geometry in the measurement and interpretation of radiation balance. en. *Agricultural Meteorology* **4**, 255–265. ISSN: 00021571 (July 1967).
15. Bolton, J. R. & Linden, K. G. Standardization of Methods for Fluence (UV Dose) Determination in Bench-Scale UV Experiments. en. *Journal of Environmental Engineering* **129**, 209–215. ISSN: 0733-9372, 1943-7870 (Mar. 2003).
16. Lawal, O. *et al.* Method for the Measurement of the Output of Monochromatic (254 nm) Low-Pressure UV Lamps. en. *IUVA News* **19**, 9–16.
17. Reed, N. G., Wengraitis, S. & Sliney, D. H. Intercomparison of Instruments Used for Safety and Performance Measurements of Ultraviolet Germicidal Irradiation Lamps. en. *Journal of Occupational and Environmental Hygiene* **6**, 289–297. ISSN: 1545-9624, 1545-9632 (Apr. 6, 2009).
18. Schmalwieser, A. W. Fifteen years of experience with standardized reference radiometers for controlling low-pressure UV disinfection plants for drinking water. en. *Water Supply* **17**, 975–984. ISSN: 1606-9749, 1607-0798 (July 1, 2017).
19. Lindblad, M. *et al.* Ultraviolet-C decontamination of a hospital room: Amount of UV light needed. en. *Burns* **46**, 842–849. ISSN: 03054179 (June 2020).
20. D2244-16, A. S. Standard Practice for Calculation of Color Tolerances and Color Differences from Instrumentally Measured Color Coordinates. *ASTM International* (2016).
21. Cui, G *et al.* Grading textile fastness. Part 1; Using a digital camera system. en. *Coloration Technology* **119**, 212–218. ISSN: 1472-3581, 1478-4408 (July 2003).
22. Carpenter, K. & Farnand, S. Assessing the use of smartphones to determine crop ripeness. en. *Electronic Imaging*. [Online; accessed 2020-04-12]. ISSN: 2470-1173. <https://www.ingentaconnect.com/content/10.2352/ISSN.2470-1173.2020.12.FAIS-173> (2020).

23. Soda, Y. & Bakker, E. Quantification of Colorimetric Data for Paper-Based Analytical Devices. en. *ACS Sensors* **4**, 3093–3101. ISSN: 2379-3694, 2379-3694 (Dec. 27, 2019).
24. Singh, G. *et al.* Colorimetric detection and ratiometric quantification of mercury(II) using azophenol dye: ‘dip read’ based handheld prototype device development. en. *Journal of Materials Chemistry C* **6**, 12728–12738. ISSN: 2050-7526, 2050-7534 (2018).
25. Yetisen, A. K. *et al.* A smartphone algorithm with inter-phone repeatability for the analysis of colorimetric tests. en. *Sensors and Actuators B: Chemical* **196**, 156–160. ISSN: 09254005 (June 2014).
26. Solari, F. *et al.* A New Method for the Validation of Ultraviolet Reactors by Means of Photochromic Materials. en. *Food and Bioprocess Technology* **8**, 2192–2211. ISSN: 1935-5130, 1935-5149 (Nov. 2015).
27. Luo, M. R., Cui, G. & Rigg, B. The development of the CIE 2000 colour-difference formula: CIEDE2000. en. *Color Research Application* **26**, 340–350. ISSN: 0361-2317, 1520-6378 (Oct. 2001).
28. NIST/SEMATECH. *2.3.6.7.1. Uncertainty for quadratic calibration using propagation of error* June 13, 2020. <https://www.itl.nist.gov/div898/handbook/mpc/section3/mpc3671.htm> DOI:10.18434/M32189.
29. NIST/SEMATECH. *4.5.2.1. Single-Use Calibration Intervals* June 13, 2020.
30. Biguri, A. *Perceptually uniform colormaps* [Online; accessed 2020-06-13]. 2020. <https://www.mathworks.com/matlabcentral/fileexchange/51986-perceptually-uniform-colormaps>.
31. Rehfuss, E. & Organization, W. H. *Global solar UV index: a practical guide*. en. OCLC: 51304373. ISBN: 978-92-4-159007-5 (World Health Organization, Geneva, Switzerland, 2002).
32. Larason, T & Ohno, Y. Calibration and characterization of UV sensors for water disinfection. en. *Metrologia* **43**, S151–S156. ISSN: 0026-1394, 1681-7575 (Apr. 2006).
33. Larason, T. & Cromer, C. Sources of error in UV radiation measurements. en. *Journal of Research of the National Institute of Standards and Technology* **106**, 649. ISSN: 1044677X (July 2001).
34. Soda, Y. *et al.* Colorimetric absorbance mapping and quantitation on paper-based analytical devices. en. *Lab on a Chip* **20**, 1441–1448. ISSN: 1473-0197, 1473-0189 (2020).
35. Abdel-Fattah, A. A., El-Kelany, M. & Abdel-Rehim, F. Development of a radiation-sensitive indicator. en. *Radiation Physics and Chemistry* **48**, 497–503. ISSN: 0969-806X (Oct. 1, 1996).
36. El Seoud, O. A., Baader, W. J. & Bastos, E. L. en. in *Encyclopedia of Physical Organic Chemistry, 5 Volume Set* (ed Wang, Z.) DOI: 10.1002/9781118468586.epoc1012, 1–68 (John Wiley Sons, Inc., Hoboken, NJ, USA, Nov. 2, 2016). ISBN: 978-1-118-47045-9. <http://doi.wiley.com/10.1002/9781118468586.epoc1012>.

37. Nixon, M. *et al.* The importance of a device specific calibration for smartphone colorimetry. en. *Color and Imaging Conference* **2019**, 49–54. ISSN: 2166-9635 (Oct. 21, 2019).
38. Martinez, A. W. *et al.* Simple Telemedicine for Developing Regions: Camera Phones and Paper-Based Microfluidic Devices for Real-Time, Off-Site Diagnosis. en. *Analytical Chemistry* **80**, 3699–3707. ISSN: 0003-2700, 1520-6882 (May 2008).
39. GmbH, S. T. G. S. *BOROFLOAT® 33 – Optical Properties* [Online; accessed 2020-07-07]. https://www.schott.com/d/borofloat/bde16ad3-70e5-48a0-b8ac-9146fcd34511/1.0/borofloat33_opt_en_web.pdf.
40. Natura, U. *et al.* Formation of radiation defects in high-purity silicate glasses in dependence on dopants and UV radiation sources. en. *Glastech. Ber. Glass Science and Technology* **74**, 23–31 (2001).
41. Furler, R. A. Angular Dependence of Optical Properties of Homogeneous Glasses. en. *ASHRAE Transactions* **98**, 1–9 (1991).
42. Lytle, C. D. & Sagripanti, J.-L. Predicted Inactivation of Viruses of Relevance to Biodefense by Solar Radiation. en. *Journal of Virology* **79**, 14244–14252. ISSN: 0022-538X (Nov. 15, 2005).

Chapter 8

Best Practices for Germicidal Ultraviolet-C Dose Measurement for N95 Respirator Decontamination

Materials reproduced, with permission, from:

A. Geldert*, H. B. Balch*, A. Gopal, A. Su, S. M. Grist, and A. E. Herr, “Best Practices for Germicidal Ultraviolet-C Dose Measurement for N95 Respirator Decontamination”, *J. Res. Natl. Inst. Stand. Technol.*, 2021.

* Equal contributors

8.1 Introduction

The coronavirus disease 2019 (COVID-19) pandemic led to severe shortages of N95 filtering facepiece respirators, which are essential personal protective equipment (PPE) for healthcare professionals worldwide. In response, the U.S. Centers for Disease Control and Prevention (CDC) issued guidelines for decontamination and reuse of N95 respirators as a crisis-capacity strategy and identified ultraviolet-C (UV-C) germicidal irradiation as one of the most promising methods for primary decontamination [1]. UV-C plays an important role in infection control across the medical industry, but, due to the complex geometry and material properties of N95 respirators, the UV-C measurement considerations for N95 respirator decontamination differ substantially from more established applications of germicidal UV-C. Safe and effective UV-C decontamination depends critically on (1) the spectral overlap between the emission spectrum of the light source and the wavelengths capable of inactivating the pathogen (i.e., the action spectrum), and (2) the amount of energy that is delivered to the pathogen (fluence, often described as dose). However, accurately measuring and reporting these characteristics for UV-C N95 respirator decontamination systems can be complicated, and measurement standards targeting the unique challenges of complex, multimaterial N95 respirators remain in development.

Accurate measurements of UV-C dose are central both for verifying that decontamination systems are operating within specification and for reproducible reporting. UV-C dose measurements provide a key link in the translation of effective and reproducible decontamination protocols across different communities, from UV-C device manufacturers and researchers to infection-control staff implementing UV-C N95 respirator decontamination. In this paper, we highlight key measurement considerations for researchers, engineers, and clinical staff who are evaluating and implementing UV-C-based decontamination of N95 respirators. First, we highlight the technical and regulatory context for UV-C N95 respirator decontamination; second, we discuss the science behind UV-C decontamination, highlighting the central importance of both wavelength and dose in viral inactivation; third, we examine techniques and common pitfalls in UV-C dose measurement; and finally, we outline best practices that help to avoid these pitfalls.

8.2 UV-C for N95 Respirator Decontamination

UV-C radiation is widely used as a secondary technique for decontamination of air [2], water [3], and nonporous surfaces [4]. Until April 2021, CDC guidance [1] and hospital protocols [5] indicated that UV-C was used during the COVID-19 pandemic as a primary and stand-alone decontamination method for N95 respirators under crisis-capacity conditions [6]. As a primary decontamination technique, the application of UV-C to N95 respirators requires specific consideration of the complex geometry, porous multimaterial electret layers, and filtration central to N95 respirator function. For example, UV-C radiation is heavily attenuated when passing through non-UV-C-transparent and scattering materials; dose received at interior layers may be orders of magnitude lower than the applied dose at the outer surface of the N95 respirator (Figure 8.1A) [7]. UV-C attenuation through the porous layers requires special consideration to ensure that the dose received at all contaminated layers within the respirator is sufficient for decontamination [7]. Consequently, decontamination of porous materials can require 100× higher applied dose at the surface than that required for nonporous surfaces with low surface roughness [8, 9], but excessive doses can reduce respirator function [10]. The electrostatic respirator filter material is also damaged by chemical disinfectants such as ethanol [11], limiting the use of some primary healthcare surface disinfectants. Furthermore, the complex three-dimensional geometry of N95 respirators can result in the received dose varying several-fold across a single N95 respirator [12, 13] and about twenty-fold across different N95 respirators within one decontamination system [13], with received dose strongly dependent on the incident angle of UV-C irradiation (Figure 8.1A–B) [14].

Due to the technical challenges and additional considerations required for implementing UV-C decontamination for N95 respirators, federal guidelines for UV-C decontamination of N95 respirators remain in development [15]. For example, the CDC has assessed the impact of several UV-C N95 respirator decontamination systems on the fit and filtration of specific N95 respirator models, but the assessment “is not to determine the effectiveness of the

decontamination procedure at killing the pathogenic microorganism” [16]. The U.S. Food and Drug Administration (FDA) guidelines emphasize that while the FDA regulates UV-C sources, the lack of clear and standardized manufacturer data on wavelength, duration, and associated dose of UV-C radiation required to inactivate severe acute respiratory syndrome coronavirus 2 (SARS-CoV-2), the strain of coronavirus that causes COVID-19, presents an outstanding challenge [17]. In addition, the FDA allows previously approved devices to be extended to SARS-CoV-2 inactivation [18]. However, the FDA requires previously approved devices to submit Emergency Use Authorizations (EUAs) and 510(k) when adapted to new applications including decontamination of N95 respirators and other single-use PPE [14]. A 510(k) is a premarket submission made to the FDA to demonstrate that a device to be marketed is as safe and effective as a legally marketed device. For example, a steam sterilization device with prior 510(k) clearance for sterilization of other materials in healthcare settings required an FDA-issued EUA before it was approved for N95 respirator decontamination [19]. While the FDA has issued numerous EUAs for devices implementing the other two PPE decontamination methods (moist heat and vaporous hydrogen peroxide) [19, 20] identified promising by the CDC for crisis-capacity conditions, as of January 2021, only one limited EUA has been issued for the use of UV-C to reduce bioburden on one N95 respirator model [21].

Despite this context, the accessibility and relatively low cost of UV-C sources have led to widespread implementation of UV-C irradiation for N95 respirator decontamination in both research [11, 22, 23] and medical [5] environments. Decontamination system specifications depend on technical measurement factors, such as the wavelengths emitted, the wavelengths detected, the type and position of UV-C detector, and the method of analysis. Reports of UV-C-based decontamination of N95 respirators often fail to report the parameters necessary to ensure validation and reproducibility despite using diverse types of UV-C sources and different measurement devices. To accurately describe, evaluate, and reproduce UV-C decontamination protocols, parameters such as type, number, and location of UV-C sources, orientation and position of both N95(s) and UV-C detector(s) relative to UV-C source(s), models of N95 respirator and UV-C detector, decontamination chamber specifications (e.g., reflectivity), and other details of dose quantification (see Section 8.7), are needed. Omitting these parameters for the source, target, or detector when reporting decontamination procedures substantially limits validation and reproducibility. In addition, standards for measurement are currently limited, which impedes comparison of UV-C sources and detectors [24]. In particular, minimum reporting standards for systems claiming UV-C decontamination of N95 respirators are urgently needed to facilitate comparison and critical evaluation. Here, we provide an overview of UV-C measurement fundamentals to inform the development of measurement and reporting standards for UV-C N95 respirator decontamination systems.

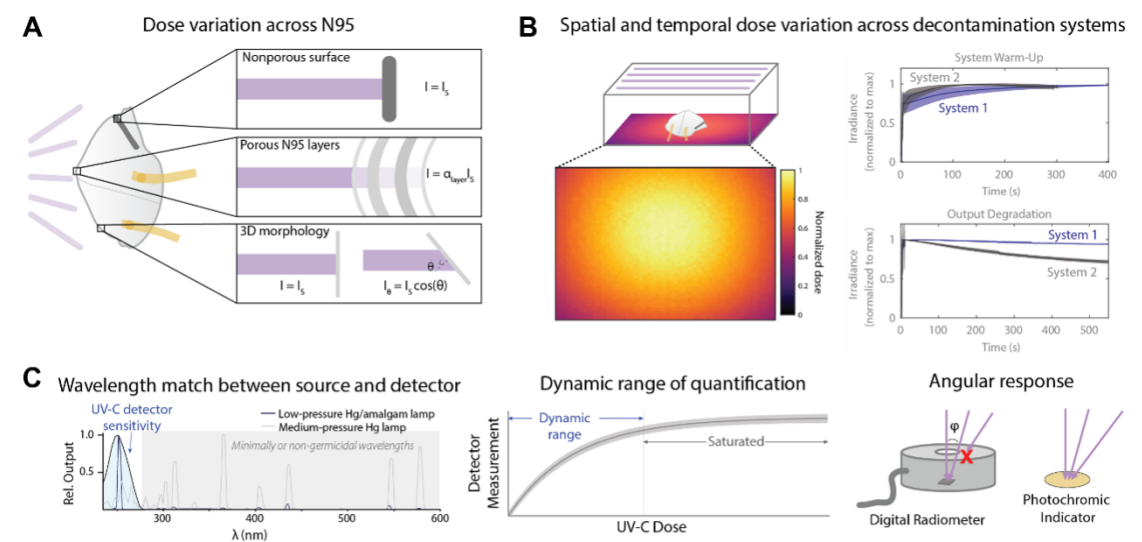


Figure 8.1: Factors affecting UV-C dose distribution and measurement for N95 respirator decontamination. (A) Factors affecting UV-C dose applied to the N95 respirator. Sloped surfaces and attenuation by the N95 layers reduce received UV-C dose. Received UV-C intensity (I) is reduced from the intensity normally incident on the top surface (I_s) by a layer-dependent attenuator factor (α_{layer}) and by a factor of the cosine of the angle of incidence (θ). (B) Factors affecting UV-C dose distribution within a decontamination system. UV-C irradiance can vary spatially and temporally. (C) Key specifications of UV-C detectors, including wavelength specificity, dynamic range, and angular response (ϕ denotes the radiometer field-of-view angle). Figure is adapted with permission from Su *et al.* [13].

8.3 Key Germicidal UV-C Specifications: Wavelength and Dose

Not all wavelengths of UV radiation offer sufficient germicidal efficacy for N95 respirator decontamination. Absorbed germicidal UV-C radiation (200 nm to 280 nm) inactivates pathogens by promoting photochemical reactions that damage proteins and genomic material [25, 26]. Distinct wavelengths have different microbe-specific germicidal efficacy, a relationship represented in what is known as the action spectrum of a microbe. The overlap between the action spectrum and the UV-C source emission spectrum will determine the efficiency of germicidal action, with higher efficiency when the overlap is greater. For many pathogens, there is a peak in the action spectrum at the absorption maximum of genomic material, around 260 nm. While research into the germicidal action spectrum of SARS-CoV-2 is ongoing, a working assumption is that the action spectrum will be similar to that of viral analogues with similar structure that exhibit a peak near 260 nm [26, 27].

Germicidal UV-C radiation sources emit close to this maximum, such as the narrow

emission around 254 nm from low-pressure mercury (Hg) lamps commonly used as germicidal sources. The relative efficacy of emerging monochromatic and polychromatic UV-C sources is also an area of active research, highlighting the importance of rigorous measurement and reporting to facilitate accurate comparison of sources with different emission spectra. While shorter wavelengths within the UV-C range (200 nm to 280 nm) can have higher germicidal efficacy [26], these wavelengths may be more strongly attenuated by the multiple N95 layers, requiring confirmation of dose and viral inactivation on interior layers. Longer-wavelength UV radiation (≥ 280 nm), such as UV-B and UV-A in sunlight, has substantially lower germicidal activity [28] and has not been shown to decontaminate porous materials such as N95 respirators. While UV-B (280 nm to 320 nm) can photochemically damage nucleic acids, UV-B is orders of magnitude less efficient than UV-C wavelengths [28] due to reduced overlap with the absorption spectrum of nucleic acids. While UV-A (320 nm to 400 nm) can generate reactive oxygen species to contribute to pathogen inactivation (particularly in water) [29, 30], UV-A is generally not considered to be germicidal [26]. Because absorption by the multiple porous N95 layers causes N95 respirator decontamination to require about $100\times$ higher applied dose [7] as compared to more common applications (e.g., air, water, nonporous surface decontamination), UV-A and UV-B likely have insufficient germicidal efficacy to be feasible for N95 respirator decontamination. Efficacy of germicidal UV-C also depends critically on dose. Studies on other coronaviruses and influenza viruses indicate that 254 nm UV-C doses (from a low-pressure mercury UV-C source) of at least 1.0 J/cm^2 at the N95 respirator surface can lead to 99.9 % viral inactivation on most N95 respirator models [8, 31]. Preliminary studies using both UV-C light-emitting diodes (LEDs) and mercury lamps have found that UV-C doses of at least 1.5 J/cm^2 are required to yield 99.9 % inactivation of SARS-CoV-2 on some N95 respirator models [11, 23], and research on SARS-CoV-2 inactivation on N95 respirators is ongoing. On the other hand, studies indicate that doses over 120 J/cm^2 can cause respirator degradation [10]. Because it is infeasible to measure UV-C dose delivered to viral particles embedded in the interior layers of the respirator during a decontamination cycle, the dose required for pathogen inactivation or degradation is typically reported in terms of dose applied at the respirator surface. However, because UV-C transmission through N95 respirator layers is dependent on the N95 model [7], the minimum dose applied at the N95 surface for pathogen inactivation throughout all N95 layers will differ from model to model. These examples underscore the importance of accurate measurement and reporting of UV-C wavelength and dose when using germicidal UV-C for effective and reproducible decontamination of N95 respirators.

8.4 Critical UV-C Source and Detector Metrics

Applying sufficient UV-C dose to N95 respirators can make—or break—effective decontamination [32]. While measurement of pathogen inactivation is the most direct way of verifying decontamination efficacy on N95 respirators, this approach is time- and resource-intensive. It is largely infeasible to perform pathogen inactivation assays at the frequency necessary

to validate the ongoing efficacy of UV-C decontamination systems, especially in healthcare settings. UV-C decontamination systems must be regularly validated because the irradiance reaching an N95 respirator can vary with UV-C light source age, environmental factors such as temperature, and setup-dependent shadowing or reflections. In particular, the material properties of nearby surfaces, such as UV-C reflectivity, have a substantial influence on the spatial pattern and magnitude of UV-C dose delivered to N95 respirators [33, 34]. Thus, even if the UV-C output or pathogen inactivation efficacy of a particular UV-C lamp or decontamination system has been rigorously characterized by the manufacturer, frequent UV-C dose measurements are a more scalable, reliable, and cost-effective method (as compared to pathogen inactivation testing) for end users to ensure the system continues to operate within specification in the particular user environment.

Despite its critical role, UV-C dose is not always calculated or reported in a standardized way [24]. Dose (energy, in J/cm^2) is the integrated irradiance measured on a surface (W/cm^2) over the exposure time (s). Germicidal efficacy is wavelength dependent. Thus, to compare UV-C sources with different emission spectra and to evaluate overlap between a UV-C source and the pathogen action spectrum, dose reported from polychromatic sources should weight each wavelength by its respective relative germicidal efficacy [35, 36]. Unless a detector is omnidirectional, measured UV-C dose will depend on the location and orientation of the UV-C detector with respect to the source. As a result, to ensure reproducibility, it is critical to measure and report UV-C dose along with parameters such as UV-C source, distance from and position with respect to the source, measured irradiance, and exposure time (see Section 8.7).

Accurate dose measurements depend on the selection of an appropriate UV-C sensor. Detectors such as radiometers, dosimeters, and dose indicator strips are all used to measure and/or calculate UV-C dose. Characteristics of UV-C sensors, such as the sensor wavelength sensitivity spectrum, dynamic range, and angular response strongly affect measured values. As a result, it is important to consider the working principle of the sensor when matching a sensor to a given application. For example, radiometers can provide quantitative measurements appropriate for research or validation environments, but radiometers that do not have an ideal cosine response (e.g., those that are designed for collimated sources) will not accurately report UV-C doses from non-normal incident radiation. Additionally, angular response of UV-C sensors is often not characterized or provided. Spherical actinometric detectors relate the detector quantum yield to the dose on a surface, are widely used to calibrate physical sensors, and accurately measure dose on complex geometries. However, actinometry can be labor intensive, and the diversity of chemical transitions used in actinometry requires careful reporting for accurate measurement and reproducibility [35, 37]. Low-cost photochromic dose indicator strips can offer a straightforward colorimetric indicator of dose range, are commonly used in healthcare settings, and may facilitate implementation of UV-C decontamination across both low- and high-resource environments. However, these qualitative indicators are subject to potential pitfalls: Dose indicator strips are commonly sensitive to both UV-B and UV-C, and those designed for nonporous or low-dose applications frequently have insufficient dynamic range, saturating below the $1.0 \text{ J}/\text{cm}^2$ dose required for

decontamination of many N95 respirator models [13, 38]. Thus, even when the goal is simply to verify that a decontamination system is operating within specification, it is critical to understand the specificity and dynamic range of qualitative UV-C dose indicators. The ability to perform reproducible UV-C decontamination of N95 respirators, whether in the laboratory or the clinic, requires applied dose to be measured with a UV-C-specific sensor capable of measuring at least 1.0 J/cm^2 and with maximum sensitivity aligned with the pathogen action spectrum (e.g., 260 nm). If the detector has a nonideal angular response, the beam divergence at the detector should be identical to the conditions under which the sensor was calibrated, without which measurement errors are common (Figure 8.1C).

8.5 Common Measurement Pitfalls

Several common pitfalls hinder accurate measurements of UV-C wavelength and dose, some of which are listed in Table 8.1. One common source of error is a mismatch between the light source and detector. For example, dose measurements with a broadband sensor will collect not only germicidal UV-C but also minimally or nongermicidal wavelengths such as UV-A/B, visible, and infrared radiation, often with even greater sensitivity. Unless UV-C is specifically isolated at the sensor (e.g., with a bandpass filter), this mismatch will yield artificially high readings of UV-C dose. While different standards define different acceptable wavelength ranges of sensor sensitivity for different applications [35, 39, 40], sensors specifically used to measure UV-C should only be responsive to UV-C wavelengths between 200–300 nm and with peak response at the emission peak of the UV-C source (e.g., 254 nm for low-pressure mercury lamps) [39]. Methods used to calculate a correction factor to account for the wavelength dependence of a sensor are further described by Bolton and Linden [35]. Another common mistake is in mapping measurements of power or irradiance to dose. Since the irradiation of a UV-C source can vary over both space and time (Figure 8.1B), calculations of dose determined by multiplying a single irradiance measurement by exposure time can result in overestimates or underestimates of the dose applied (as shown in Table 8.2). Instead, applied dose is more accurately determined by integrating irradiance measured throughout the entire exposure time, to account for fluctuations in applied irradiance.

Many of the risks associated with over- or underestimating applied dose can be managed with an understanding of the working principles of the UV-C source and detector and through adequate reporting. However, the implications of over- or underreporting UV-C dose applied to N95 respirators are wide-ranging and user-dependent, as demonstrated in Table 8.2. For example, if researchers studying viral inactivation overestimate the UV-C dose required to decontaminate N95 respirators (e.g., reported dose is higher than true delivered dose), then this can provide a margin of safety; however, if clinical staff overestimate the UV-C dose delivered to N95 respirators during a decontamination cycle, then this could result in incomplete decontamination and create a transmission risk. Understanding the best practices in UV-C dose measurement can help users choose the most conservative UV-C measurement approach for their application.

8.6 Best Practices for UV-C Measurements and Methods

Because UV-C dose is the key metric used to link research to implementation, understanding the best practices for characterizing and reporting UV-C dose for UV-C decontamination systems is critical for both the research and clinical communities. The measurement needs differ among communities (e.g., precise, quantitative UV-C dose readout may be valuable for researchers studying the effect of UV-C on pathogen inactivation or N95 respirator function, while clinical staff may solely need to verify that the UV-C dose applied to N95 respirators is within a specified range). However, a shared understanding of the factors impacting UV-C dose measurements is critical to allow users to accurately evaluate and implement UV-C methods for N95 respirator decontamination, in the context of current federal regulations. Here, we outline key considerations for multiple user groups when studying, evaluating, or implementing UV-C N95 respirator decontamination.

In Research

Researchers developing or studying UV-C N95 respirator decontamination systems can support safe and effective UV-C N95 respirator decontamination both in the way they perform and report UV-C measurements. In making UV-C measurements, consider the implications of over- and underestimating dose and choose the most conservative option (yellow cells in Table 8.2). For clinical staff to evaluate and reproducibly implement UV-C methods for N95 respirator decontamination, researchers and device manufacturers also must report in sufficient detail the way in which UV-C measurements were made [24]. Best practices, or “minimum reporting standards,” are common across scientific disciplines [41, 42]. These standards would be valuable for UV-C decontamination of N95 respirators. Standards should include physical specifications for both the UV source and the optical detector, along with necessary optical elements such as filters, diffusers, or cosine correctors. Data acquisition and analysis should also be explicitly reported, describing how dose was measured and calculated and how (or if) viral inactivation was verified. A list of suggested reporting parameters can be found in Section 8.7. Thorough and standardized reporting provides a path to sidestep common pitfalls and realize the potential for UV-C to dramatically mitigate crisis-capacity conditions.

In Clinical Implementation

In evaluating UV-C decontamination systems: When reading and interpreting research, it is important for users to understand how UV-C dose was measured and to critically evaluate the accuracy of reported UV-C dose. To ensure N95 respirator decontamination, data should establish UV-C-induced viral inactivation on the specific N95 respirator model and in an enclosure that is comparable to that available at the workplace. To ensure that

Table 8.1: Common pitfalls in UV-C dose measurement for N95 decontamination.

Pitfall	Examples
Wavelength mismatch between UV-C source and sensor	<ul style="list-style-type: none"> - Sensor does not detect the UV-C germicidal wavelengths because sensor is specific for UV-A/UV-B wavelengths (280-400 nm). - Sensor is broadband and measures a range of wavelengths across the UV, visible, or infrared spectrum, making it impossible to determine the UV-C-specific contribution to irradiance or dose without additional filters.
Dose indicators or sensors with insufficient dynamic range	<ul style="list-style-type: none"> - Photochromic dose indicator does not change color beyond 100 mJ/cm². - Incident irradiance is not matched to the sensor dynamic range (e.g., irradiance is lower than the sensor noise floor or higher than the sensor saturation limit).
Dose calculated using a single measured irradiance value	<ul style="list-style-type: none"> - Irradiance is measured at a single time point but does not remain constant throughout the exposure period due to system-dependent variation in lamp output. - Irradiance measured at a single N95 location does not represent irradiance received across all surfaces of N95s located closer/farther from the UV-C source or closer/farther from reflective surfaces.
Sensor with limited angular response	<ul style="list-style-type: none"> - Incident light is only partially collected by the radiometer (e.g., due to a sensor housing or sensor field of view that is narrower than the light source output).
Dose calculated using rated UV-C lamp power	<ul style="list-style-type: none"> - Identical UV-C lamp bulbs with identical make, model, and power ratings may have differing output efficiencies.

Table 8.2: Importance of Considering Over- and Under-reporting of UV-C Dose

Problem		Underreporting of UV-C dose <i>Measured or reported dose is lower than true delivered dose</i>	Overreporting of UV-C dose <i>Measured or reported dose is higher than true delivered dose</i>
How? <i>Example case listed; see Table 1 for additional pitfalls</i>		Dose is calculated from a single irradiance measurement made at the start of the exposure period, but lamp output increases throughout the exposure period as the lamp warms up . The irradiance measurement underestimates the average irradiance over the exposure period, and thus reported (calculated) UV-C dose is lower than the true delivered dose.	Dose is calculated from a single irradiance measurement made at the start of the exposure period, but lamp output decreases throughout the exposure period due to changes in air temperature . The irradiance measurement overestimates the average irradiance over the exposure period, and thus reported (calculated) UV-C dose is higher than the true delivered dose.
Implications <i>User is a...</i>	Researcher studying the impact of UV-C on N95 viral inactivation	The researcher attributes measured viral inactivation to an artificially low UV-C dose. <ul style="list-style-type: none"> ▶ Protocols based on these reported results can yield insufficient decontamination. 	The researcher attributes measured viral inactivation to an artificially high UV-C dose. <ul style="list-style-type: none"> ▶ Protocols based on these reported results may recommend unnecessarily high dose and unnecessarily increase decontamination time. ▶ If insufficient viral inactivation was observed, report may incorrectly claim that reported dose is ineffective for N95 decontamination, potentially conflicting with other publications in which UV-C dose was measured accurately.
	Researcher studying the impact of UV-C on N95 fit & filtration	The researcher attributes measured N95 respirator damage to an artificially low UV-C dose. <ul style="list-style-type: none"> ▶ The number of decontamination cycles an N95 can withstand prior to degradation is underestimated, leading to premature disposal of scarce resources. 	The researcher attributes measured N95 respirator damage to an artificially high UV-C dose. <ul style="list-style-type: none"> ▶ The UV-C dose (and number of decontamination cycles) N95s can withstand prior to degradation is overestimated, which may lead to application of damaging levels of UV-C to N95 respirators.
	Clinical staff implementing UV-C decontamination of N95s	Clinical staff underestimate the delivered dose during N95 decontamination treatments, exceeding the target dose for decontamination. <ul style="list-style-type: none"> ▶ Inaccurate decontamination protocols are perpetuated. ▶ N95 respirator may be damaged (if reported UV-C dose is severely underestimated). 	Clinical staff overestimate the UV-C dose delivered to N95 respirators during a decontamination cycle. <ul style="list-style-type: none"> ▶ Virus may persist due to insufficient UV-C dose delivery.

Cell color indicates the level of safety risk posed by inaccurate UV-C dose measurement in different scenarios, where yellow denotes lower risk than red.

UV-C treatment does not reduce N95 respirator function, users should also assess whether preservation of respirator fit and filtration was evaluated, and they should consider how the applied UV-C dose compares to the maximum dose at which respirator integrity is expected to be maintained [10].

In implementing UV-C N95 decontamination protocols: UV-C decontamination should be used only during critical N95 shortages when in accordance with federal guidelines. UV-C dose should be regularly measured, particularly at locations receiving the highest and lowest doses, as the range of applied dose impacts decontamination efficacy and the number of times N95 respirators can be safely decontaminated prior to material degradation. The calibrated sensors used for these measurements should have narrow-band UV-C detection. Other factors that are important to consider when implementing N95 respirator decontamination and reuse:

1. High UV-C exposure, whether through a single high-dose treatment or many UV-C cycles, can degrade respirator materials and reduce filtration efficacy [10]. Due to differences in material construction, the maximum dose that an N95 respirator can withstand may be model-dependent.
2. Decontamination and multiple donning and doffing cycles can affect fit [43].
3. Shadowing and irradiation of surfaces nonperpendicular to the incident UV-C angle decrease the received dose and increase dose nonuniformity. For example, the lower viral inactivation efficacy observed on N95 facepieces with ridges has been attributed to shadowing [8]. The irradiance reaching shadowed surfaces will depend on the absorbance of the material in the optical path between the UV-C source and shadowed surface. Additionally, because irradiance depends on the angle of incident radiation [14], N95 respirator surfaces that are steeply sloped with respect to the incident light will generally receive a lower UV-C dose (Figure 8.1A).
4. Soiling agents (saliva, oils) can modulate pathogen inactivation efficacy by reducing UV-C penetration into the respirator material [44, 45].
5. Viral inactivation can be N95 respirator model-dependent [8].
6. Other pathogens with lower UV-C susceptibility, especially bacterial spores, may remain active on N95 respirators even if the applied UV-C dose achieves viral inactivation [46–48].
7. Elastic straps may require a secondary decontamination method [8, 44].

Application of the appropriate UV-C wavelength and application of the appropriate dose are critical metrics for reproducible UV-C N95 respirator decontamination protocols under crisis-capacity conditions. Engaging vertically integrated teams with engineering, infection-control/sterile-processing, and clinical expertise promotes technical validation and safe processing workflows. Full consideration of the technical and practical considerations of UV-C

N95 respirator decontamination is key to more safely weathering pandemic-induced crisis-capacity conditions.

8.7 Reporting Summary Examples

Recommended reporting summary for authors sharing research on UV-C decontamination of N95 respirators to support dissemination of accurate and reproducible UV-C decontamination protocols.

UV-C Author Reporting Summary

This form provides structure for reproducibility and transparency in reporting on studies of viral inactivation by UV-C irradiation. Because equipment for UV-C based decontamination is not standardized and actual UV-C dose depends on numerous factors, it is important for accuracy and reproducibility to report the physical parameters as outlined below. There are additional factors that may affect the efficacy of this technique, such as N95 style, layout, and N95 model. This checklist also does not evaluate filtration efficiency or N95 degradation from the decontamination process.

Hardware

1. UV-C Source if YES: specify where this information is in the text
if NO: explain why this information is not reported/not relevant

Make (brand) and model number Yes No

Type of source Yes No
For instance: mercury lamp, xenon lamp, LED, etc.

Dimensions of the source Yes No
Dimensions of emission source can be important for determining the angular variation in UV-C illumination. For instance: mercury lamp arc length (m) from electrode tip to electrode tip.

UV-C source layout Yes No
For instance: number, location, orientation, chamber specifications

Emission spectrum Yes No
State wavelengths emitted, and either show or reference the emission spectrum.

2. Optical Detector

Radiometer and sensor probe: make and model, wavelength range, calibration Yes No
For instance: "An ILT-1254 radiometer (International Light Technologies), which measures 254 nm wavelengths, was used to measure UV-C irradiance. The radiometer is calibrated annually according to manufacturer's instructions."

Any filters, diffusers, cosine correctors, or other optical elements attached to the sensor; brand and model number; specifications (e.g., wavelength range); purpose Yes No
For instance: "To specifically quantify UV-C irradiance, the spectroradiometer was fitted with a 254 nm shortpass filter (Newport HG-SC-OEM) to block out wavelengths above 254 nm."

Data and Reporting

3. The authors report:

Confirmed	n/a	
<input type="checkbox"/>	<input type="checkbox"/>	Distance between UV-C source(s) and UV-C detector(s)
<input type="checkbox"/>	<input type="checkbox"/>	Exposure time
<input type="checkbox"/>	<input type="checkbox"/>	Measurement of UV-C dose at the treated substrate
<input type="checkbox"/>	<input type="checkbox"/>	Calculations of UV-C dose at the treated substrate, using measured irradiance and exposure time <i>If UV-C dose was calculated from measured irradiance and time, please describe in the manuscript what irradiance measurements were used and any assumptions involved in the dose calculation (e.g., irradiance measurements collected throughout the exposure time, or a single irradiance measurement which was assumed to stay constant throughout exposure). Please discuss whether the calculated dose may be an over- or under-estimate, in light of any assumptions made. Because the output of a UV-C source can vary over time (ASTM E3170-16), best practice is to measure irradiance throughout the exposure period.</i>
<input type="checkbox"/>	<input type="checkbox"/>	Details about setup and methods: spatial arrangement of N95 respirators and UV-C detector(s) relative to the UV-C source(s), any chamber/room reflectivity, and characterization of UV-C dose distribution across entire area in which respirators are placed
<input type="checkbox"/>	<input type="checkbox"/>	Is the minimally acceptable dose applied to both sides of the respirator?

4. Terminology

Confirmed	n/a	
<input type="checkbox"/>	<input type="checkbox"/>	Irradiance measurements (W/cm^2) are described as irradiance or fluence rate
<input type="checkbox"/>	<input type="checkbox"/>	Dose measurements (J/cm^2) are described as dose or fluence <i>Please note that "dosage" is a redundant term for "dose" that should be avoided [UNF]</i>

5. Measurement of viral inactivation

Confirmed	n/a	
<input type="checkbox"/>	<input type="checkbox"/>	Measured viral inactivation is tied to UV-C dose at the substrate surface (not exclusively exposure time)

6. N95 Facepiece and Straps

Authors state N95 respirator make, model, and if results are expected to be model-dependent

<input type="checkbox"/>	Yes	<input type="text"/>
<input type="checkbox"/>	No	<input type="text"/>

Authors state position of straps and that straps may require secondary decontamination

<input type="checkbox"/>	Yes	<input type="text"/>
<input type="checkbox"/>	No	<input type="text"/>

UV-C has been found to be less effective in decontaminating N95 FFP1 straps (Sills et al., 2018; Helmreich & Henrich, 2018). If viral inactivation testing of straps was not performed or found ineffective, authors should state that secondary decontamination of straps may be required.

The Content provided is for INFORMATIONAL PURPOSES ONLY. DOES NOT CONSTITUTE THE PROVIDING OF MEDICAL ADVICE and is NOT INTENDED TO BE A SUBSTITUTE FOR INDEPENDENT PROFESSIONAL MEDICAL JUDGMENT, ADVICE, DIAGNOSIS, OR TREATMENT.

Bibliography

1. *Decontamination and Reuse of Filtering Facepiece Respirators* tech. rep. (CDC, Apr. 2020). <https://www.cdc.gov/coronavirus/2019-ncov/hcp/ppe-strategy/decontamination-reuse-respirators.html> (2020).
2. Memarzadeh, F., Olmsted, R. N. & Bartley, J. M. Applications of ultraviolet germicidal irradiation disinfection in health care facilities: Effective adjunct, but not stand-alone technology. en. *American Journal of Infection Control* **38**, S13–S24. ISSN: 0196-6553. <http://www.sciencedirect.com/science/article/pii/S0196655310004207> (2020) (June 2010).
3. *Ultraviolet disinfection guidance manual for the final long term 2 enhanced surface water treatment rule* tech. rep. (US EPA Office of Water, Nov. 2006). <https://nepis.epa.gov/Exe/ZyPDF.cgi?Dockkey=600006T3.txt> (2020).
4. FDA. *21CFR880.6600* Apr. 2019. <https://www.accessdata.fda.gov/scripts/cdrh/cfdocs/cfcfr/cfrsearch.cfm?fr=880.6600> (2020).
5. Lowe, J. J. *et al.* *N95 Filtering Facepiece Respirator Ultraviolet Germicidal Irradiation (UVGI) Process for Decontamination and Reuse* tech. rep. (University of Nebraska Medical Center, Apr. 2020). <https://www.nebraskamed.com/sites/default/files/documents/covid-19/n-95-decon-process.pdf> (2020).
6. CDC. *Strategies for Optimizing the Supply of N95 Respirators* en-us. source: www.cdc.gov. Apr. 9, 2021. <https://www.cdc.gov/coronavirus/2019-ncov/hcp/respirators-strategy/>.
7. Fisher, E. M. & Shaffer, R. E. A method to determine the available UV-C dose for the decontamination of filtering facepiece respirators. en. *Journal of Applied Microbiology* **110**, 287–295. ISSN: 1365-2672. (2020) (2011).
8. Mills, D. *et al.* Ultraviolet germicidal irradiation of influenza-contaminated N95 filtering facepiece respirators. en. *American Journal of Infection Control* **46**, e49–e55. ISSN: 01966553. <https://linkinghub.elsevier.com/retrieve/pii/S0196655318301408> (2020) (July 2018).

9. Tseng, C.-C. & Li, C.-S. Inactivation of Virus-Containing Aerosols by Ultraviolet Germicidal Irradiation. en. *Aerosol Science and Technology* **39**, 1136–1142. ISSN: 0278-6826, 1521-7388. <http://www.tandfonline.com/doi/abs/10.1080/02786820500428575> (2020) (Dec. 2005).
10. Lindsley, W. G. *et al.* Effects of Ultraviolet Germicidal Irradiation (UVGI) on N95 Respirator Filtration Performance and Structural Integrity. *Journal of Occupational and Environmental Hygiene* **12**. Publisher: Taylor & Francis, 509–517. ISSN: 1545-9624. <https://doi.org/10.1080/15459624.2015.1018518> (2020) (Aug. 2015).
11. Fischer, R. J. *et al.* Early Release - Effectiveness of N95 Respirator Decontamination and Reuse against SARS-CoV-2 Virus - Volume 26, Number 9—September 2020 - Emerging Infectious Diseases journal - CDC. en-us. https://wwwnc.cdc.gov/eid/article/26/9/20-1524_article (2020).
12. Kohli, I. *et al.* UVC Germicidal Units: Determination of Dose Received and Parameters to be Considered for N95 Respirator Decontamination and Reuse. en. *Photochemistry and Photobiology* **96**. eprint: <https://onlinelibrary.wiley.com/doi/pdf/10.1111/php.13322>, 1083–1087. ISSN: 1751-1097. <https://onlinelibrary.wiley.com/doi/abs/10.1111/php.13322> (2020) (2020).
13. Su, A. *et al.* Quantitative UV-C dose validation with photochromic indicators for informed N95 emergency decontamination. en. *PLOS ONE* **16**. Publisher: Public Library of Science, e0243554. ISSN: 1932-6203. <https://journals.plos.org/plosone/article?id=10.1371/journal.pone.0243554> (2021) (Jan. 2021).
14. Reifsnnyder, W. E. Radiation geometry in the measurement and interpretation of radiation balance. en. *Agricultural Meteorology* **4**, 255–265. ISSN: 0002-1571. <http://www.sciencedirect.com/science/article/pii/000215716790026X> (2020) (July 1967).
15. Center for Devices & Radiological Health. *Decontamination Bioburden Reduction Systems for Face Masks Respirators* Publication Title: U.S. Food and Drug Administration. <https://www.fda.gov/regulatory-information/search-fda-guidance-documents/recommendations-sponsors-requesting-euas-decontamination-and-bioburden-reduction-systems-face-masks> (2020).
16. *NPPTL Respirator Assessments to Support the COVID-19 Response* tech. rep. (CDC National Institute for Occupational Safety and Health, Oct. 2020). <https://www.cdc.gov/niosh/npptl/respirators/testing/DeconResults.html> (2020).
17. FDA. *UV Lights and Lamps: Ultraviolet-C Radiation, Disinfection, and Coronavirus* en. Publisher: FDA. Aug. 2020. <https://www.fda.gov/medical-devices/coronavirus-covid-19-and-medical-devices/uv-lights-and-lamps-ultraviolet-c-radiation-disinfection-and-coronavirus> (2020).
18. *Enforcement Policy for Sterilizers, Disinfectant Devices, and Air Purifiers During the Coronavirus Disease 2019 (COVID-19) Public Health Emergency* tech. rep. (Mar. 2020). <https://www.fda.gov/media/136533/download> (2020).

19. FDA. *STERIS STEAM Decon Cycle in AMSCO Medium Steam Sterilizers - Letter of Authorization (EUA)* Emergency Use Authorization. May 2020. <https://www.fda.gov/media/138282/download> (2020).
20. FDA. *Duke Decontamination System - Letter of Authorization* Emergency Use Authorization. Jan. 2021. <https://www.fda.gov/media/137762/download> (2021).
21. FDA. *Lumin LM3000 for Bioburden Reduction of Compatible N95 Respirators - Letter of Authorization* Dec. 2020. <https://www.fda.gov/media/144147/download>.
22. Smith, J. S. *et al.* Effect of various decontamination procedures on disposable N95 mask integrity and SARS-CoV-2 infectivity. *Journal of Clinical and Translational Science*. Publisher: Cambridge University Press, 1–5. ISSN: 2059-8661. (2020).
23. Ozog, D. M. *et al.* The effect of ultraviolet C radiation against different N95 respirators inoculated with SARS-CoV-2. en. *International Journal of Infectious Diseases* **100**, 224–229. ISSN: 1201-9712. <http://www.sciencedirect.com/science/article/pii/S1201971220307098> (2020) (Nov. 2020).
24. Poster, D. L. *et al.* Innovative Approaches to Combat Healthcare-Associated Infections Using Efficacy Standards Developed Through Industry and Federal Collaboration. *Proceedings of SPIE—the International Society for Optical Engineering* **10730**. ISSN: 0277-786X. <https://www.ncbi.nlm.nih.gov/pmc/articles/PMC6512965/> (2020) (2018).
25. Kowalski, W. *Ultraviolet Germicidal Irradiation Handbook: UVGI for Air and Surface Disinfection* en. ISBN: 978-3-642-01998-2 978-3-642-01999-9. <http://link.springer.com/10.1007/978-3-642-01999-9> (2020) (Springer Berlin Heidelberg, Berlin, Heidelberg, 2009).
26. Beck, S. E. *et al.* Action spectra for validation of pathogen disinfection in medium-pressure ultraviolet (UV) systems. en. *Water Research* **70**, 27–37. ISSN: 0043-1354. <http://www.sciencedirect.com/science/article/pii/S0043135414007982> (2020) (Mar. 2015).
27. Iii, E. R. B., Petri, B. & Sun, W. SARS-CoV-2 UV Dose-Response Behavior. en, 6.
28. Lytle, C. D. & Sagripanti, J.-L. Predicted Inactivation of Viruses of Relevance to Biodefense by Solar Radiation. en. *Journal of Virology* **79**. Publisher: American Society for Microbiology Journals Section: VACCINES AND ANTIVIRAL AGENTS, 14244–14252. ISSN: 0022-538X, 1098-5514. <https://jvi.asm.org/content/79/22/14244> (2020) (Nov. 2005).
29. McGuigan, K. G. *et al.* Solar water disinfection (SODIS): A review from bench-top to roof-top. en. *Journal of Hazardous Materials* **235-236**, 29–46. ISSN: 0304-3894. <http://www.sciencedirect.com/science/article/pii/S0304389412007960> (2021) (Oct. 2012).

30. Horton, L. *et al.* Spectrum of virucidal activity from ultraviolet to infrared radiation. en. *Photochemical & Photobiological Sciences* **19**. Publisher: Royal Society of Chemistry, 1262–1270. <https://pubs.rsc.org/en/content/articlelanding/2020/pp/d0pp00221f> (2021) (2020).
31. Lore, M. B. *et al.* Effectiveness of Three Decontamination Treatments against Influenza Virus Applied to Filtering Facepiece Respirators. *The Annals of Occupational Hygiene* **56**, 92–101. ISSN: 0003-4878. <https://doi.org/10.1093/annhyg/mer054> (2021) (Jan. 2012).
32. Narla, S. *et al.* The importance of the minimum dosage necessary for UVC decontamination of N95 respirators during the COVID-19 pandemic. *Photodermatology, Photoimmunology & Photomedicine* **36**, 324–325. <https://doi.org/10.1111/phpp.12562> (Apr. 2020).
33. Rutala, W. A. *et al.* Room Decontamination Using an Ultraviolet-C Device with Short Ultraviolet Exposure Time. en. *Infection Control & Hospital Epidemiology* **35**. Publisher: Cambridge University Press, 1070–1072. ISSN: 0899-823X, 1559-6834. (2020) (Aug. 2014).
34. Rutala, W. A. *et al.* Rapid Hospital Room Decontamination Using Ultraviolet (UV) Light with a Nanostructured UV-Reflective Wall Coating. en. *Infection Control & Hospital Epidemiology* **34**, 527–529. ISSN: 0899-823X, 1559-6834. https://www.cambridge.org/core/product/identifier/S0195941700033038/type/journal_article (2021) (May 2013).
35. Bolton, J. R. & Linden, K. G. Standardization of Methods for Fluence (UV Dose) Determination in Bench-Scale UV Experiments. EN. *Journal of Environmental Engineering* **129**. Publisher: American Society of Civil Engineers, 209–215. ISSN: 0733-9372. <https://ascelibrary.org/doi/abs/10.1061/%28ASCE%290733-9372%282003%29129%3A3%28209%29> (2021) (Mar. 2003).
36. Meulemans, C. C. E. The Basic Principles of UV–Disinfection of Water. *Ozone: Science & Engineering* **9**. Publisher: Taylor & Francis, 299–313. ISSN: 0191-9512. (2021) (Sept. 1987).
37. Rahn, R. O., Xu, P. & Miller, S. L. Dosimetry of room-air germicidal (254 nm) radiation using spherical actinometry. eng. *Photochemistry and Photobiology* **70**, 314–318. ISSN: 0031-8655 (Sept. 1999).
38. *tesa 54140 UV strips: product information* tech. rep. (tesa). <https://www.tesa.com/en-sg/industry/tesa-54140-uv-strips.html> (2020).
39. *Method of Testing Ultraviolet Lamps for Use in HVAC&R Units or Air Ducts to Inactivate Microorganisms on Irradiated Surfaces* tech. rep. STD 185.2 (ASHRAE, 2014). https://global.ihs.com/doc_detail.cfm?document_name=ASHRAE%20STD%20185%2E2&item_s_key=00634862.

40. *Standard Test Method for Determining Antimicrobial Efficacy of Ultraviolet Germicidal Irradiation against Influenza Virus on Fabric Carriers with Simulated Soil* en. Tech. rep. E3179-18 (ASTM International, 2018). <http://www.astm.org/cgi-bin/resolver.cgi?E3179-18> (2020).
41. Scrutinizing lasers. en. *Nature Photonics* **11**. Number: 3 Publisher: Nature Publishing Group, 139–139. ISSN: 1749-4893. <https://www.nature.com/articles/nphoton.2017.28> (2020) (Mar. 2017).
42. A solar checklist. en. *Nature Photonics* **9**. Number: 11 Publisher: Nature Publishing Group, 703–703. ISSN: 1749-4893. <https://www.nature.com/articles/nphoton.2015.233> (2020) (Nov. 2015).
43. Bergman, M. S. *et al.* Impact of multiple consecutive donnings on filtering facepiece respirator fit. eng. *American Journal of Infection Control* **40**, 375–380. ISSN: 1527-3296 (May 2012).
44. Heimbuch, B. & Harnish, D. Research to Mitigate a Shortage of Respiratory Protection Devices During Public Health Emergencies, 275 (Sept. 2019).
45. Fisher, E. M., Williams, J. & Shaffer, R. E. The Effect of Soil Accumulation on Multiple Decontamination Processing of N95 Filtering Facepiece Respirator Coupons Using Physical Methods. en. **27**, 11. <https://www.isrp.com/the-isrp-journal/journal-public-abstracts/1136-vol-27-no-1-2010-pp-16-26-matsumura-open-access/file> (2010).
46. Lin, T.-H. *et al.* Relative survival of Bacillus subtilis spores loaded on filtering facepiece respirators after five decontamination methods. *Indoor Air* **28**, 754–762. ISSN: 1600-0668. (2020) (2018).
47. Rutala, W. A., Weber, D. J. & HICPAC. Guideline for Disinfection and Sterilization in Healthcare Facilities. <https://www.cdc.gov/infectioncontrol/pdf/guidelines/disinfection-guidelines-H.pdf> (2020) (May 2019).
48. Malayeri, A. *et al.* Fluence (UV Dose) Required to Achieve Incremental Log Inactivation of Bacteria, Protozoa, Viruses and Algae. *IUVA News* **18**, 4–6 (Sept. 2016).

Chapter 9

Conclusions and Future Directions

In this work, we explored engineering principles for the development of quantitative tools for single-cell immunoblotting (scI) and UV-C decontamination of N95 filtering facepiece respirators (FFRs). Specifically, we explored methods to push the assay capabilities of scI, including understanding the limits of stripping and reprobing for multiplex protein target detection, utilizing segmentation approaches to detect low-abundance protein targets, and assessing the feasibility of assays that aim to detect proteoforms and other biomolecules (RNA and DNA) from single cells. Furthermore, we explored the current understanding of principles of UV-C decontamination for N95 FFRs, and how use of other sensors, including photochromic indicators (PCIs), can aid quantification of dose measurements for UV-C decontamination of N95 FFRs.

In our work on understanding protein losses during stripping and reprobing of scI (chapter 2), we utilize fluorescently-labeled protein to determine that the majority of protein losses occurred in the first few rounds of stripping, followed by a plateau in protein fluorescence. We additionally discover that the extent of protein loss is target-dependent. Finally, we discover that the amount of signal loss from multiple immunoassay cycles on the same protein target is greater than the signal loss from fluorescently-labeled proteins, suggesting that inefficiencies in the immunoassay process also contribute to immunoassay signal loss. We thus demonstrate that by creating a system to quantitatively assess retention of fluorescent protein signal across multiple stripping and reprobing cycles, we can tease apart the phenomena governing immunoassay signal loss in scI.

We next assessed principles of segmentation-based quantification for scI in chapter 3. We demonstrate that our segmentation pipeline can quantify scI with as high accuracy as the Gaussian fitting pipeline, and that segmentation can additionally quantify more low-abundance protein targets than Gaussian fitting. By understanding the fundamental principles of signal-to-noise ratio (SNR) quantification in both pipelines, we provide a mechanistic understanding for why segmentation can quantify more low-abundance protein targets. However, we also discover that Gaussian fitting is more accurate in quantifying protein targets with low separation resolution ($R_S < 0.5$), unless alternate segmentation approaches (e.g., two-dimensional Gaussian fitting) are utilized. In this manner, we showcase that an under-

standing of the mathematical properties governing protein band quantification can have a strong impact on the types of scIs that are ultimately curated for downstream analysis.

In chapters 4 and 5, we demonstrate preliminary work towards dual single-cell proteoform and RNA measurements. In chapter 4, we discuss a platform that can measure few numbers of DNA, RNA, and protein from the same cell by selective lysis of cell nuclei and cytoplasm. In chapter 5, we discuss preliminary studies towards dual single-cell proteoform and RNA-sequencing measurements. Specifically, we first find that there is a timescale mismatch between the rapid cell lysis and polyacrylamide gel electrophoresis (PAGE) steps necessary for protein target detection, and the long binding times necessary for mRNA extraction via functionalized beads. We next find evidence that suggests that we may be able to reduce this mismatch, and tune lysis timescales, by modulating (i) the cell-to-bead ratio for RNA extraction, and (ii) the pore size of the polycarbonate track etch (PCTE) membranes that we aim to hybridize to the polyacrylamide (PA) gel during lysis. Finally, preliminary experiments of reverse transcription and PCR on a glass slide suggests that on-chip whole transcriptome amplification (WTA) may be possible. Thus, we demonstrate that quantification of key target metrics enables assessment of the feasibility of dual proteoform and RNA sequencing measurements from the same cell.

Finally, we investigate quantitative principles of UV-C decontamination on N95 FFRs (chapters 6 - 8). In particular, we investigate principles for designing quantitative workflows for accurate UV-C dose measurement using PCI. We further demonstrate how various factors, including respirator geometry, placement in a decontamination system, lamp irregularities, and other system components can dramatically affect the dose delivered to a respirator. We conclude by discussing common pitfalls of UV-C dose measurements, and how standardization of dose reporting can reduce errors.

Looking forward, we envision that many of the quantitative frameworks developed in this thesis for single-cell biology can be used for further quantification and assessment of specific biological questions (e.g., mechanisms of HER2+ isoform formation), and also aid the development of additional multimodal assays, including dual DNA and proteoform detection. Similarly, we expect that the development of quantitative workflows for decontamination of N95 respirators will provide a framework for decontamination of other personal protective equipment (PPE), especially in low-resource settings. We anticipate that the continued development of quantitative tools for biology and medicine, including tools for pandemic response, will be critical for addressing outstanding challenges and unmet needs in these fields.